Dispersion relations in two-photon hadronic processes

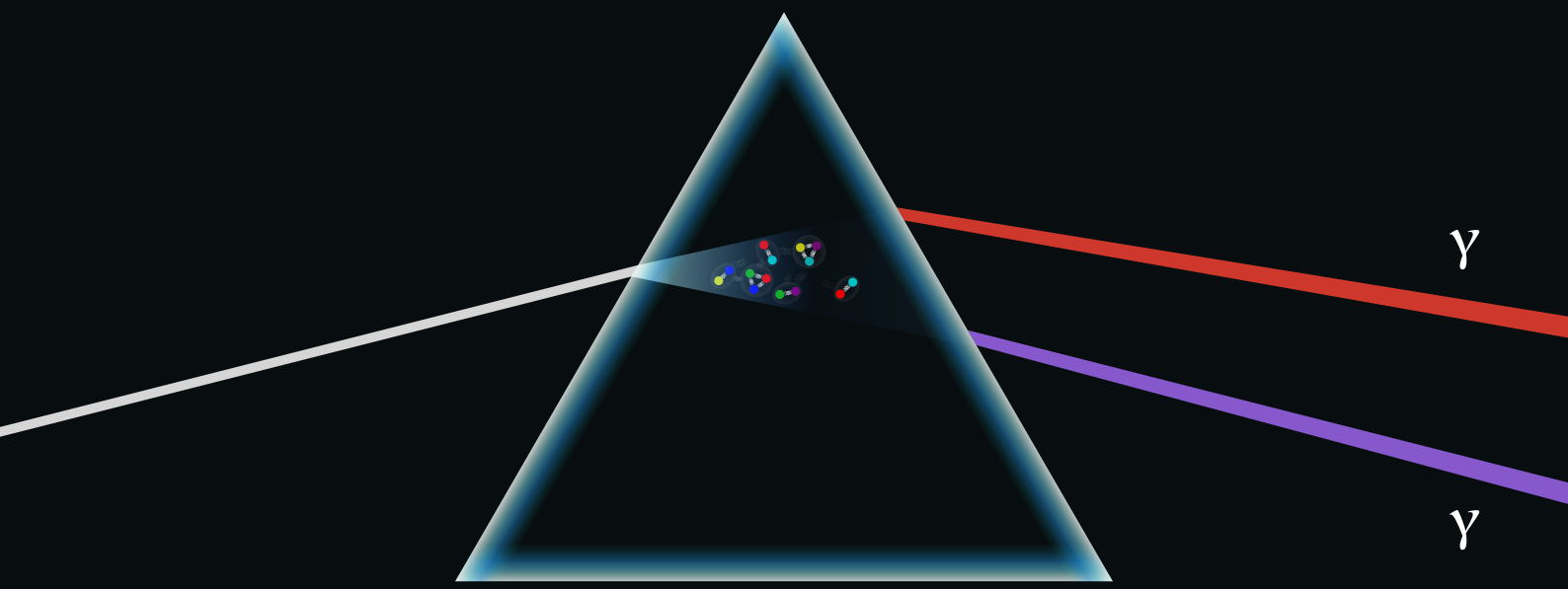

Oleksii Gryniuk

Dispersion relations in two-photon hadronic processes

Dissertation
zur Erlangung des Grades
„ Doktor der Naturwissenschaften “

am Fachbereich Physik, Mathematik und Informatik
der Johannes Gutenberg-Universität Mainz

vorgelegt von
Oleksii Gryniuk
geboren in Kyiv (Ukraine)

Mainz, 2020

Abstract

The general principles of quantum field theory, such as unitarity of the S-matrix, crossing symmetry and causality (dispersion relations), allow for construction of the full forward Compton scattering (CS) amplitude off protons based on experimental hadronic photoproduction cross sections. This amplitude is an essential test for the low-energy effective field theories, and its low-energy behaviour provides model-independent constraints on the extraction of the electromagnetic polarizabilities of the proton via sum rules. A numerical evaluation of the forward CS amplitude off the proton together with the corresponding observables and sum rules is provided.

Furthermore, the direct assessment of the forward CS amplitude is examined by utilizing the di-lepton photoproduction off protons. It is described how the real part of the unpolarized forward CS amplitude can be accessed at a regime with sufficiently low momentum transfer and outgoing photon virtuality, through the measurement of the forward-backward asymmetry of the outgoing lepton pair interchange in the di-lepton photoproduction process. Estimates of this asymmetry for various kinematics setups at Jefferson Lab and at a planned Electron-Ion Collider are provided. Such measurements may help discriminate between the existing state-of-the-art fits of the total photoabsorption data, ultimately improving our understanding of the high-energy behavior of the hadronic total cross sections, required for the planning of future high-energy colliders, as well as for interpreting cosmic ray experiments.

A similar approach to access the J/ψ – proton and Υ – proton forward scattering amplitudes is applied. An analysis of these amplitudes is performed, by relating their imaginary parts to the corresponding photoproduction cross section data. By calculating the s-wave scattering length for these quarkonia from the real parts of the amplitudes, the possibility of bound states in nuclear systems is investigated. It is shown for the J/ψ case that the forward-backward asymmetry of the di-lepton photoproduction at Jefferson Lab can be a very sensitive observable for a refined extraction of the scattering length. For the Υ state, the experimental feasibility at a planned Electron-Ion Collider is examined and a clear potential to extract the scattering length from precision photoproduction measurements is concluded.

The application of dispersion relations is extended also to the case of hadronic light-by-light scattering, which is currently one of the two dominant uncertainties in the interpretation of the $3 - 4\ \sigma$ discrepancy between experiment and the Standard Model prediction of the muon's anomalous magnetic moment a_μ. A model-independent treatment of the forward light-by-light amplitudes is considered by comparing a direct calculation of the real part of this amplitude through lattice quantum chromodynamics with a sum rule evaluation based on the phenomenological input of the $\gamma^*\gamma^*$-fusion cross sections.

Zusammenfassung

Die allgemeinen Prinzipien der Quantenfeldtheorie, wie die Unitarität der S-Matrix, Kreuzsymmetrie und Kausalität (Dispersionsrelationen), ermöglichen die Konstruktion der vollständigen, vorwärts-gerichteteten Compton-Streuamplitude (CS) am Proton, basierend auf experimentellen hadronischen Querschnitten der Photoproduktion. Diese Amplitude dient als wesentlicher Test für effektive Niedrigenergie-Feldtheorien, und ihr Verhalten bei kleinen Energien liefert modellunabhängige Einschränkungen für die Extraktion der elektromagnetischen Polarisierbarkeiten des Protons mittels Summenregeln. Eine numerische Auswertung der vorwärts gerichteten CS-Amplitude am Proton, zusammen mit den entsprechenden Observablen und Summenregeln wird bereitgestellt.

Außerdem wird die direkte Bewertung der vorwärts gerichtete CS-Amplitude unter Verwendung der Dilepton-Photoproduktion am Proton untersucht. Es wird beschrieben, wie der Realteil der unpolarisierten, vorwärts gerichteten CS-Amplitude in einem Regime mit ausreichend geringem Impulsübertrag und endlicher, ausgehender Photonenvirtualität experimentell durch die Vorwärts-Rückwärts-Asymmetrie des ausgehenden Lepton-Paars im Dilepton-Photoproduktionsprozess gemessen werden kann. Abschätzungen dieser Asymmetrie für verschiedene Kinematiken im Jefferson Lab sowie dem geplanten Elektronen-Ionen-Beschleuniger werden geliefert. Solche Messungen können dazu beitragen, zwischen den vorhandenen, auf dem neuesten Stand der Technik basierenden Anpassungen der gesamten Photoabsorptionsdaten zu unterscheiden und letztendlich unser Verständnis des Hochenergieverhaltens der hadronischen Gesamtquerschnitte zu verbessern, das beispielsweise sowohl für die Planung zukünftiger Hochenergie-Beschleuniger erforderlich ist, als auch zur Interpretation von Experimenten mit kosmischen Strahlen.

Ein ähnliches Verfahren wird verwendet, um die vorwärts gerichteten Streuamplituden von J/ψ – Proton und Υ – Proton zu bestimmen. Eine Analyse dieser Amplituden wird durchgeführt, indem ihre Imaginärteile mit den entsprechenden Querschnittsdaten der Photoproduktion in Beziehung gesetzt werden. Durch Berechnung der Streulänge der S-Wellen für diese Quarkonia aus den Realteilen der Amplituden, wird die Möglichkeit gebundener Zustände in Kernsystemen untersucht. Es wird für den Fall J/ψ gezeigt, dass die Vorwärts-Rückwärts-Asymmetrie der Dilepton-Photoproduktion im Jefferson Lab eine sehr empfindliche Observable für eine verfeinerte Extraktion der Streulänge sein kann. Für den Zustand Υ wird die experimentelle Machbarkeit eines geplanten Elektronen-Ionen-Kolliders untersucht und ein klares Potenzial zur Extraktion der Streulänge aus präzisen Photoproduktionsmessungen geschlossen.

Die Anwendung von Dispersionsrelationen wird auch auf den Fall der hadronischen Halpern-Streuung ausgedehnt, die derzeit eine der beiden vorherrschenden Unsicherheiten bei der Interpretation der 3 – 4 σ Diskrepanz zwischen Experiment und der Vorhersage des Standardmoduls zum anomalen magnetischen Moment des Myons a_μ darstellt. Eine modellunabhängige Behandlung der vorwärts gerichteten Halpern-Amplituden wird durch Vergleich einer direkten Berechnung des Realteils dieser Amplitude durch Gitterquantenchromodynamik mit einer Summenregelauswertung in Betracht gezogen, die auf experimentellen Daten des Wirkungsquerschnitts von $\gamma^*\gamma^*$-Fusion basiert.

List of publications

[1] Jeremy Green, Oleksii Gryniuk, Georg von Hippel, Harvey B. Meyer, and Vladimir Pascalutsa, "Lattice QCD calculation of hadronic light-by-light scattering", Phys. Rev. Lett. **115**, 222003 (2015), arXiv:1507.01577 [hep-lat].

[2] Oleksii Gryniuk, Franziska Hagelstein, and Vladimir Pascalutsa, "Evaluation of the forward Compton scattering off protons: Spin-independent amplitude", Phys. Rev. D **92**, 074031 (2015), arXiv:1508.07952 [nucl-th].

[3] Oleksii Gryniuk, Franziska Hagelstein, and Vladimir Pascalutsa, "Evaluation of the forward Compton scattering off protons: II. Spin-dependent amplitude and observables", Phys. Rev. D **94**, 034043 (2016), arXiv:1604.00789 [nucl-th].

[4] Oleksii Gryniuk and Marc Vanderhaeghen, "Accessing the real part of the forward J/ψ-p scattering amplitude from J/ψ photoproduction on protons around threshold", Phys. Rev. D **94**, 074001 (2016), arXiv:1608.08205 [hep-ph].

[5] Antoine Gérardin, Jeremy Green, Oleksii Gryniuk, Georg von Hippel, Harvey B. Meyer, Vladimir Pascalutsa, and Hartmut Wittig, "Hadronic light-by-light scattering amplitudes from lattice QCD versus dispersive sum rules", Phys. Rev. D **98**, 074501 (2018), arXiv:1712.00421 [hep-lat].

[6] Oleksii Gryniuk, Sylvester Joosten, Zein-Eddine Meziani, and Marc Vanderhaeghen, "Υ photo-production on the proton at the Electron-Ion Collider", arXiv:2005.09293 [hep-ph].

Conference proceedings

[7] Jeremy Green, Nils Asmussen, Oleksii Gryniuk, Georg von Hippel, Harvey B. Meyer, Andreas Nyffeler, and Vladimir Pascalutsa, "Direct calculation of hadronic light-by-light scattering", PoS **LATTICE2015**, 109 (2016), arXiv:1510.08384 [hep-lat].

[8] Antoine Gerardin, Jeremy Green, Oleksii Gryniuk, Georg von Hippel, Harvey B. Meyer, Vladimir Pascalutsa, and Hartmut Wittig, "Light-by-light forward scattering amplitudes in Lattice QCD", EPJ Web Conf. **175**, 06030 (2018), arXiv:1710.09359 [hep-lat].

[9] I. V. Anikin et al., "Nucleon and nuclear structure through dilepton production", Acta Phys. Polon. B **49**, 741–784 (2018), arXiv:1712.04198 [nucl-ex].

[10] Nils Asmussen, Antoine Gerardin, Jeremy Green, Oleksii Gryniuk, Georg von Hippel, Harvey B. Meyer, Andreas Nyffeler, Vladimir Pascalutsa, and Hartmut Wittig, "Hadronic light-by-light scattering contribution to the muon g–2 on the lattice", EPJ Web Conf. **179**, 01017 (2018), arXiv:1801.04238 [hep-lat].

Contents

Chapter 1

Introduction

1.1 Dispersion relations

The very general, yet essential physical principle, built into the quantum field theory (QFT), is *causality*, which in the mathematical language of the scattering matrix (or the S-matrix) is translated into its analyticity (holomorphicity) in the energy variables. Combined with the unitarity as the total probability conservation law consequence, and the crossing symmetry, this gives rise to the celebrated *dispersion relations*[1] (DRs). This remarkably elegant scientific concept is one distinguished example of an independent emergence of a similar idea in different fields of physics, the historical origins of which date back to at least as far as almost one and a half century ago.

The initial concept of DR naturally comes from optics, where the wave view on light phenomena was dominating scientific thinking in the middle of the 19th century [11]. The phenomenon of dispersion of light manifests itself in the functional relation between the energy (or frequency) and the wavenumber of a light wave propagating in a medium, or, equivalently, in the frequency/wavenumber dependence of the index of refraction. In the case when the phase velocity depends on the frequency, a non-monochromatic wave packet is, thus, geometrically dispersed. The idea of a relation between the absorption of light in the medium and the refractive index eventually led to the first statement of the *optical theorem* (OT) (see Ref. [12] for a historical review). The optical index of refraction can be extended to the complex values by conveniently incorporating the extinction coefficient κ in its absorptive (imaginary) part:

$$n = n_{\text{refr.}} + i\kappa. \tag{1.1}$$

The influence of the absorption coefficient on the dispersion of light was first discussed by Sellmeier [13] and independently by Lord Rayleigh [14] in 1871. In the context of his famous works on the colour and polarization of the sky, Rayleigh expressed the (complex) index of refraction in terms of the forward amplitude $f(\theta = 0)$ for light scattered off the molecules (nitrogen and oxygen) in the lower atmosphere:

$$n = 1 + \frac{2\pi N}{k^2} f(\theta = 0), \tag{1.2}$$

where N is the number density of scatterers and k is the wavenumber. Rayleigh further observed the connection between the absorptive part of n and what is now known as the total cross section, which results into the modern statement of the OT, first explicitly given by Mie in 1908 [15] for the scattering of light off the homogeneously spherical particles:

$$\sigma_{\text{tot}} = \frac{4\pi}{k} \operatorname{Im} f(\theta = 0). \tag{1.3}$$

[1] While often used as the synonym to the Hilbert transform between the real and imaginary parts of a physical amplitude (or a response function) on its own, here we specifically refer to "dispersion relation" as the former in a combination with the optical theorem, thus incorporating the total absorptive cross section inside the integral for the real part of the forward scattering amplitude.

In the later famous papers by Kronig [16] and Kramers [17] in 1926/27, the idea of causal propagation of light was used to derive the Hilbert-transform relation for the refractive index as a function of frequency. Together with the expression in terms of the forward scattering amplitude (1.2) and the OT (1.3), this leads to the dispersion relation for $\mathrm{Re}\, f(\omega, \theta = 0)$:

$$\mathrm{Re}\, f(\omega, \theta = 0) = \frac{1}{2\pi^2} \fint_0^\infty \frac{\omega'^2 \sigma_{\mathrm{tot}}(\omega')}{\omega'^2 - \omega^2} d\omega', \tag{1.4}$$

where the slash denotes the Cauchy's principal value integral. Similarly, the imaginary part of the forward amplitude can be expressed in terms of the integral over its real part. In the context of the index of refraction, causality (i.e., forbiddance for a signal transmittance over a spacelike space-time interval) thus directly implies the possibility to obtain the dispersion of light (i.e., the functional dependence $n_{\mathrm{refr.}}(\omega)$) based on its absorption, and vice versa. Equivalently, DR mutually binds the forward scattering amplitude with the total absorptive cross section. Moreover, without application of the OT, the constraint between the real and imaginary parts of an amplitude can as well be imposed for the non-forward scattering cases. The Kramers-Kronig relations, as inferred straight from the requirement of strict causality which leads to analyticity of a response function, were later rigorously formulated for the general linear physical system[2] with the time-independent interaction law by Toll in 1956 [18]. By that time, the DRs were well-known and enjoyed applications in various fields, from particle scattering to electrical network theory (where a suitable response function corresponds to impedance).

Within the quantum theory, the statement of the OT appeared first in the Feenberg's PhD thesis and his paper [19], while not initially recognized by others as particularly interesting [12]. When the S-matrix was invented by Wheeler in 1937 [20], it was shown by him to be unitary:

$$S S^\dagger = \hat{1}. \tag{1.5}$$

In 1943 Heisenberg independently reinvented the S-matrix [21], proved its unitarity and for the first time derived from it the generalized optical theorem:

$$\mathrm{Im}\, f(\hat{k}', \hat{k}) = \frac{k}{4\pi} \int d\hat{k}'' f(\hat{k}', \hat{k}'')\, f^*(\hat{k}'', \hat{k}), \tag{1.6}$$

where $\hat{k}$ ($\hat{k}'$) is the incoming (outgoing) particle unit momentum vector, the integration goes over all directions, and the interaction is assumed time-invariant. While one obvious technical application of the forward version of OT (1.3) is to calculate total cross sections, which was its common use case among theorists by the middle of 1950s [12], an important employment of the general theorem (1.6) was initiated in Ref. [22] and allows for the reconstruction of the scattering phase based on a given differential cross section. The application of the forward OT (1.3) in Eq. (1.4), though only limiting to the special case, raises the Kramers-Kronig relation to a significantly greater level of importance by inclusion of the direct experimental content, which by now is often very well measured.

DRs became one of the integral and defining principles of the S-matrix theory emerging by 1950s, which was conceptually built on the sole basis of relativity, unitarity and analyticity. After the theory was established and advocated as the first-principle approach by Heisenberg, it enjoyed a growing interest among particle physicists initially as a promising tool to describe the strong interaction, and eventually led to the birth of string theory. With the rise of quantum chromodynamics (QCD) in 1970s, the S-matrix theory was largely superseded. Nevertheless, it produced some notable achievements, and one of its long-lasting legacies is the Regge theory. Results of the latter remain relevant for hadron physics until today, as it is essentially the

[2] i.e., a system where the "output" function is a linear functional of the "input" function.

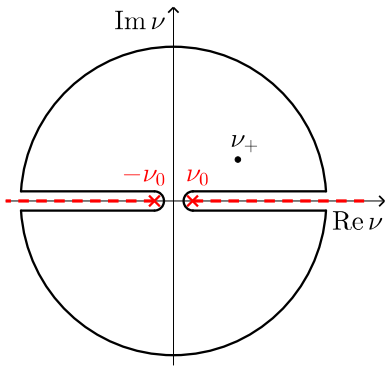

Figure 1.1: Branch cuts of an amplitude and the contour of integration for the derivation of QFT DRs. Due to causality, the amplitude is analytic on the physical sheet everywhere inside the contour.

only available non-perturbative tool for a phenomenological description of particle scattering at very high energies. So although with the advent of QFT the general principles of the S-matrix are automatically incorporated into it, in practice it is often not possible to perform a first-principle calculation of scattering processes in the non-perturbative region.

When carrying out a dispersive treatment of a scattering process in QFT, the initial requirement is to separate the dynamical amplitudes — the set of scalar functions corresponding to the given process, which are free from kinematical singularities and constraints. The analytic structure of the S-matrix is additionally guided by its crossing symmetry, which dictates the proper analytical continuation of the amplitudes as functions of the appropriate energy variable to the full complex manifold. One can construct the convenient linear combinations of the dynamical amplitudes (which we further will simply refer to as "amplitudes"), which are even or odd functions of the crossing-symmetric variable ν. Such an amplitude $f(\nu)$ will have symmetrical branch cuts on the real axis, starting with the branch points ν_0 and $-\nu_0$ corresponding to the threshold of inelastic scattering, and extending to $\pm\infty$, as shown on Fig. 1.1. With the additional assumption on a slow enough growth of $f(\nu)$ at infinities[3], the corresponding DR reads:

$$f(\nu) = \frac{2}{\pi}\int_{\nu_0}^{\infty} d\nu' \frac{\nu^{(\prime)}}{\nu'^2 - \nu^2 - i\epsilon}\,\mathrm{Im}\, f(\nu'), \tag{1.7}$$

where the limit $\epsilon \to 0^+$ is implied, and where $\nu^{(\prime)}$ stands for ν in case $f(\nu)$ is odd, and for ν' in case $f(\nu)$ is even. For the *forward* scattering this is then complemented by the OT:

$$\mathrm{Im}\, f(\nu, \theta = 0) \;=\; \frac{\nu}{4\pi}\,\sigma_{\mathrm{tot}}(\nu), \tag{1.8}$$

where σ_{tot} stands for the appropriate combination of the helicity cross sections, corresponding to the helicity amplitudes, and where the factor ν corresponds to the special case of a zero-mass particle scattering (e.g. a real photon). Note that the exact overall factor in the equality (1.8) depends on the convention for the dynamical amplitude in relation to the Feynman amplitude, which differs for different chapters of this thesis. As mentioned further in Section 1.6, definition of ν varies from chapter to chapter too.

[3] such that the dispersion integral is convergent, i.e., the integrals over infinitely large semi-circles on Fig. 1.1 vanish; if this is not the case, one may consider writing the DR for $(f(\nu) - f(0))/\nu^i$ instead, with the appropriate power i, assuming that a new pole is not introduced. The need for such subtraction may very well be inferred from the high energy Regge rise rate behaviour of the total cross section.

In the present thesis we will be utilizing Eq. (1.7) together with the OT (1.8) for the forward Compton scattering (CS) off the proton, forward scattering of a quarkonia off the proton, and the forward hadronic light-by-light scattering (HLbL).

1.2 Compton scattering

Dispersion relations in QFT as a consequence of strict causality were derived, among others, by Gell-Mann, Goldberger and Thirring in their papers in 1954-55 [23, 24], where they have also obtained for the first time the exact expression for the two forward amplitudes of CS off nucleons in terms of integrals of the corresponding photoabsorption cross sections (see Refs. [25–27] for reviews).

In practice, the consistently written relation (1.7) often requires subtraction, which can conveniently be chosen at $\nu = 0$. This is the case for the forward Compton scattering off a charged particle, and this subtraction is well-known exactly, thanks to the low-energy theorem proven first for the spin-$\frac{1}{2}$ target by Thirring in 1950 [28], who explicitly showed that in the zero-energy limit the CS amplitude reproduces the Thomson term precisely. The result was extended by Low [29] and by Gell-Mann and Goldberger in 1954 [30] to the expansion up to first order in photon energy which appends the anomalous magnetic moment of the particle and implies no assumption on its internal structure[4]. The theorem was later derived for an arbitrary-spin target by Saito [32].

In the present thesis, we consider the Compton scattering off protons, for which the further low-energy expansion combined with the DR produces a number of useful sum rules, most notably those of Gerasimov, Drell and Hearn (GDH) [33, 34] at the linear order, and of Baldin [35] at the next order. These sum rules relate the integrals over the absorptive cross sections to the experimentally measurable electromagnetic structure quantities, such as the electric and magnetic polarizabilities. The computation of the sum rules up to the fifth order is performed in Chapter 2.

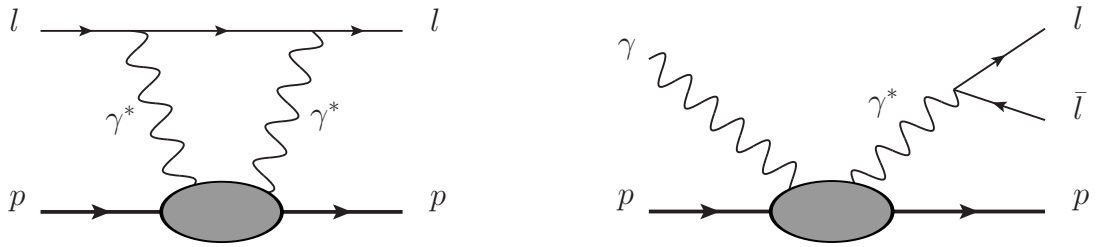

Figure 1.2: Left: double virtual CS off proton as part of the two-photon exchange diagram. Right: Di-lepton photoproduction off proton through TCS.

The forward CS serves as a basis for model calculations where a virtual CS process is involved, such as the double virtual or the near-forward single-virtual timelike CS (TCS). The former is specifically relevant for a precision extraction of the proton radius from atomic spectroscopy (see, for example, Ref. [36]), where the two-photon exchange correction (Fig. 1.2, left) to the muonic hydrogen Lamb shift remains the largest theoretical uncertainty. The TCS (Fig. 1.2, right) is involved in the process of di-lepton photoproduction, which is one of the main mechanisms responsible for depletion of cosmic-ray energy via scattering off the cosmic microwave background. While in that case it is dominated by the Bethe-Heitler process [37],

[4] The proofs of Low and Gell-Mann and Goldberger are made with the assumptions of C, P and T-invariance, while the generalized theorem without these assumptions was derived by Almond [31].

the TCS outweighs for a certain kinematics. A recent proposal to measure the ratio between photoproduction of the electron-positron and the muon-antimuon pairs on the proton was made by Pauk and Vanderhaeghen [38], with the aim to test lepton universality, which is again of interest in a precision extraction of the proton charge radius. While in the latter study the full differential cross sections are considered and the kinematics was chosen specifically for the TCS part to be a negligible background, in Chapter 3 of the present thesis we will explore a task to measure the interference between the BH and TCS.

The extension of DRs to the non-forward real CS was in development since 1960s, but only recently became practical thanks to the newly conducted high-precision experiments. There were multiple recent advances in the extraction of the static and dynamical nucleon polarizabilities with the help of various approaches with the non-forward DRs (e.g. see Refs. [25, 39, 40]). Moreover, an access through DRs for the virtual (incident photon) CS to the so called generalized polarizabilities (GPs) [41, 42], which map out the spatial distribution at the quark level of the polarizability of a hadron, was developed more recently and successfully applied for the extraction of scalar GPs of the proton [43, 44].

1.3 Quarkonium – nucleon interaction

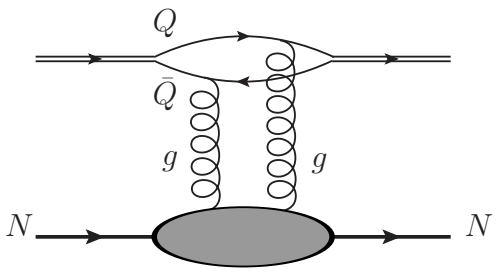

Figure 1.3: Two-gluon exchange interaction between a quarkonium $Q\bar{Q}$ and a nucleon N.

The interaction between heavy quarkonia, such as J/ψ and Υ, and light hadrons or nuclei provides a unique setup to study the gluonic van der Waals interaction in Quantum Chromodynamics (QCD). Being a small sized system, the heavy quarkonium $Q\bar{Q}$ can be treated as a color dipole, and the effective two-gluon exchange interaction between the quarkonium and the light hadron or nucleus (see Fig. 1.3) may be estimated from the knowledge of its chromo-electric polarizability, see Refs. [45–47] for reviews and references therein.

If this effective interaction is strong enough, a bound state between the $Q\bar{Q}$ state and the light hadron or nucleus may be formed [48–50]. Early calculations for the chromo-electric polarizability, treating the heavy quarkonium as a Coulombic bound state [51, 52], yielded estimates for the quarkonium binding energy in nuclear matter $B_{J/\psi} \sim 10$ MeV for J/ψ, and $B_\Upsilon \sim 2-4$ MeV for Υ [50]. Many follow-up calculations have explored the possibility of quarkonium nuclear bound states within different theoretical frameworks [53–59].

DRs provide one such framework by describing the forward scattering of a heavy quarkonium off a proton or nuclear target in terms of the $Q\bar{Q}N \to X$ total cross section, and thus infer from this its scattering length, which in turn determines the binding energy in nuclear matter. While quarkonium – nucleon scattering cross sections are not available from direct experiments, it is reasonable to employ the vector meson dominance model [60] to relate these to the corresponding photoproduction cross sections. We will utilize this approach for the J/ψ and Υ scatterings off a proton in Chapter 4.

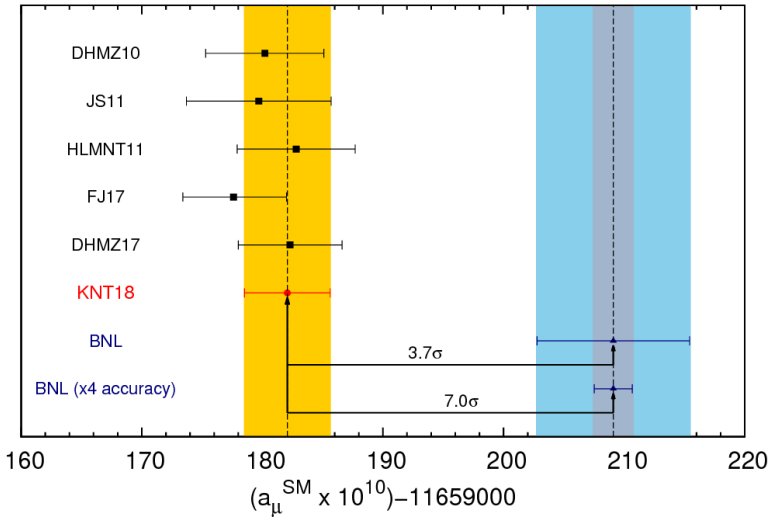

Figure 1.4: Figure from Ref. [64]: The current theory/experiment discrepancy for a_μ. The yellow band represents the estimated theoretical uncertainty, while the wider blue band stands for uncertainty of the BNL measurement [65]. The narrower blue band is the projected uncertainty for the ongoing experiment at Fermilab [66]. The recent KNT18 analysis is from Ref. [64].

1.4 Hadronic light-by-light contribution to $g-2$

The non-vanishing probability of two photons scattering off each other is a striking prediction of quantum electrodynamics (QED) [61, 62]. The smallness of the cross section has so far prohibited a direct experimental observation, although evidence for the phenomenon has recently been found by the ATLAS experiment in relativistic heavy-ion collisions [63]. Equally interesting is the scattering of spacelike virtual photons, $\gamma^*\gamma^* \to \gamma^*\gamma^*$. While the contributions of virtual leptons are calculable in QED perturbatively, the hadronic contributions require a non-perturbative approach.

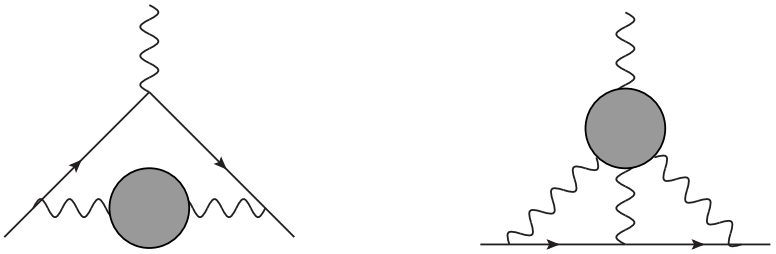

Figure 1.5: Leading-order contributions from the hadronic vacuum polarization (left) and the hadronic light-by-light scattering (right) to a_μ. The blobs incorporate the hadronic interaction part.

One very timely application of hadronic light-by-light (HLbL) scattering is the anomalous magnetic moment of the muon, $a_\mu = \frac{1}{2}(g-2)_\mu$. The current discrepancy between the direct measurement of a_μ and the Standard Model prediction amounts to about 3.7 standard deviations [64, 67]. While the current theory and experimental errors are comparable in size, two new $(g-2)_\mu$ experiments [68, 69] in preparation at J-PARC and ongoing at Fermilab aim at reducing the experimental error by a factor of four (see narrower blue band on Fig. 1.4).

The largest sources of theory error are contributions from the hadronic vacuum polarization and from HLbL scattering (Fig. 1.5, left and right, respectively). The latter is expected to dominate in the future in view of the dedicated measurements at e^+e^- colliders ever better constraining the former. Although an active area of research, the experimental data needed for the recently proposed data-driven dispersive approaches to HLBL [70–74] are harder to obtain, and lattice QCD calculations are in particularly high demand.

At the same time, lattice calculations necessarily contain systematical simplifications and restrictions, including the challenge to perform simulation at the physical quark masses, which ultimately heavily limits its power of the first-principle approach, sometimes making it difficult to verify the particular yields. A cross-check with an independent model approach is thus often desired. When the photons are real or spacelike, DRs can be used to express the forward $\gamma^*\gamma^*$ scattering amplitudes in terms of experimentally more accessible $\gamma^*\gamma^*$-fusion cross sections [75–78]. The hadronic contributions to the $\gamma^*\gamma^* \to \gamma^*\gamma^*$ amplitudes can be computed on the lattice [1] and compared to the DR model.

1.5 Thesis outline

This thesis is heavily based on the content of seven co-authored papers, five of which are published (Refs. [1–5]), one has been submitted for a publication (Ref. [6]), and one more is currently in preparation for the submission.

Namely, Chapter 2 is compiled based on Refs. [2] and [3]. Chapter 3 is based on the paper in preparation. Chapter 4 incorporates the content of the published paper [4] and the recently submitted paper [6]. The relevant part of Ref. [5] is composed into Chapter 5. Most of the figures and tables presented in the thesis are taken from the listed published (and submitted) co-authored material, as indicated in the corresponding captions.

The subsequent Chapters are thus organized as follows. We start by considering the process of the forward CS off protons in Chapter 2. After introducing the motivation for the calculation performed further, we briefly establish its theoretical basis and evaluate the full forward CS amplitude by substituting the empirical total photoabsorption cross sections into dispersive sum rules. We then turn our sight onto the TCS, namely as involved in the process of di-lepton photoproduction off protons, in Chapter 3. After a short introduction and discussion of the fits to the high energy photoproduction cross section, we explain in detail how to measure the real part of the forward CS off the proton via the di-lepton photoproduction at a near-forward kinematics. For the purpose of the feasible experimental estimates, we make use of the spin-averaged forward CS amplitude, obtained in the previous Chapter. In Chapter 4 we continue on the TCS topic and first apply the established technique to the di-lepton photoproduction off protons through the J/ψ resonance. In this case, we shift our attention onto the quarkonium – proton interaction, and perform an analysis with the aim to extract the binding energy of the J/ψ in nuclear matter. We furthermore do the same for the Υ – proton case, but we emphasize the need for the new experimental assessment, and thus make predictions for an EIC setting. We next turn in Chapter 5 onto a separate, but adjacent topic of the application of a formalism, which is analogous to the case of forward CS: we build a model of the $\gamma^*\gamma^*$-fusion cross section comprised of hadronic resonances, and relate it to the forward HLbL amplitudes through the dispersion relations. This Chapter is dedicated to showing how we connect this phenomenological model with the lattice QCD calculations of HLbL, with further applications to the computation of the muon's anomalous magnetic moment. Finally, the results of the thesis are summarized in Chapter 6.

1.6 Notations and physical constants

Throughout the text, we use natural units $\hbar = c = 1$ ($\alpha = e^2/4\pi$) and the Einstein summation convention $a_\mu b^\mu \equiv \sum_\mu a_\mu b^\mu$ is implied. We use the Minkowski metric tensor

$$\mathrm{g}^{\mu\nu} = \mathrm{diag}(1, -1, -1, -1),$$

and the covariant gamma-matrices are defined by the following anticommutation relation:

$$\frac{1}{2}\{\gamma^\mu, \gamma^\nu\} = \mathrm{g}^{\mu\nu}\,\hat{1}.$$

We denote the commutator of the gamma-matrices as $\gamma^{\mu\nu} = \frac{1}{2}[\gamma^\mu, \gamma^\nu]$.

For the Compton and di-lepton photoproduction off proton processes everywhere we denote the following *four-momenta*:

p (p') – incoming (outgoing) proton four-momentum,

q (q') – incoming (outgoing) photon (or a virtual meson) four-momentum,

$l_\pm$ – electron/positron four-momentum,

$P = \frac{1}{2}(p + p')$ – proton symmetrized four-momentum,

$K = \frac{1}{2}(q + q')$ – photon symmetrized four-momentum.

We also normally refer to the "four-momentum" while using the term "momentum".

Two Mandelstam variables are heavily used in the text: the center-of-mass energy squared

$$s = (p + q)^2 = (p' + q')^2,$$

and the four-momentum transfer

$$t = (q - q')^2 = (p - p')^2,$$

which is negative in the case of timelike Compton scattering, and thus by "momentum transfer" we often mean $-t$. Moreover, by "minimum momentum transfer" $t_{\min}$ we understand its minimum *absolute* value.

The mass of the system is denoted by W, while ν initially (Chapters 2 and 3) stands for the incoming photon energy in the laboratory frame (i.e. the frame of the target proton at rest):

$$s = W^2 = M^2 + 2M\nu_{[\text{cpt.2,3}]}, \quad \nu_{[\text{cpt.2,3}]} \equiv E_\gamma^{\text{Lab}}.$$

Throughout the text by M we interchangeably denote the proton mass M_p.

Note that some notation, for the sake of clarity of expressions, varies from chapter to chapter, but is consistent within each one. In general, by ν we denote the crossing variable which is used throughout the dispersion relation expressions. However, while in Chapters 4 and 5 it is *redefined* as

$$\left[\nu_{[\text{cpt.4,5}]} = \frac{s-u}{4}\right] = \left[\text{GeV}^2\right], \tag{1.9}$$

we initially use the divided by proton mass definition in Chapter 2 and Chapter 3:

$$\left[E_\gamma^{\text{Lab}} \equiv \nu_{[\text{cpt.2,3}]} = \frac{s-u}{4M}\right] = [\text{GeV}]. \tag{1.10}$$

Here, u is the third Mandelstam variable, which in both cases corresponds to *forward* scatterings, but for *different* processes: the forward Compton scattering in Chapters 2 and 3, the forward quarkonium – proton scattering in Chapter 4 and the forward light-by-light scattering in Chapter 5.

Within our calculations we take the following values of the physical constants from CODATA (2014) and PDG (2014, 2018):

fine structure constant $\alpha = e^2/4\pi = 7.2973525664(17) \times 10^{-3}$ [79];

fm to 1/GeV conversion constant $\hbar c = 0.1973269788(12)$ fm·GeV [79];

proton mass $M_p = 0.9382720813(58)$ GeV [79];

proton anomalous magnetic moment $\kappa = 1.7928473508(85)$ [79];

pions masses $m_{\pi^\pm} = 139.57018(35)$ MeV, $m_{\pi^0} = 134.9766(6)$ MeV [80];

electron mass $m_e = 510.9989461(31)$ keV [79];

J/ψ meson mass $M_\psi = 3.096916(11)$ GeV [80];

J/ψ meson total width $\Gamma_\psi = 92.9 \pm 2.8$ [keV] [80];

J/$\psi \to e^+e^-$ decay width $\Gamma_{\psi\to e^+e^-} = 5.55(14)$ keV [80];

D mesons masses $M_{D^0} = 1.86484(7)$ GeV $M_{D^\pm} = 1.86961(10)$ GeV [80];

Υ meson mass $M_\Upsilon = 9.46030(26)$ GeV [80];

Υ meson total width $\Gamma_\Upsilon = 54.02 \pm 1.25$ [keV] [80];

$\Upsilon \to e^+e^-$ decay width $\Gamma_{\Upsilon\to e^+e^-} = 1.34(2)$ keV [81];

B mesons masses $M_{B^0} = 5.27958(17)$ GeV, $M_{B^\pm} = 5.27926(17)$ GeV [80];

$\rho(770)$ meson mass $M_\rho \approx 775.5$ MeV;

pion decay constant $f_\pi \approx 92.4$ MeV.

Most numerical values used for the calculations of Chapter 5 are provided in tables therein (see Table 5.2 and Table 5.4).

Chapter 2

Evaluation of the forward Compton scattering (CS) off protons

Given the photoabsorption cross sections, a reliable assessment of some of the static electromagnetic properties of the nucleon and nuclei can be provided, as well as of the forward CS amplitudes in general. For the proton, the first such assessments were performed in the early 1970s [82, 83]. Since then, the knowledge of the photoabsorption cross sections appreciably improved, and yet for the unpolarized case only the Baldin sum rule has been updated [84–86]. In the present Chapter, we provide a reassessment of both the forward spin-averaged (f) and spin-dependent (g) amplitudes of proton CS, and evaluate the associated sum rules involving the dipole, quadrupole and the forward spin polarizabilities of the proton. Having both of the amplitudes, we reconstruct all observables of the forward CS off the proton.

Dispersion integrals is essentially the only way to gain empirical knowledge of the forward CS observables: it is impossible to access the forward kinematics in real CS experiments. The measurement of the forward spin-averaged CS amplitude can be done through the process of di-lepton photoproduction ($\gamma\, p \to p\, e^+ e^-$) [87], to which we will come back with a closer look in the next Chapter 3. The timelike CS involved in the process of di-lepton photoproduction yields access to the real CS amplitude given the small virtuality of the outgoing photon, or equivalently, the nearly vanishing invariant mass of the produced pair. The experimental result [87] compared well with the aforementioned evaluations [82, 83]. Until now, while the spin-dependent amplitude has been essentially untouched, despite the substantial additions to the database of total photoabsorption cross sections, the works of Damashek and Gilman (DG) [82] as well as Armstrong *et al.* [83] remained to be the only evaluations of the spin-averaged amplitude.

The newer data were used, however, in the recent evaluations of the Baldin sum rule [85, 86], which yields the sum of the electric and magnetic dipole polarizabilities, Eq. (2.13). These recent analyses obtained a somewhat lower value for the sum than DG; cf. Table 2.4. In this Chapter we find that the difference between the early and the recent evaluations arises from systematic inconsistencies in the experimental database. We also obtain the sum rule value for a combination of higher-order quadrupole polarizabilities and compare it with several theoretical predictions.

The spin-dependent amplitude g has not yet been measured through the di-lepton photoproduction and not much is known about it empirically. Until now, only its low-energy expansion has been studied. The leading-order term yields the Gerasimov–Drell–Hearn (GDH) sum rule [33, 34], which has recently been verified for the proton by the GDH Collaboration [88–91]. The forward spin polarizability (FSP) sum rules, arising at the next two orders, have been evaluated by Pasquini *et al.* [92]. In this Chapter, having evaluated spin-dependent forward amplitude over a broad energy range, we consider its low-energy expansion and hence reevaluate the corresponding sum rules. The results are compared with the previous evaluations in Table 2.7.

The results for the energy dependence of the amplitude and the observables can be compared to theoretical calculations. At low energies we shall compare to the calculations based on chiral perturbation theory (χPT). More specifically, in the lower panels of Figs. 2.7, 2.8, and 2.9,

our results are compared to the calculations of Lensky *et al.* [93–95] done in the manifestly covariant baryon χPT (BχPT). Other state-of-the-art χPT calculations of proton CS, based on the heavy-baryon expansion (HBχPT) [96, 97], were shown [98] to be in agreement with the aforementioned BχPT calculation, within the estimated theoretical uncertainties. Therefore, in the figure, we only plot one of the two, whereas the forward spin polarizabilities can be compared to either of them in Table 2.7.

An interesting issue arises when studying the elastic contribution to the sum rules in perturbative QED: the low-energy expansion, which goes into the sum rule derivation, is inapplicable. It is nonetheless possible to write down the elastic sum rules for both the spin-averaged and the spin-dependent cases as covered in Appendix 2.B and 2.C.

The present Chapter is based on the co-authored works of Ref. [2, 3], and is organized as follows. We begin with a brief theoretical framework of the dispersion relations for the forward Compton scattering in Section 2.1. In Section 2.2 we describe our fitting procedure for the total unpolarized photoabsorption cross section. We then continue with evaluation of the sum rules in Section 2.3 and the amplitude in Section 2.4. We finally discuss our results for the observables in Section 2.5 and present conclusions in Section 2.6. Apart from the aforementioned consideration of the elastic sum rules cases, Appendix includes an expression for the gauge-invariant Lorentz structure of the forward CS amplitude (2.A). Additionally, our uncertainty estimation procedure is described in details in Appendix 2.D.

2.1 Forward CS amplitude and sum rules

The Lorentz structure of the *forward* CS amplitude for a spin-1/2 target, such as the nucleon, can be decomposed into two terms, [1]

$$T^{\mu\nu}_{\rm fCS}(p,q) = -\left[\mathrm{g}^{\mu\nu} f(\nu) + \gamma^{\mu\nu} g(\nu)\right], \tag{2.1}$$

where $\mathrm{g}^{\mu\nu} = \mathrm{diag}(1,-1,-1,-1)$ is the metric tensor and $\gamma^{\mu\nu} = \frac{1}{2}[\gamma^\mu,\gamma^\nu]$ is the antisymmetrized product of Dirac matrices. The amplitudes f and g are complex functions of the variable $\nu = p\cdot q/M$, with p and q being the target and photon 4-momentum; $p^2 = M^2$, $q^2 = 0$. The corresponding helicity amplitudes are found as

$$T^{\rm fCS}_{\lambda'\sigma'\lambda\sigma} = \chi^\dagger_{\sigma'}\left\{f(\nu)\,\boldsymbol{\varepsilon}^*_{\lambda'}\cdot\boldsymbol{\varepsilon}_\lambda \;+\; g(\nu)\,i\,(\boldsymbol{\varepsilon}^*_{\lambda'}\times\boldsymbol{\varepsilon}_\lambda)\cdot\boldsymbol{\sigma}\right\}\chi_\sigma, \tag{2.2}$$

where $\boldsymbol{\sigma}$ is the nucleon spin matrix, $\lambda(\lambda')$ is the incoming (outgoing) photon helicity, $\sigma(\sigma')$ is the incoming (outgoing) nucleon helicity, $\boldsymbol{\varepsilon}$ are the photon polarization three-vectors, and the Pauli spinors χ denote the target polarization. In terms of the total helicity $\Lambda = \lambda - \sigma$, the amplitude is diagonal: $T_{\Lambda'\Lambda} = \delta_{\Lambda'\Lambda}\mathcal{T}_\Lambda$. Hence, there are only two independent helicity amplitudes: $\mathcal{T}_{\pm 3/2} = (f-g)$ and $\mathcal{T}_{\pm 1/2} = (f+g)$. The optical theorem (unitarity) relates the imaginary part of these amplitudes to the corresponding photoabsorption cross sections,

$$\mathrm{Im}\,\mathcal{T}_\Lambda(\nu) = \frac{\nu}{4\pi}\,\sigma_\Lambda(\nu), \tag{2.3}$$

with $\Lambda = 1/2, 3/2$. Rewriting these relations for f and g, one obtains the usual,

$$\mathrm{Im}\,f(\nu) \;=\; \frac{\nu}{8\pi}\left[\sigma_{1/2}(\nu)+\sigma_{3/2}(\nu)\right] \equiv \frac{\nu}{4\pi}\,\sigma(\nu), \tag{2.4a}$$

$$\mathrm{Im}\,g(\nu) \;=\; \frac{\nu}{8\pi}\left[\sigma_{1/2}(\nu)-\sigma_{3/2}(\nu)\right] \equiv -\frac{\nu}{8\pi}\,\Delta\sigma(\nu), \tag{2.4b}$$

[1] The tensors can in principle be written in an explicitly current-conserving form (i.e., such that $q_\mu T^{\mu\nu} = 0$, see Eq. (2.28) in Appendix 2.A); however, additional terms vanish when contracted with the photon polarization vector ε^μ, because of $q\cdot\varepsilon = 0$.

where by σ and $\Delta\sigma$ we denote, respectively, the unpolarized and the helicity-difference cross sections of total photoabsorption.

Furthermore, the analytic and crossing properties of the amplitudes f and g, in conjunction with Eq. (2.4), allow one to write the following dispersion relations,

$$\mathrm{Re}\, f(\nu) = -\frac{Z^2\alpha}{M} + \frac{\nu^2}{2\pi^2} \fint_0^\infty \mathrm{d}\nu' \frac{\sigma(\nu')}{\nu'^2 - \nu^2}, \tag{2.5a}$$

$$\mathrm{Re}\, g(\nu) = -\frac{\nu}{4\pi^2} \fint_0^\infty \mathrm{d}\nu' \frac{\nu' \Delta\sigma(\nu')}{\nu'^2 - \nu^2}, \tag{2.5b}$$

where M is the nucleon mass and $Z = 1$ or 0 for the proton or neutron, respectively; the slashed integral denotes the principal-value integration. The crossing symmetry implies that the spin-averaged amplitude f is an even and the spin-dependent amplitude g is an odd function of ν.

We next would like to consider the low-energy expansion of f. At this point, it is important to note that the elastic scattering, i.e., the CS process itself, is one of the photoabsorption processes. The total CS cross section does not vanish for $\nu \to 0$ but goes to a constant — the Thomson cross section:

$$\sigma(0) = \frac{8\pi\alpha^2}{3M_p^2}. \tag{2.6}$$

This means Eq. (2.5b) does not admit a Taylor-series expansion around $\nu = 0$ (each coefficient in that expansion is infrared divergent; cf. the Appendix 2.B). Such expansion is, nonetheless, important for establishing the polarizability sum rules. We, hence, prefer to take the CS out of the total cross section, i.e.,

$$\sigma(\nu) = \sigma_{\mathrm{CS}}(\nu) + \sigma_{\mathrm{abs}}(\nu), \tag{2.7}$$

where σ_{abs} can be assumed to be dominated by hadron-production processes, for which there is a threshold at some $\nu_0 > m_\pi$.

We can neglect the processes of CS, as well as the multi-photon production, in the total cross sections, since these are of course suppressed by at least one order of α with respect to hadron-production processes, such as the pion photoproduction (more details on leading radiative corrections can be found in the Appendix 2.B and 2.C).

The cross sections which exclude electromagnetic radiation will be denoted by σ_{abs} and are assumed to begin with the lowest hadron-production threshold. We thus deal with the following relation for the forward CS amplitudes:

$$\mathrm{Re}\, f(\nu) = -\frac{\alpha}{M_p} + \frac{\nu^2}{2\pi^2} \fint_{\nu_0}^\infty \mathrm{d}\nu' \frac{\sigma_{\mathrm{abs}}(\nu')}{\nu'^2 - \nu^2}, \tag{2.8}$$

$$\mathrm{Re}\, g(\nu) = -\frac{\nu}{4\pi^2} \fint_{\nu_0}^\infty \mathrm{d}\nu' \frac{\nu' \Delta\sigma_{\mathrm{abs}}(\nu')}{\nu'^2 - \nu^2}, \tag{2.9}$$

where ν_0 is the pion photoproduction threshold.

The low-energy expansion of both sides of Eq. (2.8) and Eq. (2.9) lead to the sum rules for polarizabilities. At the first order $[O(\nu)]$, the expansion of Eq. (2.9) yields the GDH sum rule:

$$I_{\mathrm{GDH}} \equiv \int_{\nu_0}^\infty \mathrm{d}\nu \frac{\Delta\sigma_{\mathrm{abs}}(\nu)}{\nu} = \frac{2\pi^2\alpha}{M^2}\kappa^2, \tag{2.10}$$

where κ is the anomalous magnetic moment of the nucleon. Substituting the proton mass M_p and the anomalous magnetic moment κ_p into the right-hand side, we obtain the GDH sum rule prediction quoted in the last row of Table 2.7.

By expanding Eq. (2.9) further, at the next odd orders in ν $[O(\nu^3)]$ and $[O(\nu^5)]$, one finds the FSP sum rules:

$$\gamma_0 = -\frac{1}{4\pi^2}\int_{\nu_0}^{\infty} \mathrm{d}\nu\, \frac{\Delta\sigma_{\rm abs}(\nu)}{\nu^3}, \tag{2.11}$$

$$\bar{\gamma_0} = -\frac{1}{4\pi^2}\int_{\nu_0}^{\infty} \mathrm{d}\nu\, \frac{\Delta\sigma_{\rm abs}(\nu)}{\nu^5}\,. \tag{2.12}$$

At the second order $[O(\nu^2)]$, expansion of Eq. (2.8) produces the the Baldin sum rule [35] for the sum of electric (α_{E1}) and magnetic (β_{M1}) dipole polarizabilities:

$$\alpha_{E1} + \beta_{M1} = \frac{1}{2\pi^2}\int_{\nu_0}^{\infty} \mathrm{d}\nu\, \frac{\sigma_{\rm abs}(\nu)}{\nu^2}. \tag{2.13}$$

At $O(\nu^4)$, one obtains 'the $4^{\rm th}$-order sum rule':

$$\alpha_{E\nu} + \beta_{M\nu} + \frac{1}{12}\left(\alpha_{E2} + \beta_{M2}\right) = \frac{1}{2\pi^2}\int_{\nu_0}^{\infty} \mathrm{d}\nu\, \frac{\sigma_{\rm abs}(\nu)}{\nu^4}, \tag{2.14}$$

which involves the quadrupole polarizabilities α_{E2}, β_{M2}, as well as the leading dispersive contribution to the dipole polarizabilities denoted as $\alpha_{E\nu}$, $\beta_{M\nu}$; see [99] for more details.

In what follows, we assess the total unpolarized and the helicity-difference cross sections, evaluate the scalar amplitudes $f(\nu)$ and $g(\nu)$, the corresponding sum rules based on the above integrals, and the observables.

2.2 Fitting the total photoproduction cross section

In order to evaluate the dispersion integrals based on the experimental photoproduction total cross section, we have to obtain smooth fits of the available data. The cross section fitting and the sum rule evaluations are accomplished with the help of the SciPy package for Python. We used the weighted nonlinear least-squares optimization procedure of SciPy's wrapper around minpack's lmdif and lmder algorithms. The latter implement the modified Levenberg-Marquardt algorithm [100, 101].

The error estimates of the fits are linearly propagated from the experimental data uncertainties, as described in details in the Appendix 2.D.

2.2.1 Unpolarized cross section

The presently available experimental data, together with the results of the empirical analyses MAID and SAID, as well as our fits, are displayed in Fig. 2.1. In our fitting, we distinguish the following three regions:

- *low energy*, $\nu \in [\nu_0\,,\ \nu_1)$,
- *medium energy*, $\nu \in [\nu_1\,,\ 2\ \mathrm{GeV})$,
- *high energy*, $\nu \in [2\ \mathrm{GeV}\,,\ \infty)$,

where ν_0 ($\simeq 0.145$ GeV) and ν_1 ($\simeq 0.309$ GeV) are, respectively, the thresholds for the single- and double-pion photoproduction on the proton.

In the *low-energy* region, we use the pion-production ($\pi^+ n$ and $\pi^0 p$) cross sections from the MAID [102] and SAID [103] partial-wave analyses. In our error estimate, we assign a 2% uncertainty on these values.

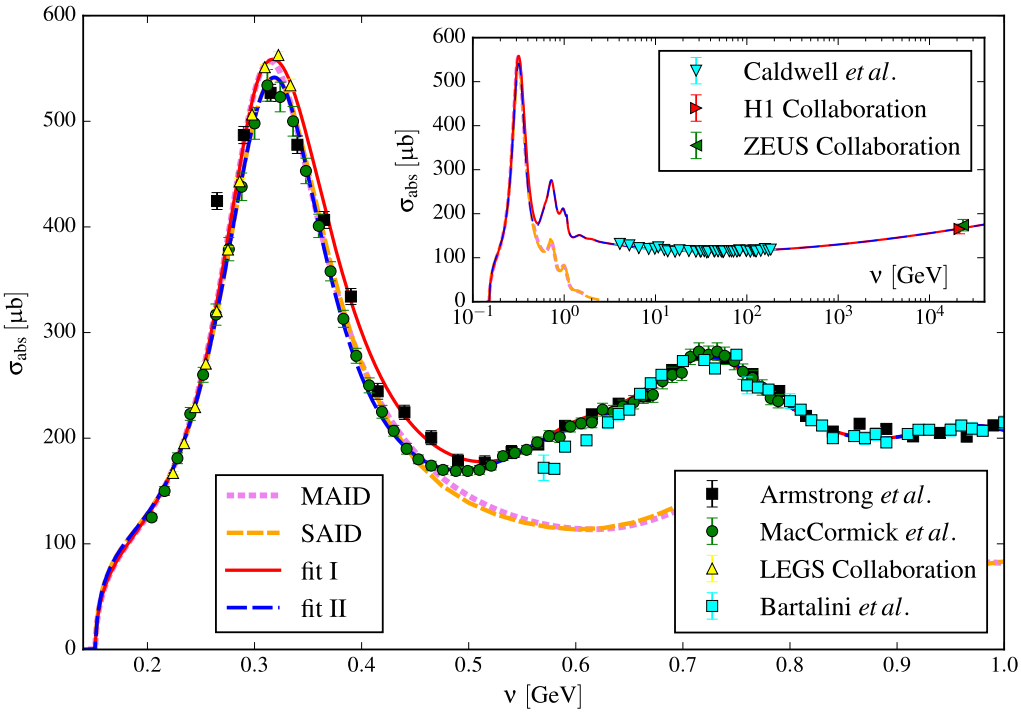

Figure 2.1: Figure from Ref. [2]: Fits of the experimental data for the total photoabsorption cross section on the proton. Fit I is obtained using MAID [102] results below the 2π production, and data from LEGS [65] and Armstrong *et al.* [83] above it. Fit II uses SAID [103] and the data of MacCormick *et al.* [104]. Both fits use Bartalini *et al.* [105] and the high-energy data [106–108] displayed in the inset.

In the *medium-energy* region, we fit the actual experimental data using a sum of Breit-Wigner resonances and a background. Following [85], we take six Breit-Wigner resonances, each parametrized as

$$\sigma_R(W) = A\frac{\Gamma^2/4}{(W-M)^2+\Gamma^2/4}, \tag{2.15}$$

where $W=\sqrt{s}$ is the total energy of the γp system. The background function is of the form [83]:

$$\sigma_B(W) = \sum_{k=-2}^{2} C_k (W-W_0)^k, \tag{2.16}$$

where $W_0 = M_p + m_\pi$ corresponds with the pion photoproduction threshold.

Observing a significant discrepancy between SAID and MAID around the $\Delta(1232)$-resonance peak and a similar discrepancy between two sets of experimental data, we have made two different fits:

I. MAID[102] + LEGS [65] + Armstrong *et al.* [83],

II. SAID [103] + MacCormick *et al.* [104].

They are shown in Fig. 2.1 by the red solid and blue dashed lines, respectively. The corresponding values of parameters are given in Tables 2.1 and 2.2. In both fits, we have also made

	M [MeV]	Γ [MeV]	A [μb]
Fit I	1213.6 ± 0.1	117.6 ± 1.9	522.7 ± 17.0
	1412.8 ± 5.9	82.8 ± 26.8	40.1 ± 33.8
	1496.0 ± 2.8	136.5 ± 11.1	161.8 ± 32.4
	1649.4 ± 4.1	135.3 ± 15.3	83.2 ± 22.7
	1697.5 ± 2.6	18.8 ± 12.6	18.2 ± 26.0
	1894.3 ± 15.6	302.0 ± 41.3	31.5 ± 8.7
Fit II	1214.8 ± 0.1	99.0 ± 1.1	502.3 ± 12.3
	1403.9 ± 6.2	118.2 ± 19.6	51.8 ± 23.8
	1496.9 ± 2.1	133.4 ± 9.4	162.0 ± 29.2
	1648.0 ± 4.4	135.2 ± 15.9	83.6 ± 23.8
	1697.2 ± 2.7	21.2 ± 13.2	18.7 ± 25.9
	1893.7 ± 17.4	323.5 ± 45.3	31.7 ± 9.1

Table 2.1: Table from Ref. [2]: Fitting parameters for the resonances (2.15) obtained for fits I and II.

	Fit I	Fit II
C_{-2} [μb GeV^2]	0.44 ± 0.22	0.26 ± 0.17
C_{-1} [μb GeV]	-11.06 ± 3.69	-7.97 ± 2.89
C_0 [μb]	74.38 ± 20.16	57.27 ± 16.09
C_1 [μb GeV^{-1}]	22.18 ± 37.71	54.26 ± 31.07
C_2 [μb GeV^{-2}]	37.69 ± 21.48	19.51 ± 18.17

Table 2.2: Table from Ref. [2]: Fitting parameters for the background (2.16) obtained for fits I and II in the resonance region.

use of the GRAAL 2007 data [105] shown in the figure by light blue squares. These data were not available at the time of the previous sum rule evaluations.

Finally, for the *high-energy region*, we use the standard Regge form [109, p. 191]:

$$\sigma_{\text{Regge}}(W) = c_1\, W^{p_1} + c_2\, W^{p_2}. \tag{2.17}$$

For W in GeV and the cross section in μb, we obtain the following parameters (for both of our fits):

$$c_1 = 62.0 \pm 8.1, \quad c_2 = 126.3 \pm 4.3,$$
$$p_1 = 0.184 \pm 0.032, \quad p_2 = -0.81 \pm 0.12.$$

We also tried the high-energy parametrization used in [85] but obtained a worse fit and abandoned it.

The resulting chi-square evaluated as

$$\chi^2 = \sum_i \frac{\left(\sigma_i^{\text{fit}} - \sigma_i^{\text{exp}}\right)^2}{(\Delta\sigma_i^{\text{exp}})^2}, \tag{2.18}$$

is of about the same quality for the two fits. In the intermediate region, we obtain χ^2/point $= 0.7$ for fit I and χ^2/point $= 0.6$ for fit II. In the high-energy region, χ^2/point $= 1.2$ in both cases.

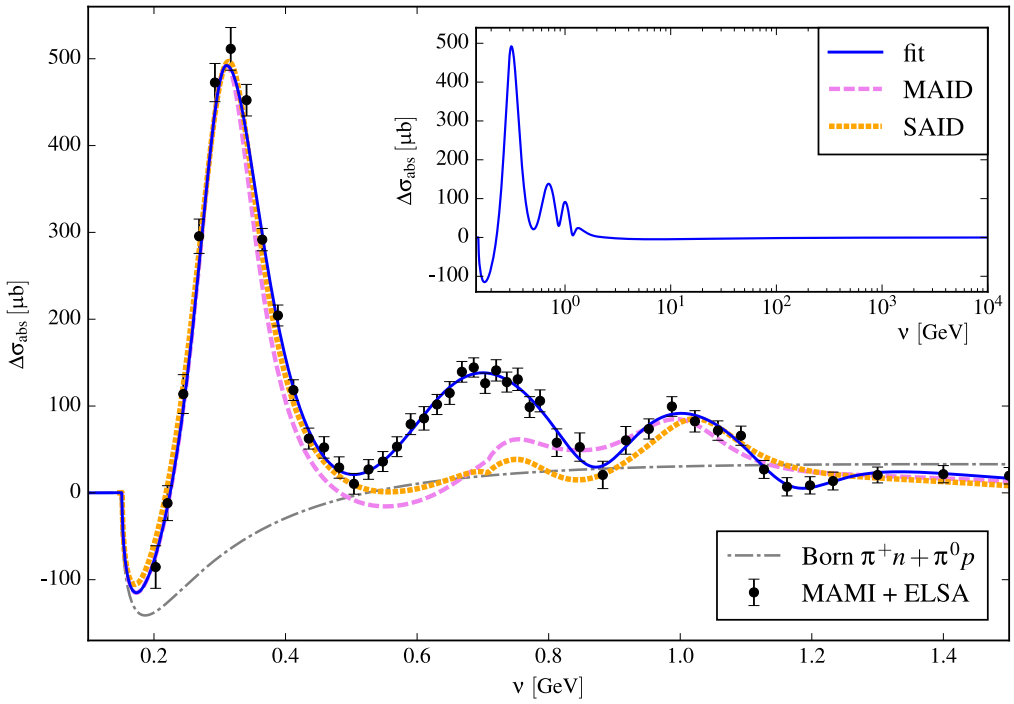

Figure 2.2: Figure from Ref. [3]: Fit of experimental data for the helicity-difference cross section of total photoproduction on the proton. The solid curve shows our fit. The other curves, according to the legend, show the Born contribution (single-pion production on a point-like proton), as well as the results of MAID [102] and SAID [103] multipole analyses.

2.2.2 Helicity-difference cross section

The fitting procedure is similar to the one applied for the unpolarized photoabsorption cross section $\sigma_{\rm abs}$. We divide the integration domain into the same three *low-*, *medium-* and *high-energy* regions. In the *low-energy* region, we use the cross sections generated by MAID [102] (single-pion production only). Again, we assume a 2% uncertainty to the MAID values. In the *medium-energy* region, a fit to the data from the MAMI (Mainz) and ELSA (Bonn) experiments of the GDH and A2 collaborations [88–91] is applied in the form of a sum of six non-relativistic Breit-Wigner resonances of the form (2.15). The resulting fitted values for the widths (Γ), masses (M), and couplings (A) are given in Table 2.2.2.

M (MeV)	Γ (MeV)	$A \cdot \frac{1}{4}\Gamma^2$ (nb·GeV^2)
1210.2	119.3	1047.3
1405.0	493.5	−9008.4
1460.8	239.8	1964.0
1585.5	111.7	−226.9
1616.4	360.7	3829.3
1752.5	105.0	−103.4

Table 2.3: Table from Ref. [3]: Fitted resonances parameters entering Eq. (2.15).

In the *high-energy* region, a function of the Regge form (2.17)) is used. For W in GeV and the cross section in μb, we use the following fixed parameters [110]:

$$c_1 = -17.05 \pm 2.85\,, \quad c_2 = 104.7 \pm 14.5\,,$$
$$p_1 = -1.16 \pm 0.46\,, \quad p_2 = -3.32 \pm 0.44\,.$$

The resulting fit of the helicity-difference photoabsorption cross section is shown in Fig. 2.2. Also shown is the Born contribution for the $\pi^+ n + \pi^0 p$ photoproduction off a point-like proton (with the vanishing anomalous magnetic moment), as well as the results of MAID [102] and SAID [103] multipole analyses.

2.3 Evaluation of the sum rules

Having obtained the fits of the total photoabsorption cross section $\sigma_{\rm abs}$, we evaluate the integrals in Eqs. (2.13) and (2.14); the results are presented in Table 2.4.

The corresponding full results (sum of the three regions) are given in Table 2.4 and compared with the results of previous works. In this table, we also give the result for the 6th-order integral, and for the full amplitude f at $\nu = 2.2$ GeV.

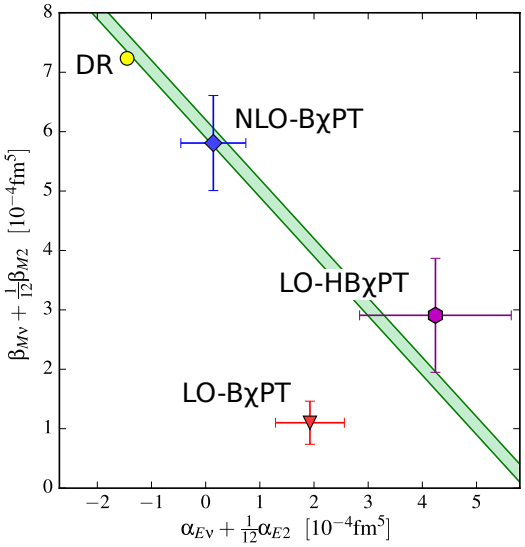

Figure 2.3: Figure from Ref. [2]: The 4$^{\rm th}$-order sum rule constraint for $\alpha_{E\nu} + \frac{1}{12}\alpha_{E2}$ and $\beta_{M\nu} + \frac{1}{12}\beta_{M2}$ combinations of polarizabilities, compared to results from dispersion relation approaches (DR) [25, 99], baryon chiral perturbation theory (BχPT) [95], and heavy baryon chiral perturbation theory (HBχPT) [111]. The errors of the χPT derive from our crude estimate of the next-order corrections.

Tables 2.3 and 2.6 show contributions of each region to the Baldin and the 4$^{\rm th}$-order sum rule, respectively. The uncertainty in calculating an integral, for the case of the unpolarized

[2] $\int_{\nu_0}^{\infty} {\rm d}\nu\, \nu^{-6}\, \sigma_{\rm abs}(\nu)/(2\pi^2)$
[3] Interpolated value.
[4] Based on the cross section parametrization from [89].
[5] Integrated from threshold to $\nu_{\rm max} = 1.663$ GeV.
[6] Integrated from threshold to $\nu_{\rm max} = 2$ GeV.

	Baldin $[10^{-4}\ \mathrm{fm}^3]$	4^{th} order $[10^{-4}\ \mathrm{fm}^5]$	6^{th} order[2] $[10^{-4}\ \mathrm{fm}^7]$	Re $f(2.2\ \mathrm{GeV})$ [μb GeV]
Damashek–Gilman [82]	14.2 ± 0.3			-11.5[3]
Armstrong *et al.* [83]				-10.8
Schröder [84]	14.7 ± 0.7	6.4		
Babusci *et al.* [85]	13.69 ± 0.14			
A2 Collaboration [86]	13.8 ± 0.4			-10.5[4]
MAID (π chan.) [102]	11.63[5]			
SAID (π chan.) [103]	11.5[6]			
Our work [2]				
Fit I	14.29 ± 0.27	6.08 ± 0.12	4.36 ± 0.09	-10.35
Fit II	13.85 ± 0.22	6.01 ± 0.11	4.42 ± 0.08	-9.97
Experiment				
Alvensleben *et al.* [87]				-12.3 ± 2.4

Table 2.4: Table from Ref. [2]: Empirical evaluations of sum rules and verification of the Kramers-Kronig relation for the proton.

total cross section, $I_n = \int \mathrm{d}\nu\, \nu^{-n} \sigma(\nu)$, has been evaluated as follows:

$$\Delta I_n = \sum_i \frac{\Delta\nu_i}{\nu_i^n} \chi_i^2\, \Delta\sigma_i^{\mathrm{exp}}, \tag{2.19}$$

where χ_i^2 is the chi-square at the point i; cf. Eq. (2.18).

Our two results for the sum of dipole polarizabilities (or Baldin sum rule) correspond nicely with the results of previous evaluations, which too can be separated into two groups: the *old* [82, 84], with the value slightly above 14 (in units of 10^{-4} fm^3), and the *new* [85, 86], with the value slightly below 14. The 1996 DAPHNE@MAMI experiment [104] superseding the 1972 experiment of Armstrong *et al.* [83] is clearly responsible for this difference. Neglecting the older data in favor of the newer ones yields the lower value of the Baldin sum rule and vice versa. While one can take a preference in one of the two fits and the corresponding results, we prefer to think of their difference as a systematic uncertainty in the present evaluation of the polarizabilities and of the forward spin-averaged amplitude of the proton.

$\alpha_{E1} + \beta_{M1}$ $[10^{-4}\ \mathrm{fm}^3]$

Fit \ Region	*low-energy*	*medium-energy*	*high-energy*
I	6.12 ± 0.12	7.53 ± 0.13	0.64 ± 0.02
II	6.06 ± 0.12	7.15 ± 0.08	0.64 ± 0.02

Table 2.5: Table from Ref. [2]: Contributions of different regions to the Baldin sum rule for the two fits in Fig. 2.1.

We present a first study of the sum rule involving the quadrupole polarizabilities, Eq. (2.14), here referred to as 'the 4^{th}-order sum rule'. Our weighted average value for this sum rule in the proton case is $6.04(4) \times 10^{-4}\,\mathrm{fm}^5$. It agrees very nicely with the state-of-the-art calculations of these polarizabilities based on fixed-t dispersion relations and chiral perturbation theory; see Fig. 2.3. We note that, while the calculations demonstrate significant differences in the values of individual higher-order polarizabilities, these differences apparently cancel out from the forward combination of these polarizabilities which enters the sum rule.

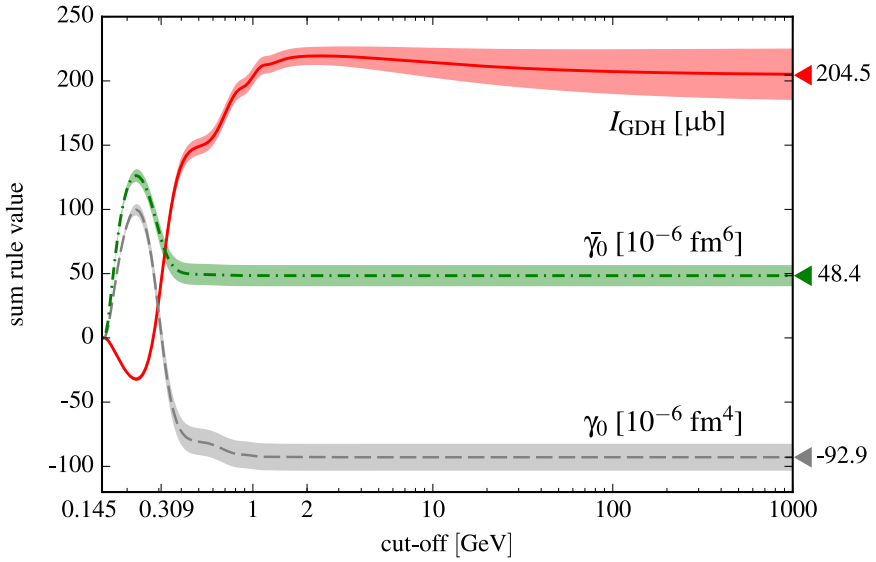

Figure 2.4: Figure from Ref. [3]: The GDH and FSP integrals as a function of the upper integration bound. Bands represent estimated errors. Asymptotic values of the integrals are displayed on the right and marked with colored triangles.

$$\alpha_{E\nu} + \beta_{M\nu} + \tfrac{1}{12}(\alpha_{E2} + \beta_{M2}) \quad [10^{-4}\ \text{fm}^5]$$

Fit \ Region	*low-energy*	*medium-energy*	*high-energy*
I	4.50 ± 0.09	1.58 ± 0.03	$(219 \pm 8) \times 10^{-5}$
II	4.53 ± 0.09	1.48 ± 0.01	$(219 \pm 8) \times 10^{-5}$

Table 2.6: Table from Ref. [2]: Contributions to the 4^{th}-order sum rule for the two fits in Fig. 2.1.

We proceed to the evaluation of the GDH and FSP sum rules.Our results for the sum rule integrals are presented in Table 2.4, where they can be compared with some of the previous empirical evaluations, as well as the recent χPT results.

To estimate the uncertainty of our fits and dispersive integrals, in the case of the helicity-difference total cross section, we compute the covariance matrix of the fitted parameters. In the medium-energy region, the covariance matrix is simply obtained based on the experimental uncertainties of the data points. In the high-energy region, we make use of the uncertainties for the Regge parameters from Ref. [110], assuming that these four parameters are uncorrelated. We then apply the standard, linear error propagation to find the uncertainty of the dispersive integrals.

$$\left[\Delta I(\{p\})\right]^2 = \sum_{i,j} M_{i,j}^{\{p\}} \frac{\partial I}{\partial p_i}(\{p_0\}) \frac{\partial I}{\partial p_j}(\{p_0\}),$$

where $M_{i,j}^{\{p\}}$ is the covariance matrix, and $\{p_0\}$ is a set of optimal (fitted) values of the parameters. More details on the uncertainty estimation can be found in Appendix 2.D.

In the low-energy region, where the cross sections are not fit but obtained from the partial-wave analyses, we judiciously estimate the systematic error of each of the photoabsorption

[7] Right-hand side of Eq. (2.10) with CODATA [79] values of proton M and κ.

	I_{GDH} (μb)	γ_0 (10^{-6} fm^4)	$\bar{\gamma}_0$ (10^{-6} fm^6)
GDH & A2 [89, 91]	≈ 212	≈ -86	
Helbing [110]	$212 \pm 6 \pm 12$		
Bianchi-Thomas [112]	207 ± 23		
Pasquini *et al.* [92]	$210 \pm 6 \pm 14$	$-90 \pm 8 \pm 11$	$60 \pm 7 \pm 7$
Our work [3]	204.5 ± 21.4	-92.9 ± 10.5	48.4 ± 8.2
GDH sum rule	204.784481(4)[7]		
BχPT [95]		-90 ± 140	110 ± 50
HBχPT [97]		-260 ± 190	

Table 2.7: Table from Ref. [3]: Empirical evaluations of the GDH and FSP integrals.

Sum Rule \ Region	*low-energy*	*medium-energy*	*high-energy*
I_{GDH} (μb)	43.6 ± 6.0	175.7 ± 3.7	-14.8 ± 19.9
γ_0 (10^{-6} fm^4)	3.6 ± 10.3	-96.5 ± 2.0	$(2 \pm 7) \times 10^{-2}$
$\bar{\gamma}_0$ (10^{-6} fm^6)	77.1 ± 8.2	-28.7 ± 0.6	$(2 \pm 36) \times 10^{-5}$

Table 2.8: Table from Ref. [3]: Contributions to the GDH and FSP integrals by regions.

cross sections to be 2% of the magnitude of the unpolarized cross section, $\sigma(\nu)$. As the result, the error on $\Delta\sigma(\nu)$ is equal to 4% of $\sigma(\nu)$. This error is then linearly propagated to the dispersion integrals.

Within the calculated uncertainties, our evaluation appears to be consistent with the previous ones, as well as with the GDH sum rule value quoted in the bottom part of Table 2.7. The discrepancy in the central value of the GDH integral can be traced back to the fact that our fit at the Δ-resonance peak happens to lie well below the central value of the data point; see Fig. 2.2. In particular, the GDH Collaboration [91] obtains $(254 \pm 5 \pm 12)$ μb in the interval of available data (i.e., $0.2 < \nu < 2.9$ GeV), while our fit of the same data yields (246.4 ± 6.8) μb.

Table 2.3 shows the contributions from each of the three energy regions. One can clearly see that the high-energy contribution is negligible for the FSPs. A more detailed behavior of the running sum rule integrals (functions of the cut-off — the upper integration bound) can be seen in Fig. 2.4. One can see the good convergence properties of all the integrals. It is interesting to observe the significant cancellations between the contribution below and above 0.2 GeV.

We note that the main contribution to the estimated uncertainty of the GDH integral comes from the high-energy Regge behavior, which is possibly both due to the fact that parameters seem to be not well "fixed" and because we have used a simplified covariance matrix estimation for these parameters. As for the higher-order sum rules, it appears that the main contribution to the uncertainty comes from our assumption about the systematic uncertainty of the partial-wave analyses (low-energy region).

2.4 Evaluation of the amplitude

In this Section we discuss results of our evaluation of the dispersion relation integrals for the spin-averaged and the spin-dependent amplitudes f and g, given by Eqs. (2.8) and (2.9), respectively. Since we perform the calculation numerically, we have to avoid the straightforward integration of the pole divergence at $\nu = \nu'$ when $\nu \geq \nu_0$. We do a simple trick of

"extraction" of the divergence ($a(\nu)$ stands for a pole-free function inside the integral):

$$\fint_{\nu_0}^{\infty} \frac{a(\nu')}{(\nu'^2-\nu^2)}d\nu' = \fint_{\nu_0}^{\infty} \frac{(a(\nu')-a(\nu))}{(\nu'^2-\nu^2)}d\nu' + \frac{a(\nu)}{2\nu}\ln\left|\frac{\nu'-\nu}{\nu'+\nu}\right|\Big|_{\nu_1}^{\nu_2}. \tag{2.20}$$

2.4.1 Spin-averaged amplitude

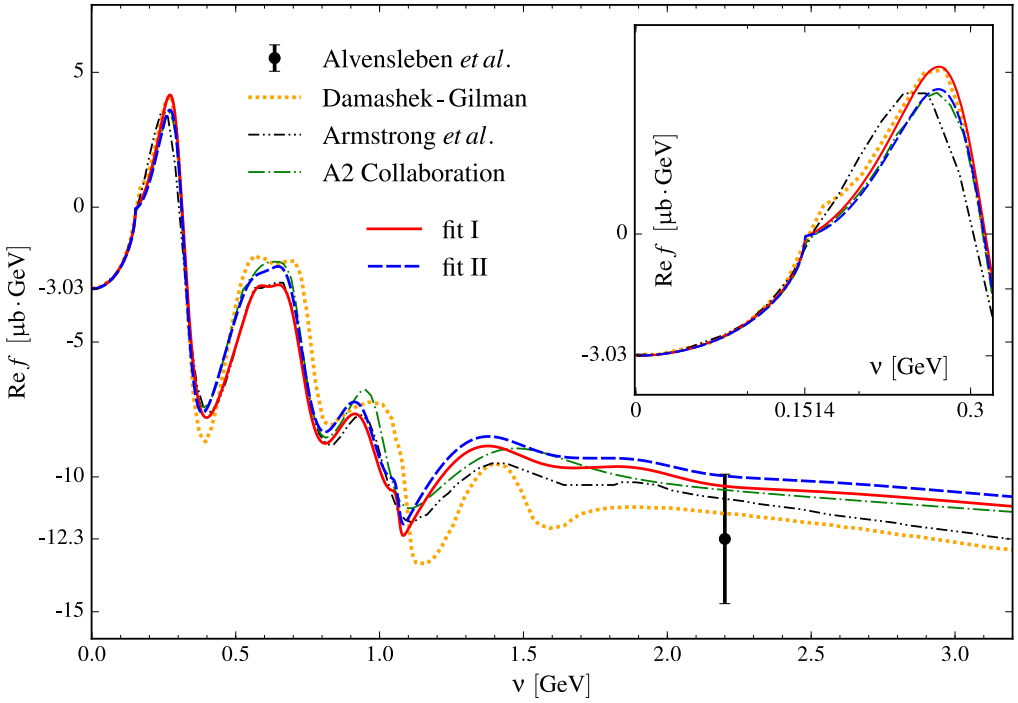

Figure 2.5: Figure from Ref. [2]: Our evaluation of Re f based on the two fits of the photoabsorption cross section, compared with previous evaluations [82, 83, 86]. The experimental data point is from Ref. [87].

The real part of f is plotted in Fig. 2.5 over a broad energy range and compared with previous evaluations and the experimental number from the 1973 DESY experiment at 2.2 GeV. Although none of the evaluations really contradicts the experiment, there is a clear tendency to a higher central value.

The new di-lepton photoproduction experiments planned at the Mainz Microtron (MAMI) could, perhaps, provide experimental values in the lower-energy range. Obviously, the regions of the extrema (e.g., the $\Delta(1232)$ region or the interval between 0.6 and 0.7 GeV) are most interesting as the different evaluations seem to differ there the most. In the region around 0.6 GeV, for example, one of our evaluations (fit I) is nearly identical with Armstrong's [83], while the other one (fit II) is aligning with DG [82] and the A2 Collaboration [86]. An appropriately precise experiment could tell which of the groups is correct, if any. We furthermore discuss multiple opportunities for the di-lepton photoproduction measurements at Jefferson Lab and for much higher energies at a planned Electron-Ion Collider in the following Chapter 3.

Figure 2.6 shows both the real and imaginary parts of f at lower energies, where it can be compared with a calculation done within chiral perturbation theory (χPT) [94]. A rather nice

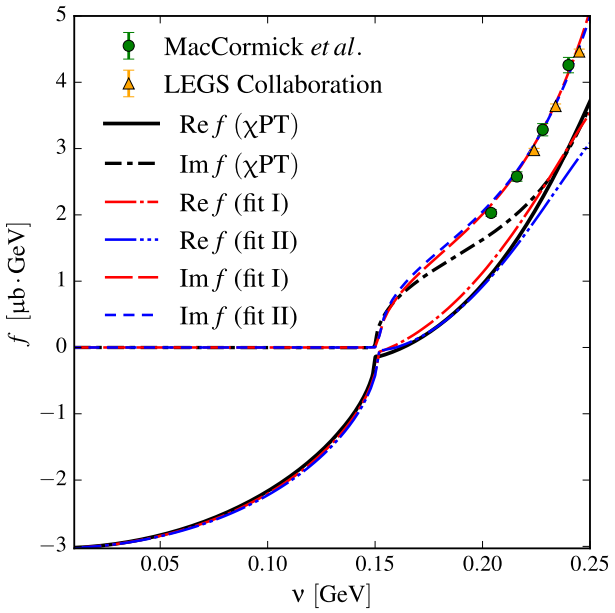

Figure 2.6: Figure from Ref. [2]: Our evaluations of $f(\nu)$ compared to the χPT calculation of Ref. [94].

agreement between theory and empirical evaluations is observed for energies up to about the pion-production threshold.

For very low energy this comparison can be made more quantitative by looking at the polarizabilities. While for the Baldin sum rule the situation was extensively discussed in the literature (cf. [96] for a recent review), the 4^{th}-order sum rule was not studied at all. It can, however, be very useful in unraveling the higher-order polarizabilities, as illustrated by Fig. 2.3. This is the plot of a combination of proton magnetic polarizabilities versus electric, where the various theory predictions are compared with our 4^{th}-order sum rule evaluation. The band representing the sum rule covers the interval between the two values given in Table 2.4 (rows 'fit I' and 'fit II'). The sum rule clearly provides a model-independent constraint on these polarizabilities and a rather stringent test for the theoretical approaches.

2.4.2 Spin-dependent amplitude

We next evaluate the entire spin-dependent amplitude $g(\nu)$. In order to improve on the accuracy, we use the subtracted dispersion relation:

$$\mathrm{Re}\, g(\nu) \;=\; -\frac{\alpha\kappa^2}{2M^2}\nu \;-\; \frac{\nu^3}{4\pi^2}\fint_{\nu_0}^{\infty} \mathrm{d}\nu' \,\frac{\Delta\sigma_{\text{abs}}(\nu')}{(\nu'^2-\nu^2)\,\nu'}. \tag{2.21}$$

The only difference with the unsubtracted one, Eq. (2.9), is accuracy. Indeed, the subtraction replaces the value of the GDH integral (see "Our work" in Table 2.7) by the much more accurate GDH sum rule value (next row) and leads to the smaller uncertainty.

The remaining integral in Eq. (2.21) converges very fast in the considered energy range. The resulting amplitude is plotted in Fig. 2.7. The upper panel shows the real and imaginary parts in the energy range where the data (for the imaginary part) are available.

The lower panel of Fig. 2.7 zooms into the lower energy range where our results can be compared with next-next-to-leading order χPT calculations of Lensky *et al.* [95]. One notes

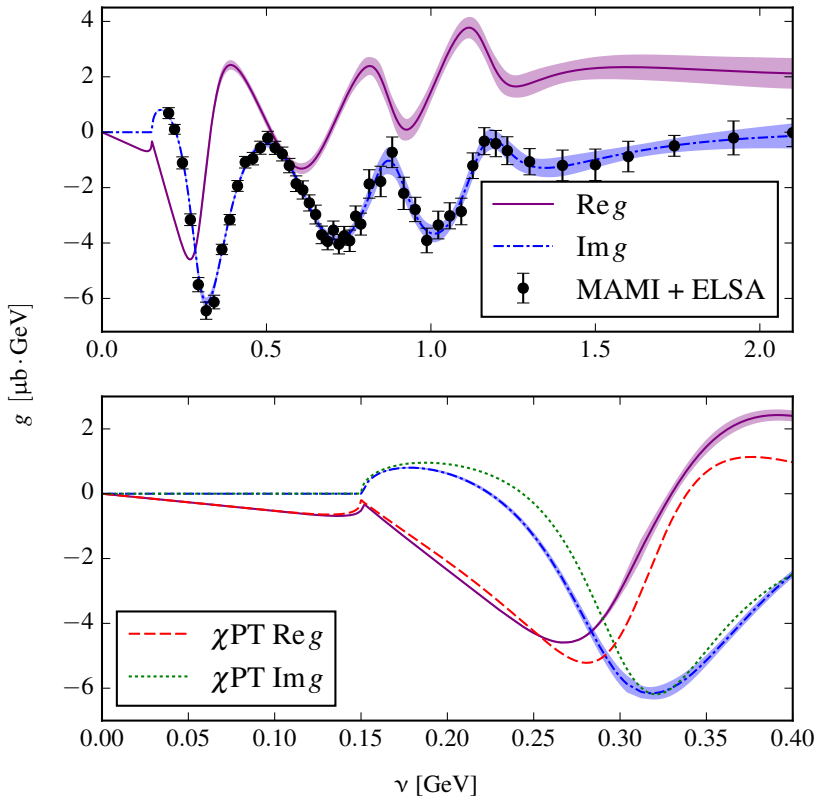

Figure 2.7: Figure from Ref. [3]: Spin-dependent amplitude $g(\nu)$ as obtained from numerical integration of the fit of data for the helicity-difference photoproduction cross section. Dashed and dotted curves in the bottom panel are the BχPT predictions of Ref. [95]. Bands represent the error estimate.

here that the imaginary parts differ appreciably at energies around 0.25 GeV. Nevertheless, their integrals (i.e., the real parts) agree perfectly at low ν. This is a "scientific miracle" of the effective field theory — the low-energy quantities are well described, even though they are obtained as loop or dispersive integrals which include higher-energy domains where the theory is inapplicable.

2.5 Results for the observables

Given both amplitudes, $f(\nu)$ and $g(\nu)$, one can reconstruct the energy dependence of the forward CS observables. The differential cross section of the forward CS in the laboratory frame is expressed simply as follows:

$$\left.\frac{\mathrm{d}\sigma}{\mathrm{d}\Omega_{\mathrm{lab}}}\right|_{\theta=0} = |f|^2 + |g|^2. \tag{2.22}$$

The other non-vanishing observables involve the photon and nucleon spin polarization along the z axis. When only the initial particles are polarized, the corresponding asymmetry is known as Σ_{2z} and can be defined as

$$\Sigma_{2z} = \frac{\mathrm{d}\sigma_{3/2} - \mathrm{d}\sigma_{1/2}}{\mathrm{d}\sigma_{3/2} + \mathrm{d}\sigma_{1/2}}, \tag{2.23}$$

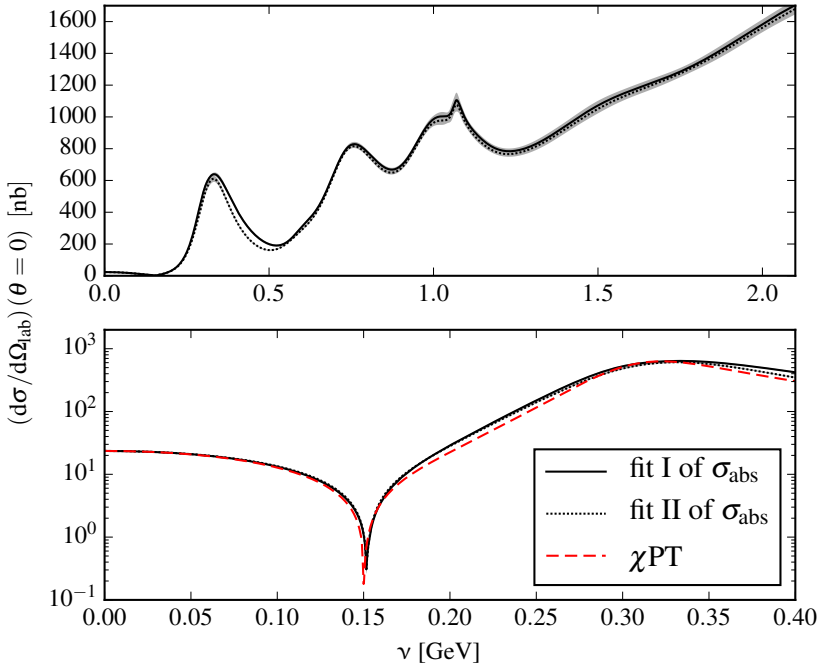

Figure 2.8: Figure from Ref. [3]: Differential cross section of the forward CS off the proton for the two distinctive fits of the unpolarized photoabsorption cross section, obtained in Ref. [2]. The solid gray band represents the resulting estimated uncertainty on the observable. The red dashed curve shows the BχPT calculation of Ref. [95].

where σ_Λ denotes the doubly polarized CS cross section with Λ being the combined helicity of the initial state. When the initial photon and the final nucleon are polarized, the asymmetry is called $\Sigma_{2z'}$. For the forward scattering, all asymmetries involving such pairwise polarization are equal and in terms of f and g are given as follows:

$$\Sigma_{2z}\big|_{\theta=0} = -\frac{2\,\mathrm{Re}(fg^*)}{|f|^2+|g|^2}. \tag{2.24}$$

We list the empirical values of the real part of the forward amplitudes $f(\nu)$ and $g(\nu)$ for several values of ν in Ref. [113]. Below the pion-production threshold ($\nu < m_\pi + m_\pi^2/2M_p$), where the amplitudes are real, the observables can simply be obtained by substituting these values in Eq. (2.22) and (2.24). Above the pion threshold, one obviously needs the photoabsorption cross sections [cf. Eq. (2.4)], which we include in the Supplemental Material [113].

The resulting unpolarized and helicity-difference CS differential cross sections at zero angle are shown in Figs. 2.8 and 2.9, respectively. The lower panels show the comparison with χPT predictions at lower energies. Note the logarithmic scale in the case of the unpolarized cross section, Fig. 2.8 (lower panel). Incidentally, both f and g amplitudes happen to nearly vanish at the pion-production threshold, and so do the cross sections.

A remarkable agreement with the χPT calculations at low energies is observed. For the case of the beam asymmetry, however, the cusp at $\nu \approx 151.5$ MeV, caused by the second pion production threshold (namely the $\pi^+ n$ channel), appears to be somewhat sharper than the one obtained within χPT. This is mainly because the neutral and charged pion production thresholds coincide in the χPT calculation due to unbroken isospin symmetry.

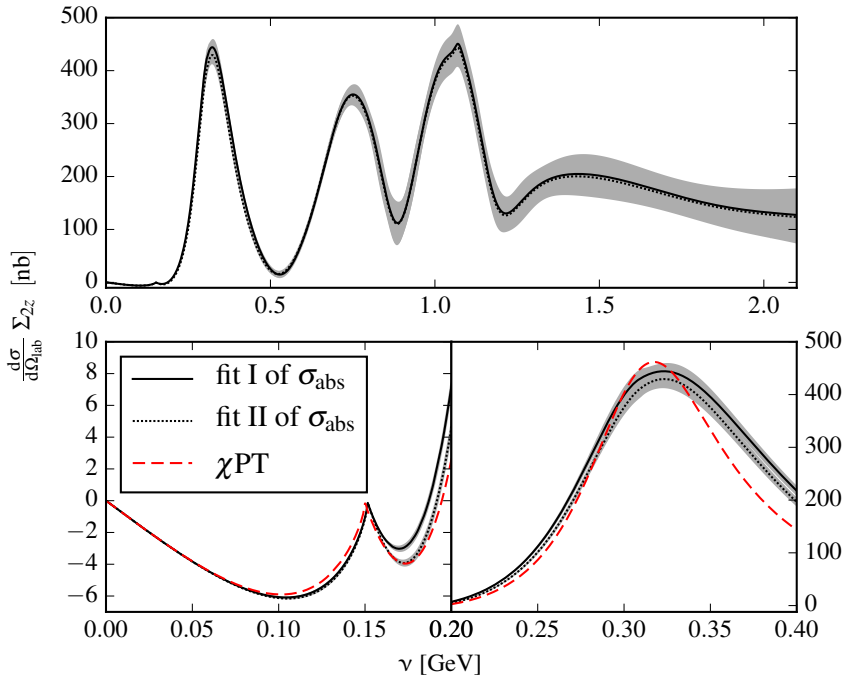

Figure 2.9: Figure from Ref. [3]: Unpolarized differential cross section multiplied with Σ_{2z}-asymmetry for the forward CS off the proton. The two distinctive fits of the unpolarized photoabsorption cross section are obtained in Ref. [2]. The solid gray band represents the resulting estimated uncertainty on the observable. The red dashed curve shows the BχPT calculation of Ref. [95].

The error estimation for the observables is accomplished with the same basic approach as for the case of dispersion integrals, described above. We account for the uncertainty contribution of both f and g.

2.6 Conclusions

We have obtained a first complete model-independent evaluation of the forward Compton scattering off the proton. Our results are based on dispersive sum rules for which the empirical total photoabsorption cross sections serve as input. Putting together the fits of the unpolarized photoabsorption cross section and the helicity-difference cross section obtained here, we have computed the sum rule integrals as well as the energy dependence of the forward CS amplitudes.

The present database of the unpolarized photoabsorption cross section ($\sigma_{\rm abs}$) is not entirely consistent, and so as to reflect that, we obtain two distinct fits to it. The two fits yield slightly different results for the spin-averaged amplitude $f(\nu)$ and, hence, for its low-energy expansion characterized by the scalar polarizabilities of the proton. The new evaluation of the Baldin sum rule is performed, which agrees with the previous ones. The quadrupole polarizability sum rule value is obtained for the first time.

As far as polarizabilities are concerned, only the Baldin sum rule is appreciably affected by the inconsistency in the photoabsorption database. Nevertheless, the two results (fit I and II in Table 2.4) are not in conflict with each other, given the overlapping error bars. It is

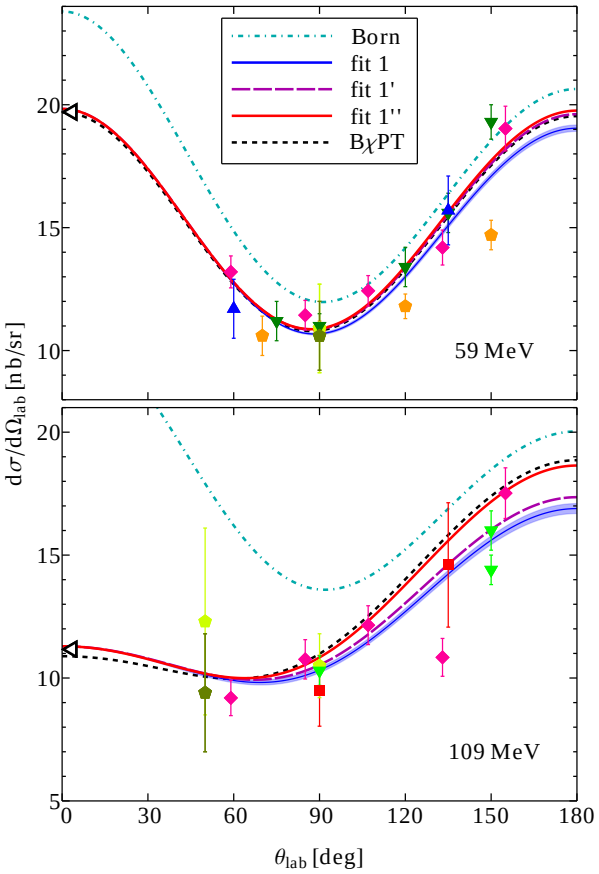

Figure 2.10: Figure from Ref. [114]: Unpolarized cross section of proton CS as function of scattering angle in the lab frame at photon-beam energy 59 MeV (top panel) and 109 MeV (bottom panel). The legend for experimental data points is given in Table I of ref. [114], and the multipole expansion fits correspond to the various scenarios described therein. The white triangles on the left mark the values of the forward differential cross section plotted in Fig. 2.8.

customary to take a statistical average in such cases. Taking a weighted average[8] over our two values for the Baldin sum rule we obtain $\alpha_{E1}^{(\mathrm{p})} + \beta_{M1}^{(\mathrm{p})} = (14.0 \pm 0.2) \times 10^{-4}\,\mathrm{fm}^3$. The error bar here does not directly include the aforementioned systematic uncertainty of the cross section database. However, since the two results are fairly well surmised by the weighted average, the latter should be less prone to the systematic uncertainty of the database.

The existing database for the helicity-difference photoabsorption cross section ($\Delta\sigma_{\mathrm{abs}}$) is, nevertheless, not as comprehensive as for the unpolarized cross section. It consists of only the MAMI (Mainz) and ELSA (Bonn) experimental data between 0.2 and 2.9 GeV. Yet, it proved to be sufficient for a reliable evaluation of the spin-dependent amplitude $g(\nu)$, and subsequently the observables, for photon lab energies up to several GeV. The influence of the experimentally unknown high-energy behavior of the helicity-difference cross section is largely diminished by using a subtraction in the form of the GDH sum rule, cf. Eq. (2.21). Considering

[8] For the weighted average, $\bar{x} \pm \bar{\sigma}$, over a set $\{x_i \pm \sigma_i\}$, we use [115, p. 120]:

$$\bar{x} = \frac{\sum_i x_i/\sigma_i^2}{\sum_j 1/\sigma_j^2}\,,\quad \bar{\sigma} = \left(\frac{\sum_i (x_i - \bar{x})^2/\sigma_i^2}{\sum_j 1/\sigma_j^2}\right)^{1/2}.$$

the low-energy expansion of the forward spin-dependent amplitude, we have (re)evaluated the GDH integral and the two first forward spin polarizabilities. These results are in agreement with the previous evaluations, cf. Table 2.4.

As already mentioned, it is very difficult to access the forward CS experimentally. Most of the CS data for the proton are in fact obtained at scattering angles of 90 deg and above. On the other hand, the relation of the forward CS to the photoabsorption data exploited here is exact, and this sort of evaluation is the next best thing to the real CS data. In some aspects, it is even better (e.g., accuracy and costs). The main advantage is that we directly access the amplitudes, rather than observables, and hence one has, for example, simpler (linear, rather than bi-linear) constraints on the multipole amplitudes. Such multipole analysis of the proton CS data using our stringent constraints of the forward scattering has already been successfully performed in a recent work of Ref. [114], see Fig. 2.10.

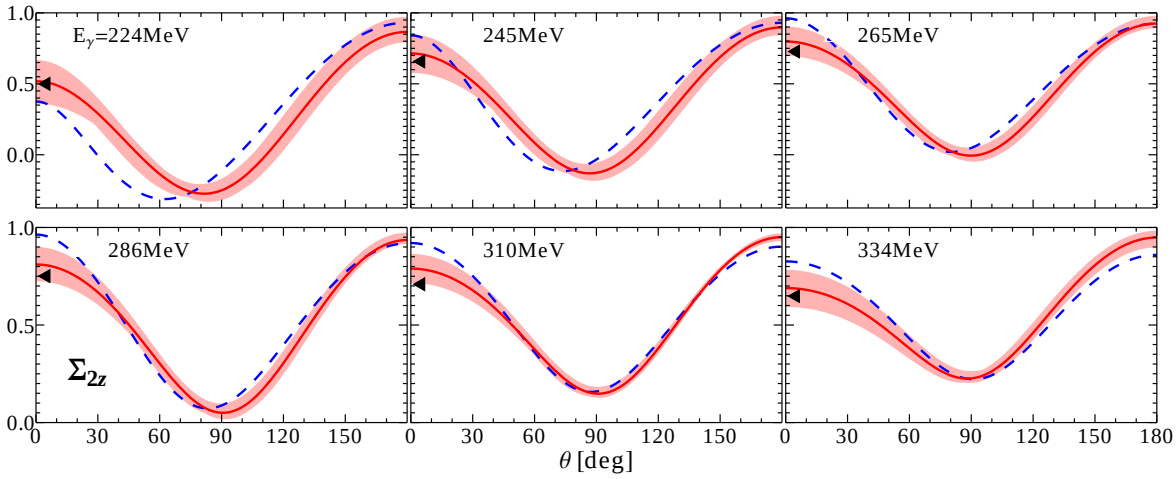

Figure 2.11: Figure from Ref. [95]: Σ_{2z} asymmetry as a function of the center-of-mass-frame angle at different values of $E_\gamma \equiv \nu$. The black triangles show the results of our evaluation. The theoretical bands correspond to the full calculation and their width is determined as explained in the text of ref. [95]. The blue dashed lines correspond to only the Born + Delta pole graphs included in the calculation therein.

Figure 2.11 shows our empirical extraction of Σ_{2z} at $\theta = 0^\circ$ used in Ref. [95]. Similar to the Fig. 2.10, the BχPT theoretical curves demonstrate a remarkable agreement with the forward values extracted within our evaluation. As mentioned in Ref. [95], the dashed curve shown on the Figure 2.11 does not contain the chiral loops, and thus the difference yields the great importance of the latter in this observable.

Appendices

2.A Compton scattering amplitude decomposition

Let us consider the general case of the Compton scattering off a nucleon (proton in our case). Here, we denote the incoming (outgoing) photon and nucleon four-momenta by q and p (q' and p'), with the corresponding spin indices λ and σ (λ' and σ').

Then the invariant amplitude of the general CS is given by

$$\mathcal{M}_{\rm CS} \;=\; i\epsilon^*_\mu(q',\lambda')\bar{N}(p',\sigma')\;\left[4\pi\, T^{\nu\mu}(q,q',P)\right]\;N(p,\sigma)\epsilon_\nu(q,\lambda), \tag{2.25}$$

where $P = \frac{1}{2}(p + p')$ is the symmetrized nucleon four-momentum, and where ϵ and N are the photon polarization vector and the nucleon four-spinor, respectively.

Following definitions given in Ref. [116], the tensor structure of the amplitude is expanded in terms of a set of amplitudes A_i – scalar functions of kinematic variables:

$$T^{\nu\mu}(q, q', P) = \sum_i \tau_i^{\nu\mu}(q, q', P) A_i(q^2, q'^2, q \cdot q', P \cdot K), \tag{2.26}$$

with $\tau_i^{\nu\mu}(q, q', P)$ being the basis of the gauge-invariant tensors, and the symmetrized photon momentum given by $K = \frac{1}{2}(q + q')$.

One may then deduce expressions for the various special cases, e.g. putting photons on the mass shell or considering forward angle scattering. By applying the constraints, we arrive at simplified decompositions (2.26) with reduced numbers of independent scalar amplitudes. Subsequent application of the physical condition $q' \cdot \epsilon(q') = q \cdot \epsilon^*(q) = 0$ further shrinks these numbers down to the expected minimal ones, namely:

- *virtual CS* ($q^2 = 0$):
  18 amplitudes in total / 12 physical, 3 scalar kinematic variables ($P \cdot K$, t, q'^2);

- *real CS* ($q^2 = q'^2 = 0$):
  12 in total / 6 physical amplitudes, 2 scalar kinematic variables ($P \cdot K$, t);

- *double virtual forward CS* ($q^2 = q'^2$; $t = 0$):
  4 total / 4 physical amplitudes, 2 scalar kinematic variables ($p \cdot q$, q'^2);

- *real forward CS* ($q^2 = q'^2 = 0$; $t = 0$):
  4 amplitudes / 2 physical, one scalar kinematic variable ($p \cdot q$).

Specifically, for the latter case of the real forward CS, which is considered in current Chapter, we write down the explicitly gauge-invariant expression with $A_3(p \cdot q)$ and $A_7(p \cdot q)$ being thus proportional to the spin-averaged amplitude $f(\nu)$ and the spin-dependent amplitude $g(\nu)$ in our notation, respectively:

$$\begin{aligned} T^{\nu\mu} &= \left(g^{\nu\mu} - \frac{p^\nu q^\mu}{p \cdot q} - \frac{p^\mu q^\nu}{p \cdot q} \right) \cdot (p \cdot q)^2 \, A_3 \\ &+ \left(\gamma^{\nu\mu} - \frac{p^\nu q_\alpha}{p \cdot q} \gamma^{\alpha\mu} - \frac{p^\mu q_\alpha}{p \cdot q} \gamma^{\nu\alpha} \right) \cdot \frac{4(p \cdot q)^2}{M} \, A_7 \\ &+ \left(\frac{q^\nu q_\alpha}{p \cdot q} \gamma^{\alpha\mu} + \frac{q^\mu q_\alpha}{p \cdot q} \gamma^{\nu\alpha} \right) \cdot \left[4(p \cdot q)^2 \, A_{10} - 2(p \cdot q) \, A_{17} \right] \\ &- \left(\frac{q^\nu q^\mu}{p \cdot q} \right) \cdot \left[(p \cdot q) \, A_1 + 2 (p \cdot q)^2 \, A_4 \right] ; \end{aligned} \tag{2.27}$$

$$\begin{aligned} T^{\nu\mu}_{\text{physical}} = T^{\nu\mu}|_{A_{1,4,10,17}=0} &= \left(g^{\nu\mu} - \frac{p^\nu q^\mu}{p \cdot q} - \frac{p^\mu q^\nu}{p \cdot q} \right) \cdot (p \cdot q)^2 \, A_3 \\ &+ \left(\gamma^{\nu\mu} - \frac{p^\nu q_\alpha}{p \cdot q} \gamma^{\alpha\mu} - \frac{p^\mu q_\alpha}{p \cdot q} \gamma^{\nu\alpha} \right) \cdot \frac{4(p \cdot q)^2}{M} \, A_7 \quad ; \end{aligned} \tag{2.28}$$

where within our notation $p \cdot q \equiv M\nu$, and $M \equiv M_{\text{p}}$ for the proton.

Figure 2.12: Figure from Ref. [2]: Tree-level CS graphs.

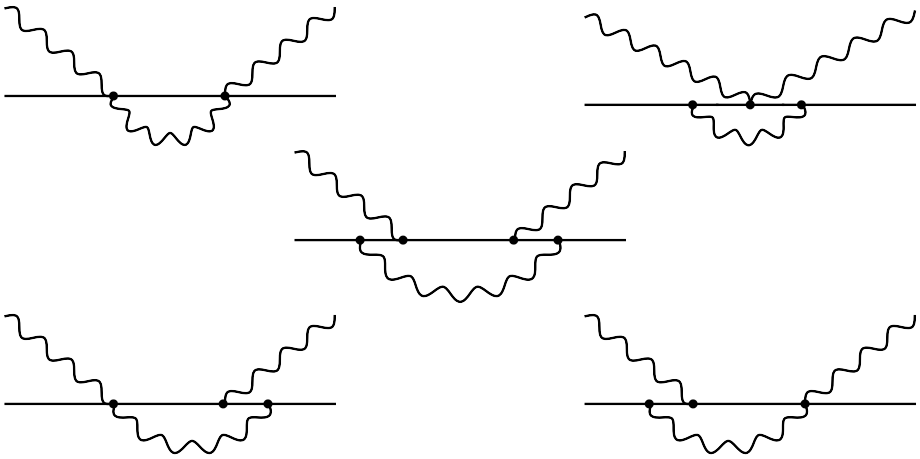

Figure 2.13: Figure from Ref. [2]: One-loop graphs contributing to the forward CS. Graphs obtained from these by crossing of the photon lines are included too.

2.B Sum rules for elastic contribution in scalar QED

This is an Appendix from Ref. [2].

Consider the elastic forward scattering of a photon with momentum q from a charged spinless particle with four-momentum p and mass M. In the forward direction ($t = 0$), this process is completely described by a single amplitude $f(\nu)$. The tree-level QED calculation (Fig. 2.12) yields immediately $f^{(1)}(\nu) = -\alpha/M$, where we have chosen the normalization of this amplitude to coincide with the analogous amplitude for the spin-1/2 case [see Eq. (2.1)]; the superscript indicates the order of α.

Next, we consider the one-loop corrections. Figure 2.13 shows the one-particle-irreducible diagrams appearing in scalar QED. The corresponding one-particle-reducible diagrams vanish in forward direction, due to the transversality of the photon polarization vector ϵ with respect to any of the four-momenta, i.e.: $q \cdot \epsilon = 0 = p \cdot \epsilon$.

Renormalization of these diagrams amounts to subtracting their contribution at $\nu = 0$. We, thus, find the following expression for the renormalized amplitude at order $O(\alpha^2)$:

$$\begin{aligned} f^{(2)}(\nu) &= \frac{\alpha^2}{2\pi M}\left\{\frac{\pi^2 M(M-\nu)+12\nu^2}{6\nu^2}+\frac{8\nu^2}{(M^2-4\nu^2)}\ln\frac{2\nu}{M}+\frac{M(M+\nu)}{\nu^2}\ln\frac{2\nu}{M}\ln\left(1+\frac{2\nu}{M}\right)\right. \\ &+ \left.\frac{M}{\nu^2}\left[(M+\nu)\,\mathrm{Li}_2\Big(-\frac{2\nu}{M}\Big)-(M-\nu)\,\mathrm{Li}_2\Big(1-\frac{2\nu}{M}\Big)\right]\right\}+\frac{i}{4\pi}\nu\sigma^{(2)}(\nu), \end{aligned} \tag{2.29}$$

where $\mathrm{Li}_2(x)$ is the dilogarithm, and $\sigma^{(2)}(\nu)$ is the total CS cross section arising at the tree level (cf. Fig. 2.12),

$$\sigma^{(2)}(\nu) = \frac{2\pi\alpha^2}{\nu^2}\left\{\frac{2(M+\nu)^2}{M^2+2M\nu}-\left(1+\frac{M}{\nu}\right)\ln\left(1+\frac{2\nu}{M}\right)\right\}. \tag{2.30}$$

We note that in the low-energy limit, it reproduces the Thomson cross section: $\sigma^{(2)}(0) = 8\pi\alpha^2/3M^2$, a result that is unaltered by loop corrections, i.e., $\sigma(0) = \sigma^{(2)}(0)$.

As the total photoabsorption cross section to this order in α is given entirely by the tree-level CS cross section, the fact that $\operatorname{Im} f^{(2)}(\nu) = \nu\,\sigma^{(2)}(\nu)/4\pi$ coincides in this case with the statement of the optical theorem. We have also checked that the one-loop amplitude satisfies the once-subtracted dispersion relation:

$$f^{(2)}(\nu) = \frac{\nu^2}{2\pi^2}\int_0^\infty \mathrm{d}\nu'\,\frac{\sigma^{(2)}(\nu')}{\nu'^2-\nu^2-i0^+}, \tag{2.31}$$

and, hence, the full amplitude, $f^{(1)}+f^{(2)}$, indeed enjoys the Kramers-Kronig relation given in Eq. (2.5b).

Now, the whole point of this exercise is to understand the low-energy expansion and, thus, the polarizability sum rules in the case when the photoabsorption cross section is not vanishing at $\nu = 0$. Expanding the real part of Eq. (2.31) around $\nu = 0$, we find

$$\frac{\alpha^2}{\pi M}\left(\frac{1+24\ln\frac{2\nu}{M}}{9M^2}\,\nu^2+\frac{8(14+330\ln\frac{2\nu}{M})}{225M^4}\,\nu^4+\frac{4(17+616\ln\frac{2\nu}{M})}{49M^6}\,\nu^6+\dots\right) = \tag{2.32}$$
$$= \frac{1}{2\pi^2}\sum_{n=1}^{\infty}\nu^{2n}\int_0^\infty \mathrm{d}\nu'\,\frac{\sigma^{(2)}(\nu')}{\nu'^{2n}}.$$

Hence, the coefficients diverge in the infrared. However, there is an apparent mismatch: they are logarithmically divergent on one side and power divergent on the other. To match the sides exactly at each order of ν, thus defining the sum rules for "quasi-static" polarizabilities, we subtract all the power divergences on the right-hand side (rhs) and regularize both sides with the same infrared cutoff (equal to ν):

$$\frac{\alpha^2}{\pi M}\left(\frac{1+24\ln\frac{2\nu}{M}}{9M^2}\,\nu^2+\frac{8(14+330\ln\frac{2\nu}{M})}{225M^4}\,\nu^4+\dots\right) = \tag{2.33}$$

$$= \frac{1}{2\pi^2}\sum_{n=1}^{\infty}\nu^{2n}\int_\nu^\infty \mathrm{d}\nu'\,\frac{\sigma^{(2)}(\nu')-\sum\limits_{k=0}^{2(n-1)}\frac{1}{k!}\frac{\mathrm{d}^k\sigma^{(2)}(\nu)}{\mathrm{d}\nu^k}\Big|_{\nu=0}\nu'^k}{\nu'^{2n}}. \tag{2.34}$$

Both sides are now identical at each order of ν. This is nontrivial, at least for the analytic terms; the logs are fairly easily obtained from the non-regularized right-hand side (rhs) in Eq. (2.32); cf. [117].

Extending these arguments to all orders in α, we find that the proper low-energy expansion for the 'elastic' part of the amplitude reads as

$$f_{\mathrm{el}}(\nu) = -\frac{\alpha}{M}+\frac{1}{2\pi^2}\sum_{n=1}^{\infty}\nu^{2n}\int_\nu^\infty \mathrm{d}\nu'\,\frac{\sigma(\nu')-\bar\sigma_n(\nu')}{\nu'^{2n}}, \tag{2.35}$$

where σ is the total cross section of Compton scattering and $\bar\sigma_n$ are the infrared subtractions:

$$\bar\sigma_n(\nu') \equiv \sum_{k=0}^{2(n-1)}\frac{1}{k!}\frac{\mathrm{d}^k\sigma(\nu)}{\mathrm{d}\nu^k}\Big|_{\nu=0}\nu'^k. \tag{2.36}$$

Now we can, for instance, formulate the Baldin sum rule for the elastic contribution to the dipole polarizabilities. By definition

$$f_{\mathrm{el}}(\nu) = -\alpha/M + (\alpha_{E1}+\beta_{M1})_{\mathrm{el}}\,\nu^2 + O(\nu^4), \tag{2.37}$$

and hence, matching it with the rhs of Eq. (2.35), we obtain

$$(\alpha_{E1}+\beta_{M1})_{\rm el}=\frac{1}{2\pi^2}\int_\nu^\infty {\rm d}\nu'\,\frac{\sigma(\nu')-\sigma(0)}{\nu'^2}. \tag{2.38}$$

In our scalar QED example, where σ is the tree-level cross section $\sigma^{(2)}$, we obtain

$$(\alpha^{(2)}_{E1}+\beta^{(2)}_{M1})_{\rm el}=\frac{\alpha^2}{9\pi M^3}\left(1+24\ln\frac{2\nu}{M}\right), \tag{2.39}$$

which, of course, reproduces the one-loop result [cf. the first term in the expansion of $f^{(2)}$ in Eq. (2.33)].

2.C Sum rules for elastic contribution in spinor QED

This is an Appendix from Ref. [3].

Let us examine the CS (elastic) contribution to the sum rules in spinor QED at $O(\alpha^2)$. Consider the scattering of a photon from a charged spin-1/2 particle with mass M. The helicity amplitudes are expressed in terms of the Feynman amplitude as

$$T_{\lambda'\sigma'\lambda\sigma}=\bar u_{\sigma'}(p')\,\varepsilon^*_{\lambda'}(q')\cdot T(q',q,p',p)\cdot\varepsilon_\lambda(q)\,u_\sigma(p)\,,$$

where we denote the helicity and momentum of the incoming (outgoing) photon by $\lambda(\lambda')$ and $q(q')$ and the helicity and momentum of the incoming (outgoing) spin-1/2 particle by $\sigma(\sigma')$ and $p(p')$. The spinors are normalized according to

$$\bar u_{\sigma'}(p)\,u_\sigma(p)=\delta_{\sigma'\sigma}, \tag{2.40}$$

where p is the nucleon momentum. In general, there are six independent helicity amplitudes for the CS process. The $O(\alpha^2)$ unpolarized and double-polarized cross sections [117] can be deduced from the tree-level helicity amplitudes [118, 119],

$$\sigma^{(2)} = \frac{2\pi\alpha^2}{M^2}\left\{\frac{1+x}{x^3}\left[\frac{2x(1+x)}{1+2x}-\ln(1+2x)\right]\right. \tag{2.41a}$$

$$\left.+\frac{1}{2x}\ln(1+2x)-\frac{1+3x}{(1+2x)^2}\right\}, \tag{2.41b}$$

$$\Delta\sigma^{(2)} = -\frac{2\pi\alpha^2}{M^2x}\left\{\left[1+\frac{1}{x}\right]\ln(1+2x)-2\left[1+\frac{x^2}{(1+2x)^2}\right]\right\}, \tag{2.41c}$$

with $x=\nu/M$. We note that in the low-energy limit the total unpolarized cross section, σ, reproduces the Thomson cross section, $\sigma^{(2)}(0)=8\pi\alpha^2/3M^2$, a result that is unaltered by loop corrections. In the same limit, the helicity-difference cross section, $\Delta\sigma$, is vanishing.

In the forward limit, only two helicity amplitudes are non-vanishing. These are the amplitudes without spin flip: $T_{+1\,+1/2\,+1\,+1/2}$ and $T_{-1\,+1/2\,-1\,+1/2}$. They can be used to reconstruct the spin-dependent and spin-averaged forward CS amplitudes:

$$f = \frac{1}{2}\left[T_{+1\,+1/2\,+1\,+1/2}+T_{-1\,+1/2\,-1\,+1/2}\right], \tag{2.42a}$$

$$g = \frac{1}{2}\left[T_{+1\,+1/2\,+1\,+1/2}-T_{-1\,+1/2\,-1\,+1/2}\right]. \tag{2.42b}$$

Figure 2.14: Figure from Ref. [3]: Tree-level CS graphs.

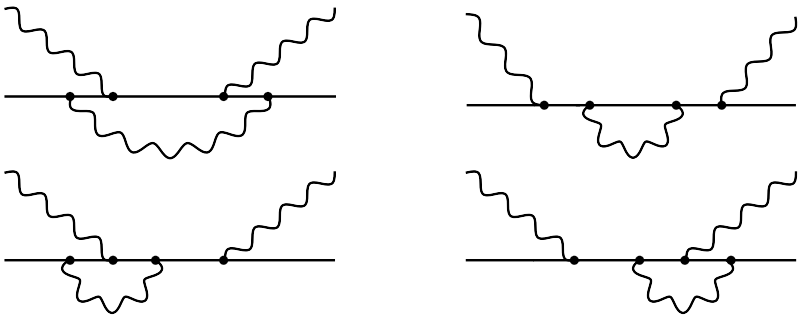

Figure 2.15: Figure from Ref. [3]: One-loop graphs contributing to the forward CS. Graphs obtained from these by crossing of the photon lines are included, too.

At tree level (Fig. 2.14), the spinor QED calculation yields $f^{(1)}(\nu) = -\alpha/M$ and $g^{(1)}(\nu) = 0$, where the superscript indicates the order of α. Next, we consider the one-loop corrections (Fig. 2.15). Tsai *et al.* [118, 119] calculated the Compton scattering helicity amplitudes up to $O(\alpha^2)$. From their result, we obtain the forward CS amplitudes:

$$f^{(2)}(x) = \frac{\alpha^2}{4\pi M}\left\{\frac{24x^2\left(1-3x^2\right)+\pi^2\left(4x^4+8x^3-9x^2-2x+2\right)}{6x^2\left(1-4x^2\right)} - \frac{4x^2\left(4x^2-3\right)}{\left(4x^2-1\right)^2}\ln 2x \right. \tag{2.43a}$$
$$\left. -\frac{x^2-2x-2}{x^2}\left[\ln 2x \ln(1+2x) + \mathrm{Li}_2\left(-2x\right)\right] + \frac{x^2+2x-2}{x^2}\mathrm{Li}_2\left(1-2x\right)\right\} + \frac{iMx}{4\pi}\,\sigma^{(2)}(x),$$

$$g^{(2)}(x) = \frac{\alpha^2}{4\pi M}\left\{\frac{12x^2+\pi^2\left(4x^3-4x^2-x+1\right)}{6x\left(4x^2-1\right)} - \frac{16x^3}{\left(4x^2-1\right)^2}\ln 2x \right. \tag{2.43b}$$
$$\left. -\frac{x+1}{x}\left[\ln 2x \ln(1+2x) + \mathrm{Li}_2\left(-2x\right)\right] - \frac{x-1}{x}\mathrm{Li}_2\left(1-2x\right)\right\} - \frac{iMx}{8\pi}\,\Delta\sigma^{(2)}(x).$$

The fact that $\mathrm{Im}\, f^{(2)}(\nu) = \nu\,\sigma^{(2)}(\nu)/4\pi$ and $\mathrm{Im}\, g^{(2)}(\nu) = -\nu\,\Delta\sigma^{(2)}(\nu)/8\pi$ is in accordance with the optical theorem, cf. Eq. (2.4). Also, we have checked that the one-loop amplitudes indeed satisfy the dispersion relations:

$$f^{(2)}(\nu) = \frac{2\nu^2}{\pi}\int_0^\infty \mathrm{d}\nu' \,\frac{\mathrm{Im}\, f^{(2)}(\nu')}{\nu'\left(\nu'^2-\nu^2-i0^+\right)}, \tag{2.44a}$$

$$g^{(2)}(\nu) = \frac{2\nu}{\pi}\int_0^\infty \mathrm{d}\nu' \,\frac{\mathrm{Im}\, g^{(2)}(\nu')}{\nu'^2-\nu^2-i0^+}, \tag{2.44b}$$

where the subtraction in Eq. (2.44a) corresponds to $f^{(2)}(0) = 0$.

Now, we want to understand the low-energy expansion, and thus the polarizability sum rules in spinor QED. In the previous Appendix, we already performed this exercise in scalar QED.

Expanding the real part of Eq. (2.44) around $\nu = 0$, we find

$$\frac{\alpha^2}{\pi M}\left(\frac{11+48\ln\frac{2\nu}{M}}{18M^2}\nu^2+\frac{7(257+1140\ln\frac{2\nu}{M})}{450M^4}\nu^4+\frac{68(107+672\ln\frac{2\nu}{M})}{441M^6}\nu^6+\ldots\right)= \tag{2.45}$$
$$=\frac{1}{2\pi^2}\sum_{n=1}^{\infty}\nu^{2n}\int_0^{\infty}\mathrm{d}\nu'\,\frac{\sigma^{(2)}(\nu')}{\nu'^{2n}},$$
$$\frac{\alpha^2}{\pi M}\left(\frac{37+60\ln\frac{2\nu}{M}}{18M^3}\nu^3+\frac{64(29+105\ln\frac{2\nu}{M})}{225M^5}\nu^5+\frac{18(89+504\ln\frac{2\nu}{M})}{49M^7}\nu^7+\ldots\right)= \tag{2.46}$$
$$=\frac{1}{4\pi^2}\sum_{n=1}^{\infty}\nu^{2n-1}\int_0^{\infty}\mathrm{d}\nu'\,\frac{\Delta\sigma^{(2)}(\nu')}{\nu'^{2n-1}}.$$

Hence, the coefficients diverge in the infrared. However, once again, they are logarithmically divergent on one side and power divergent on the other. We hence, again, subtract all the power divergences on the right-hand-side (rhs) and regularize both sides with the same infrared cutoff (equal to ν), in order to match the sides exactly at each order of ν, thus defining the sum rules for "quasi-static" polarizabilities:

$$\frac{\alpha^2}{\pi M}\left(\frac{11+48\ln\frac{2\nu}{M}}{18M^2}\nu^2+\frac{7(257+1140\ln\frac{2\nu}{M})}{450M^4}\nu^4+\ldots\right)= \tag{2.47}$$
$$=\frac{1}{2\pi^2}\sum_{n=1}^{\infty}\nu^{2n}\int_{\nu}^{\infty}\mathrm{d}\nu'\,\frac{\sigma^{(2)}(\nu')-\sum_{k=0}^{2(n-1)}\frac{1}{k!}\frac{\mathrm{d}^k\sigma^{(2)}(\nu)}{\mathrm{d}\nu^k}\Big|_{\nu=0}\nu'^k}{\nu'^{2n}},$$
$$\frac{\alpha^2}{\pi M}\left(\frac{37+60\ln\frac{2\nu}{M}}{18M^3}\nu^3+\frac{64(29+105\ln\frac{2\nu}{M})}{225M^5}\nu^5+\ldots\right)= \tag{2.48}$$
$$=\frac{1}{4\pi^2}\sum_{n=2}^{\infty}\nu^{2n-1}\int_{\nu}^{\infty}\mathrm{d}\nu'\,\frac{\Delta\sigma^{(2)}(\nu')-\sum_{k=0}^{2n-3}\frac{1}{k!}\frac{\mathrm{d}^k\Delta\sigma^{(2)}(\nu)}{\mathrm{d}\nu^k}\Big|_{\nu=0}\nu'^k}{\nu'^{2n-1}}.$$

Both sides are now identical at each order of ν. Again, this is nontrivial, at least for the analytic terms; the logs are fairly easily obtained from the non-regularized rhs of the low-energy expanded dispersion relation, cf. Ref. [117]. Since the GDH sum rule only differs from zero starting from $O(\alpha^3)$, we omitted the $O(\nu)$ term in the last equation.

Extending these arguments to all orders in α, we find that the proper low-energy expansion for the "elastic" part of the amplitudes reads as

$$f_{\mathrm{el}}(\nu) = -\frac{\alpha}{M}+\frac{1}{2\pi^2}\sum_{n=1}^{\infty}\nu^{2n}\int_{\nu}^{\infty}\mathrm{d}\nu'\,\frac{\sigma(\nu')-\overline{\sigma}_n(\nu')}{\nu'^{2n}}\,, \tag{2.49a}$$
$$g_{\mathrm{el}}(\nu) = \frac{1}{4\pi^2}\sum_{n=1}^{\infty}\nu^{2n-1}\int_{\nu}^{\infty}\mathrm{d}\nu'\,\frac{\Delta\sigma(\nu')-\overline{\Delta\sigma}_n(\nu')}{\nu'^{2n-1}}\,, \tag{2.49b}$$

where the bar denotes the infrared subtractions:

$$\overline{\sigma}_n(\nu') \equiv \sum_{k=0}^{2(n-1)}\frac{1}{k!}\frac{\mathrm{d}^k\sigma(\nu)}{\mathrm{d}\nu^k}\Big|_{\nu=0}\nu'^k, \tag{2.50a}$$
$$\overline{\Delta\sigma}_n(\nu') \equiv \begin{cases}0 & n=1\\ \sum_{k=0}^{2n-3}\frac{1}{k!}\frac{\mathrm{d}^k\Delta\sigma(\nu)}{\mathrm{d}\nu^k}\Big|_{\nu=0}\nu'^k & n>1.\end{cases} \tag{2.50b}$$

Accordingly, the elastic contributions to the polarizabilities are given by

$$(\alpha_{E1}+\beta_{M1})_{\rm el} = \frac{1}{2\pi^2}\int_\nu^\infty {\rm d}\nu'\,\frac{\sigma(\nu')-\sigma(0)}{\nu'^2}, \tag{2.51a}$$

$$(\gamma_0)_{\rm el} = -\frac{1}{4\pi^2}\int_\nu^\infty {\rm d}\nu'\,\frac{\Delta\sigma(\nu')-\overline{\Delta\sigma}_2(0)}{\nu'^3}, \tag{2.51b}$$

$$(\bar\gamma_0)_{\rm el} = -\frac{1}{4\pi^2}\int_\nu^\infty {\rm d}\nu'\,\frac{\Delta\sigma(\nu')-\overline{\Delta\sigma}_3(0)}{\nu'^5}. \tag{2.51c}$$

In our one-loop spinor QED example, plugging in the tree-level cross sections from Eq. (2.41), we obtain

$$(\alpha_{E1}+\beta_{M1})_{\rm el} = \frac{\alpha^2}{18\pi M^3}\left(11+48\ln\frac{2\nu}{M}\right), \tag{2.52a}$$

$$(\gamma_0)_{\rm el} = -\frac{\alpha^2}{18\pi M^4}\left(37+60\ln\frac{2\nu}{M}\right), \tag{2.52b}$$

$$(\bar\gamma_0)_{\rm el} = -\frac{64\,\alpha^2}{225\pi M^6}\left(29+105\ln\frac{2\nu}{M}\right), \tag{2.52c}$$

which obviously matches the corresponding terms in the low-energy expansion of the tree-level amplitudes.

2.D Uncertainty propagation

The error for a general scalar function $F(x,\{p\})$ of a variable x and a set of parameters $\{p\}$ is estimated by means of the *linear uncertainty propagation*:

$$\left[\Delta F(x,\{p\})\right]^2 = \sum_{i,j}{\rm M}_{i,j}^{\{p\}}\,\frac{\partial F}{\partial p_i}(x,\{p\})\,\frac{\partial F}{\partial p_j}(x,\{p\}), \tag{2.53}$$

where ${\rm M}_{i,j}^{\{p\}}$ is an element of the covariance matrix of the parameters. This can be written in a shorter matrix-notation form as

$${\rm M}_F(x) \equiv \left[\Delta F(x,\{p\})\right]^2 = \mathbf{J}_F(x)\cdot\hat{\mathbf{M}}_p\cdot\mathbf{J}_F^{\rm T}(x), \tag{2.54}$$

where $\hat{\mathbf{M}}_p$ is the covariance matrix, $\mathbf{J}_F(x)\equiv\partial F/\partial\mathbf{p}\;(x,\{p\})$ is the row-vector of derivatives of F over parameters ($\mathbf{p}$ — vector of the parameters), transpose is denoted by "T" and the parameter dependence everywhere is implied.

2.D.1 Covariance matrix

The cross sections fitting is accomplished by means of the *weighted least-squares* optimization algorithm. The algorithm aims to minimize S (the total χ-squared of the fit of $f(x,\{p\})$):

$$S=\sum_i W_{ii}r_i^2,\quad W_{ii}=\frac{1}{\sigma_i^2},\quad r_i=f(x_i,\{p\})-y_i, \tag{2.55}$$

where (x_i,y_i) is a set of data-points with error-bars $\sigma_i\equiv\Delta y_i$. This can be written in a matrix-notation form as follows:

$$S=\mathbf{r}\cdot\hat{\mathbf{W}}\cdot\mathbf{r}^{\rm T}, \tag{2.56}$$

where $\hat{\mathbf{W}}$ is the diagonal matrix of inversed squared data errors (assuming data errors for different points are uncorrelated) and dependence on x and $\{p\}$ is implied.

Given a linear function of parameters

$$f(x, \{p\}) = \mathbf{J}_f(x) \cdot \mathbf{p}^{\mathrm{T}}, \tag{2.57}$$

one obtains the optimal value of χ-squared by finding its extremum. This leads to the solution:

$$\mathbf{p} = \mathbf{y}\hat{\mathbf{W}}^{\mathrm{T}}\hat{\mathbf{J}}_f \left(\hat{\mathbf{J}}_f^{\mathrm{T}}\hat{\mathbf{W}}^{\mathrm{T}}\hat{\mathbf{J}}_f\right)^{-1}, \tag{2.58}$$

where $\hat{\mathbf{J}}_f$ is a (Jacobian) matrix with the rows $\mathbf{J}_f(x = x_i)$. This expression is essentially a linear relation between $\mathbf{p}$ and $\mathbf{y}$. Hence, the covariance matrix of the parameters $\hat{\mathbf{M}}_p$ can be found by means of the usual linear uncertainty propagation as follows:

$$\hat{\mathbf{M}}_p = \left(\hat{\mathbf{J}}_f^{\mathrm{T}}\hat{\mathbf{W}}\hat{\mathbf{J}}_f\right)^{-1} \hat{\mathbf{J}}_f^{\mathrm{T}}\hat{\mathbf{W}}\,\hat{\mathbf{M}}_{\boldsymbol{y}}\,\hat{\mathbf{W}}^{\mathrm{T}}\hat{\mathbf{J}}_f \left(\hat{\mathbf{J}}_f^{\mathrm{T}}\hat{\mathbf{W}}^{\mathrm{T}}\hat{\mathbf{J}}_f\right)^{-1}. \tag{2.59}$$

Since in our case $\hat{\mathbf{M}}_y = \hat{\mathbf{W}}^{-1}$, this simplifies to:

$$\hat{\mathbf{M}}_p = \left(\hat{\mathbf{J}}_f^{\mathrm{T}}\,\hat{\mathbf{W}}\,\hat{\mathbf{J}}_f\right)^{-1}. \tag{2.60}$$

The non-linear least-squares optimization procedure is accomplished with the help of SciPy's wrapper around MINPACK's lmdif and lmder algorithms. These are implementations of the modified Levenberg-Marquardt algorithm [100, 101]. The variance-covariance matrix of parameters is in fact obtained the same way as in the case of linear problem (2.60) (with the Jacobian $\hat{\mathbf{J}}$ being computed at the optimum values of the parameters).

In order to account for the errors of the Regge fit parameters, given no information on the full covariance matrix, we are left to assume the parameters of the fit to be uncorrelated. We, hence, assume the covariance matrix for the Regge parameters (4×4) to be diagonal matrix of parameters' errors squared:

$$\mathrm{M}^{ij}_{p(Regge)} = \delta^{ij}(\sigma_i)^2. \tag{2.61}$$

Since we use a smooth transition between medium- and high-energy regions at 2.03 GeV, the cross section function is not strictly separable at the transition point. Hence, it is appropriate to account for the region (ν_1, ∞) as a whole. That is, we in principle work with a cross section function which is effectively dependent on all the 22 parameters (18 for the resonances in the medium-energy region and 4 for the Regge). For this reason, it is convenient to introduce the total covariance matrix (22×22), which is a block-diagonal matrix of $M_{p(res.)}$ and $M_{p(Regge)}$.

2.D.2 Total uncertainty

Given a function of interest (dispersion integral/observable), which can be decomposed into multiple parts which depend on non-interlacing sets of parameters

$$F(x, \{p\}) = \sum_i F_i(x, \{p\}_i), \quad \{p\} = \bigcup_i \{p\}_i, \tag{2.62}$$

and given the sets of parameters are non-correlated, one estimates the total uncertainty of the function as a sum of squared uncertainties of each F_i:

$$[\Delta F]^2 = \sum_i [\Delta F_i]^2. \tag{2.63}$$

In our case we have 2 regions of cross section with different sources of errors, which we eventually have to combine: the low-energy region with artificial 2% error and the "fitted"

region. By analogy, assuming the sources of errors for the 2 regions to be uncorrelated, the total error on the given function is then:

$$[\Delta F]^2 = [\Delta F_{\text{low-en.}}]^2 + [\Delta_p F_{\text{fitted}}]^2, \tag{2.64}$$

where Δ_p stands for the error which is estimated based on covariance matrix of the parameters of F.

In the low-energy region we simply assume the error-bars of cross section to be 2% of its (absolute) value. The contribution to the error of the dispersion integral coming from the low-energy region is estimated by assuming a simple linear dependence of cross section on a single parameter — scale coefficient of the whole cross section, which has an error of 2%. That is, the error of the integral is simply 2% of its (absolute) value. The sum rule integral error contribution is estimated similarly, except for one thing: instead of integrating 2% of cross section value (which sometimes is negative in our case), we integrate 2% of *absolute value* of cross section.

At the threshold of 2-pion photoproduction (ν_1) the cross section fitting procedure utilizes a couple of points which belong to SAID as additional constraining data-points (which are accounted in total χ-square inside the procedure). This is done in order to achieve proper connection of fixed cross section of the low-energy region with the fitted one in the medium-energy region. When computing the actual covariance matrix (independently of the fitting procedure), in addition to the actual data-points from MAMI/ELSA, a single closest to the threshold point from SAID (with error of 2%) is taken into account as well. This makes the transition of error band across the threshold appear relatively smooth (at a certain level of energy-step) [9]. This also leads, however, to a somewhat underestimated error band at the top of the Δ-resonance. Which in principle is simply caused by a requirement of "smooth" connection to SAID. The same notes apply to the case of unpolarized cross section (for both MAID and SAID).

The error on the observables is estimated based on (2.53) and (2.64) with the account of errors on both the spin-averaged and the spin-dependent amplitudes. The contribution to the error originating from the fitted region is estimated based on (2.53) by calculating the derivatives of observables over parameters:

$$\partial \frac{d\sigma}{d\Omega} / \partial p_i = \partial \left[(\mathrm{Re}f)^2 + (\mathrm{Im}f)^2 + (\mathrm{Re}g)^2 + (\mathrm{Im}g)^2 \right] / \partial p_i = 2 \left(\mathrm{Re}f \, \frac{\partial \mathrm{Re}f}{\partial p_i} + ... \right), \tag{2.65}$$

$$\partial \left[\frac{d\sigma}{d\Omega} \Sigma_{2z} \right] / \partial p_i = \partial \left[\mathrm{Re}f \, \mathrm{Re}g + \mathrm{Im}f \, \mathrm{Im}g \right] / \partial p_i = 2 \left(\mathrm{Re}f \, \frac{\partial \mathrm{Re}g}{\partial p_i} + ... \right). \tag{2.66}$$

Note that, though the error contribution comes solely from the fitted region, the values of $\mathrm{Re}f$ and $\mathrm{Re}g$ here are the *full* values of these dispersion integrals (not partial values coming from this particular region).

Account for the low-energy region on the errors of the observables is accomplished in a similar way by assuming a one-parameter (scale) dependence of the cross section in this region. This basically leads to the following error estimation expressions:

$$\left[\Delta \frac{d\sigma}{d\Omega} \right]^2 = 4 \left(\mathrm{Re}f \, \tilde{\Delta}\mathrm{Re}f + \mathrm{Im}f \, \tilde{\Delta}\mathrm{Im}f + \mathrm{Re}g \, \tilde{\Delta}\mathrm{Re}g + \mathrm{Im}g \, \tilde{\Delta}\mathrm{Im}g \right)^2, \tag{2.67}$$

$$\left[\Delta \frac{d\sigma}{d\Omega} \Sigma_{2z} \right]^2 = 4 \left(\mathrm{Re}f \, \tilde{\Delta}\mathrm{Re}g + \mathrm{Re}g \, \tilde{\Delta}\mathrm{Re}f + \mathrm{Im}f \, \tilde{\Delta}\mathrm{Im}g + \mathrm{Im}g \, \tilde{\Delta}\mathrm{Im}f \right)^2, \tag{2.68}$$

[9] in fact, the error band eventually raises to infinity (logarithmically) at the very threshold, however, this is more a technical feature rather than principal, which can be avoided by introduction of some additional smoothing, and can be ignored with a common energy-step

where $\tilde{\Delta}F = F_{\mathrm{low-en.}} \cdot 2\%$ (in contrast to $\Delta F = |F_{(...)}| \cdot 2\%$). Again, the values of Ref and Reg here are the total values of integrals, while $\tilde{\Delta}$ stands for the error (with sign) coming solely from the low-energy region.

Chapter 3

Direct assessment of the forward CS off protons

While the real part of the spin-averaged forward Compton scattering amplitude can be connected directly through the dispersion relation to the total photoproduction cross section data, the latter is only sufficiently reach for the reasonably low beam energy region $\lesssim$ 2 GeV. As mentioned in the previous Chapter 2 (Ref. [2]), even for this case, however, there exists some discrepancy between current data, which leaves a window for the precise determination of the amplitude. Above the resonance region, the total photoproduction cross section as well as the total hadronic cross sections drop and reach a shallow minimum around $\sqrt{s}$ = 10 - 20 GeV, which is usually interpreted as being due to mesonic Regge exchanges. For higher values of s, the total cross sections for pp, $p\bar{p}$, $\pi^{\pm}p$, γp, $\gamma^{*}p$, and $\gamma\gamma$ show a rise with energy. Understanding the energy dependence of the total cross sections is an important field of study in strong interactions, for reviews see Refs. [120, 121]. On one side, some descriptions solely rely on basic principles such as unitarity, analyticity, and factorization assumptions between different processes, containing a few non-perturbative parameters. For example Regge fits [122] connect pp, $p\bar{p}$, γp, $\gamma^{*}p$, and $\gamma\gamma$ processes using universal parameters. On the other side are models based on QCD, in which the increase at high-energy is described through parton-parton scattering multiplied by parton distributions [123]. Eventually the cross section rise has to saturate, and can behave asymptotically at most as $\ln^2 s$ given by the Froissart bound [124], which was derived for hadronic scattering processes based on unitarity and analyticity. An analysis of total γp cross sections, requiring that the high-energy cross sections interpolate smoothly into the resonance region, has shown strong evidence for a $\ln^2 s$ behavior of the cross section in the region up to $\sqrt{s} \sim 200$ GeV, a behavior which saturates the Froissart bound [125]. To test whether the γp and $\gamma\gamma$ cross sections saturate the Froissart bound at accessible energies, or to distinguish between different descriptions of the forward Compton amplitude above resonance region, direct measurements of the real over imaginary part of the forward Compton amplitude would be extremely useful.

Recently, the TOTEM Collaboration extracted the ratio of real over imaginary parts of the forward pp amplitude at $\sqrt{s}$ = 13 TeV [126] with unprecedented accuracy, thanks to the effects of the Coulomb-nuclear interference in the t-dependence of the differential cross section. These results were interpreted as evidence for the presence of a C-odd contribution to the pp elastic scattering amplitude, which would correspond to a compound three gluon state (known as the Odderon). However recent works have pointed out that to unambiguously reach such conclusion, it is important to understand the t-dependence of the real part of the forward pp scattering amplitude, as an extrapolation to $t = 0$ is needed in extracting the forward amplitude from data [127].

A study of high-energy photoproduction may also be serving as the guide to solving puzzles such as the ultrahigh energy cosmic rays decomposition [128].

We, hence, argue that a direct assessment of the real part of the Compton scattering amplitude could provide a sensitive independent constraint on the various total photoproduction cross section analyses, and test the early saturation of the unitarity bound as spelled out by [125].

The only existing experiment so far aimed to access the forward γp amplitude directly was conducted by Alvensleben *et al.* at DESY in 1973 [87]. By measuring the forward-backward asymmetry of the $\gamma p \to e^- e^+ p$ process, the Collaboration performed a proof-of-principle measurement for the real part of the forward Compton scattering amplitude at the photon lab beam energy $\nu = 2.2$ GeV.

In the present Chapter, we provide updated calculations based on new analyses of photoproduction cross sections in the resonance region, combined with different asymptotic parametrizations, in order to propose an update on the precise extraction of the forward Compton scattering off the proton, following the pioneering measurement of Alvensleben *et al.*, by measuring the forward-backward asymmetry of the di-lepton photoproduction off the proton. In particular we investigate the feasibility of such an experiment in the energy region accessible at Jefferson Lab and at a planned Electron-Ion Collider [129].

The Chapter incorporates material which is currently in preparation for a publication. In Section 3.1 we mention the present status of the parametrization of the total photoproduction cross section off the proton based on existing experimental data, as well as an effect of discrepancy between different models translated onto the real part of the unpolarized forward Compton scattering amplitude. We then describe the process of di-lepton photoproduction off the proton through two leading contributions of Bethe-Heitler and timelike virtual Compton scattering in Section 3.2. In Section 3.3 we present calculations for the forward-backward asymmetry of the aforementioned process and show its sensitivity to the real part of the real forward Compton scattering. Finally, we state our conclusions in Section 3.4. We give the details of the two high-energy parametrizations for the forward Compton scattering amplitudes in Appendix 3.A, as well as some kinematical relations for the di-lepton photoproduction process and the analytical expression for the Bethe-Heitler and timelike Compton scattering interference term in Appendix 3.B.

3.1 Forward CS amplitude and total photoproduction cross section

We would now reiterate over the part of initial analysis from the previous Chapter, and consider the total photoproduction cross section as a function of total mass of the system $W = \sqrt{s}$. We would look at four various fits for the total photoproduction cross section: two fits in the low energy region ($W \lesssim 2$ GeV) from Ref. [2] and two different model for the high-energy behavior ($W \gtrsim 2$ GeV): fit 1 from Block-Halzen (BlHa) and fit of Donnachie-Landshoff (DL) (Refs. [122, 125]).

In the resonance region, the two fits are based on slightly contradictory measurements of the cross section in the region of the $\Delta(1232)$ resonance peak, as described in Chapter 2.

For the fit of the high-energy region, we firstly consider the Donnachie-Landshoff fit [122] (written here in terms of photon energy in the lab frame $\nu = p\cdot q/M = (W^2 - M^2)/2M$) to the total photo- and electroproduction cross sections on a proton as a sum of three Regge poles: a meson Regge pole describing the falling cross section behavior up to $W \simeq 10$ GeV, and a sum of two pomeron Regge poles describing the cross section at high energies as:

$$\sigma_{\gamma p}^{DL}(\nu) \;=\; \beta_m \left(\frac{\nu}{M}\right)^{\alpha_m - 1} + \beta_s \left(\frac{\nu}{M}\right)^{\alpha_s - 1} + \beta_h \left(\frac{\nu}{M}\right)^{\alpha_h - 1}, \tag{3.1}$$

with α_m the meson Regge intercept, and α_s (α_h) the soft (hard) pomeron intercepts. In the DL fit to the world data set of proton structure functions as well as $\gamma\gamma$ data, the effective Regge intercepts are given by [122]:

$$\alpha_m = 0.524, \quad \alpha_s = 1.0667, \quad \alpha_h = 1.452. \tag{3.2}$$

The fit values for the Regge residues β_m, β_s, and β_h are given in Appendix 3.A, see Table 3.1. As the pomeron intercepts are both larger than 1, they have to be considered as effective descriptions at intermediate energies because at asymptotic energies they lead to a violation of unitarity.

In Ref. [125], Block-Halzen performed an alternative high-energy fit to the total photoproduction cross section as the sum of a meson Regge pole term and a $\ln^2 \nu$ asymptotic behavior, corresponding to a saturation of the Froissart bound:

$$\sigma_{\gamma p}^{BlHa}(\nu) \;=\; c_0 + c_1 \ln\left(\frac{\nu}{M}\right) + c_2 \ln^2\left(\frac{\nu}{M}\right) + \beta\left(\frac{\nu}{M}\right)^{\alpha-1} . \tag{3.3}$$

In the Block-Halzen fit, the meson Regge intercept is given by $\alpha = 0.5$, and the other parameter values, as obtained from a fit to the total photoproduction cross section on a proton in the energy range $4 < W < 210$ GeV, are given in Appendix 3.A, see Table 3.2. The Block-Halzen fit respects unitarity, and corresponds to an early saturation of the Froissart bound. At c.m. energy $W = 200$ GeV, the $\ln^2 \nu$ term already contributes around 50 % to the total photoabsorption cross section.

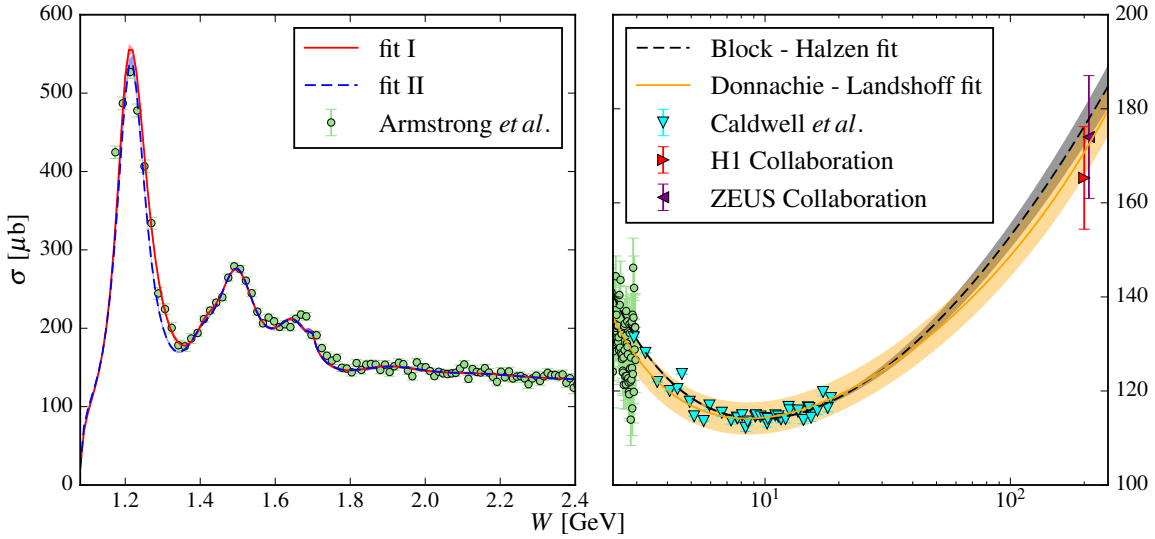

Figure 3.1: Low- and high-energy fits of the total photoproduction cross section data for a proton target. Both resonance fits (I and II) displayed below $W = 2.4$ GeV are from Ref. [2], while the high-energy data are parametrized by two different model fits performed by Block-Halzen [125] and Donnachie-Landshoff [122], as described in the text. The data points displayed here are from Refs. [83, 106–108]. The bands represent estimated uncertainties of the fits.

We show the different fits in Fig. 3.1. We connect our fits for the resonance region smoothly with the high-energy region around $W \simeq 2.1$ GeV ($\nu = 1.8$ GeV) for the DL fit, and around $W \simeq 1.9$ GeV ($\nu = 1.5$ GeV) for the BlHa fit.

For the purpose of our further calculations we carry out the error estimate for the fit of Block-Halzen (Fit 1 of Ref. [125]) by means of linear propagation, given the reconstructed covariance matrix of the fitting parameters therein. We note that this way, however, the actual uncertainty of the cross section curve may be considered underestimated in a sense that the fit performed has an explicit constraint at $W = 2.01$ GeV, where it is assumed to smoothly connect to the resonance region. Since we cannot easily determine the covariance matrix the

same way for the case of the composite fit performed by Donnachie-Landshoff [122], we simply set a reasonable 3% error value for it.

We next consider the process of real forward Compton scattering (CS) off the proton. We thus come back to the Lorentz structure of its amplitude (non-gauge-invariant form), Eq. (2.1):

$$T^{\mu\nu}(p,q) = -g^{\mu\nu} f(\nu) - \gamma^{\mu\nu} g(\nu), \tag{3.4}$$

where the two functions of photon energy in the lab frame, $f(\nu)$ and $g(\nu)$, are the spin-averaged and spin-dependent amplitudes, respectively.

The imaginary part of the spin-averaged forward CS amplitude is related through the optical theorem to the total photoabsorption cross section on the nucleon with Eq. (2.4), while the real part of the spin-averaged forward CS amplitude is expressed through a once-subtracted dispersion integral Eq. (2.5a) (with $Z = 1$ in case of the proton). In Fig. 3.1, we show the total cross section fits both for the resonance region as well as the two high-energy fits, with their respective error bands, as discussed above.

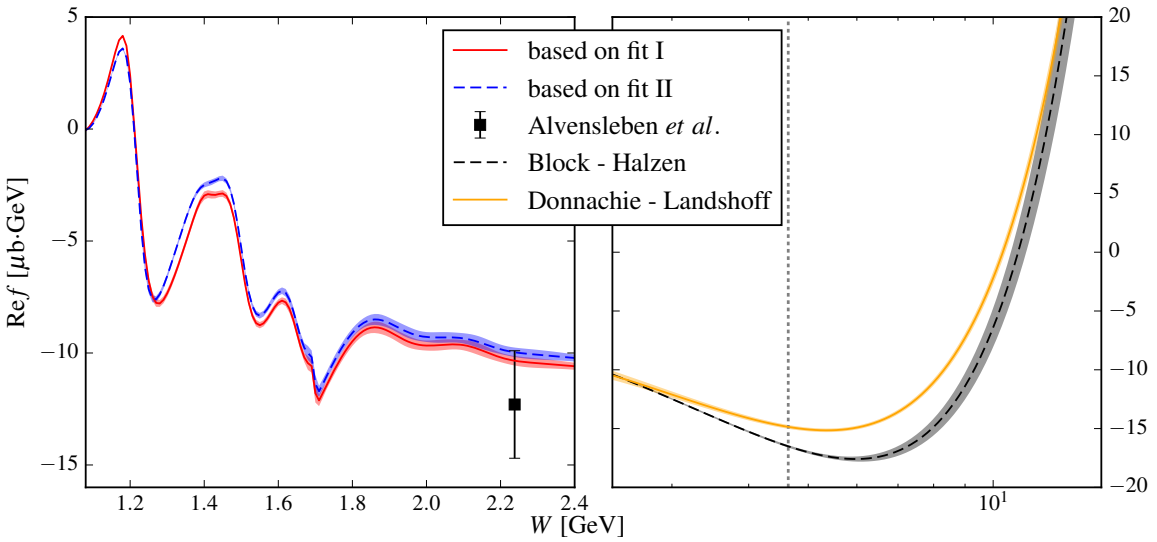

Figure 3.2: Real part of the spin-averaged forward Compton amplitude, calculated based on the fits of the total photoproduction cross section shown in Fig. 3.1. The vertical dotted line on the right panel corresponds to the JLab energy $\nu = 11$ GeV. The bands represent uncertainties estimated by linear propagation from the corresponding fits.

The different cross section fits considered yield differences when looking at the real part of the amplitude, as can be seen on Fig. 3.2. Specifically, at low energies, where the discrepancy between fit I and II comes from the data sets in the $\Delta(1232)$-resonance region, one notices that the real part also has the sensitivity to distinguish between the fits (e.g. $W \sim 1.4$ GeV). We treat the error estimation for the dispersion integral through the linear propagation from the fits based on the computed covariance matrix for the parameters the same way as it is done in Chapter 2.

In the high-energy region the difference between $\mathrm{Re}\, f$ based on BlHa and DL is clearly significant. This effect is, however, dominantly not due to the different asymptotic behavior of the fits, but rather due to differences in the fits within the data region. To demonstrate this, we define the cutoff (Λ) dependent dispersion integral as follows:

$$\mathrm{Re}\, f_\Lambda(W) = -\frac{\alpha}{M} + \frac{(W^2-M^2)^2}{2\pi^2 M} \fint_M^\Lambda \frac{\mathrm{d}W'\, W'\, \sigma(W')}{(W'^2-M^2)^2 - (W^2-M^2)^2},$$

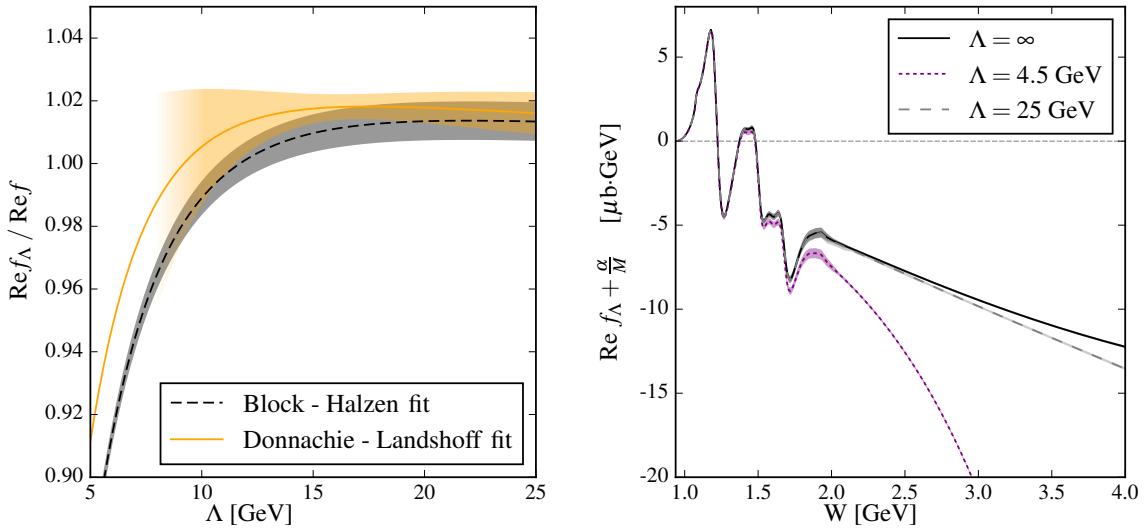

Figure 3.3: Left panel: Cutoff dependence of the W-dependent dispersion integral of Eq. (3.5) for JLab energy $\nu = 11$ GeV (corresponding to $W \approx 4.64$ GeV). The bands represent uncertainties of the cutoff dependent dispersion integral, which are estimated with the linear uncertainty propagation procedure and scaled by the value of full Re f. For the Donnachie-Landshoff fit, the band is only assumed representative at $\Lambda \gtrsim 10$ GeV. Right panel: W-dependence of the integral part of Eq. (3.5) for different values of the cutoff parameter Λ. The full integral corresponding to $\Lambda = \infty$ is shown in black. The high-energy cross section fit is from Block - Halzen. At $W = \Lambda$ the dispersion integral is divergent.

One of the typical energy regimes currently available at JLab is $\nu = 11$ GeV (i.e. $W \approx 4.6$ GeV). One can see, however, from the left panel of Fig. 3.3 that the main contribution to the dispersion integral at such energy, in fact, comes from the energy region up to $W \sim 10$ GeV, where the behavior of the cross section is mainly defined by the already existing data. This particular observation allows to conclude that distinguishing between the asymptotic analyses of BlHa and DL for the photoproduction cross section requires to also measure the real part at high energies. It is additionally notable to observe the energy (W) behaviour of the dispersion integral in Eq. (3.5) in the resonance region for various cutoff values Λ, as shown on the right panel of Fig. 3.3. As the cutoff energy reaches values above the resonance region — the integral closely converges to the full one (corresponding to $\Lambda = \infty$) inside that region, thus indicating insignificant influence of the asymptotic part of the cross section on the forward amplitude at lower energies.

3.2 Di-lepton photoproduction on proton

To access the real part of the forward Compton amplitude, we consider the di-lepton photoproduction process

$$\gamma(q,\lambda) + p(p,\sigma) \;\to\; e^-(l_-,\sigma_-) + e^+(l_+,\sigma_+) + p(p',\sigma'), \tag{3.5}$$

where we denote the incoming 4-momenta for the photon and proton as q and p, and the outgoing 4-momenta for the proton, lepton (electron) and anti-lepton (positron) — as p', l_- and l_+, respectively. λ, σ, σ', σ_-, σ_+ are the corresponding helicities. In the following, we will also use the symmetrized proton 4-momentum as P and the sum of di-lepton four-momenta

as q':

$$P = \frac{1}{2}(p + p'), \quad q' = l_- + l_+. \tag{3.6}$$

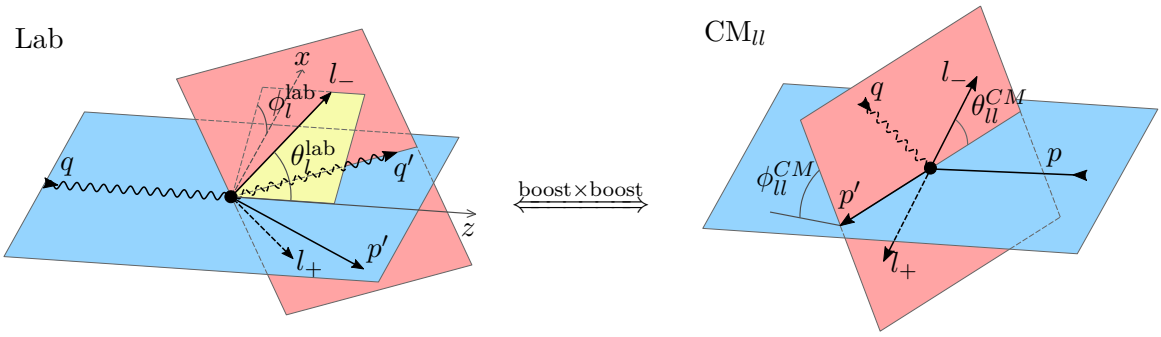

Figure 3.4: Schematical kinematics of the process of di-lepton (e^+e^-) photoproduction on proton depicted in the Lab (left) and the lepton pair center-of-mass frame (right).

The kinematics of the di-lepton photoproduction process is parametrized by five independent variables. Apart from two degrees of freedom of the lepton pair, we use the following set of invariants:

$$s = (p+q)^2 = W^2 = M^2 + 2M\nu, \tag{3.7}$$
$$t = (p-p')^2, \tag{3.8}$$
$$q'^2 = (l_- + l_+)^2 = M_{\rm ll}^2. \tag{3.9}$$

We define the angles θ_{ll}^{CM}, ϕ_{ll}^{CM} of the electron in the rest frame of the di-lepton pair, where the polar angle θ_{ll}^{CM} is defined with respect to the direction of $-\boldsymbol{p}'$ in the lepton pair c.m. frame (see Fig. 3.4, right).

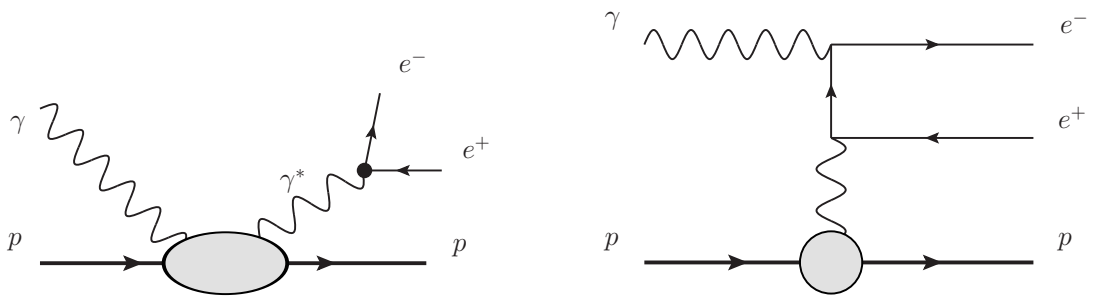

Figure 3.5: Feynman diagrams of the di-lepton (e^+e^-) photoproduction through timelike Compton (left) and Bethe-Heitler (right) processes. For the Bethe-Heitler process the diagram with crossed electron and positrons lines is also assumed.

At leading order in α, the two contributions to the $\gamma p \to e^-e^+p$ reaction arise from the timelike Compton (TCS) process (left diagram in Fig. 3.5) and the Bethe-Heitler mechanism (right diagram in Fig. 3.5, plus analogous crossed diagram).

As we are interested to access the forward real Compton amplitude, we will consider the $\gamma p \to e^-e^+p$ process in the particular kinematics of small values of the lepton pair mass M_{ll} and small momentum transfer $-t$ (relative to s). This allows us to approximate the di-lepton production through near-forward TCS by a proper kinematical extrapolation of the real forward CS.

The invariant amplitude of the TCS contribution to the di-lepton photoproduction reaction (Fig. 3.5, left) is given by:

$$\mathcal{M}_{\rm TCS} = \frac{ie^3}{q'^2}\,\bar{u}(l_-,\sigma_-)\,\gamma_\nu\,v(l_+,\sigma_+)\,\varepsilon_\mu(q,\lambda)\,\bar{N}(p',\sigma')\,\left[\frac{1}{\alpha}T^{\mu\nu}_{\rm fTCS}\right]\,(P,q,q')\,N(p,\sigma), \tag{3.10}$$

with the electric charge e given through $\alpha = e^2/(4\pi) \simeq 1/137$ and where we use covariant normalization conventions for the spinors. Furthermore, $u(v)$ denote the $e^-(e^+)$ spinors, and ε_μ is the initial photon polarization vector. The $l_\pm$ and $\sigma_\pm$ denote the momentum and helicity of the leptons. The quasi-real-forward TCS amplitude (fTCS) is then obtained based on the Lorentz structure of the doubly-virtual CS and is thus given by:

$$\begin{aligned} T^{\mu\nu}_{\rm fTCS}(P,q,q') \;&=\; \left(-g^{\mu\nu} + \frac{q'^\mu q^\nu}{q\cdot q'}\right) T_1(\tilde{\nu},t,q'^2) \\ &+\frac{1}{M^2}\left(P^\mu - \frac{q\cdot P}{q\cdot q'}q'^\mu\right)\left(P^\nu - \frac{q\cdot P}{q\cdot q'}q^\nu\right) T_2(\tilde{\nu},t,q'^2). \end{aligned} \tag{3.11}$$

Here, $\tilde{\nu} = q\cdot P/M$, M is the mass of the target (proton), and T_1 and T_2 denote the two spin-averaged near-forward amplitudes. We find in the limit $t, q' \to 0$

$$T_1(\tilde{\nu},t,q'^2) \;\simeq\; f(\tilde{\nu})\,, \tag{3.12}$$

$$T_2(\tilde{\nu},t,q'^2) \;\simeq\; -\frac{q\cdot q'}{\tilde{\nu}^2}\,f(\tilde{\nu})\,, \tag{3.13}$$

where $f(\tilde{\nu})$ denotes the spin-averaged forward real Compton amplitude of Eq. (3.4). Note that the T_2 term in the amplitude decouples in the exact forward limit ($q = q'$).

An irreducible background to the above $\gamma p \to \psi p \to e^-e^+p$ process arises from the Bethe-Heitler (BH) process (Fig. 3.5, right, plus crossed diagram). The tree-level BH invariant amplitude, contributing to the $\gamma\, p \to e^-e^+\, p$ reaction, is given by

$$\begin{aligned} \mathcal{M}_{BH} \;&=\; \frac{ie^3}{t}\varepsilon^\mu(q,\lambda)\cdot\bar{N}(p',s'_p)\Gamma^\nu N(p,s_p) \\ &\times\; \bar{u}(l_-,s_-)\left\{\gamma_\mu\frac{\gamma\cdot(l_- - q)+m}{-2l_-\cdot q}\gamma_\nu + \gamma_\nu\frac{\gamma\cdot(q-l_+)+m}{-2l_+\cdot q}\gamma_\mu\right\}v(l_+,s_+), \end{aligned} \tag{3.14}$$

with nucleon vertex given by

$$\Gamma^\nu = F_1(t)\gamma^\nu + F_2(t)\frac{i\sigma^{\nu\alpha}(p'-p)_\alpha}{2M}, \tag{3.15}$$

where $F_1(F_2)$ are the Dirac (Pauli) proton electromagnetic form factors, which we take from the recent fit of elastic e-p scattering data of Refs. [130, 131].

The unpolarized differential cross section for the $\gamma p \to e^-e^+p$ reaction is then written as

$$\frac{d\sigma}{dt\,dq'^2\,d\Omega^{l-l+}_{\rm CM}} = \frac{1}{64(2\pi)^4}\,\frac{1}{(2M\nu)^2}\,\sqrt{1-\frac{4m^2}{q'^2}}\,\frac{1}{4}\sum_{\sigma,\lambda}\sum_{\sigma',\sigma_-,\sigma_+}|\mathcal{M}_{\rm BH}+\mathcal{M}_{\rm TCS}|^2, \tag{3.16}$$

with the lepton (electron in our case) mass m.

Now, an observable of special interest to us, which allows to access the Compton amplitude, is the forward-backward (or charge) asymmetry — the asymmetry of outgoing lepton and anti-lepton interchange, defined as

$$A_{FB} \equiv \frac{d\sigma(\theta^{\rm CM}_{ll}) - d\sigma(\theta^{\rm CM}_{ll} - 180^\circ)}{d\sigma(\theta^{\rm CM}_{ll}) + d\sigma(\theta^{\rm CM}_{ll} - 180^\circ)}, \tag{3.17}$$

with $\theta_{ll}^{\rm CM}$ being the lepton polar angle as defined above. Because of opposite symmetry of the competing processes (Fig. 3.5) under charge conjugation, the asymmetry allows for a direct assessment of the interference term between the Bethe-Heitler and the real part of the CS, whereas the Bethe-Heitler and Compton processes separately yield a zero asymmetry. One thus has:

$$A_{FB} \;=\; \frac{2\,\sum_{\sigma,\lambda}\,\sum_{\sigma',\sigma_-,\sigma_+}\,{\rm Re}\,(\mathcal{M}_{\rm BH}\,\mathcal{M}^*_{\rm TCS})}{\sum_{\sigma,\lambda}\,\sum_{\sigma',\sigma_-,\sigma_+}\,(|\mathcal{M}_{\rm BH}|^2\;+\;|\mathcal{M}_{\rm TCS}|^2)}. \tag{3.18}$$

Hence, by having determined ${\rm Re}\,T_1$, up to leading order and within the near-forward kinematics constraints, one gets an estimate for the asymmetry. And vise versa: by measuring the asymmetry at appropriate kinematics, one gets a direct access to the real part of the forward Compton scattering.

While the full analytical expression for the interference term is rather cumbersome, given both the momentum transfer $-t$ and the lepton pair mass M_{ll} are small enough (relative to s), to a reasonable accuracy one can approximate the expression by the following leading terms (leaving only terms of at most t^2, tM_{ll}^2 or M_{ll}^4 behavior):

$$\begin{aligned}\frac{1}{4}\sum_{\sigma,\lambda}\sum_{\sigma',\sigma_-,\sigma_+}{\rm Re}\,(\mathcal{M}_{\rm BH}\,\mathcal{M}^*_{\rm TCS}) \;&\approx\; \frac{2e^6 M}{D\,L\,M_{ll}^2\,t}\,G_E(t)\;[{\rm Re}\,f]\\ \times\,\Big\{\frac{2(a^2-x^2)}{(2x-y)^2}\,[K+ytb]+4m^2\,[CD+yb]+K\;+\;\mathcal{O}\left(\left(t^2+M_{ll}^4\right)^{\frac{3}{2}}\right)\Big\},\end{aligned} \tag{3.19}$$

where we have introduced the notations

$$x \;=\; 2p\cdot q = 2M\nu, \tag{3.20}$$

$$y \;=\; 2q\cdot q' = M_{ll}^2 - t. \tag{3.21}$$

and (following the notation of L from [132]):

$$D \;=\; 1-\frac{t}{4M^2}, \qquad L=\frac{1}{4}(y^2-b^2), \tag{3.22}$$

$$C \;=\; \frac{1}{2}(ya-xb), \qquad K=2(yC-xtb). \tag{3.23}$$

The di-lepton angle-dependent kinematic variables a and b are defined in Appendix 3.B.1. Furthermore, $G_E(t)$ is the electric form-factor

$$G_E(t) = F_1(t) + \frac{t}{4M^2}F_2(t), \tag{3.24}$$

with F_1 (F_2) the Dirac (Pauli) FFs of the proton. The corresponding full expression for the interference term is provided in the Appendix 3.B.2 (Eq. (3.39))

3.3 Results and discussion

We show our estimate of the asymmetry for the case of kinematics of the experiment carried out by Alvensleben *et al.* at DESY [87] at the beam energy $\nu = 2.2$ GeV on Fig. 3.6. This energy region is mainly driven by the distinctive low-energy fits I and II. One can observe here the cleavage of the two fits to be within the order of the uncertainty estimate — a couple of percent, while the asymmetry itself reaching values of around 20%. By looking at the comparison to existing experimental points (Fig. 3.6, right), one can see even within the large uncertainty these do not fully agree with much more constrained uncertainty estimate of our analysis.

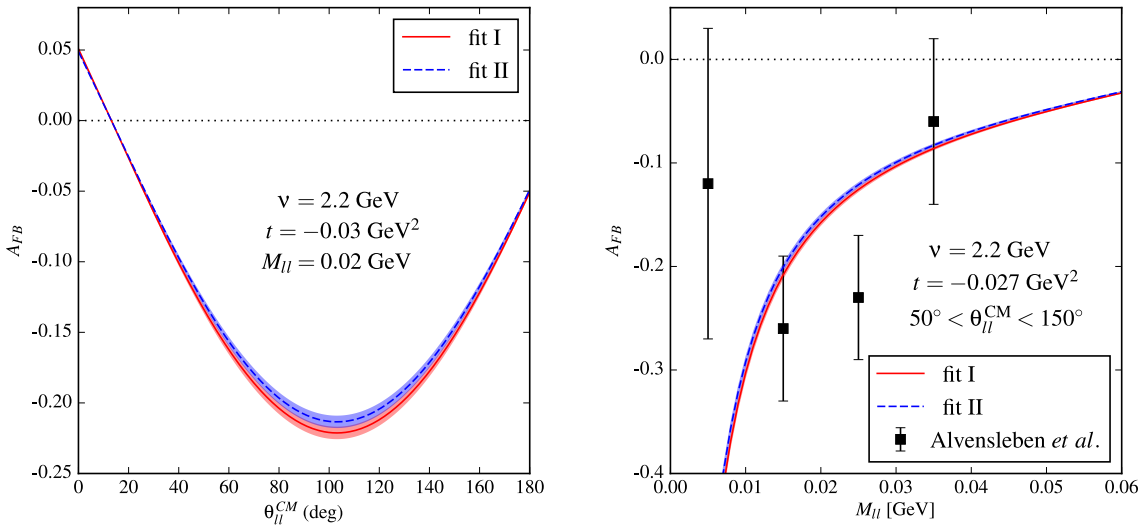

Figure 3.6: Our calculation of the forward-backward asymmetry for the $\gamma p \to e^- e^+ p$ process for kinematics of the DESY experiment [87]. Left: angular dependence of the asymmetry for two low-energy fits of $\sigma_{\rm tot}$. Right: asymmetry as a function of lepton pair mass, compared to the DESY data, for integrated differential cross sections over the angular range. The bands represent the propagated uncertainty estimate.

Based on the fits of the total photoproduction cross section, we present estimates for the forward-backward asymmetry both in the resonance region and above the resonance region in Fig. 3.7. The left panel of Fig. 3.7 corresponds to the energy region close to Δ-resonance, where we distinguish between two fits from the previous Chapter (Ref. [2]). The procedure of uncertainty estimation follows the same linear propagation algorithm as for the dispersion integral, also mentioned in Appendix 2.D. One observes the discrepancy between these two fits at the order of estimated uncertainty — around 5%. On the right panel of Fig. 3.7 we consider a possible kinematics at JLab with the JLab photon beam energy of 11 GeV. Here, one can see that the two analyses with either the Block-Halzen or the Donnachie-Landshoff fits can clearly be distinguished with the asymmetry difference of the order of 2%. As discussed in Section 3.1 above, this difference does not in fact define the asymptotic behaviour of the cross sections, but rather the distinct fitting particularities based on the data in the medium-energy resonance region. One therefore has to look for the higher energy di-lepton photoproduction measurement opportunities. We also note here that the simplified approximate expression for the interference term (3.19) is accurate enough to be used in calculations within the precision of the order of uncertainty of the fits of photoproduction cross section.

We furthermore compare the forward-backward asymmetry in the energy range between $W = 3$ GeV and $W = 100$ GeV Fig. 3.8. As one expects a zero crossing in the real part of f around $W \simeq 10$ GeV, a measurement well below such energy at Jlab and above that energy at an Electron-Ion Collider (EIC) [129] will be sensitive to the sign change in f. In Fig. 3.8, for the two energies well below the zero crossing: $W = 3$ GeV ($\nu \approx 4.4$ GeV) and $W = 4.6$ GeV ($\nu \approx 11$ GeV), which are both accessible at JLab, the forward-backward asymmetry reaches values in the range -10% to -25% for $-t = 0.1$ GeV^2. On the other hand at $W = 25$ GeV, which is above the zero crossing and accessible at an EIC, the asymmetry has changed sign. One notices that a further increase of the energy yields a decreasing asymmetry, through

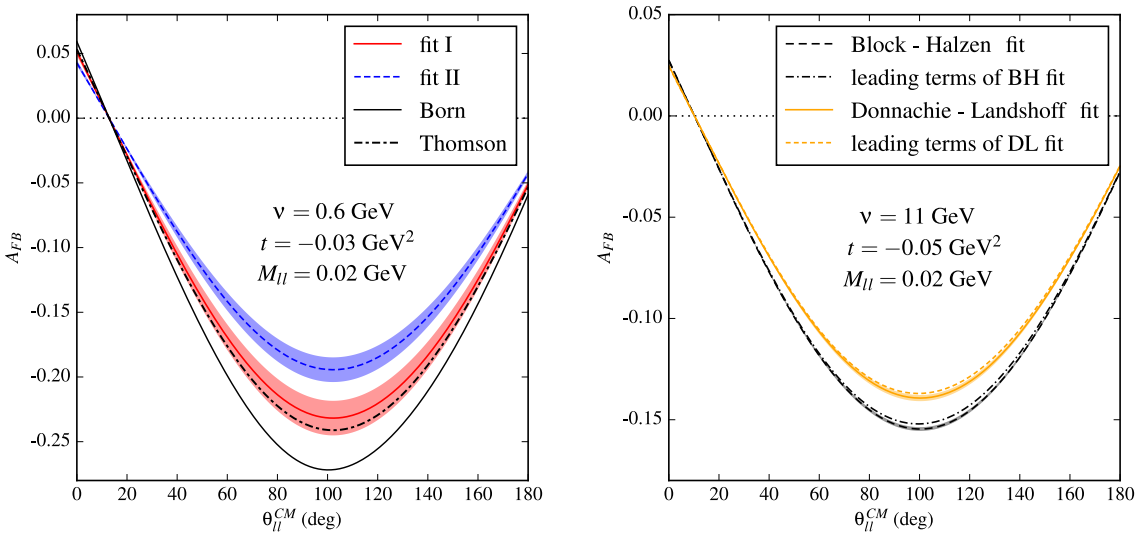

Figure 3.7: Forward-backward asymmetry for the $\gamma p \to e^- e^+ p$ process as a function of the lepton polar angle in the lepton pair CM frame for different fits of σ_{tot} and for two different values of the photon energy ν and momentum transfer $-t$. The bands represent the propagated uncertainty estimate. Also shown are the "Born" and "Thomson" curves, which stand for the exact Born contribution to TCS and Thomson limit substitution into Eq. (3.11), respectively. On the right panel, the calculation is compared to the leading terms expression of Eq. (3.19).

interference with the Bethe-Heitler process, and yields a value around -15% for $W = 100$ GeV, providing a clear signal to extract f at an EIC.

3.4 Conclusions

We have presented the estimates of the forward-backward asymmetry for the di-lepton photoproduction process in the kinematical range of small momentum transfer $-t$ and lepton pair mass M_{ll}, which serves as an observable for the direct access to the forward Compton scattering off the proton.

We have shown that the estimate of the asymmetry based on the current fits for the total photoproduction cross section can reach values of around -20%. At the same time we show that it is possible, within the estimated uncertainties, to distinguish between the two different fits in the low-energy region $W \lesssim 2$ GeV. and even much more accurately — between the analyses [122, 125] in the medium-energy resonance region. Distinguishing between the principal types of asymptotic behaviour, however, calls upon sufficiently high energy measurements. Considering a planned Electron-Ion Collider is one such option, which in combination with a measurement at JLab may additionally provide an improved constraint in the energy range of the amplitude zero crossing.

We have provided the expression for the tree-level interference term between the TCS and Bethe-Heitler processes Eq. (3.39). In addition to the full analytic expression (3.39), we write down a simplified form (3.19), which is shown to have a reasonable precision for our kinematics case in order to be used in possible calculations for the specific experimental setups.

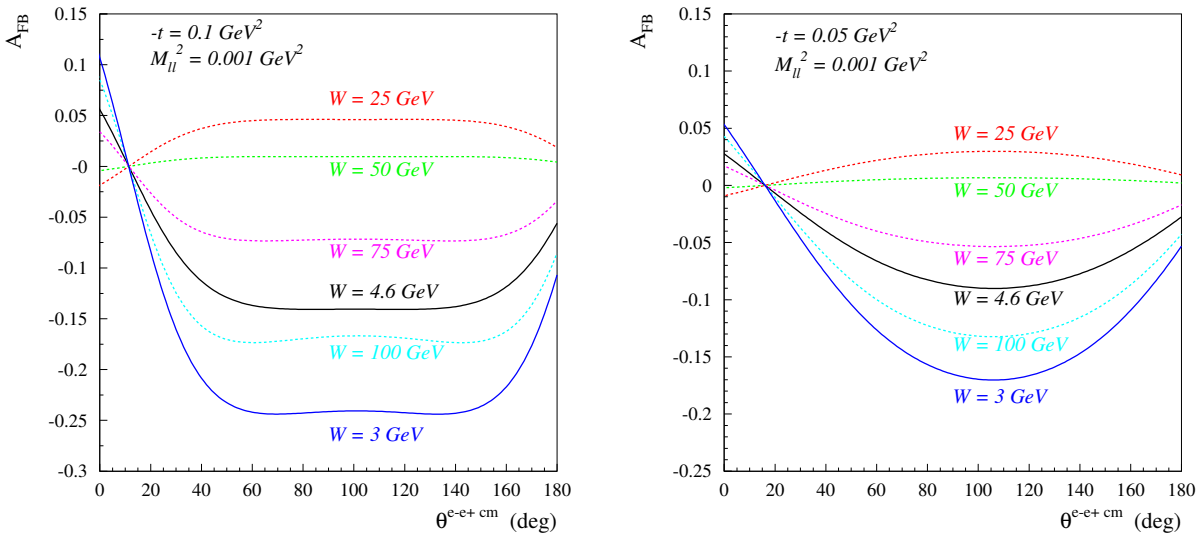

Figure 3.8: Forward-backward asymmetry for the $\gamma\, p \to e^- e^+\, p$ process for $M_{ll}^2 = 0.001$ GeV^2 and two values of t, as a function of the lepton polar angle in the lepton pair CM frame for different values of the c.m. energies accessible at JLab (solid curves for $W = 3$ GeV and $W = 4.6$ GeV) as well as the EIC (dashed curves for $W = 25, 50, 75, 100$ GeV). We use our fit of $\sigma_{\rm tot}$ with Block-Halzen asymptotic parametrization.

Appendices

3.A High-energy parametrizations for the unpolarized forward CS amplitude

3.A.1 Donnachie-Landshoff Regge pole parametrization

In Ref. [122], Donnachie-Landshoff performed a high-energy fit to the total photo- and electroproduction cross sections as a sum of three Regge poles: a meson Regge pole describing the falling cross section behavior up to around $W \simeq 10$ GeV, and a sum of two pomeron Regge poles describing the rise at higher energies, as given by Eq. (3.1). Through a fit to the world data of proton structure functions, the Regge intercepts were determined as given by Eq. (3.2), whereas the Regge residues for real photons were determined by a fit to the γp total cross section. The resulting parameter values of the fit are shown in Table 3.1.

parameter	Fit of [122]
β_m (μb)	86.36
β_s (μb)	76.48
β_h (μb)	0.218

Table 3.1: Fit values of the Regge pole residues entering the Donnachie-Landshoff γp total cross section parametrization [122] of Eq. (3.1), as described in the text.

Based on the fit form of Eq. (3.1) for the total cross section, one obtains an analytic form

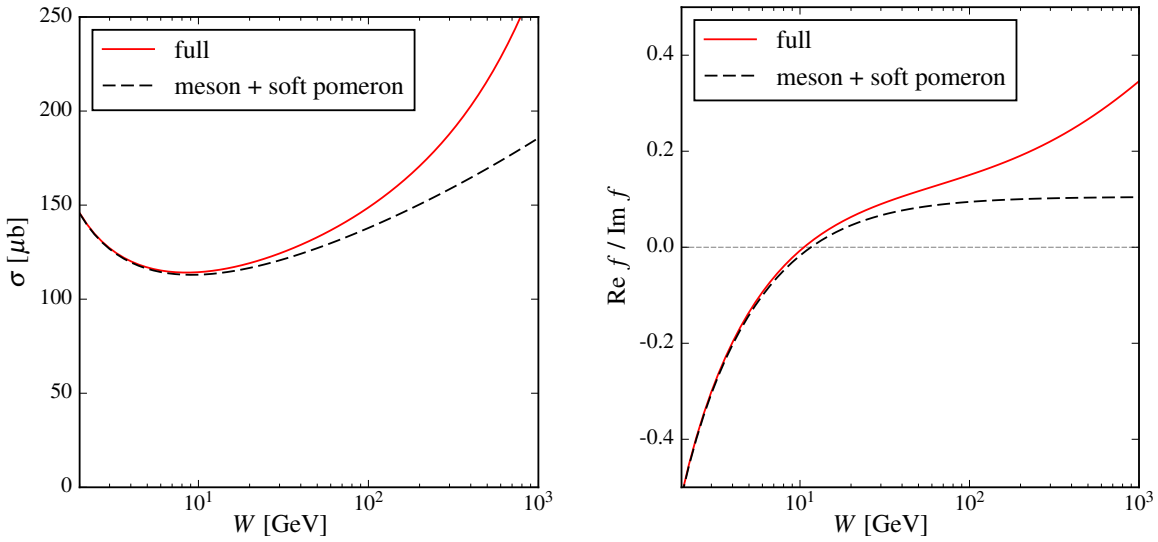

Figure 3.9: W-dependence of the total cross section (left panel) and the real over imaginary part of f in the Donnachie-Landshoff parametrization of Eqs. (3.26) and (3.27). The curves show the contribution of the meson plus soft pomeron Regge term (black dashed curves), and the full contribution including the hard pomeron term (red solid curves).

for the forward real Compton amplitude, denoted by $f^{DL}(\nu)$, as (for real $\nu \geq 0$):

$$f^{DL}(\nu) - f(0) = \frac{M}{4\pi} \sum_{i=m,s,h} (-\beta_i) \frac{1 + e^{-i\pi\alpha_i}}{\sin \pi\alpha_i} \left(\frac{\nu}{M}\right)^{\alpha_i}, \tag{3.25}$$

with $f(0)$ the subtraction constant at $\nu = 0$. From Eq. (3.25), the imaginary part directly follows from unitarity

$$\text{Im}\, f^{DL}(\nu) = \frac{\nu}{4\pi} \sigma_{\gamma p}^{DL}(\nu), \tag{3.26}$$

given the cross section parametrization of Eq. (3.1). Furthermore, the real part is given by :

$$\text{Re}\, f^{DL}(\nu) - f(0) \quad = \quad \frac{M}{4\pi} \sum_{i=m,s,h} (-\beta_i) \cot\left(\frac{\pi\alpha_i}{2}\right) \left(\frac{\nu}{M}\right)^{\alpha_i}. \tag{3.27}$$

As the forward amplitude is an analytic function, it satisfies the subtracted dispersion relation:

$$\text{Re}\, f^{DL}(\nu) - f(0) = \frac{\nu^2}{2\pi^2} \fint_0^\infty d\nu' \frac{\sigma^{DL}(\nu')}{\nu'^2 - \nu^2}. \tag{3.28}$$

Note that Eqs. (3.1) and (3.27) satisfy the subtracted dispersion relation of Eq. (3.28) exactly with lower integration limit $\nu' = 0$. If we were to integrate Eq. (3.28) from the ν value corresponding with $W \simeq 2$ GeV, above which we use the DL parametrization, this would yield a constant term, which can be absorbed in the subtraction constant $f(0)$, as well as power suppressed terms of order $\mathcal{O}(1/\nu^2)$, which are irrelevant at high energies. Therefore to

determine the real part of the amplitude in the asymptotic region, the precise value of the lower integration limit in Eq. (3.28), below $W \lesssim 2$ GeV, is not relevant. In this Chapter, we connect the asymptotic form σ^{DL} of Eq. (3.1) of the Donnachie-Landshoff parametrization above $W \simeq 2$ GeV, and match it with our resonance cross section fits from threshold up to $W \simeq 2$ GeV. We then reconstruct the total real part of the forward Compton amplitude at any energy using the subtracted dispersion relation. This yields a real amplitude which at high energies approaches Eq. (3.27).

3.A.2 Block-Halzen $\ln^2 s$ asymptotic parametrization

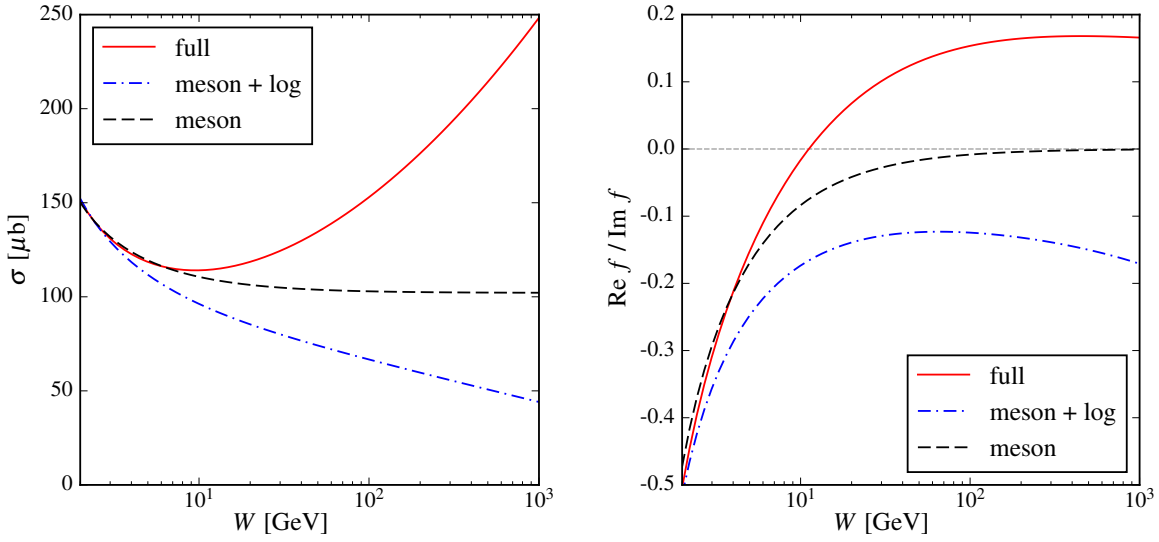

Figure 3.10: W-dependence of the total cross section (left panel) and the real over imaginary part of f in the Block-Halzen parametrization (Fit 1) of Eqs. (3.30) and (3.31). The curves show the different contributions to f: the meson Regge term (black dashed curve), the meson Regge plus $\ln\nu$ term (blue dash-dotted curve), and the full contribution including the $\ln^2\nu$ term (red solid curve).

In Ref. [125], the total photoproduction cross section is described by the sum of a meson Regge pole term and a $\ln^2\nu$ asymptotic behavior, corresponding to a saturation of the Froissart bound, as given by Eq. (3.3). To determine the parameter values in this parametrization, two fits to the total photoproduction data on a proton were performed in Ref. [125], in the energy range $4 < W < 210$ GeV. These fits were connected smoothly to the resonance region parametrization of Damashek-Gilman [82] at $W = 2$ GeV, which constrains the parameter c_0 in both fits. In the first fit (Fit 1), the Regge residue β was furthermore constrained by requiring a smooth first derivative at the matching point, whereas this parameter was left free in a second fit (Fit 2). The resulting parameter values of both fits are shown in Table 3.2.

Based on the fit form of Eq. (3.3) for the total cross section, Block-Halzen proposed an analytic form for the forward real Compton amplitude, denoted by $f^{BlHa}(\nu)$, as (for real $\nu \geq 0$):

$$f^{BlHa}(\nu) - f(0) = \frac{\nu}{4\pi} i \Bigg\{ c_0 + c_1 \left[\ln\left(\frac{\nu}{M}\right) - i\frac{\pi}{2} \right] + c_2 \left[\ln\left(\frac{\nu}{M}\right) - i\frac{\pi}{2} \right]^2 + c_2 \frac{\pi^2}{4} + i\beta \frac{1 + e^{-i\pi\alpha}}{\sin\pi\alpha} \left(\frac{\nu}{M}\right)^{\alpha-1} \Bigg\}, \quad (3.29)$$

parameter	Fit 1 of [125]	Fit 2 of [125]
c_0 (μb)	105.64	92.5
c_1 (μb)	-4.74 ± 1.17	-0.46 ± 2.88
c_2 (μb)	1.17 ± 0.16	0.803 ± 0.273
β (μb)	64.0	78.4 ± 9.1
α	0.5	0.5

Table 3.2: Fit parameter values entering the Block-Halzen γp total cross section parametrization [125] of Eq. (3.3), as described in the text.

with $f(0)$ the subtraction constant at $\nu = 0$. From Eq. (3.29), the imaginary part directly follows from unitarity

$$\mathrm{Im}\, f^{BlHa}(\nu) = \frac{\nu}{4\pi}\sigma_{\gamma p}^{BlHa}(\nu), \tag{3.30}$$

given the cross section parametrization of Eq. (3.3). Furthermore, the real part is given by:

$$\mathrm{Re}\, f^{BlHa}(\nu) - f(0) = \frac{\nu}{4\pi}\left\{c_1\frac{\pi}{2} + c_2\pi \ln\left(\frac{\nu}{M}\right) - \beta\cot\left(\frac{\pi\alpha}{2}\right)\left(\frac{\nu}{M}\right)^{\alpha-1}\right\}. \tag{3.31}$$

As the forward amplitude is constructed as an analytic amplitude in the Block-Halzen parametrization, it satisfies the subtracted dispersion relation:

$$\mathrm{Re}\, f^{BlHa}(\nu) - f(0) = \frac{\nu^2}{2\pi^2}\fint_0^\infty d\nu' \frac{\sigma^{BlHa}(\nu')}{\nu'^2 - \nu^2}, \tag{3.32}$$

with lower integration limit $\nu' = 0$. As noted above for the Donnachie-Landshoff Regge parametrization, we connect in this Chapter the asymptotic form σ^{BH} of Eq. (3.3) of the Block-Halzen parametrization above $W \simeq 2$ GeV, with our resonance cross section fits from threshold up to $W \simeq 2$ GeV, and reconstruct the total real part of the forward Compton amplitude at any energy using the subtracted dispersion relation. This yields a real amplitude which at high energies approaches Eq. (3.31).

3.B Tree-level Bethe-Heitler – timelike CS interference

3.B.1 Kinematics

The kinematics of the $\gamma p \to e^- e^+ p$ process in both the Lab frame and di-lepton rest frame is shown in Fig. 3.4.

To write down the cross section interference term explicitly, we follow notations for kinematical invariants involved in analytical expressions for the BH unpolarized cross section defined in Ref. [132]. In particular, we use the 2 scalar products

$$a = 2(l^- - l^+)\cdot p' = \beta\tilde{a}\cos\theta_l, \tag{3.33}$$

$$b = 2(l^- - l^+)\cdot(p - p') = \beta\left(\tilde{b}_1\cos\theta_l + \tilde{b}_2\sin\theta_l\cos\phi_l\right), \tag{3.34}$$

which contain all the dependencies on the lepton scattering angles θ_l and ϕ_l (in di-lepton rest

frame). Here,

$$\tilde{a} = \sqrt{(s-M^2-q'^2)^2-4M^2q'^2}, \tag{3.35}$$

$$\tilde{b}_1 = \frac{1}{\tilde{a}}\left(q'^2(s-M^2-q'^2)+t(s-M^2+q'^2)\right), \tag{3.36}$$

$$\tilde{b}_2 = -\sqrt{(q'^2-t)^2-\tilde{b}_1^2}, \tag{3.37}$$

and

$$\beta = \sqrt{1-\frac{4m^2}{q'^2}}, \tag{3.38}$$

where m is the lepton mass.

3.B.2 Analytical expression for the interference term

We have obtained the analytical expression for the tree-level interference term between the *quasi-real-forward* TCS and the Bethe-Heitler amplitudes:

$$\begin{aligned}
\frac{1}{4}\sum_{\sigma,\lambda}\sum_{\sigma',\sigma_-,\sigma_+}\mathrm{Re}\left(\mathcal{M}_{\mathrm{BH}}\,\mathcal{M}^*_{\mathrm{TCS}}\right) = \frac{e^6}{4LMM_{ll}^2\tilde{\nu}^2 t}\,G_E(t)\;[\mathrm{Re}\,T_1]\;\times\;\Bigg[&32LM\tilde{\nu}\left\{M^2b+at\right\}\\
&+2L\left(M_{ll}^2-t\right)\left\{8\nu Ma+2\nu Mb+8M^2a+4M^2b-M_{ll}^2\left(5a+b\right)+3at\right\}\\
&-16M^2\tilde{\nu}^2\Bigg\{8\nu Mbm^2-M_{ll}^4\left(a+b\right)-M_{ll}^2t\left(-2a-b\right)-M_{ll}^2\left(-2\nu Mb+4am^2+4bm^2\right)\\
&\qquad -at^2-t\left(-2\nu Mb-4am^2-4bm^2\right)\Bigg\}\\
&+8M\tilde{\nu}t\Bigg\{4\nu^2M^2b+2\nu Mbt-M_{ll}^4a-M_{ll}^2t\left(-2a-b\right)\\
&\qquad -M_{ll}^2\left(2\nu Mb+4M^2b\right)-a^2b-at^2\Bigg\}\\
&+\left(M_{ll}^2-t\right)\Bigg\{16\nu^3M^3b-4\nu Ma^2b+2M_{ll}^6a+M_{ll}^4t\left(-7a-b\right)\\
&+M_{ll}^4\left(4\nu Mb+4M^2a+4M^2b\right)+M_{ll}^2t^2\left(6a+b\right)+M_{ll}^2t\left(-6\nu Mb-4M^2b\right)\\
&+M_{ll}^2\left(-8\nu^2M^2a-16\nu^2M^2b-8\nu M^3b+2a^3+4a^2b\right)-at^3+t^2\left(2\nu Mb-4M^2a\right)\\
&+t\left(8\nu^2M^2a+16\nu^2M^2b+8\nu M^3b-2a^3-4a^2b\right)\Bigg\}\Bigg]
\end{aligned} \tag{3.39}$$

where $G_E(t)$ is the electric form-factor, given by Eq. (3.24).

Chapter 4

Quarkonium – proton interaction

In recent years, the study of the excitation spectrum in the charmonium and bottomonium sectors above open charm and open bottom thresholds has revealed a plethora of new states, which cannot be explained as conventional $Q\bar{Q}$ bound states, see e.g. [133] for a recent experimental review. Several explanations for the nature of these exotic states have been put forward, ranging, among others, from tetraquark states based on QCD diquarks, QCD hybrids, hadronic molecules, or hadro-charmonium states. In contrast to conventional $Q\bar{Q}$ states above open charm or open bottom thresholds, for which the branching fractions in open flavor decay modes are found to be 2 or 3 orders of magnitudes larger than their hidden flavor decay modes, many of the newly found exotic states have in common that hidden flavor decay modes are discovery channels, and are only suppressed by a factor of 10 or less relative to the open flavor decay modes. The understanding of the nature of these states may therefore shed another light on how hidden charm or hidden bottom systems interact with light quark systems. This is especially prominent in the hadro-quarkonium models for the exotic hadrons [134], in which the charm or bottom $Q\bar{Q}$ pair remains tightly bound while interacting with the light quarks through a van der Waals interaction.

Also in the baryon sector, narrow resonances involving two heavy quarks have been discovered in recent years. In the weak decay process $\Lambda_b \to J/\psi p K^-$, the LHCb Collaboration [135, 136] has found evidence for such states in the $J/\psi p$ mass spectrum, and interpreted them as hidden-charm pentaquark states. As two of these states were found approximately 5 MeV and 2 MeV below the $\Sigma_c^+ \bar{D}^0$ and $\Sigma_c^+ \bar{D}^{*0}$ thresholds respectively, these states were interpreted in various studies as loosely bound meson-baryon molecular states through π- or ρ-exchange interactions (see e.g. [137] among many others). Alternatively, the two narrow pentaquark states near $\Sigma_c^+ \bar{D}^{*0}$ threshold, $P_c(4440)^+$ and $P_c(4457)^+$ were predicted in [138] as the $1/2^-$ and $3/2^-$ hyperfine partners of deeply bound hadro-charmonium states of $\psi(2S)$ and the proton, while the narrow pentaquark state $P_c(4312)^+$ near $\Sigma_c^+ \bar{D}^0$ threshold was interpreted as a $1/2^+$ hadro-charmonium state of the $\chi_{c0}(1P)$ and the proton [139]. In such picture, the binding is due to the two-gluon exchange interaction between a compact quarkonium state within a proton, and is proportional to the chromo-electric polarizability of the quarkonium state. The hadro-charmonium framework therefore relates the nature of such exotic states involving heavy quarks to the interaction of the heavy quarkonia with light hadrons.

The present Chapter is based on the co-authored works of Ref. [4, 6]. In the first Section 4.1 we consider the forward J/ψ – proton scattering. We then extend the study of J/ψ to the similar Υ case in Section 4.2. The overall conclusions are then presented in Section 4.3.

4.1 Threshold J/ψ photoproduction off protons

The quantitative study of a possible formation of the exotic bound states requires a more precise knowledge of the J/ψ-nucleon interaction at low energies, which may be characterized by its (spin-independent) s-wave scattering length $a_{\psi p}$, corresponding to a J/ψ-proton (p) total cross section at threshold of $\sigma_{\psi p} \equiv 4\pi a_{\psi p}^2$. In the absence of a J/ψ-p bound state, a small positive

(negative) value of $a_{\psi p}$ would indicate a weakly attractive (repulsive) J/ψ-p interaction. If the attraction is sufficiently strong, it may then support J/ψ-nuclear bound states [56]. It has been estimated using QCD sum rules [140] that $a_{\psi p} \sim 0.1$ fm, corresponding with $\sigma_{\psi p} \sim 1.26$ mb. Calculations based on the rather uncertain value of the J/ψ chromo-electric polarizability [141] provide estimates for $a_{\psi p}$ ranging between a value of $a_{\psi p} = 0.05$ fm [142] at the lower end, and a value of $a_{\psi p} = 0.37$ fm [143] at the higher end. The latter value would lead to J/ψ binding energy in nuclear matter exceeding 20 MeV.

In recent years, the question whether J/ψ-nuclear bound states exist became amenable to lattice QCD calculations [57, 59, 144, 145]. Ref. [57] inferred a charmonium-nuclear matter binding energy $B_\psi \lesssim 40$ MeV. The current lattice calculations were however performed at large pion masses ($m_\pi \sim 805$ MeV), and it is possible that the systems involving the lightest nuclei will therefore be unbound at the physical pion mass. Future calculations for smaller quark masses are clearly called for. More recently, the HAL QCD Collaboration [59] has performed improved lattice QCD studies of the s-wave effective potentials for the J/ψ-nucleon system ($J = 1/2$ and $J = 3/2$), although still for an unphysical pion mass value of $m_\pi = 700$ MeV. For the J/ψ-nucleon system, the potential was found to be attractive, but not strong enough to allow for bound states. The lattice study extracted J/ψ-nucleon scattering lengths for both spin states: $a_{\psi p}(J = 1/2) = 0.66 \pm 0.07$ fm, and $a_{\psi p}(J = 3/2) = 0.38 \pm 0.05$ fm, indicating that the J/ψ-N state with $J = 1/2$ obtains significantly stronger attraction than the $J = 3/2$ state.

The J/ψ-p interaction was furthermore studied in Refs. [146, 147] as a probe of the color deconfinement in high-energy nucleus-nucleus collisions. Based on the small size of the J/ψ, around $r_\psi \sim 0.2$ fm $\ll \Lambda_{QCD}^{-1}$, the J/ψ-p cross section was estimated in those works in terms of the gluon distribution in the nucleon and related through Vector Meson Dominance (VMD) to the J/ψ photo-production cross section on the proton. Using different parametrizations of the gluon distributions in a proton from deep inelastic scattering, the experimental behavior of the cross section was well reproduced in Ref. [147]. In a related work [148], by using VMD and using data for hidden and open charm photo-production on a proton as input, a phenomenological estimate of the J/ψ-p elastic cross section was given. In the present work, we will provide an update along these lines, with the aim to provide an improved extraction of the threshold J/ψ-p scattering amplitude. For this purpose we will evaluate the J/ψ-p forward scattering amplitude in a dispersive formalism. As in Ref. [148], we will constrain the imaginary part from the present world data of hidden and open-charm photo-production. The real part will be evaluated through a dispersion relation, which involves one subtraction constant, which can be related to $a_{\psi p}$. We will be able to substantially improve the precision of the fit, by including the forward differential cross section data for $\gamma p \to J/\psi p$ in the fit, and study the sensitivity of the $\gamma p \to J/\psi p$ cross section in the threshold region to the subtraction constant. This will then allow us to make a quantitative study for planned experiments at the Jefferson Laboratory (JLab) [149–151], which are aimed to measure the $\gamma p \to J/\psi p$ process in the threshold region. We note, however, that the recently published data from the GlueX Collaboration at JLab [152] is not considered in the present Section, as our study was performed earlier.

Current Section is based on the co-authored work of Ref. [4]. We will describe the forward J/ψ-p scattering amplitude in Subsection 4.1.1, relating its imaginary part to $\gamma p \to J/\psi p$ and $\gamma p \to c\bar{c}X$ data. We subsequently calculate the real part from a dispersion relation, involving one subtraction constant. In our framework, the 6 parameters describing the discontinuities, and the one subtraction constant are obtained from a global fit to both total and forward differential photo-production cross sections. In Subsection 4.1.2, we then start from this $\gamma p \to J/\psi p$ amplitude to describe the $\gamma p \to J/\psi p \to e^- e^+ p$ process, and calculate the forward-backward asymmetry for the $\gamma p \to e^- e^+ p$ process around the J/ψ resonance, We will show that this forward-backward asymmetry, which is proportional to the real part of the J/ψ-

p amplitude, provides a very sensitive observable to extract the subtraction constant in the forward J/ψ-p scattering amplitude, which in turn allows to extract $a_{\psi p}$. We will present results for this forward-backward asymmetry, including error bands resulting from our fitting procedure, in the kinematics of planned experiments at JLab.

4.1.1 J/ψ-proton forward scattering amplitude and photoproduction

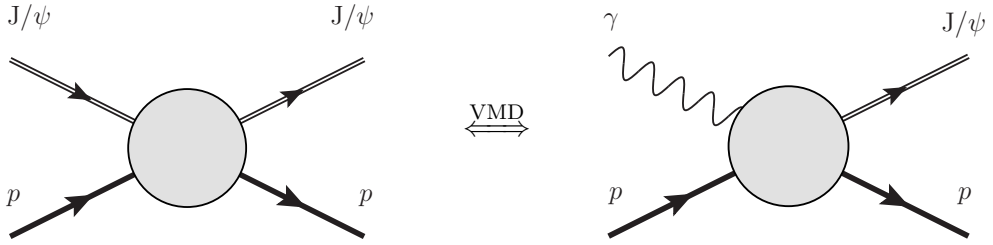

Figure 4.1: J/ψ elastic scattering off a proton (left) and J/ψ photoproduction on a proton (right) processes can be related through the vector meson dominance (VMD).

We consider the *forward* J/ψ-p elastic scattering process (Fig. 4.1, left), which is described by the spin-averaged forward scattering amplitude $T_{\psi p}(\nu)$, where the shorthand ψ denotes the J/ψ state. The amplitude $T_{\psi p}$ depends on the crossing variable ν, defined in terms of the Mandelstam invariants as:

$$\nu \equiv \frac{s-u}{4} = \frac{1}{2}(s - M^2 - M_\psi^2), \tag{4.1}$$

where $M(M_\psi)$ stand for the masses of the proton (ψ), respectively. Notice the new definition differs from the notation in the previous Chapters by a factor M and by presence of the non-zero M_ψ.

The forward differential cross section for the $\psi\, p \to \psi\, p$ process can then be expressed as:

$$\left.\frac{d\sigma}{dt}\right|_{t=0} (\psi p \to \psi p) = \frac{1}{64\,\pi\, s\, q_{\psi p}^2} \left|T_{\psi p}(\nu)\right|^2, \tag{4.2}$$

where in the forward direction the momentum transfer $t = 0$, and where $q_{\psi p}$ denotes the magnitude of the ψ three-momentum in the c.m. frame, given by:

$$q_{\psi p}^2 = \frac{1}{4s}\left[s - (M_\psi + M)^2\right]\left[s - (M_\psi - M)^2\right]. \tag{4.3}$$

The optical theorem relates the imaginary part of $T_{\psi p}(\nu)$ to the $\psi\, p \to X$ total cross section $\sigma_{\psi p}^{tot}$ as:

$$\mathrm{Im}\, T_{\psi p}(\nu) = 2\sqrt{s}\, q_{\psi p}\, \sigma_{\psi p}^{tot}(\nu). \tag{4.4}$$

The amplitude $T_{\psi p}(\nu)$ has the property that it is even under crossing, i.e. $T_{\psi p}(-\nu) = T_{\psi p}(\nu)$. The real part of the amplitude $T_{\psi p}(\nu)$ can be reconstructed from the knowledge of the imaginary part along the real ν-axis using a dispersion relation, provided the integral converges. For large ν, the amplitude is diffractive following approximately the behavior $\mathrm{Im}\, T_{\psi p}(\nu) \sim \nu^a$,

with $1 \leq a < 2$. The convergence of the dispersion integral therefore requires one subtraction. This leads to the subtracted dispersion relation:

$$\mathrm{Re}\, T_{\psi p}(\nu) = T_{\psi p}(0) + \frac{2}{\pi}\nu^2 \int_{\nu_{el}}^{\infty} d\nu' \frac{1}{\nu'} \frac{\mathrm{Im}\, T_{\psi p}(\nu')}{\nu'^2 - \nu^2}, \tag{4.5}$$

where $\nu_{el} \equiv M M_\psi$, corresponds with the elastic threshold $s = s_{el} = (M_\psi + M)^2 = 16.28$ GeV^2. Furthermore in Eq. (4.5), the real subtraction constant $T_{\psi p}(0)$ denotes the amplitude at $\nu = 0$. This subtraction constant can be predicted in models, see e.g. [147], or has to be obtained from lattice QCD. Alternatively, we can use it as a fit parameter and extract it from data. In the following, we will show the sensitivity to extract this subtraction constant from the measurement of the $\gamma\, p \to \psi\, p$ process in the threshold region, and will relate it with the ψ-p s-wave scattering length $a_{\psi p}$.

Physically, the discontinuity of the amplitude $T_{\psi p}(\nu)$ entering the integrand of Eq. (4.5) has two contributions: an elastic cut starting at s_{el}, and an inelastic contribution corresponding with open charm (meson) production on the proton. We will parametrize the inelastic contribution to $T_{\psi p}$ by an effective inelastic cut which starts at the $D\bar{D}$ meson production threshold, corresponding with $s_{inel} = (M + 2M_D)^2 = 21.79$ GeV^2, or equivalently $\nu_{inel} = 5.66$ GeV^2. The imaginary part of $T_{\psi p}$ is then obtained as sum of elastic and inelastic discontinuities:

$$\mathrm{Im}\, T_{\psi p}(\nu) = \theta(\nu - \nu_{el})\, \mathrm{Disc}_{el} T_{\psi p}(\nu) + \theta(\nu - \nu_{inel})\, \mathrm{Disc}_{inel} T_{\psi p}(\nu). \tag{4.6}$$

We will parametrize the elastic and inelastic discontinuities by the following 3-parameter forms:

$$\mathrm{Disc}_{el} T_{\psi p}(\nu) = C_{el} \left(1 - \frac{\nu_{el}}{\nu}\right)^{b_{el}} \left(\frac{\nu}{\nu_{el}}\right)^{a_{el}} \tag{4.7}$$

$$\mathrm{Disc}_{inel} T_{\psi p}(\nu) = C_{inel} \left(1 - \frac{\nu_{inel}}{\nu}\right)^{b_{inel}} \left(\frac{\nu}{\nu_{inel}}\right)^{a_{inel}}, \tag{4.8}$$

where the factors $\sim (1 - \nu_{thr}/\nu)^b$ determine the behavior around the respective threshold ν_{thr}, and the factors $\sim \nu^a$ determine the Regge behavior of the amplitude at large ν. In the following we will discuss how we can determine the respective parameters appearing in the elastic and inelastic discontinuities.

The discontinuity across the elastic cut, Disc_{el}, is related through the optical theorem to the $\psi\, p \to \psi\, p$ elastic scattering cross section $\sigma^{el}_{\psi p}$ as :

$$\mathrm{Disc}_{el} T_{\psi p}(\nu) = 2\sqrt{s}\, q_{\psi p}\, \sigma^{el}_{\psi p}. \tag{4.9}$$

We will use the vector meson dominance (VMD) assumption to relate the elastic cross section $\sigma^{el}_{\psi p}$ to the $\gamma p \to \psi p$ cross section [148, 153]:

$$\sigma^{el}_{\psi p} = \left(\frac{M_\psi}{e f_\psi}\right)^2 \left(\frac{q_{\gamma p}}{q_{\psi p}}\right)^2 \sigma(\gamma p \to \psi p), \tag{4.10}$$

where f_ψ is the ψ decay constant, which is obtained from the $\psi \to e^+ e^-$ decay as

$$\Gamma_{\psi \to ee} = \frac{4\pi\alpha^2}{3} \frac{f_\psi^2}{M_\psi}. \tag{4.11}$$

The experimental value $\Gamma_{\psi \to ee} \approx 5.55$ keV [80] yields $f_\psi \approx 0.278$ GeV. Furthermore, $q_{\gamma p}$ denotes the magnitude of the γ three-momentum in the c.m. frame of the $\gamma p \to \psi p$ process:

$$q_{\gamma p} = \frac{(s - M^2)}{2\sqrt{s}}. \tag{4.12}$$

Eqs. (4.7), (4.9) and (4.10) then yield the parametrization for the $\gamma p \to \psi p$ total cross section:

$$\sigma(\gamma p \to \psi p) = \left(\frac{e f_\psi}{M_\psi}\right)^2 \frac{C_{el}}{2\sqrt{s}\, q_{\gamma p}} \left(\frac{q_{\psi p}}{q_{\gamma p}}\right) \left(1 - \frac{\nu_{el}}{\nu}\right)^{b_{el}} \left(\frac{\nu}{\nu_{el}}\right)^{a_{el}}. \tag{4.13}$$

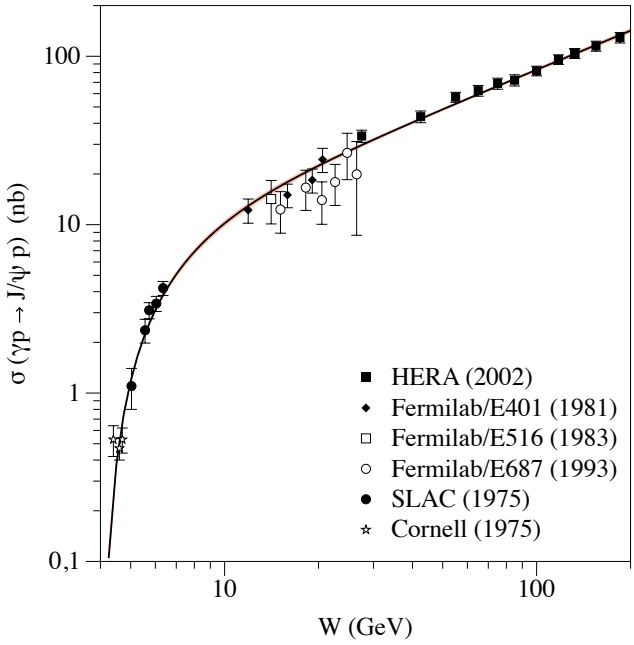

Figure 4.2: Figure from Ref. [4]: W-dependence of the $\gamma p \to J/\psi p$ total cross section. The data are from Cornell [154], SLAC [155], Fermilab [156–158], and HERA [159]. The curve and band is the result of our global fit using Eq. (4.13) with parameters given in Table 4.1 (second column, $x = el$).

The discontinuity across the inelastic cut, Disc_{inel}, is related through the optical theorem to the $\psi\, p \to c\bar{c}X$ inelastic cross section $\sigma^{inel}_{\psi p}$ as :

$$\mathrm{Disc}_{inel} T_{\psi p}(s) = 2\sqrt{s}\, q_{\psi p}\, \sigma^{inel}_{\psi p}. \tag{4.14}$$

Using again VMD allows to relate the inelastic cross section $\sigma^{inel}_{\psi p}$ to the $\gamma p \to c\bar{c}X$ cross section, with an analogous relation as in Eq. (4.10):

$$\sigma^{inel}_{\psi p} = \left(\frac{M_\psi}{e f_\psi}\right)^2 \left(\frac{q_{\gamma p}}{q_{\psi p}}\right)^2 \sigma(\gamma p \to c\bar{c}X). \tag{4.15}$$

Eqs. (4.8), (4.14) and (4.15) then yield the parametrization for the $\gamma p \to c\bar{c}X$ total cross section:

$$\sigma(\gamma p \to c\bar{c}X) = \left(\frac{e f_\psi}{M_\psi}\right)^2 \frac{C_{inel}}{2\sqrt{s}\, q_{\gamma p}} \left(\frac{q_{\psi p}}{q_{\gamma p}}\right) \left(1 - \frac{\nu_{inel}}{\nu}\right)^{b_{inel}} \left(\frac{\nu}{\nu_{inel}}\right)^{a_{inel}}. \tag{4.16}$$

Having fixed the imaginary part of the ψ-p forward scattering amplitude, we then calculate its real part using the subtracted dispersion relation of Eq. (4.5). With the knowledge of

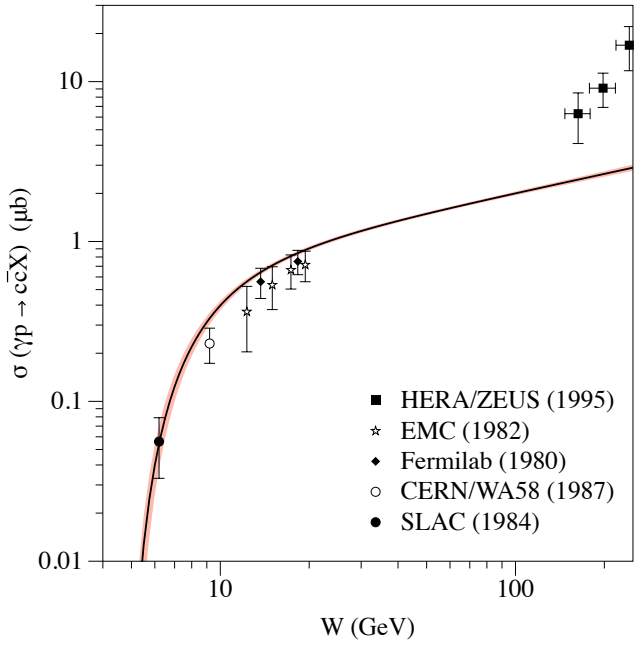

Figure 4.3: Figure from Ref. [4]: W-dependence of the $\gamma p \to c\bar{c}X$ total cross section. The data are from SLAC [160], Fermilab [161], EMC [162], CERN/WA58 [163], and HERA/ZEUS [164]. The curve and band is the result of our global fit using Eq. (4.16) with parameters given in Table 4.1 (third column, $x = inel$).

the real and imaginary parts of the forward scattering amplitude $T_{\psi p}$, we can determine the forward ($t = 0$) differential cross section for the $\gamma p \to \psi p$ process (Fig. 4.1, right) using VMD:

$$\begin{aligned} \left.\frac{d\sigma}{dt}\right|_{t=0}(\gamma p \to \psi p) &= \left(\frac{e f_\psi}{M_\psi}\right)^2 \left(\frac{q_{\psi p}}{q_{\gamma p}}\right)^2 \left.\frac{d\sigma}{dt}\right|_{t=0}(\psi p \to \psi p) \\ &= \left(\frac{e f_\psi}{M_\psi}\right)^2 \frac{1}{64\,\pi\, s\, q_{\gamma p}^2} \left|T_{\psi p}(\nu)\right|^2. \end{aligned} \tag{4.17}$$

Note that on the *lhs* of Eq. (4.17) the $\gamma p \to \psi p$ differential cross section is obtained at the unphysical point $t = 0$. Its experimental determination thus requires an extrapolation from $t = t_{min}$ to $t = 0$.

Our formalism has 7 parameters: 3 parameters describing the elastic discontinuity, 3 describing the inelastic discontinuity, and the subtraction constant $T_{\psi p}(0)$. We obtain the values for these 7 parameters ($T_{\psi p}(0)$, $a_{el/inel}$, $b_{el/inel}$, $c_{el/inel}$) by simultaneously fitting the available data for $\sigma(\gamma p \to \psi p)$, $\sigma(\gamma p \to c\bar{c}X)$ and $d\sigma/dt|_{t=0}\,(\gamma p \to \psi p)$. For this purpose we use the Levenberg-Marquardt algorithm [100, 101] of the non-linear least-squares optimization procedure implemented in MINPACK [165]. For our fits we estimate the error, following the same procedure introduced in Appendix 2.D, based on a covariance matrix for the parameters and a linear uncertainty propagation for each of the functions. The covariance matrix $\mathbf{\Sigma}_p$, again, is obtained based on the experimental uncertainties of the data values as follows:

$$\mathbf{\Sigma}_p = \left(\mathbf{J}_f^{\mathrm{T}} \cdot \mathbf{\Sigma}_e^{-1} \cdot \mathbf{J}_f\right)^{-1}, \quad \mathrm{J}_f^{(i,j)} = \frac{\partial f}{\partial p_j}(W_i), \quad \Sigma_e^{(i,j)} = \delta^{(i,j)}(\sigma_e^i)^2, \tag{4.18}$$

where W_i is the W-value of the i-th data point (with $s = \mathrm{W}^2$), σ_e^i is the total experimental

uncertainty of the i-th data-point, and f is the fit function of interest which depends on the energy variable (W) and the set of 7 parameters ($\{p\}$). The derivatives over the parameters are taken at their fitted values.

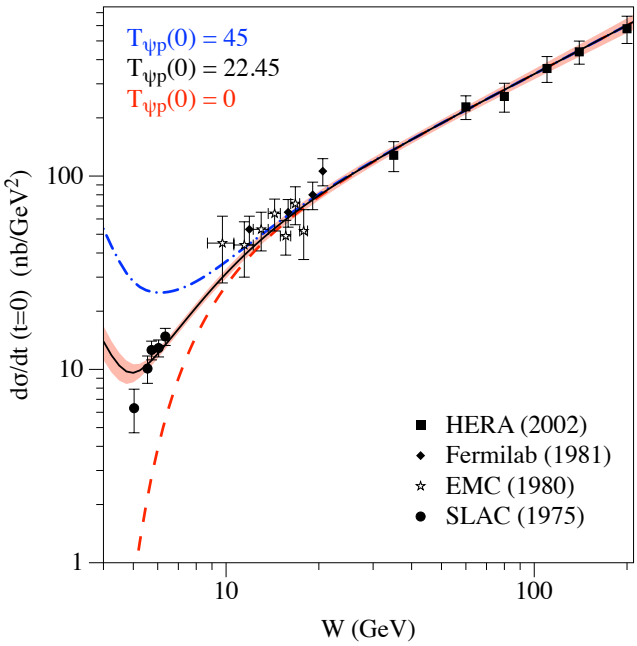

Figure 4.4: Figure from Ref. [4]: W-dependence of the $\gamma p \to J/\psi p$ differential cross section, extrapolated to the forward direction ($t = 0$), for different values of the subtraction constant $T_{\psi p}(0)$ in the forward ψ-p scattering amplitude. The data are from SLAC [155], CERN/EMC [166], Fermilab [156], and HERA [159]. The black curve $T_{\psi p}(0) = 22.45$ shows the best fit value, with corresponding error band resulting from our fitting procedure.

We show our fit to the $\gamma p \to \psi p$ ($\gamma p \to c\bar{c}X$) total cross section world data in Fig. 4.2 (Fig. 4.3) respectively as function of the c.m. energy W. By comparing Figs. 4.2 and 4.3 one notices that the ratio of the inelastic over elastic cross sections $\sigma(\gamma p \to c\bar{c}X)/\sigma(\gamma\, p \to \psi\, p)$ is around a factor of 30 - 50. Therefore, the inelastic discontinuity dominates the determination of the forward ψ-p amplitude. Furthermore, we show the forward differential cross section for the $\gamma p \to \psi p$ process in Fig. 4.4 for three values of the subtraction constant $T_{\psi p}(0)$. We note that the few HERA data points for the inelastic cross section in Fig. 4.3 at the highest energies (W $>$ 100 GeV) are not so well reproduced. However, these data points only marginally influence the fit, which in this region is mainly driven by the precise forward differential cross section data of Fig. 4.4. Our global fit yields the parameters for the elastic and inelastic discontinuities shown in Table 4.1 (second column: $x = el$, third column: $x = inel$). For the subtraction constant we obtain the fitted value of $T_{\psi p}(0) = 22.45 \pm 2.45$. As an indicator of the quality of our fit, we evaluated the reduced chi-squared,

$$\chi^2_{\rm red} = \chi^2/(N_{\rm d} - N_{\rm p}), \tag{4.19}$$

with $N_{\rm d}$ being the total number of the data points we use in our fitting procedure and $N_{\rm p}$ being the number of fitting parameters. With the values of $N_{\rm d} = 62$ and $N_{\rm p} = 7$, we get $\chi^2_{\rm red} = 1.36$. Its value shows that the present fit is decent (i.e. one is not over fitting) although

	$x = el$	$x = inel$
C_x	0.10 ± 0.01	20.51 ± 1.70
b_x	1.27 ± 0.17	3.53 ± 0.66
a_x	1.38 ± 0.01	1.20 ± 0.01

Table 4.1: Table from Ref. [4]: Fit results for the coefficients entering the elastic discontinuity (second column, $x = el$) of Eq. (4.7), and the inelastic discontinuity (third column, $x = inel$) of Eq. (4.8).

not perfect, indicating the lack of a sufficient rich database. Forthcoming more precise data especially in the threshold region, as expected from the planned JLab experiments [149–151], will have a strong impact on the quality of such a fit.

We also like to note that the $\gamma p \to \psi p$ reaction in the threshold region might by modified due to the presence of pentaquark resonances, which have recently been reported by the LHCb Collaboration [135]. A new experiment at JLab [151] aims to search for such resonances in the $\gamma p \to \psi p$ reaction in the threshold region. If a sizable excitation strength of such pentaquark states in the $\gamma p \to \psi p$ threshold cross section would be present, it was estimated in Ref. [151], based on a model calculation [167], that this would most likely occur at larger values of $-t$, away from the forward region, and thus not influence our analysis. If, on the other hand, such resonances would yield sizeable excitation strength in the forward region, they could be added to the parametrization of the elastic discontinuity. The dispersion relation of Eq. (4.5) would then allow to quantify the change to the real part of the forward ψ-p amplitude.

We show the real and imaginary parts of $T_{\psi p}$ in Fig. 4.5 for our best fit value of the subtraction constant $T_{\psi p}(0) = 22.45$, as well as for two values around this: $T_{\psi p}(0) = 0$ and $T_{\psi p}(0) = 45$. We notice that for W $<$ 10 GeV the real part dominates over the imaginary part, whereas at very high energies (W $\gg$ 10 GeV) the amplitude is largely dominated by the imaginary part, as expected for a diffractive process.

We can relate the forward ψ-p amplitude at threshold, $T_{\psi p}(\nu = \nu_{el})$, corresponding with $\sqrt{s} = M + M_\psi$, with the value of the ψ-p s-wave scattering length, $a_{\psi p}$, defined as

$$T_{\psi p}(\nu = \nu_{el}) = 8\pi(M + M_\psi)\, a_{\psi p}, \tag{4.20}$$

where our sign definition of $T_{\psi p}$ is fixed by Eq. (4.4). Note that in this convention, in the absence of a ψ-p bound state, a positive (negative) value of $a_{\psi p}$ corresponds to a positive (negative) s-wave phase shift, describing low-energy scattering from a weakly attractive (repulsive) potential. Using the dispersion relation Eq. (4.5) to relate $T_{\psi p}(0)$ with $T_{\psi p}(\nu_{el})$, we show the corresponding scattering lengths for three choices of the subtraction constant in Table 4.2. Note that our best fit value $T_{\psi p}(0) = 22.45$ results in a ψ-p scattering length $a_{\psi p} \sim 0.05$ fm, which is at the lower end of the range of values estimated in the literature, ranging from $a_\psi = 0.05$ fm [142] to $a_\psi = 0.37$ fm [143]. The value $a_{\psi p} \sim 0.05$ fm corresponds with a threshold ψ-p total cross section of $\sigma_{\psi p} \sim 0.3$ mb.

In a linear density approximation, the ψ-p scattering length $a_{\psi p}$ can be related to the ψ binding energy in nuclear matter, B_ψ, corresponding with the depth of the potential well seen by ψ in nuclear matter, as [142]

$$B_\psi \simeq \frac{8\pi(M + M_\psi)a_{\psi p}}{4MM_\psi}\,\rho_{nm}, \tag{4.21}$$

where $\rho_{nm} \simeq 0.17$ fm^{-3} denotes the nuclear matter density. We show the B_ψ values corresponding with the three values of $T_{\psi p}(0)$ considered in our calculations in Table 4.2 (last

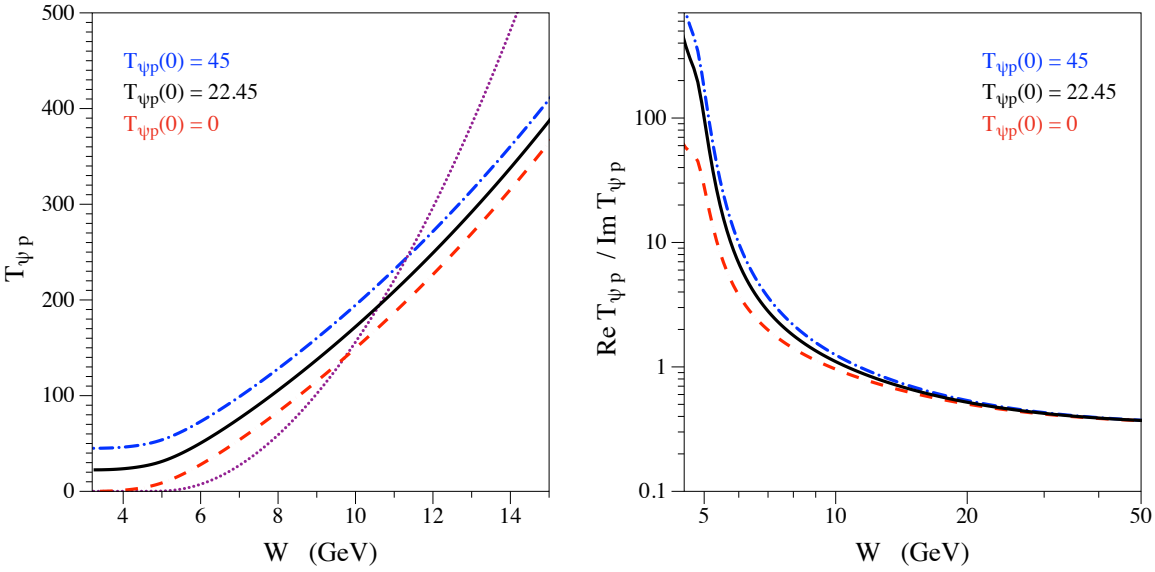

Figure 4.5: Figure from Ref. [4]: Left panel: Imaginary part (dotted curve) and real part of the forward scattering amplitude $T_{\psi p}$ as function of W. The real part is shown for three values of the subtraction constant as indicated on the figure. Right panel: corresponding ratios of real over imaginary parts.

$T_{\psi p}(0)$	$T_{\psi p}(\nu = \nu_{el})$	$a_{\psi p}$ (in fm)	B_ψ (in MeV)
0	1.30	0.003	0.2
22.45 ± 2.45	23.74 ± 2.59	0.046 ± 0.005	2.7 ± 0.3
45	46.30	0.090	5.2

Table 4.2: Table from Ref. [4]: Values of the subtraction term $T_{\psi p}(0)$ (first column), the corresponding values of the threshold amplitude $T_{\psi p}(\nu_{el})$ (second column), the corresponding ψ-p s-wave scattering lengths $a_{\psi p}$ (third column), and the corresponding ψ-nuclear matter binding energy B_ψ, according to Eq. (4.21) (fourth column).

column). Our best fit value $a_{\psi p} \sim 0.05$ fm thus corresponds to a ψ binding energy in nuclear matter of $B_\psi \sim 3$ MeV.

4.1.2 Forward-backward asymmetry

The value of $T_{\psi p}(0)$ extracted in the previous Section is mainly sensitive to the forward differential cross section of the $\gamma p \to \psi p$ process in the threshold region. The experimental access of the $\gamma p \to \psi p$ process proceeds through the reconstruction of the decay $\psi \to e^- e^+$ (or $\psi \to \mu^- \mu^+$), shown in Fig. 4.6 (left). In the threshold region in the forward direction (at a small value of $-t$), one may have a significant interference with the competing Bethe-Heitler mechanism, shown in Fig. 4.6 (right), which results in the same final state.

Following the same idea as described in the previous Chapter 3, we will calculate the observables for the process $\gamma(q,\lambda) + p(p,\sigma) \to e^-(l_-,\sigma_-) + e^+(l_+,\sigma_+) + p(p',\sigma')$.

For the small values of $-t$, the near-forward invariant amplitude for the $\gamma p \to \psi p \to e^- e^+ p$ process (Fig. 4.6, left) is given by essentially the same expression Eq. (3.10) from the previous Chapter, in which the fTCS amplitude (3.11) is replaced by the corresponding

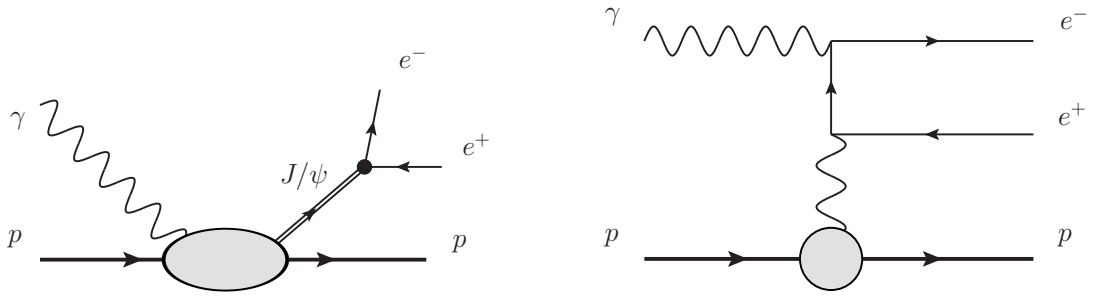

Figure 4.6: Figure from Ref. [4]: Di-lepton (e^+e^-) photoproduction through J/ψ (left) and Bethe-Heitler (right) processes.

$\gamma\, p \to \psi$ amplitude with the VMD-connected ψ resonance:

$$\mathcal{M}_\psi \simeq \frac{ie^3}{q'^2}\,\frac{f_\psi^2}{2M}\,\frac{1}{q'^2 - M_\psi^2 + iM_\psi\Gamma_\psi}\,T_{\psi p}\left(\nu = \frac{1}{2}(s - M_\psi^2 - M^2)\right)$$
$$\times\, \bar{N}(p',\sigma')\left\{\left(g^{\mu\nu} - \frac{q'^\mu q^\nu}{q\cdot q'}\right) + \frac{q\cdot q'}{(q\cdot P)^2}\left(P^\mu - \frac{q\cdot P}{q\cdot q'}q'^\mu\right)\left(P^\nu - \frac{q\cdot P}{q\cdot q'}q^\nu\right)\right\} N(p,\sigma)$$
$$\times\, \bar{u}(l_-,\sigma_-)\,\gamma_\nu\, v(l_+,\sigma_+)\,\varepsilon_\mu(q,\lambda). \quad (4.22)$$

Here, $T_{\psi p}(\nu)$ is the forward ψp elastic scattering amplitude discussed above, and $\Gamma_\psi = 92.9 \pm 2.8$ keV is the total ψ width. We stress again that the expression of Eq. (4.22) corresponds to a near-forward approximation, as it involves the ψ-p amplitude $T_{\psi p}$ at $t = 0$, where terms of order $-t/s$ are neglected.

The $\gamma p \to \psi p \to e^-e^+p$ cross section, differential in t, M_{ll}^2, and the electron solid angle $d\Omega^{e^-e^+cm}$ in the c.m. frame of the di-lepton pair is given by :

$$\frac{d\sigma}{dt dM_{ll}^2 d\Omega^{e^-e^+cm}} = \frac{1}{(2\pi)^4}\,\frac{1}{64(s-M^2)^2}\cdot\frac{1}{4}\sum_\lambda\sum_\sigma\sum_{\sigma'}\sum_{\sigma_-}\sum_{\sigma_+}|\mathcal{M}_\psi|^2, \quad (4.23)$$

with amplitude $\mathcal{M}_\psi$ given by Eq. (4.22). We performed the check that when integrating Eq. (4.23) over the electron solid angle and di-lepton invariant mass, one obtains:

$$\int dM_{ll}^2 \int d\Omega^{e^-e^+cm}\left.\frac{d\sigma}{dt dM_{ll}^2 d\Omega^{e^-e^+cm}}\right|_{t=0} = \left(\frac{\Gamma_{\psi\to ee}}{\Gamma_\psi}\right)\cdot\left.\frac{d\sigma}{dt}\right|_{t=0}(\gamma p \to \psi p), \quad (4.24)$$

with $d\sigma/dt|_{t=0}$ being the $\gamma p \to \psi p$ forward differential cross section given by Eq. (4.17), multiplied by the $\Gamma_{\psi\to ee}/\Gamma_\psi$ branching ratio.

Again, the background to the process comes from the Bethe-Heitler (BH) process (Fig. 4.6, right). The BH invariant amplitude, contributing to the $\gamma\, p \to e^-e^+\, p$ reaction, is given by Eq. (3.14). In the presence of the Bethe-Heitler, the amplitudes $\mathcal{M}_\psi$ and $\mathcal{M}_{BH}$ interfere, and the differential cross section is obtained by an analogous expression as Eq. (4.23), with the replacement $\mathcal{M}_\psi \to \mathcal{M}_\psi + \mathcal{M}_{BH}$.

We will next study this interference between ψ-production and Bethe-Heitler mechanisms for typical kinematics of the $\gamma p \to e^-e^+p$ process around the ψ production threshold, accessible at JLab [149–151]. In Fig. 4.7, left panel, we show the in-plane di-lepton angles in the laboratory frame as function of the electron angle $\theta^{e^-e^+cm}$, defined in the e^-e^+ c.m. frame, around the ψ resonance for JLab kinematics.

Fig. 4.7, right panel, shows the differential cross section for the $\gamma p \to e^-e^+p$ process around the ψ resonance. For selected values of the lepton angle (θ^{e-e+cm}), we show the ψ + BH

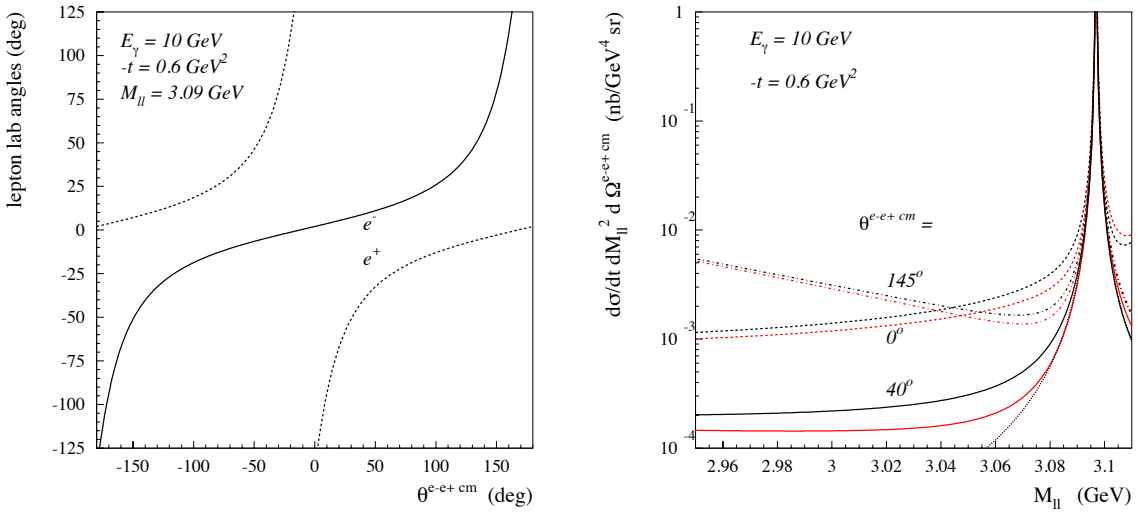

Figure 4.7: Figures from Ref. [4]: Left panel: Di-lepton angles in the *lab* frame as function of the electron angle θ^{e-e+cm}, defined in the e^-e^+ c.m. frame. Solid (dashed) curves denote the $e^-(e^+)$ *lab* angles. Right panel: Cross section for the in-plane $\gamma\, p \to e^-e^+\, p$ process differential in t, M_{ll}^2, and electron solid angle $\Omega^{e^-e^+cm}$ in the di-lepton c.m. frame, as function of the di-lepton mass M_{ll} around the ψ resonance, and for different values of the electron angle in the di-lepton c.m. frame. The dotted curve denotes the ψ contribution. The other curves are the Bethe-Heitler + ψ results according to Eqs. (4.22) and (3.14)) for $T_{\psi p}(0) = 22.45$. Lower red (upper black) curves show the forward (backward) angle cross sections.

cross sections (denoted by forward angle cross sections), and compare them with the ψ + BH cross sections for the corresponding opposite lepton angle value ($\theta^{e-e+cm} - 180°$, denoted by backward angle cross sections). One notices a sizable interference in the lower tail of the ψ resonance.

We are therefore able to directly access the real part of the ψ amplitude, again, by exploiting this interference with the BH amplitude through the forward-backward asymmetry A_{FB} in the c.m. frame of the di-lepton pair (Eq. (3.17)), which is zero for both the BH process and the J/ψ process separately. The scattering picture is completely the same as displayed in the previous Chapter on Fig. 3.4, except that the outgoing virtual photon is now the ψ particle.

Fig. 4.8 shows the forward-backward asymmetry A_{FB} and its sensitivity on the subtraction constant $T_{\psi p}(0)$ in the kinematics of the JLab experiments. We notice that the asymmetry A_{FB} can reach values around -25 % in these kinematics for the value $T_{\psi p}(0) = 22.45$ which was obtained in the fit above. In Fig. 4.8, we apply the same procedure of linear error propagation, mentioned above for the case of the cross section fits, to the asymmetry. Following this approach, the error of the asymmetry is estimated based on the first-order derivatives over the parameters:

$$\sigma^2_{A_{FB}} = \frac{\partial A_{FB}}{\partial \mathbf{p}} \cdot \mathbf{\Sigma}_p \cdot \frac{\partial A_{FB}}{\partial \mathbf{p}}, \tag{4.25}$$

where derivatives are taken at the fitted values of the parameters. We remark that in the particular case of the asymmetry all the derivatives become zero at particular values of kinematical variables — the values at which the Bethe-Heitler cross section becomes equal to the ψ cross section. This is why our error bands show nodes at specific values of M_{ll}. One notices

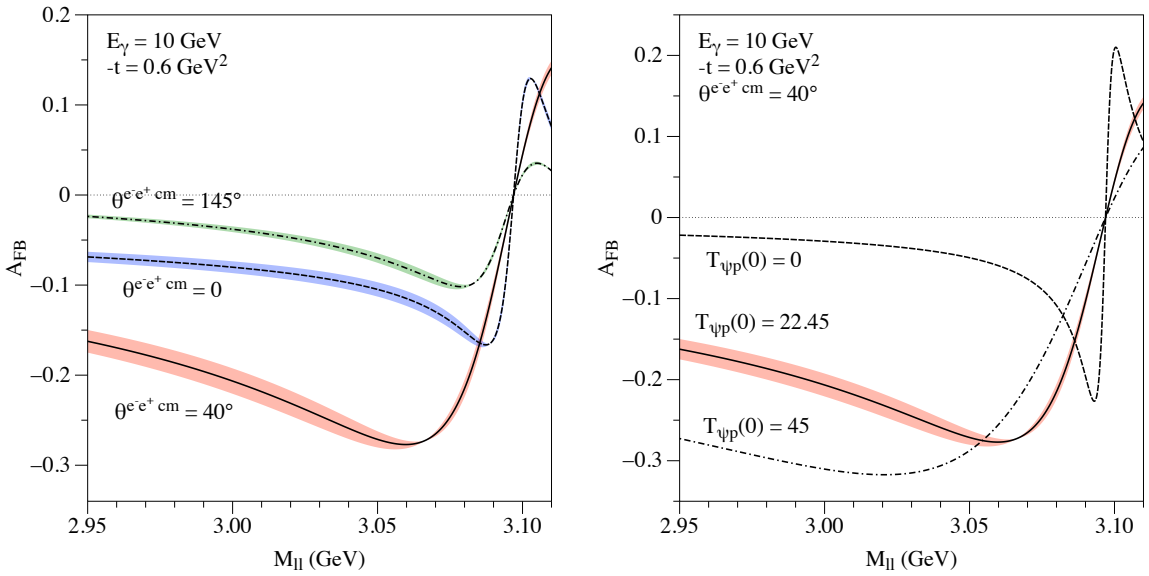

Figure 4.8: Figure from Ref. [4]: Forward-backward asymmetry for the $\gamma p \to e^- e^+ p$ process as function of the di-lepton mass M_{ll} around the ψ resonance. Dotted curve (corresponding with $A_{FB} = 0$): ψ contribution only. The other curves are the Bethe-Heitler + ψ results. Left panel: Results for $T_{\psi p}(0) = 22.45$ and for different values of the electron angle in the di-lepton c.m. frame. Right panel: Results for $\theta^{e^- e^+ cm} = 40°$ and for different values of $T_{\psi p}(0)$. The bands represent the error resulting from our cross section fitting procedure.

from Fig. 4.8 (right panel) that away from the ψ resonance position, the asymmetry A_{FB} depends in good approximation linearly on the value of $T_{\psi p}(0)$. It therefore provides a very sensitive observable to extract $T_{\psi p}(0)$. A future measurement of A_{FB} at Jefferson Lab [149–151] may thus provide us with a clean way to extract $T_{\psi p}(0)$, or equivalently $a_{\psi p}$, and provide a cross-check of the value obtained from the cross section fits, as discussed in Section 2.

4.2 Threshold Υ photoproduction off protons at the EIC

One may consider quarkonium production on a nucleon at the future Electron-Ion Collider (EIC) machine [129]. Here, it is worth noting that access to the threshold region of the J/ψ production is not possible due to the lower limit of the center of mass energy of the machine. Therefore, it is best to consider a higher center of mass energy provided by the threshold production of Υ, hence reachable by the current machine design. With sufficient integrated luminosity a precision measurement of the photo- and electro-production of Υ is possible, and gives a way to address the question of the existence of bottom pentaquarks. As the Υ production probes the gluon fields in the nucleon, such study will also shed light on the origin of the proton mass. Gluons are estimated to account for more than half of the proton mass due to the strong gluon chromo-electric and chromo-magnetic fields inside the proton [168]. At an EIC, the mass of the bottom quark as well as the probe resolution in electro-production give two independent knobs in the investigation of the gluonic interaction between the Υ and the nucleon.

To prepare for such a program of Υ production at an EIC, we will extend in the present Section our dispersive study of J/ψ photoproduction to the case of Υ photoproduction. The Section is based on the co-authored work of Ref. [6]. We will construct the Υ-proton forward

scattering amplitude in Subsection 4.2.1, relating its imaginary part to $\gamma p \to \Upsilon p$ data. The real part will be calculated from a dispersion relation, involving one subtraction constant, which is directly related to the scattering length. In Subsection 4.2.2, we will constrain the high-energy region from existing HERA and LHC data. As no data are available so far in the threshold region, we will consider several scenarios for the scattering length providing a range of estimates for the subtraction constant. In Subsection 4.2.3, we will show results of a feasibility study for Υ photoproduction at the EIC, considering different beam settings, and discuss the sensitivity and precision in the extraction of the Υ-p scattering length from such experiments. Some technical details on the EIC simulations are presented in Appendix 4.A.

4.2.1 Υ-proton forward scattering amplitude

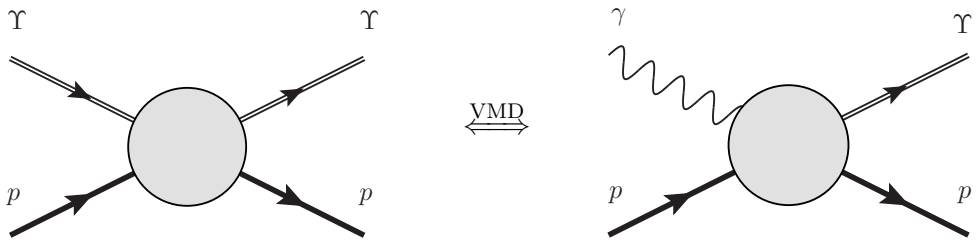

Figure 4.9: Υ elastic scattering off a proton (left) and Υ photoproduction on a proton (right) processes are related through VMD.

In the current Section we follow the same notation as for the J/ψ case (with "J/ψ" $\to$ "Υ" for the quarkonium), and are aimed to straight-forwardly apply similar analysis for the amplitude constraints from fits of the photoproduction data.

We thus consider the spin-averaged $\Upsilon p \to \Upsilon p$ forward elastic scattering process (Fig. 4.9, left), which is described by an invariant amplitude $T_{\Upsilon p}$, depending on the crossing-symmetry variable ν. The latter is defined in terms of the Mandelstam invariant $s = W^2$ as:

$$\nu = \frac{1}{2}(s - M^2 - M_\Upsilon^2), \tag{4.26}$$

where M and M_Υ stand for the masses of the proton and $\Upsilon(1S)$ state, respectively. The forward differential cross section for the $\Upsilon\, p \to \Upsilon\, p$ scattering process can then be expressed as:

$$\left.\frac{d\sigma}{dt}\right|_{t=0} (\Upsilon p \to \Upsilon p) = \frac{1}{64\,\pi\, s\, q_{\Upsilon p}^2} \left|T_{\Upsilon p}(\nu)\right|^2, \tag{4.27}$$

where in the forward direction the momentum transfer $t = 0$, and where $q_{\Upsilon p}$ denotes the magnitude of the Υ three-momentum in the c.m. frame, given by:

$$q_{\Upsilon p}^2 = \frac{1}{4s}\left[s - (M_\Upsilon + M)^2\right]\left[s - (M_\Upsilon - M)^2\right]. \tag{4.28}$$

The imaginary part of the amplitude $T_{\Upsilon p}$ can be obtained as sum of elastic and inelastic discontinuities:

$$\begin{aligned} \mathrm{Im}\, T_{\Upsilon p}(\nu) &= \theta(\nu - \nu_{el})\, \mathrm{Disc}_{\mathrm{el}} T_{\Upsilon p}(\nu) \\ &+ \theta(\nu - \nu_{inel})\, \mathrm{Disc}_{\mathrm{inel}} T_{\Upsilon p}(\nu). \end{aligned} \tag{4.29}$$

The elastic discontinuity starts from elastic threshold $s = s_{el} = (M_\Upsilon + M)^2 = 108.13$ GeV^2, or equivalently $\nu_{el} = M_\Upsilon M = 8.88$ GeV^2, whereas the inelastic discontinuity starts at the $B\bar{B}$ meson production threshold, corresponding with $s_{inel} = (M + 2M_B)^2 = 132.18$ GeV^2, or equivalently $\nu_{inel} = 20.90$ GeV^2.

Analogous to the J/ψ case from the previous Section 4.1, we will parametrize the elastic and inelastic discontinuities of the Υp forward scattering amplitude by the following 3-parameter forms, for $x =$ el/inel:

$$\mathrm{Disc}_x T_{\Upsilon p}(\nu) \quad = \quad C_x \left(1 - \frac{\nu_x}{\nu}\right)^{b_x} \left(\frac{\nu}{\nu_x}\right)^{a_x}, \tag{4.30}$$

where the factors $\sim (1 - \nu_x/\nu)^{b_x}$ determine the behavior around the respective threshold ν_x, and the factors $\sim \nu^{a_x}$ determine the Regge behavior of the amplitude at large ν. In the following we will discuss how we can determine the respective parameters appearing in the elastic and inelastic discontinuities.

For the discontinuity across the elastic cut, $\mathrm{Disc}_{el} T_{\Upsilon p}$, again, we again use the VMD assumption to relate the Υp elastic cross section $\sigma^{el}_{\Upsilon p}$ to the total $\gamma p \to \Upsilon p$ photoproduction cross section [148, 153]:

$$\mathrm{Disc}_{\mathrm{el}} T_{\Upsilon p}(\nu) = 2\sqrt{s}\, q_{\Upsilon p} \sigma^{el}_{\Upsilon p} \simeq 2\sqrt{s}\, q_{\Upsilon p} \left(\frac{M_\Upsilon}{e f_\Upsilon}\right)^2 \left(\frac{q_{\gamma p}}{q_{\Upsilon p}}\right)^2 \sigma(\gamma p \to \Upsilon p), \tag{4.31}$$

where f_Υ is the Υ decay constant, which is obtained from the $\Upsilon \to e^+e^-$ decay as

$$\Gamma_{\Upsilon \to ee} = \frac{4\pi\alpha^2}{3} \frac{f_\Upsilon^2}{M_\Upsilon}. \tag{4.32}$$

The experimental value $\Gamma_{\Upsilon \to ee} = 1.34 \pm 0.02$ keV [81] yields $f_\Upsilon = 0.238$ GeV. Furthermore, $q_{\gamma p}$ denotes the magnitude of the photon three-momentum in the c.m. frame of the $\gamma p \to \Upsilon p$ process:

$$q_{\gamma p} = \frac{(s - M^2)}{2\sqrt{s}}. \tag{4.33}$$

The discontinuity across the inelastic cut, $\mathrm{Disc}_{inel} T_{\Upsilon p}$, is related through the optical theorem to the $\Upsilon p \to b\bar{b}X$ inelastic cross section $\sigma^{inel}_{\Upsilon p}$ as:

$$\mathrm{Disc}_{\mathrm{inel}} T_{\Upsilon p}(\nu) = 2\sqrt{s}\, q_{\Upsilon p}\, \sigma^{inel}_{\Upsilon p}. \tag{4.34}$$

Using VMD, one can relate the total $\gamma p \to b\bar{b}X$ photoproduction cross section to the inelastic cross sections for the sum over Υ states (labeled by index i):

$$\sigma(\gamma p \to b\bar{b}X) = \sum_{\Upsilon_i} \left(\frac{q_{\Upsilon_i p}}{q_{\gamma p}}\right)^2 \left(\frac{e f_{\Upsilon_i}}{M_{\Upsilon_i}}\right)^2 \sigma^{inel}_{\Upsilon_i p}. \tag{4.35}$$

In contrast to the elastic process, where the final state is fixed to be the $\Upsilon(1S)$-p state, and for which the elastic photoproduction cross section $\sigma(\gamma p \to \Upsilon p)$ can be expected to be approximately dominated by its lowest term in the sum over vector bottomonia states, the open bottom $b\bar{b}$ final state in the inelastic photoproduction cross section of Eq. (4.35) can be expected to get sizeable contributions from several vector bottomonia states. We will therefore refrain from approximating Eq. (4.35) by its lowest vector bottomonium contribution

in the following analysis, and instead constrain the inelastic discontinuity through the forward differential cross section $d\sigma/dt$ for $\gamma p \to \Upsilon p$ as discussed in the next Section.

The real part of the scattering amplitude $T_{\Upsilon p}$ is related to its imaginary part through a once-subtracted forward dispersion relation:

$$\mathrm{Re}\, T_{\Upsilon p}(\nu) = T_{\Upsilon p}(0) + \frac{2}{\pi}\nu^2 \int_{\nu_{el}}^{\infty} d\nu' \frac{1}{\nu'} \frac{\mathrm{Im}\, T_{\Upsilon p}(\nu')}{\nu'^2 - \nu^2}, \tag{4.36}$$

with $T_{\Upsilon p}(0)$ the subtraction constant at $\nu = 0$. In this thesis, the subtraction constant is suggested to be obtained by performing a fit of the differential $\gamma p \to \Upsilon p$ photoproduction cross section data at $t = 0$, which is related to $T_{\Upsilon p}$ as:

$$\left.\frac{d\sigma}{dt}\right|_{t=0} (\gamma p \to \Upsilon p) = \left(\frac{e f_\Upsilon}{M_\Upsilon}\right)^2 \frac{1}{64\,\pi\, s\, q_{\gamma p}^2} \left|T_{\Upsilon p}(\nu)\right|^2. \tag{4.37}$$

The real part of the forward scattering amplitude at threshold $T_{\Upsilon p}(\nu_{el})$ is directly related to the Υ-p scattering length $a_{\Upsilon p}$ as:

$$T_{\Upsilon p}(\nu = \nu_{el}) = 8\pi(M + M_\Upsilon)\, a_{\Upsilon p}. \tag{4.38}$$

Analogously to the J/ψ case, we may relate a positive Υ-p scattering length, corresponding to an attractive interaction, to an Υ binding energy B_Υ in nuclear matter, using a linear density approximation [142]:

$$B_\Upsilon \simeq \frac{8\pi(M + M_\Upsilon) a_{\Upsilon p}}{4 M M_\Upsilon}\, \rho_{nm}, \tag{4.39}$$

where $\rho_{nm} \simeq 0.17$ fm^{-3} denotes the nuclear matter density.

As the aim of this Section is to extract $a_{\Upsilon p}$ from fitting the subtraction constant $T_{\Upsilon p}(0)$ to future Υ photoproduction data in the threshold region, we will consider three scenarios for the subtraction constant in order to explore the data sensitivity to its extraction.

The simplest scenario corresponds with having zero value of the subtraction constant, i.e. $T_{\Upsilon p}(0) = 0$. The real part of the Υ-p scattering amplitude is then fully determined by its imaginary part through the dispersion integral in Eq. (4.36). The resulting value of the Υ-p scattering length is then extremely small, around $a_{\Upsilon p} \sim 10^{-3}$ fm.

A second scenario is to estimate the subtraction constant by a scaling from its value for the $J/\psi p$ scattering, which was obtained from a fit to data in [4] as $T_{J/\psi p}(0) \simeq 22.5 \pm 2.5$. Observing that at high energies the normalizations of both the $J/\psi p$ and Υp scattering amplitudes are completely driven by their inelastic discontinuities, as discussed in the following Section, and making the strong assumption that the subtraction constants scale in the same way, yields the estimate:

$$T_{\Upsilon p}(0) \approx T_{J/\psi p}(0) \cdot C^{\Upsilon}_{\mathrm{inel}} / C^{J/\psi}_{\mathrm{inel}} \approx T_{J/\psi p}(0). \tag{4.40}$$

With cross section normalization estimate at high energies $C^{\Upsilon}_{\mathrm{inel}}/C^{J/\psi}_{\mathrm{inel}} \approx 0.9$, which we discuss in the next Section, this second scenario yields $T_{\Upsilon p}(0) = 20.5$, which corresponds with a scattering length $a_{\Upsilon p} \simeq 0.016$ fm.

We also consider a third, theoretically more motivated, scenario, in which an estimate of the Υ-p threshold amplitude is obtained by considering, in the leading approximation, the heavy bottomonium as a Coulombic bound state which interacts with the proton through its chromo-electric polarizability [51] yielding:

$$T_{\Upsilon p}(\nu_{el}) = \frac{16\pi^2}{9} \alpha_\Upsilon M_\Upsilon M^2, \tag{4.41}$$

with α_Υ the chromo-electric polarizability. For a Coulombic bound state, α_Υ is given by [51, 52]

$$\alpha_\Upsilon = \frac{28}{81}\pi a_0^3, \tag{4.42}$$

where a_0 is the Bohr radius of the Υ state, given by

$$a_0^{-1} = \frac{2}{3}\alpha_s m_b. \tag{4.43}$$

Using the parameter values for the strong coupling $\alpha_s \approx 0.37$ and the bottom quark mass $m_b \approx 4.76$ GeV from a recent potential model calculation for the bottomonium spectrum [169], the Bohr radius for the Υ takes on the value $a_0^{-1} \simeq (0.85)^{-1}$ GeV. Eq. (4.42) then yields a chromo-electric polarizability $\alpha_\Upsilon \simeq 0.67$ GeV^{-3}, in good agreement with the recent evaluation given in Ref. [170]: $\alpha_\Upsilon = 0.5^{+0.42}_{-0.38}$ GeV^{-3}, using color octet intermediate states in the calculation of the polarizability instead of free ones as in [51, 52]. For the purpose of providing cross section estimates in our third scenario, we will use an average between both results: $\alpha_\Upsilon \simeq 0.6$ GeV^{-3}, which yields $T_{\Upsilon p}(\nu_{el}) \simeq 88$ and for the s-wave scattering length $a_{\Upsilon p} \simeq 0.066$ fm. Using the dispersion integral of Eq. (4.36) in making the small extrapolation between the amplitudes at $\nu = \nu_{\rm el}$ and $\nu = 0$, this third scenario then yields as value for the subtraction constant: $T_{\Upsilon p}(0) \simeq 87$.

4.2.2 Fitting the existing data for Υ photoproduction off protons

In this Section, we discuss the fit of the elastic and inelastic discontinuities, which are parametrized according to the three-parameter forms of Eq. (4.30), to available Υ-p photoproduction data, following similar strategy as our previous analysis for the J/ψ-p system [4].

At present, the $\gamma p \to \Upsilon p$ photoproduction database consists of four data points from HERA [171–173], shown in Fig. 4.10 (Left panel). Furthermore at Large Hadron Collider (LHC) energies, the $\gamma p \to \Upsilon p$ cross section has been extracted from central pp production data at LHCb [174] and from ultra-peripheral pPb collisions at CMS [175].

The inclusive $b\bar{b}$ photoproduction database is represented by one data point from HERA [176]. Additionally, the lower energy cross section upper limit from EMC [177] is added to guide the low-energy behavior, as shown in Fig. 4.10 (right panel).

For high energies $\sqrt{s} = W \sim 100$ GeV, the differential cross section has been measured by the ZEUS Collaboration and follows an exponential t-dependence:

$$\frac{d\sigma}{dt}(\gamma p \to \Upsilon p) \;=\; A \cdot e^{Bt}, \qquad A = \left.\frac{d\sigma}{dt}\right|_{t=0}(\gamma p \to \Upsilon p), \tag{4.44}$$

with an empirical slope parameter $B(W = 100\ \text{GeV}) = 4.5 \pm 0.5$ GeV^{-2} [173]. The exponential dependence of Eq. (4.44) allows us to express the extrapolated value of the differential cross section at $t = 0$ as

$$A \simeq B e^{-Bt_{\rm min}} \cdot \sigma(\gamma p \to \Upsilon p), \tag{4.45}$$

where

$$t_{\rm min} = M_\Upsilon^2 - 2q_{\gamma p}\left(\sqrt{q_{\Upsilon p}^2 + M_\Upsilon^2} - q_{\Upsilon p}\right) \tag{4.46}$$

is the minimum (modulo) physical momentum transfer, corresponding to the forward scattering ($\theta_{\gamma\Upsilon} = 0$).

On physical grounds, one may expect the exponential dependence of Eq. (4.44) to hold in a limited t-range only, turning into a power dependence at larger t values. At high W, this only gives a minor correction to Eq. (4.45), but at lower W-values one may expect the correction

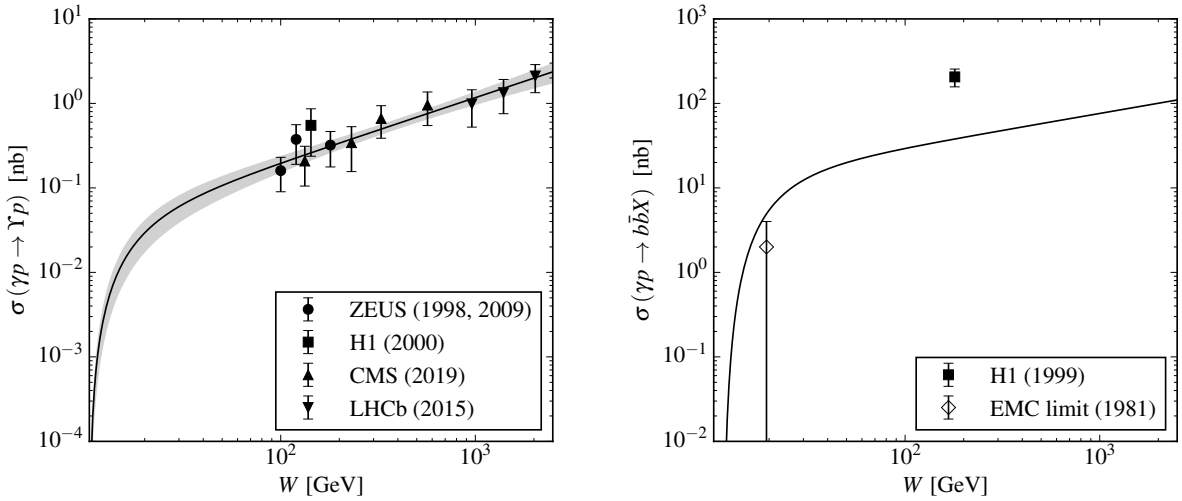

Figure 4.10: Figure from Ref. [6]: Left panel: W-dependence of the $\gamma p \to \Upsilon p$ total cross section. The curve is the result of our fit with parameters given in Table 4.3. The elastic ϒ photoproduction data are from HERA: H1 [171] and ZEUS [172, 173], and from LHC: LHCb [174] and CMS [175]. Right panel: W-dependence of the total inelastic photoproduction cross section $\gamma p \to b\bar{b}X$. The curve gives a lower limit arising from the contribution of the $\Upsilon(1S)$ state only in the sum of Eq. (4.35) for the $\gamma p \to b\bar{b}X$ cross section. The open beauty photoproduction data points are from HERA [176] and EMC [177].

to be more important. In this case, one should apply the fit form of Eq. (4.45) only in the limited t-range in order to extrapolate to A.

The present database for ϒ photoproduction is unfortunately insufficient to perform a good fit using the forms of Eq. (4.30) with all parameters unconstrained. Especially the lack of low-energy data prevents a direct determination of the low-energy slope parameters b_x of the cross sections at present. Assuming a similarity in the energy dependence of the cross sections for charm and bottom photoproduction, we thus start by simply fixing $b_{\rm el}$ and $b_{\rm inel}$ to the values obtained in the J/ψ analysis [4]. The high-energy elastic slope parameter $a_{\rm el}$ and the elastic normalization constant $C_{\rm el}$ are then fitted to the available data points for the elastic ϒ photoproduction total cross section, as shown in Fig. 4.10 (left panel), yielding the parameter values shown in Table 4.3 (second column), with the χ^2/d.o.f. = 0.3 (11 points, 2 parameters).

	x = el	x = inel
C_x	$(13.8 \pm 8.1) \times 10^{-3}$	18.7 ± 2.3
b_x	1.27 (fixed)	3.53 (fixed)
a_x	1.38 ± 0.06	1.2 (fixed)

Table 4.3: Table from Ref. [6]: Fit results for the coefficients entering the elastic discontinuity (second column, x = el), and the inelastic discontinuity (third column, x = inel). The parameters $b_{\rm el}, b_{\rm inel}$, and $a_{\rm inel}$ are fixed from the J/ψ analysis of Ref. [4].

To determine the inelastic normalization constant $C_{\rm inel}$, it was observed in [4] for the J/ψ case that around $W = 100$ GeV the inelastic discontinuity is around two orders of magnitude larger than its elastic counterpart. Although there is only one data point for the inclusive

$\gamma p \to b\bar{b}X$ cross section, shown in the right panel of Fig. 4.10, it also confirms this finding for the Υ-p discontinuities. The amplitude $T_{\Upsilon p}$ entering the forward differential cross section A in Eq. (4.45) is thus dominated by the normalization constant $C_{\rm inel}$. At high energies around $W \sim 100$ GeV, where the subtraction constant makes a negligible contribution to A, we thus solve Eq. (4.45) and fix the normalization $C_{\rm inel}$ by the available high-energy data for the t-slope parameter B.

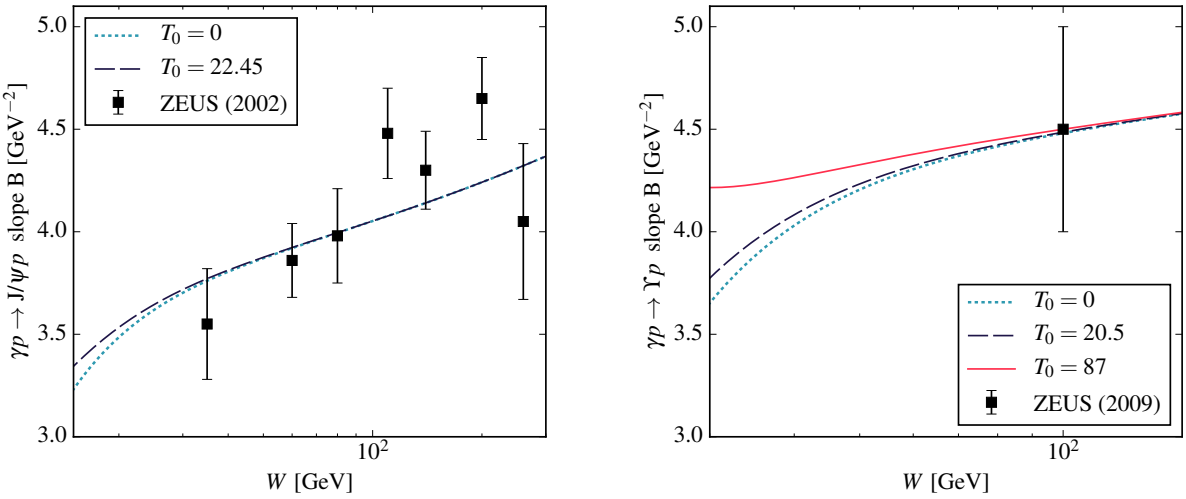

Figure 4.11: Figure from Ref. [6]: The W-dependence of the t-slope parameter B in Eq. (4.44). The curves are obtained by solving Eq. (4.45) for different values of the subtraction constant T_0 in the $J/\psi p$ (left) and Υp (right) forward scattering amplitudes. The t-slope data points are from HERA: for J/ψ from [159], and for Υ from [173]. The red solid curve, corresponding to $T_{\Upsilon p}(0) = 87$, passes through the central value of the data point exactly, according to our constraint on the $C_{\rm inel}$.

We show this constraint based on the t-slope parameter B in Fig. 4.11, and illustrate the calculation procedure first for the J/ψ case (left panel). In solving Eq. (4.45) for B, we use the total cross section data for $\sigma(\gamma p \to J/\psi p)$ which fixes the elastic discontinuity. Furthermore, on the left hand side of Eq. (4.45), we need the real and imaginary parts of the forward scattering amplitude to determine A, according to Eq. (4.37). For the imaginary part of the amplitude, which is described by its elastic and inelastic discontinuities, we use $C_{\rm inel}$ and $a_{\rm inel}$ as fit parameters. The real part of the amplitude is calculated from the dispersion relation of Eq. (4.36) for three values of the subtraction constant $T_0 \equiv T_{\psi p}(0)$, considered in Ref. [4]. The solution of Eq. (4.45) for these three values of T_0 is shown in Fig. 4.11 and compared with the HERA data for the t-slope. One firstly sees from Fig. 4.11 that for $W \geq 50$ GeV, the sensitivity to the subtraction constant becomes vanishingly small, thus allowing to determine $a_{\rm inel}$ and $C_{\rm inel}$ from a fit to the HERA data as: $a_{\rm inel} = 1.20$ and $C_{\rm inel} = 20.5$.

We apply the same procedure to the Υ t-slope parameter in the right panel of Fig. 4.11, and show our results for the three scenarios for the subtraction constant $T_0 \equiv T_{\Upsilon p}(0)$ discussed above. We again observe that for $W \geq 100$ GeV, the sensitivity to the subtraction constant becomes vanishingly small. As there is only one data point at $W = 100$ GeV in this case, we fix $a_{\rm inel}$ to the J/ψ value and extract $C_{\rm inel}$ by constraining the t-slope to the data point at 100 GeV. The obtained value for $C_{\rm inel}$ is listed in Table 4.3. It is seen that the value of the thus extracted dimensionless parameter $C_{\rm inel}$ is similar within 10 % between the J/ψ and Υ cases. We also note that in the sum of Eq. (4.35) the Υ contribution to the inelastic open beauty

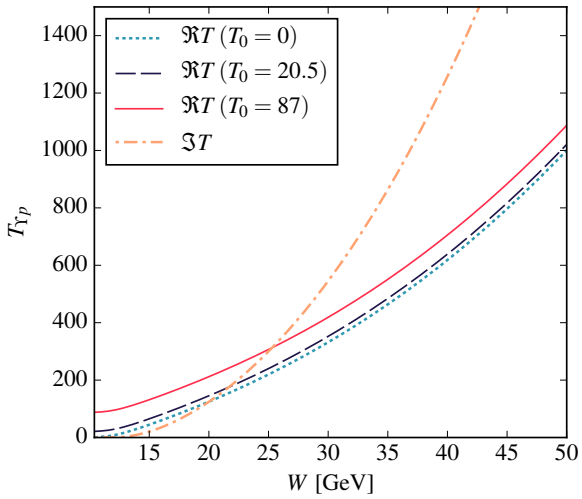

Figure 4.12: Figure from Ref. [6]: Imaginary part (dash-dotted curve) and real part of the forward scattering amplitude $T_{\Upsilon p}$ as function of W. The real part is shown for different values of the subtraction constant as indicated on the figure.

photoproduction cross section is around 20 %.

In Fig. 4.12, we show the W-dependence of real and imaginary parts of the scattering amplitude $T_{\Upsilon p}$ in our dispersive formalism, for the three choices of the subtraction constant discussed above. We notice that the real part of the amplitude dominates in the threshold region, whereas the imaginary part dominates at high energies as expected for a diffractive process. For the largest value of the subtraction constant $T_0 = 87$ considered, the imaginary part overtakes the real part around $W \approx 25$ GeV.

4.2.3 Results for Υ photoproduction at the EIC and discussion

We investigate in this Section how to extract the subtraction constant from a fit to the differential $\gamma p \to \Upsilon p$ cross section data at an Electron-Ion Collider (EIC).

We consider both a medium-energy and high-energy EIC configuration. The medium-energy configuration (setting 1) has a 10 GeV electron beam incident on a 100 GeV proton beam ($\sqrt{s_{ep}} = 63$ GeV), while the high-energy configuration (setting 2) has a 18 GeV electron beam incident on a 275 GeV proton beam ($\sqrt{s_{ep}} = 140$ GeV), corresponding to nominal configurations for the EIC design.

For the $\gamma p \to \Upsilon p$ cross section, we use the dispersive model discussed above with t-dependence as in Eq. (4.44). We show results for the three scenarios for the subtraction constant $T_{\Upsilon p}(0)$, and corresponding s-wave scattering length $a_{\Upsilon p}$ in Table 4.4. The uncertainties correspond to the simulated EIC $\gamma p \to \Upsilon p$ data for the two beam settings.

We use the Argonne l/A-event generator [178] to simulate a realistic event sample for the $\gamma p \to \Upsilon p$ process at the EIC, and refer to Appendix 4.A for more details on the exact implementation of the simulation. For our simulations, we assumed a total integrated luminosity of 100 fb^{-1} for each of the settings, which corresponds to 116 days at 10^{34}cm^{-2}s^{-1}. We simulated both the $\Upsilon \to e^+e^-$ and $\Upsilon \to \mu^+\mu^-$ decay channels, and only considered events where we fully detect the exclusive final state. We assumed nominal EIC detector parameters in line with the EIC white paper, where we have lepton detection for pseudo-rapidities between $-5 < \eta_l < 5$, and recoil proton detection for angles $\theta_p > 2$ mrad. Furthermore, we assumed

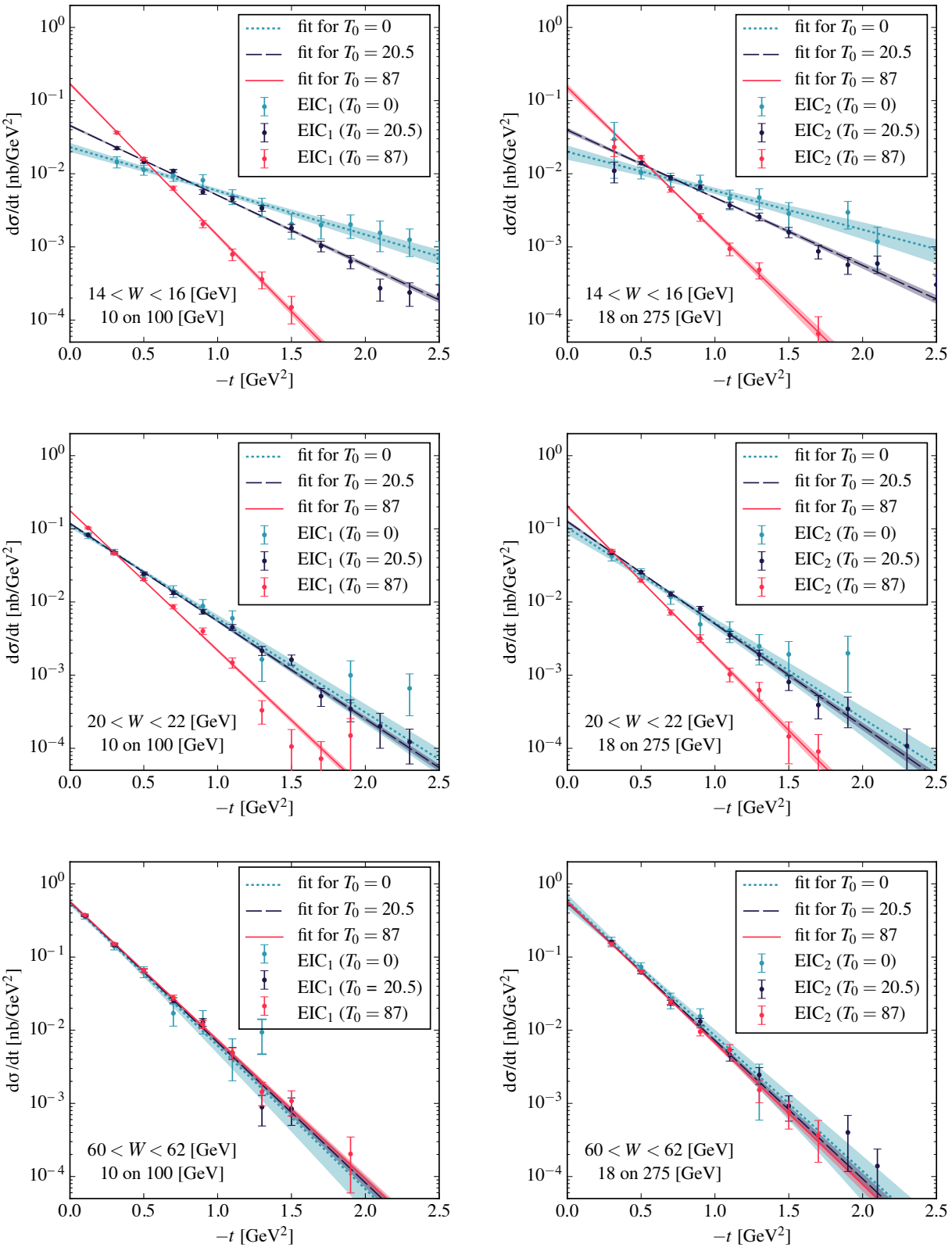

Figure 4.13: Figure from Ref. [6]: t-dependence of the $\gamma p \to \Upsilon p$ differential cross section for different values of the subtraction constant $T_0 \equiv T_{\Upsilon p}(0)$ as indicated on the figure. The EIC data points are simulated based on the theoretical elastic Υ photoproduction cross section, assuming an exponential t-dependence. The bands represent the uncertainty propagated based on the simulated data points, assuming the two-parameter exponential fits.

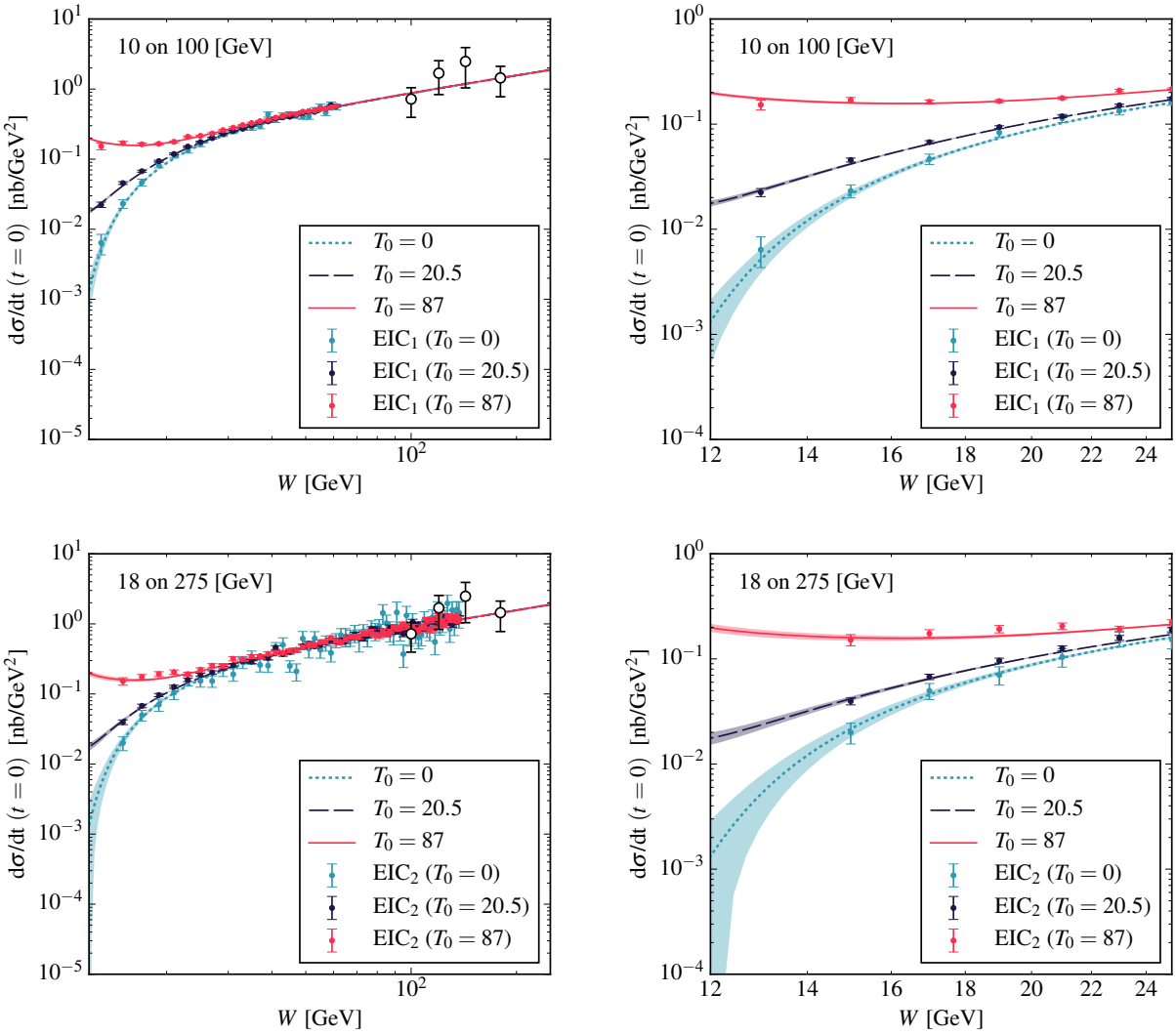

Figure 4.14: Figure from Ref. [6]: W-dependence of the $\gamma p \to \Upsilon p$ differential cross section, extrapolated to $t = 0$, for different values of the subtraction constant $T_0 \equiv T_{\Upsilon p}(0)$. The data points (open circles) are obtained from the elastic ϒ photoproduction cross section from HERA [171–173] by using the empirically measured slope parameter, using Eq. (4.45). The bands represent the uncertainty propagated based on the EIC simulated data points, assuming a one-parameter fit of T_0. Upper (lower) panels are for EIC beam setting 1 (beam setting 2) respectively. Right panels give a more detailed view of the lower energy region $W < 25$ GeV.

setting	$T_{\Upsilon p}(0)$	$a_{\Upsilon p}$ (in fm)	B_Υ (in MeV)
1	0	$\simeq 0$	$\simeq 0$
	20.5 ± 0.9	0.016 ± 0.001	0.78 ± 0.03
	87 ± 2	0.066 ± 0.001	3.23 ± 0.06
2	0	$\simeq 0$	$\simeq 0$
	20.5 ± 1.9	0.016 ± 0.001	0.78 ± 0.07
	87 ± 4	0.066 ± 0.003	3.23 ± 0.16

Table 4.4: Table from Ref. [6]: Values of the subtraction constant $T_{\Upsilon p}(0)$ (second column), the corresponding Υ-p s-wave scattering length $a_{\Upsilon p}$ (third column), and the corresponding Υ-nuclear matter binding energy B_Υ, according to Eq. (4.39) (fourth column). The uncertainty estimates are propagated based on the generated EIC differential cross section data points.

we can reconstruct the scattered electron for $y = P.q/P.k$ between $0.01 < y < 0.8$, and we ensured a quasi-real regime by requiring that $Q^2 < 1$ GeV^2.

In Fig. 4.13, we show the simulated results for the t-dependence of the $\gamma p \to \Upsilon p$ differential cross sections for different values of W, corresponding to the two EIC beam settings. In each case we consider the three scenarios for the subtraction constant T_0 discussed above. For the generated EIC data, the exponential t-slope B is obtained through solution of Eq. (4.45). The error bands represent the uncertainty propagated based on the data points, assuming the two-parameter exponential fits of Eq. (4.44). Only points generated up to $-t$ values of 2.5 GeV are considered in the fits.

In Fig. 4.14, we show the W-dependence of the $\gamma p \to \Upsilon p$ differential cross sections extrapolated to t = 0 for the two EIC beam settings considered. We see that in the $W < 25$ GeV region, the precision that can be reached for beam setting 1 at the EIC will allow to clearly distinguish between the three scenarios for the subtraction constant, and allow to extract this parameter with a statistical precision of the order of a few percent, see Table 4.4. Furthermore, beam setting 1 at the EIC will allow to perform an independent fit of the b_{inel} parameter, which governs the low-energy behavior of the $\gamma p \to \Upsilon p$ forward differential cross section, according to Eq. (4.30). For the region $W > 25$ GeV, beam setting 2 will allow to connect the data with the existing HERA measurement and furthermore allow to perform an independent fit of the parameter a_{inel}, which governs the high-energy behavior of the $\gamma p \to \Upsilon p$ forward differential cross section.

4.3 Conclusions

We have provided an updated phenomenological analysis of the *forward* quarkonium (J/ψ and Υ) – proton scattering amplitudes within a dispersive framework. Using VMD, we related the imaginary parts of the forward $Q\bar{Q}$-p scattering amplitudes to $\gamma p \to \psi p$ and $\gamma p \to c\bar{c}X$ and $\gamma p \to \psi p$ and $\gamma p \to b\bar{b}X$ cross sections data for the J/ψ and Υ cases, respectively. Furthermore, we calculated their real parts through a once-subtracted dispersion relation.

We first considered in details the case of ψ-p forward scattering in Section 4.1. In our framework, the 6 parameters describing the discontinuities, and the one subtraction constant are obtained from a global fit to both total and forward differential hidden and open charm photo-production cross sections. This fit allowed us to extract a value for the spin-averaged s-wave ψ-p scattering length $a_{\psi p} = 0.046 \pm 0.005$ fm, which can be translated into a ψ binding energy in nuclear matter of $B_\psi = 2.7 \pm 0.3$ MeV.

Starting from this $\gamma p \to \psi p$ amplitude we then calculated the $\gamma p \to \psi p \to e^- e^+ p$ pro-

cess. This allowed us to estimate the forward-backward asymmetry for the $\gamma p \to e^- e^+ p$ process around the ψ resonance, which results from interchanging the leptons in the interference between the ψ production mechanism and the competing Bethe-Heitler mechanism. This forward-backward asymmetry, which in this case accesses the real part of the ψ-p amplitude, displays to good approximation a linear dependence on $a_{\psi p}$, away from the ψ resonance position. Using the forward $\gamma p \to \psi p$ amplitude obtained from our fitting procedure, we estimated that the forward-backward asymmetry can reach values around -25 % for forthcoming ψ threshold electro- and photo-production experiments at Jefferson Lab. Such forthcoming measurements can thus lead to a refined extraction of the ψ-p scattering length $a_{\psi p}$, and better constrain the ψ binding energy in nuclear matter.

In Section 4.2, we have extended the dispersive study of the J/ψ photoproduction to the case of Υ photoproduction on a proton target, with the aim to extract the Υ-p scattering length from future $\gamma p \to \Upsilon p$ experiments. The imaginary part of the Υ-p forward scattering amplitude is constrained at high energies from existing HERA and LHC data for the $\gamma p \to \Upsilon p$ total and differential cross sections. Its real part is calculated through a once-subtracted dispersion relation, and the subtraction constant is proportional to the Υ-p scattering length. As no data are available so far in the threshold region, we have considered three scenarios for the subtraction constant: one of them corresponds to a zero value, the other to a value for the Υ study similar to that of the J/ψ case, and a third where we estimate the subtraction constant by considering the Υ as a Coulombic bound state which interacts with the proton through its chromo-electric polarizability. Using these three scenarios, we have performed a feasibility study for Υ quasi-real photon ($Q^2 < 1$ GeV^2) production experiments at an Electron-Ion Collider, and considered a low-energy and a high-energy beam setting. For our simulations, we have assumed a total integrated luminosity of 100 fb^{-1} for each of the settings, assuming nominal EIC detector parameters in line with the EIC white paper. In both beam settings, the simulated data for the $\gamma p \to \Upsilon p$ cross section were found to clearly distinguish between the three considered scenarios for the subtraction constant. The low-energy beam setting, accessing the range 12 GeV $\lesssim W \lesssim$ 60 GeV, was found to yield the higher statistical precision on the cross section. Furthermore, the high-energy beam setting, accessing the range 15 GeV $\lesssim W \lesssim$ 140 GeV, will allow to connect the EIC data with the existing HERA data, and thus provide an independent measurement of the high-energy behavior of the $\gamma p \to \Upsilon p$ forward differential cross section, further constraining the dispersive formalism. It is worth noting that our projection of the statistical error analysis shows that the Υ-p scattering length can be extracted from such data with a statistical precision of the order of 2% or less. The total experimental uncertainty of this determination will be dominated by the systematic error in the measurement of the absolute value of the differential cross section expected to be in the few percent range, leading to a very potent determination of the scattering length.

We have shown that an experimental program on Υ quasi-real photoproduction at the EIC has the potential to provide a unique view on the gluonic van der Waals interaction in QCD.

Appendices

4.A Event generation for Υ photoproduction at EIC

This is an Appendix from Ref. [6].

In order to simulate a realistic event sample for Υ events at the EIC, we added the formalism of Section 4.2 to the Argonne l/A-event Generator (LAGER) [178]. LAGER is a modular accept-reject generator capable of simulating both fixed-target and collider kinematics. Below we describe the model components used to obtain the event samples for the Section 4.2.

The differential cross section for the process ($ep \to e'\gamma^* p \to e'\Upsilon p$) can be written as,

$$\frac{d\sigma}{dQ^2 dy dt}(ep \to e'\Upsilon p) = \Gamma_T(1 + \epsilon R)\frac{d\sigma}{dt}(\gamma^* p \to \Upsilon p), \tag{4.47}$$

with transverse virtual photon flux Γ_T, virtual photon polarization ϵ, and $R \equiv \sigma_L/\sigma_T$ parametrized as in Ref. [179],

$$R(Q^2) = \left(\frac{AM_\Upsilon^2 + Q^2}{AM_\Upsilon^2}\right)^{n_1} - 1. \tag{4.48}$$

We use the values for parameters (A, n_1) as determined for J/ψ production in Ref. [180]. In order to estimate the unknown Q^2 dependence of the differential $\gamma^* p \to \Upsilon p$ cross section, we use the following factorized ansatz,

$$\frac{d\sigma}{dt}(\gamma^* p \to \Upsilon p) = D(Q^2)\frac{d\sigma}{dt}(\gamma p \to \Upsilon p), \tag{4.49}$$

where for D we assumed a dipole-like form-factor, similar to what is typically done in VMD,

$$D(Q^2) = \left(\frac{M_\Upsilon^2}{M_\Upsilon^2 + Q^2}\right)^{n_2}. \tag{4.50}$$

This formula deviates from its standard VMD form through the value for n_2, which was tuned to optimally describe the Q^2 dependence for exclusive ρ production in a wide range of kinematic regions. Note that this assumption has very little impact on the projections in Section 4.2, as we only consider quasi-real events.

In order to determine the slope B of the t-dependence of the differential cross section for the $\gamma p \to \Upsilon p$ process, we numerically solve the transcendental equation (4.45). Note that both normalization A and slope B depend on the choice of the subtraction constant $T_{\Upsilon p}(0)$, while the total integrated cross section $\sigma(\gamma p \to \Upsilon p)$ is independent of the subtraction constant.

We included both the $\Upsilon \to e^+e^-$ and $\Upsilon \to \mu^+\mu^-$ decay channels in our simulation, using s-channel helicity conservation (SCHC) to describe the angular distribution for a vector meson decaying into two fermions [159, 181, 182]:

$$\mathcal{W}(\cos\theta_{\mathrm{CM}}) = \frac{3}{8}(1 + r_{00}^{04} + (1 - 3r_{00}^{04})\cos^2\theta_{\mathrm{CM}}), \tag{4.51}$$

where we relate the spin-density matrix element r_{00}^{04} to R as,

$$R = \frac{1}{\epsilon}\frac{r_{00}^{04}}{1 - r_{00}^{04}}. \tag{4.52}$$

Chapter 5

Hadronic light-by-light scattering (HLbL)

Lattice QCD calculations of hadron structure have been steadily advancing in recent years. Several collaborations calculate hadronic observables directly at physical values of the quark masses. At least two collaborations are addressing the HLbL contribution to $(g-2)_\mu$ on the lattice [1, 7, 183–187]. Although the calculation poses serious challenges due to the complexity of the four-point function and the long-range nature of the dominant contribution, as a spacelike quantity it is well suited for a first-principles treatment directly in the Euclidean theory. A second role of lattice QCD is to provide the necessary hadronic input for the model and dispersive approaches to a_μ^{HLbL}. Model calculations (see e.g. [188] for a recent overview) consistently suggest that the contribution of the pseudoscalar mesons (π^0, η, η') is dominant, and therefore determining their respective transition form factors is of primary importance. A first calculation of the $\pi^0 \to \gamma^*\gamma^*$ transition form factor in the range of photon virtualities relevant to $(g-2)_\mu$ has been carried out on the lattice [189]. An extension of this calculation to the η, η' mesons is possible, though more demanding, due to the appearance of disconnected Wick-contraction diagrams. Computing the spectrum and two-photon coupling of the scalar, axial-vector and tensor mesons is qualitatively more complicated in lattice QCD, since these states are resonances and require a dedicated treatment.

In many ways, the light-by-light scattering amplitudes are the more accessible observable in lattice calculations, because they involve spacelike photons that can be treated directly in the Euclidean theory. The lattice calculation of the cross section $\gamma^*\gamma^* \to \pi\pi$ is for instance more complex than calculating the cross section $\gamma^*\gamma^* \to \gamma^*\gamma^*$ for spacelike photons. In experiments, the weakness of the electromagnetic coupling would make such a measurement impractical, but in lattice QCD the factor e^4 merely multiplies a four-point correlation function at the end of the calculation.

In this Chapter, we present the computation of the HLbL scattering amplitude for spacelike photons in lattice QCD, based on the co-authored work of Ref. [5]. Being parametrized by functions of six Lorentz invariants, it is a complicated object. We focus on the forward amplitudes because they are simpler functions of three invariants and, using the optical theorem, they are related to $\gamma^*\gamma^* \to$ hadrons cross sections. Our objectives are:

- Provide a stringent test that the light-by-light amplitude for spacelike photons is correctly described by the type of hadronic model used so far to estimate a_μ^{HLbL}. The model includes the exchange of pseudoscalar, scalar, axial-vector and tensor mesons.
- Provide information on their two-photon transition form factors via global fits.
- Compare the transition form factors to phenomenological determinations based on light-by-light sum rules.

As the first step, in Ref. [1], we laid out the method and computed the forward amplitude sensitive to the total transverse $\gamma^*\gamma^*$ cross section, $\mathcal{M}_{\mathrm{TT}}$, via a dispersive sum rule. In Ref. [5], we extended the comparison between lattice data and phenomenological parametrizations of the $\gamma^*\gamma^* \to$ hadrons cross sections to encompass all eight forward amplitudes. This more

extensive analysis allowed us to place much stronger constraints on the size of the contributions of different resonances, because they contribute to different amplitudes with different weight factors, often even with opposite signs.

The lattice calculation was performed in QCD with two flavors of light quarks; it involves pion masses down to 190 MeV and two lattice spacings. While a fully realistic lattice calculation would have to include at least a dynamical strange quark, the present calculation does provide a suitable test of hadronic models via dispersive sum rules, since at the required level of precision it is fairly straightforward to adapt these models to QCD without the strange quark, as discussed in Section 5.3.

We will start by introducing the theoretical background for the forward light-by-light scattering in Section 5.1, where we establish the corresponding sum rules. We then present our numerical results in two-flavor lattice QCD in Section 5.2. After introducing the details of the hadronic model for the $\gamma^*\gamma^* \to$ hadrons cross sections in Section 5.3 and appendix 5.A, we perform fits to the lattice data in Section 5.4. We compare the results for the transition form factors to existing phenomenological estimates, and finally conclude in Section 5.5.

5.1 Forward light-by-light scattering

In order to establish our notation, we start by recalling the dispersive sum rules for the scattering of spacelike photons [75, 76]. Just as for real photons [190], they are based on unitarity and analyticity of the forward scattering amplitude. More specifically, the optical theorem allows one to relate the absorptive part of the $\gamma^*(\lambda_1, q_1)\gamma^*(\lambda_2, q_2) \to \gamma^*(\lambda_1', q_1)\gamma^*(\lambda_2', q_2)$ forward scattering amplitude to fusion cross sections for the process $\gamma^*\gamma^* \to \mathrm{X}$, where X stands for any C-parity even final state. The relevant kinematic variables are the photon virtualities, $q_i^2 = -Q_i^2$, $(i = 1, 2)$, and the crossing-symmetric variable $\nu = q_1 \cdot q_2$, which is related to the squared center-of-mass energy by $s = 2\nu - Q_1^2 - Q_2^2$. Denoting the absorptive part of the helicity amplitude $\mathcal{M}_{\lambda_1'\lambda_2',\lambda_1\lambda_2}$ by

$$W_{\lambda_1'\lambda_2',\lambda_1\lambda_2} = \mathrm{Im}\left(\mathcal{M}_{\lambda_1'\lambda_2',\lambda_1\lambda_2}\right), \tag{5.1}$$

the optical theorem yields (with a factor of one half because both photons are identical, and $\mathrm{d}\Gamma_\mathrm{X}$ is the phase space for a final state X)

$$W_{\lambda_1'\lambda_2',\lambda_1\lambda_2} = \frac{1}{2}\int \mathrm{d}\Gamma_X\ (2\pi)^4\delta^4(q_1 + q_2 - p_\mathrm{X})\,\mathcal{M}_{\lambda_1\lambda_2}(q_1, q_2; p_\mathrm{X})\,\mathcal{M}^*_{\lambda_1'\lambda_2'}(q_1, q_2; p_\mathrm{X}), \tag{5.2}$$

where $\mathcal{M}_{\lambda_1\lambda_2}(q_1, q_2; p_\mathrm{X})$ denotes the invariant helicity amplitude for the fusion process

$$\gamma^*(\lambda_1, q_1) + \gamma^*(\lambda_2, q_2) \to \mathrm{X}(p_\mathrm{X}). \tag{5.3}$$

The helicity amplitudes are related to the Feynman amplitudes by

$$\mathcal{M}_{\lambda_1'\lambda_2'\lambda_1\lambda_2}(q_1, q_2) = \mathcal{M}_{\mu\nu\rho\sigma}(q_1, q_2)\ \epsilon^{*\mu}(\lambda_1', q_1)\ \epsilon^{*\nu}(\lambda_2', q_2)\ \epsilon^{\rho}(\lambda_1, q_1)\ \epsilon^{\sigma}(\lambda_2, q_2), \tag{5.4}$$

where ϵ are the photons polarization vectors. Using parity and time-reversal invariance, we are left with only eight independent amplitudes $\mathcal{M}_{\lambda_1'\lambda_2',\lambda_1\lambda_2}$ [191]. Forming linear combinations, we can consider eight amplitudes which are either even (first six amplitudes) or odd (last two amplitudes) with respect to the variable ν:

$$\mathcal{M}_{TT} = \frac{1}{2}(\mathcal{M}_{++,++} + \mathcal{M}_{+-,+-}),\ \mathcal{M}^\tau_{TT} = \mathcal{M}_{++,--},$$
$$\mathcal{M}_{TL} = \mathcal{M}_{+0,+0},\ \mathcal{M}_{LT} = \mathcal{M}_{0+,0+},\ \mathcal{M}^\tau_{TL} = \frac{1}{2}(\mathcal{M}_{++,00} + \mathcal{M}_{0+,-0}),\ \mathcal{M}_{LL} = \mathcal{M}_{00,00},$$
$$\mathcal{M}^a_{TT} = \frac{1}{2}(\mathcal{M}_{++,++} - \mathcal{M}_{+-,+-}),\ \mathcal{M}^a_{TL} = \frac{1}{2}(\mathcal{M}_{++,00} - \mathcal{M}_{0+,-0}).$$

In terms of the Feynman amplitudes, the eight independent helicity amplitudes are then given by [191][1]

$$\mathcal{M}_{TT} = \frac{1}{4} R^{\mu\mu'} R^{\nu\nu'} \mathcal{M}_{\mu'\nu'\mu\nu} \,, \tag{5.5a}$$

$$\mathcal{M}^{\tau}_{TT} = \frac{1}{4} \left[R^{\mu\nu} R^{\mu'\nu'} + R^{\mu\nu'} R^{\mu'\nu} - R^{\mu\mu'} R^{\nu\nu'} \right] \mathcal{M}_{\mu'\nu'\mu\nu} \,, \tag{5.5b}$$

$$\mathcal{M}^{a}_{TT} = \frac{1}{4} \left[R^{\mu\nu} R^{\mu'\nu'} - R^{\mu\nu'} R^{\mu'\nu} \right] \mathcal{M}_{\mu'\nu'\mu\nu} \,, \tag{5.5c}$$

$$\mathcal{M}_{TL} = \frac{1}{2} R^{\mu\mu'} k_2^{\nu} k_2^{\nu'} \mathcal{M}_{\mu'\nu'\mu\nu} \,, \tag{5.5d}$$

$$\mathcal{M}_{LT} = \frac{1}{2} k_1^{\mu} k_1^{\mu'} R^{\nu\nu'} \mathcal{M}_{\mu'\nu'\mu\nu} \,, \tag{5.5e}$$

$$\mathcal{M}_{LL} = k_1^{\mu} k_1^{\mu'} k_2^{\nu} k_2^{\nu'} \mathcal{M}_{\mu'\nu'\mu\nu} \,, \tag{5.5f}$$

$$\mathcal{M}^{a}_{TL} = -\frac{1}{8} \left[R^{\mu\nu} k_1^{\mu'} k_2^{\nu'} + R^{\mu\nu'} k_1^{\mu'} k_2^{\nu} + (\mu\nu \leftrightarrow \mu'\nu') \right] \mathcal{M}_{\mu'\nu'\mu\nu} \,, \tag{5.5g}$$

$$\mathcal{M}^{\tau}_{TL} = -\frac{1}{8} \left[R^{\mu\nu} k_1^{\mu'} k_2^{\nu'} - R^{\mu\nu'} k_1^{\mu'} k_2^{\nu} + (\mu\nu \leftrightarrow \mu'\nu') \right] \mathcal{M}_{\mu'\nu'\mu\nu} \,, \tag{5.5h}$$

where the projector $R^{\mu\nu}$ onto the subspace orthogonal to q_1 and q_2, and the vectors k_1 and k_2 are defined in Appendix 5.A. The eight helicity amplitudes are functions of (ν, Q_1^2, Q_2^2). Then, for fixed photon virtualities Q_1^2 and Q_2^2, the sum rules can be generically written as [76]

$$\mathcal{M}_{\rm even}(\nu) = \frac{2}{\pi} \int_{\nu_0}^{\infty} d\nu' \frac{\nu'}{\nu'^2 - \nu^2 - i\epsilon} W_{\rm even}(\nu') \,, \tag{5.6a}$$

$$\mathcal{M}_{\rm odd}(\nu) = \frac{2\nu}{\pi} \int_{\nu_0}^{\infty} d\nu' \frac{1}{\nu'^2 - \nu^2 - i\epsilon} W_{\rm odd}(\nu') \,, \tag{5.6b}$$

assuming the convergence of the integral. Here $\nu_0 \equiv \frac{1}{2}(Q_1^2 + Q_2^2)$. If the integral does not converge, it is necessary to introduce a subtraction

$$\mathcal{M}_{\rm even}(\nu) = \mathcal{M}_{\rm even}(0) + \frac{2\nu^2}{\pi} \int_{\nu_0}^{\infty} d\nu' \frac{1}{\nu'(\nu'^2 - \nu^2 - i\epsilon)} W_{\rm even}(\nu') \,, \tag{5.7a}$$

$$\mathcal{M}_{\rm odd}(\nu) = \nu \mathcal{M}'_{\rm odd}(0) + \frac{2\nu^3}{\pi} \int_{\nu_0}^{\infty} d\nu' \frac{1}{\nu'^2(\nu'^2 - \nu^2 - i\epsilon)} W_{\rm odd}(\nu') \,. \tag{5.7b}$$

Finally, the absorptive parts $W_{\lambda_1'\lambda_2',\lambda_1\lambda_2}$ of those eight independent amplitudes, given by Eq. (5.2), are expressed in terms of the $\gamma^*\gamma^* \to {\rm X}$ fusion cross sections [192],

$$W_{++,++} + W_{+-,+-} \equiv 2\sqrt{X}\,(\sigma_0 + \sigma_2) = 2\sqrt{X}\,\left(\sigma_{\parallel} + \sigma_{\perp}\right) \equiv 4\sqrt{X}\,\sigma_{TT} \,, \tag{5.8a}$$

$$W_{++,--} \equiv 2\sqrt{X}\,\left(\sigma_{\parallel} - \sigma_{\perp}\right) \equiv 2\sqrt{X}\,\tau_{TT} \,, \tag{5.8b}$$

$$W_{++,++} - W_{+-,+-} \equiv 2\sqrt{X}\,(\sigma_0 - \sigma_2) \equiv 4\sqrt{X}\,\tau^a_{TT} \,, \tag{5.8c}$$

$$W_{+0,+0} \equiv 2\sqrt{X}\,\sigma_{TL} \,, \tag{5.8d}$$

$$W_{0+,0+} \equiv 2\sqrt{X}\,\sigma_{LT} \,, \tag{5.8e}$$

$$W_{++,00} + W_{0+,-0} \equiv 4\sqrt{X}\,\tau_{TL} \,, \tag{5.8f}$$

$$W_{++,00} - W_{0+,-0} \equiv 4\sqrt{X}\,\tau^a_{TL} \,, \tag{5.8g}$$

$$W_{00,00} \equiv 2\sqrt{X}\,\sigma_{LL} \,, \tag{5.8h}$$

[1] Our definitions of $\mathcal{M}^a_{TL}$ and $\mathcal{M}^{\tau}_{TL}$ are swapped relative to [191], so that our $\mathcal{M}^a_{TL}$ is odd in ν and our $\mathcal{M}^{\tau}_{TL}$ is even.

where $X = \nu^2 - Q_1^2 Q_2^2$ is the virtual-photon flux factor. Here, L and T refer to longitudinal and transverse polarizations respectively. The cross sections σ are positive, but the interference terms τ are not sign-definite. The relevant cross sections for resonance contributions in each channel are explicitly given in Appendix 5.A in terms of transition form factors.

Thus, using Eqs. (5.6) and (5.8), we obtain the following dispersive sum rules, valid for fixed photon virtualities $Q_1^2, Q_2^2 > 0$ [76]:

$$\overline{\mathcal{M}}_{TT} = \frac{1}{2}\left(\overline{\mathcal{M}}_{++,++}(\nu) + \overline{\mathcal{M}}_{+-,+-}(\nu)\right) = \frac{4\nu^2}{\pi}\int_{\nu_0}^{\infty} d\nu' \frac{\sqrt{X'}\sigma_{TT}(\nu')}{\nu'(\nu'^2 - \nu^2 - i\epsilon)}, \tag{5.9a}$$

$$\overline{\mathcal{M}}^{\tau}_{TT} = \overline{\mathcal{M}}_{++,--}(\nu) = \frac{4\nu^2}{\pi}\int_{\nu_0}^{\infty} d\nu' \frac{\sqrt{X'}\tau_{TT}(\nu')}{\nu'(\nu'^2 - \nu^2 - i\epsilon)}, \tag{5.9b}$$

$$\overline{\mathcal{M}}^{a}_{TT} = \frac{1}{2}\left(\overline{\mathcal{M}}_{++,++}(\nu) - \overline{\mathcal{M}}_{+-,+-}(\nu)\right) = \frac{4\nu^3}{\pi}\int_{\nu_0}^{\infty} d\nu' \frac{\sqrt{X'}\,\tau^a_{TT}(\nu')}{\nu'^2(\nu'^2 - \nu^2 - i\epsilon)}, \tag{5.9c}$$

$$\overline{\mathcal{M}}_{TL} = \overline{\mathcal{M}}_{+0,+0}(\nu) = \frac{4\nu^2}{\pi}\int_{\nu_0}^{\infty} d\nu' \frac{\sqrt{X'}\sigma_{TL}(\nu')}{\nu'(\nu'^2 - \nu^2 - i\epsilon)}, \tag{5.9d}$$

$$\overline{\mathcal{M}}_{LT} = \overline{\mathcal{M}}_{0+,0+}(\nu) = \frac{4\nu^2}{\pi}\int_{\nu_0}^{\infty} d\nu' \frac{\sqrt{X'}\sigma_{LT}(\nu')}{\nu'(\nu'^2 - \nu^2 - i\epsilon)}, \tag{5.9e}$$

$$\overline{\mathcal{M}}^{\tau}_{TL} = \frac{1}{2}\left(\overline{\mathcal{M}}_{++,00}(\nu) + \overline{\mathcal{M}}_{0+,-0}(\nu)\right) = \frac{4\nu^2}{\pi}\int_{\nu_0}^{\infty} d\nu' \frac{\sqrt{X'}\,\tau_{TL}(\nu')}{\nu'(\nu'^2 - \nu^2 - i\epsilon)}, \tag{5.9f}$$

$$\overline{\mathcal{M}}^{a}_{TL} = \frac{1}{2}\left(\overline{\mathcal{M}}_{++,00}(\nu) - \overline{\mathcal{M}}_{0+,-0}(\nu)\right) = \frac{4\nu^3}{\pi}\int_{\nu_0}^{\infty} d\nu' \frac{\sqrt{X'}\,\tau^a_{TL}(\nu')}{\nu'^2(\nu'^2 - \nu^2 - i\epsilon)}, \tag{5.9g}$$

$$\overline{\mathcal{M}}_{LL} = \overline{\mathcal{M}}_{00,00}(\nu) = \frac{4\nu^2}{\pi}\int_{\nu_0}^{\infty} d\nu' \frac{\sqrt{X'}\,\sigma_{LL}(\nu')}{\nu'(\nu'^2 - \nu^2 - i\epsilon)}, \tag{5.9h}$$

where we use the notation $\overline{\mathcal{M}}(\nu) \equiv \mathcal{M}(\nu) - \mathcal{M}(0)$ or $\overline{\mathcal{M}}(\nu) \equiv \mathcal{M}(\nu) - \nu\mathcal{M}'(0)$ respectively for the even and odd amplitudes. We always consider the subtracted sum rules, even when the unsubtracted version is well defined, since the subtraction has the effect of suppressing the high-energy contributions. Evaluating the sum rules using phenomenological inputs on the two-photon fusion processes, one can confront the results with the light-by-light forward amplitudes computed on the lattice. In the next Section, we will present an empirical model for the description of the two-photon fusion processes and subsequently, by comparing it with our lattice results, we will be able to extract information about the $\gamma^*\gamma^* \to M$ transition form factors.

5.2 Lattice results

The four-point correlation functions are computed on a subset of the $N_f = 2$ CLS (Coordinated Lattice Simulations) ensembles generated using the plaquette gauge action for gluons [194] and the $\mathcal{O}(a)$-improved Wilson-Clover action for fermions [195] with the non-perturbative parameter $c_{\rm SW}$ [196]. The fermionic boundary conditions are periodic in space and antiperiodic in time. We consider two different values of the lattice spacing and different pion masses in the range from 190 to 440 MeV. The parameters of the ensembles used in this Chapter are summarized in Table 5.1.

For each ensemble, the connected four-point correlation function is computed at a few values of $Q_1 = (n \cdot 2\pi/T, 0, 0, 0)$, the first-listed component corresponding to the time direction, with $n = 1, 2, 3$ on ensemble E5; $n = 1, 3$ on F6 and F7; $n = 1, 4$ on G8 and $n = 2$ on N6. For the (2+2) diagrams, we use $n = 2$ (E5) and $n = 3$ (F6). Then, for each value of Q_1, the four-point

CLS	β	$L^3 \times T$	κ	a [fm]	m_π [MeV]	m_ρ [MeV]	$m_\pi L$	# confs
E5	5.3	$32^3 \times 64$	0.13625	0.0652(6)	437(4)	971	4.7	500
F6		$48^3 \times 96$	0.13635		314(3)	886	5.0	150
F7		$48^3 \times 96$	0.13638		270(3)	841	4.3	124
G8		$64^3 \times 128$	0.136417		194(2)	781	4.1	86
N6	5.5	$48^3 \times 96$	0.13667	0.0483(4)	342(3)	917	4.0	236

Table 5.1: Table from Ref. [5]: Parameters of the simulations: the bare coupling $\beta = 6/g_0^2$, the lattice resolution, the hopping parameter κ, the lattice spacing a in physical units extracted from [193], the pion mass m_π, the rho mass m_ρ and the number of gauge configurations.

correlation function is evaluated for many different values of Q_2, corresponding to different values of Q_2^2 and ν.

For the fully-connected diagrams, we used two source positions on ensembles E5, F6, F7; one source position on N6; and eight source positions on G8. In the latter case, we used the truncated-solver method [197] for the eight sources and a computation with exact inversions of the Dirac operator for bias correction on one source.

To estimate the even subtracted amplitudes, we compute the subtraction term directly at $\nu = 0$, i.e., with Q_2 orthogonal to Q_1. For the odd subtracted amplitudes, we use the approximation $\overline{\mathcal{M}}(\nu) \approx \mathcal{M}(\nu) - \frac{\nu}{\nu_1}\mathcal{M}(\nu_1)$, where ν_1 is the smallest available nonzero value of ν. In both cases we linearly interpolate the subtraction term in Q_2^2 to match the value in the unsubtracted term.

In all tables and figures, our results for the HLbL amplitudes are multiplied by a factor of 10^6 for better readability.

The results for the connected contribution to the eight amplitudes are depicted in Figs. 5.1–5.2 for the ensemble F6. For F6 we show the amplitudes for two different values of the virtuality Q_1^2. We used all lattice momenta Q_2 up to $Q_2^2 \lesssim 4$ GeV^2. The variable ν is then bounded by $\nu \leq (Q_1^2 Q_2^2)^{1/2}$. The four amplitudes $\overline{\mathcal{M}}_{TT}$, $\overline{\mathcal{M}}_{TL}$, $\overline{\mathcal{M}}_{LT}$ and , $\overline{\mathcal{M}}_{LL}$ are positive as they are related to cross sections, while the amplitudes $\overline{\mathcal{M}}^a_{TT}$, $\overline{\mathcal{M}}^\tau_{TT}$, $\overline{\mathcal{M}}^\tau_{TL}$, $\overline{\mathcal{M}}^a_{TL}$, corresponding to interference terms, are not sign-definite. Since all amplitudes vanish in the limit of either Q_1 or $Q_2 \to 0$, the signal deteriorates at small Q_1^2 (for fixed Q_2^2) as can be seen by comparing the left and right panels of Fig. 5.1.

We now come to our results for the (2+2) disconnected diagram contribution to the eight subtracted amplitudes. We obtain this contribution with a reasonable statistical precision; however, some of the amplitudes are significantly different from zero when $Q_2^2 = 0$, as shown in the left panel of Fig. 5.3. In infinite volume, the Euclidean four-point function should vanish at this kinematic point, since a conserved current can be written as the divergence of a tensor field, $J_\mu(x) = \partial_\nu(x_\mu J_\nu(x))$, so that $\int d^4x\, J_\mu(x)$ is a pure boundary term, which vanishes in the presence of a mass gap. Therefore this is a sign of significant finite-volume effects. The bulk of the effect may be removed when subtracting the amplitude at $\nu = 0$, but some of it may remain. Figure 5.3 also shows that due to correlations, the subtraction significantly reduces the statistical uncertainty. The full set of subtracted amplitudes on ensemble F6 is shown in Fig. 5.4.

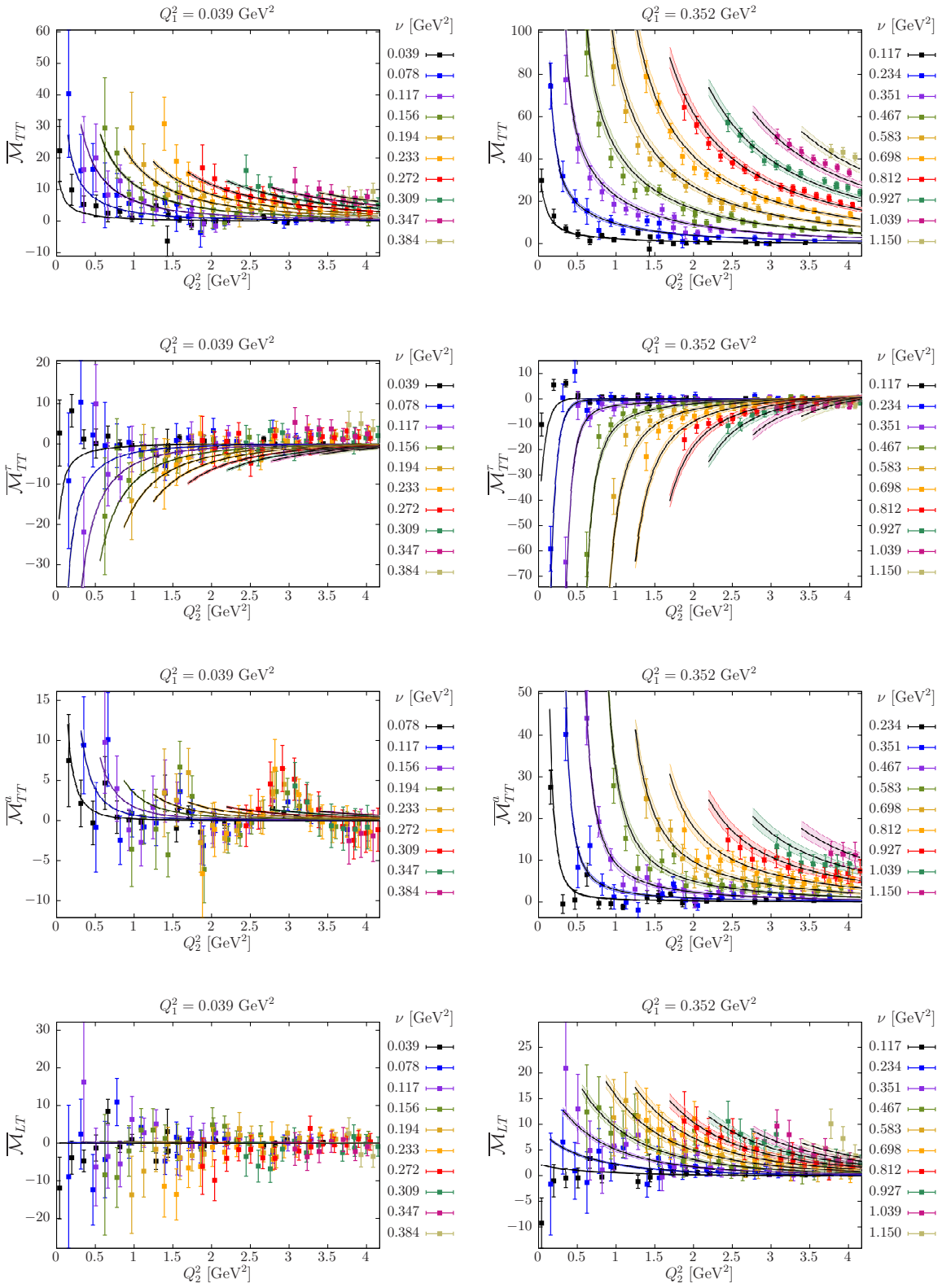

Figure 5.1: Figure from Ref. [5]: Amplitudes $\overline{\mathcal{M}}_{TT}$, $\overline{\mathcal{M}}^{\tau}_{TT}$, $\overline{\mathcal{M}}^{a}_{TT}$ and $\overline{\mathcal{M}}_{LT}$ ($\times 10^6$) for the ensemble F6 and for two different values of Q_1^2 (left: $Q_1^2 = 0.039$ GeV^2, right: $Q_1^2 = 0.352$ GeV^2). The curves with error-bands represent the fit results discussed in Sec. 5.4.

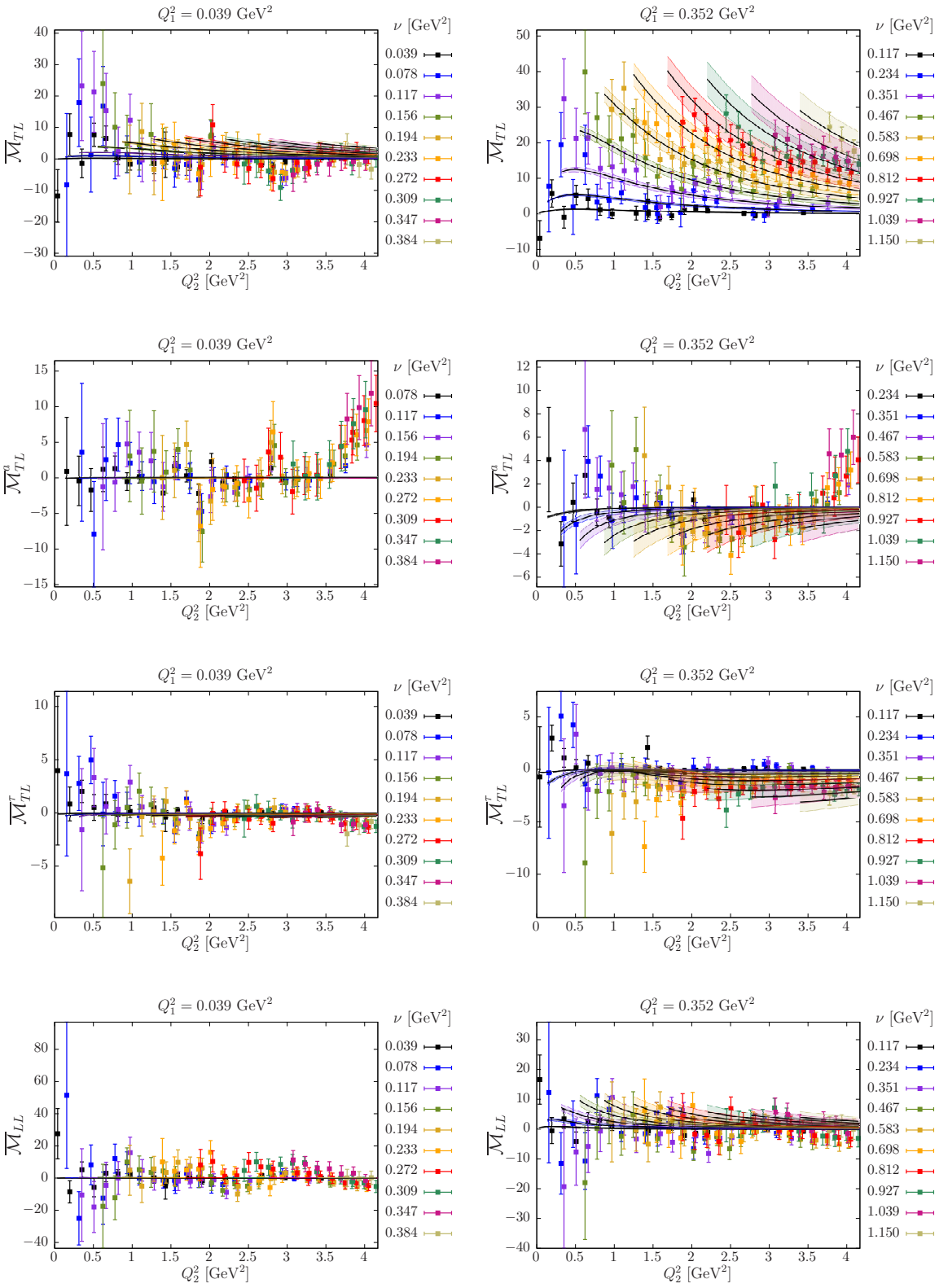

Figure 5.2: Figure from Ref. [5]: Amplitudes $\overline{\mathcal{M}}_{TL}$, $\overline{\mathcal{M}}^a_{TL}$, $\overline{\mathcal{M}}^\tau_{TL}$ and $\overline{\mathcal{M}}_{LL}$ ($\times 10^6$) for the ensemble F6 and for two different values of Q_1^2 (left: $Q_1^2 = 0.039$ GeV^2, right: $Q_1^2 = 0.352$ GeV^2). The curves with error-bands represent the fit results discussed in Sec. 5.4.

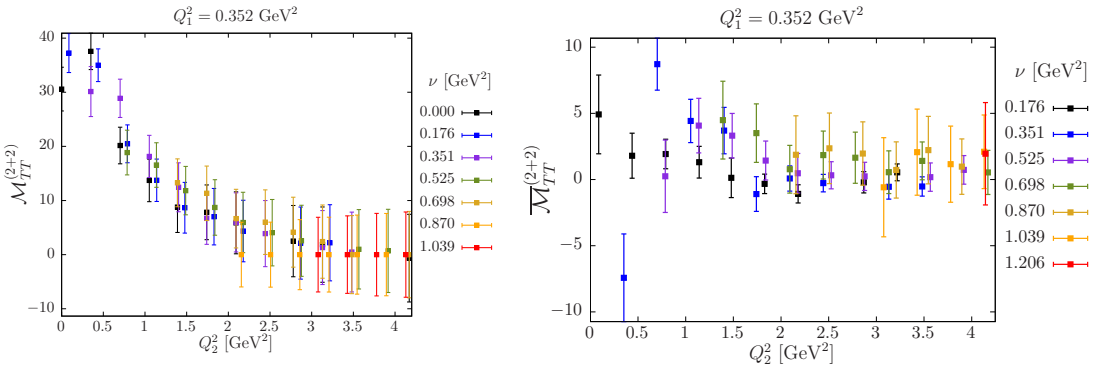

Figure 5.3: Figure from Ref. [5]: Contribution ($\times 10^6$) from $(2+2)$-disconnected diagrams to the forward scattering amplitude $\mathcal{M}_{TT}$ on ensemble E5, without (left) and with (right) subtraction of the value at $\nu = 0$.

5.3 Empirical parametrization of the hadronic $\gamma^*\gamma^*$-fusion cross section

In this Section, we describe how we model the hadronic $\gamma^*\gamma^*$-fusion cross section. We represent it as a sum of contributions from charge-conjugation even mesonic resonances produced in the s-channel. Specifically, we include the pseudoscalar ($J^{PC} = 0^{-+}$), scalar ($J^{PC} = 0^{++}$), axial-vector ($J^{PC} = 1^{++}$) and tensor ($J^{PC} = 2^{++}$) mesons. Table 5.2 lists the most relevant light mesons with these quantum numbers. In our implementation, we limit ourselves to the lightest state in each symmetry channel. The assumption that those states are sufficient to saturate the sum rules is motivated by the fact that, at small energies, higher mass singularities are suppressed in Eq. (5.9). Moreover, we have revised the model used in [1] to better account for the fact that we perform fits to the fully-connected diagrams. Rather than including isovector and isoscalar mesons, we consider only isovector mesons, enhanced by a factor 34/9: we refer the reader to the full text of Ref. [5] for a justification of this approximation, which we expect to be superior. The procedure mostly modifies the contribution of the pseudoscalar sector, due to the large mass difference between the pion and the η' meson. Also, since lattice simulations are performed using $N_f = 2$ dynamical quarks, we do not include the η meson. Finally, we include the Born approximation to the $\gamma^*\gamma^* \to \pi^+\pi^-$ cross section using scalar QED, as described in Ref. [76], using a monopole vector form factor, the monopole mass being set to the ρ meson mass. Explicit formulae for cross sections used in our model are given in Appendix 5.A. The individual contributions to the eight amplitudes from each channel are summarized in Table 5.3.

Our lattice simulations are performed at larger-than-physical quark masses. For each ensemble, the pion and ρ meson masses are determined from the pseudoscalar and vector two-point correlation functions respectively; see Table 5.1 for the obtained values. To obtain an estimate of the lowest-lying meson mass m_X in every other symmetry channel, we assume that m_X admits a constant additive shift relative to its physical value m_X^{phys}. The shift δm is determined from the difference between the ρ mass computed on the lattice and its experimental value,

$$m_X = m_X^{\text{phys}} + \delta m, \qquad \delta m = m_\rho^{\text{lat}} - m_\rho^{\text{phys}}\,. \tag{5.10}$$

In Section 5.4, we will test the sensitivity of our results to variations of δm by a factor of two. As for resonances, we assume that their contributions are well approximated by Breit-Wigner distributions and use the following formal substitution in the cross sections given in

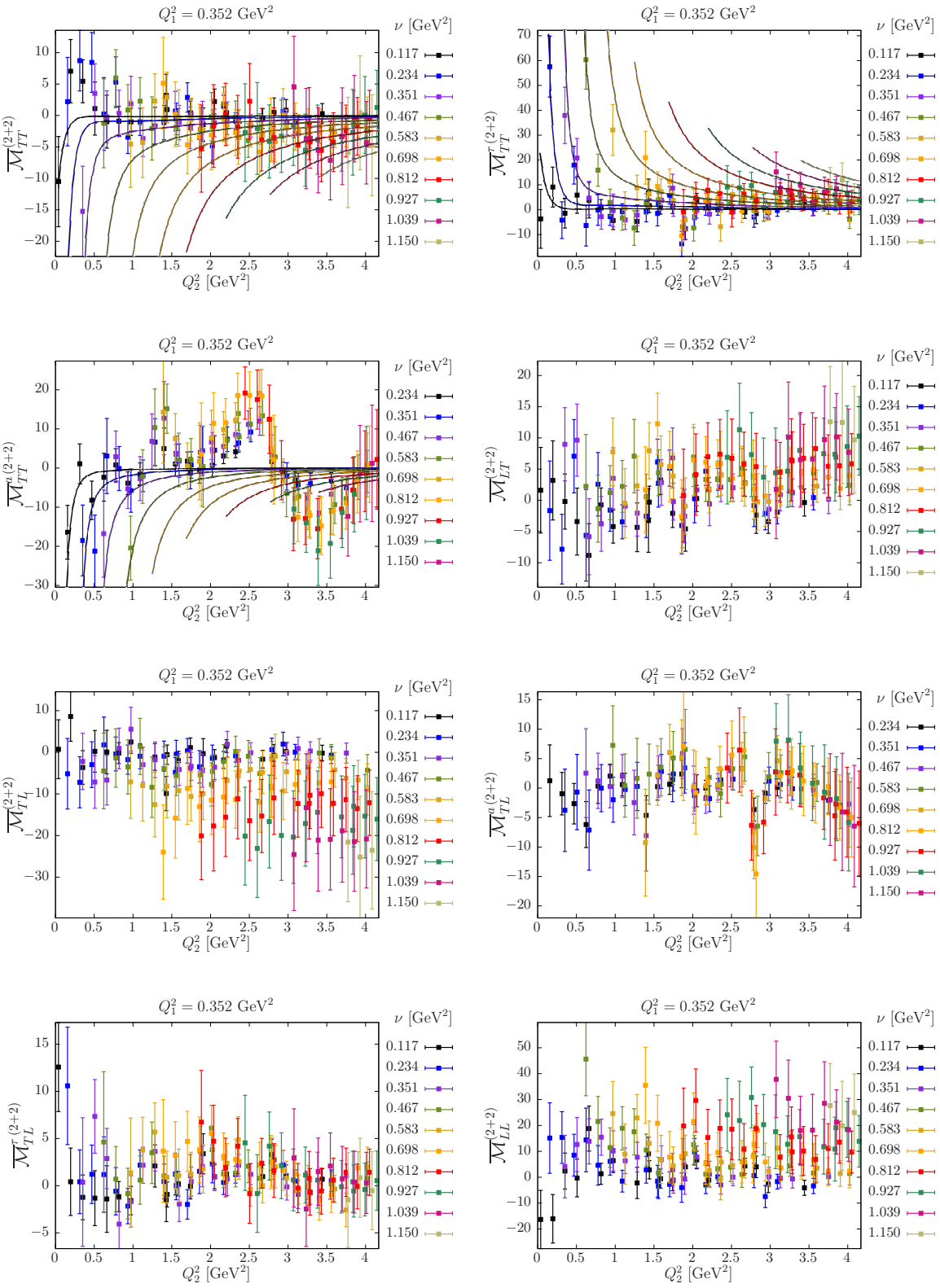

Figure 5.4: Figure from Ref. [5]: Contribution ($\times 10^6$) from $(2+2)$-disconnected diagrams to the eight subtracted forward scattering amplitudes on ensemble F6 with one fixed virtuality $Q_1^2 = 0.352\,\mathrm{GeV}^2$.

	Isovector		
	name	m [MeV]	$\Gamma_{\gamma\gamma}$ [keV]
0^{-+}	π	134.98	0.0078(2)
0^{++}	$a_0(980)$	980(20)	0.30(10)
1^{++}	$a_1(1260)$	1230(40)	1.26*
2^{++}	$a_2(1320)$	1318.3(0.6)	1.00(6)
	Isoscalar		
	name	m [MeV]	$\Gamma_{\gamma\gamma}$ [keV]
0^{-+}	η'	957.78(6)	4.35(25)
0^{++}	$f_0(600)$	×	×
1^{++}	$f_1(1285)$	1281.8(0.6)	3.5(0.8)
2^{++}	$f_2(1270)$	1275.5(0.8)	2.93(40)
	Isoscalar		
	name	m [MeV]	$\Gamma_{\gamma\gamma}$ [keV]
0^{-+}	η	547.86(2)	0.515(18)
0^{++}	$f_0(980)$	990(20)	0.31(5)
1^{++}	$f_1(1420)$	1426.4(0.9)	3.2(0.9)
2^{++}	$f_2'(1525)$	1525(5)	0.081(9)

Table 5.2: Table from Ref. [5]: Particle multiplets and physical values for the mass and two-photon width as quoted by the PDG [80], as well as by [198] for the two-photon width of the $f_2(1270)$ meson and [199] for the π^0 width. In the case of the axial-vector mesons, the indicated width is the effective width defined in Eq. (5.20) and obtained phenomenologically in [77]. A cross indicates an absent or imprecise value in the PDG. An asterisk means that we use the isoscalar result divided by a factor 25/9 (explained in Ref. [5]).

Appendix 5.A,

$$\delta(s - m_X^2) \;\leftrightarrow\; \frac{m_X}{\pi} \frac{\Gamma_X}{(s - m_X^2)^2 + m_X^2 \Gamma_X^2}\,, \tag{5.11}$$

where m_X and Γ_X are the mass and the total width of the particle respectively. However, the remaining part of the cross section is still evaluated at $s = m_X^2$. For the (very narrow) pseudoscalar mesons, one can perform the integration explicitly and obtain the following contribution to the sum rules (using $\delta(\nu - \nu_P) = 2\delta(s - s_P)$, where $\nu_P = \frac{1}{2}(m_P^2 + Q_1^2 + Q_2^2)$) :

$$\frac{4\nu^2}{\pi} \int_{\nu_0}^{\infty} d\nu' \, \frac{\sqrt{X'}\sigma_0(\nu')}{\nu'(\nu'^2 - \nu^2 - i\epsilon)} = 64\pi \, \frac{\Gamma_{\gamma\gamma}}{m_P} \, \frac{\nu^2 X_P}{m_P^2 \, \nu_P(\nu_P^2 - \nu^2)} \left[\frac{F_{\mathcal{P}\gamma^*\gamma^*}(Q_1^2, Q_2^2)}{F_{\mathcal{P}\gamma^*\gamma^*}(0,0)} \right]^2 \tag{5.12}$$

$$= 16\pi^2 \alpha^2 \, \frac{\nu^2 X_P}{\nu_P(\nu_P^2 - \nu^2)} \left[F_{\mathcal{P}\gamma^*\gamma^*}(Q_1^2, Q_2^2) \right]^2 , \tag{5.13}$$

	$\mathcal{M}_{TT}$	$\mathcal{M}^{\tau}_{TT}$	$\mathcal{M}^{a}_{TT}$	$\mathcal{M}_{TL}$	$\mathcal{M}_{LT}$	$\mathcal{M}^{\tau}_{TL}$	$\mathcal{M}^{a}_{TL}$	$\mathcal{M}_{LL}$
Pseudoscalar	$\sigma_0/2$	$-\sigma_0$	$\sigma_0/2$	$\times$	$\times$	$\times$	$\times$	$\times$
Scalar	$\sigma_0/2$	σ_0	$\sigma_0/2$	$\times$	$\times$	τ_{TL}	τ_{TL}	σ_{LL}
Axial	$\sigma_0/2$	$-\sigma_0$	$\sigma_0/2$	σ_{TL}	σ_{LT}	τ_{TL}	$-\tau_{TL}$	$\times$
Tensor	$\frac{\sigma_0+\sigma_2}{2}$	σ_0	$\frac{\sigma_0-\sigma_2}{2}$	σ_{TL}	σ_{LT}	τ_{TL}	τ^{a}_{TL}	σ_{LL}
Scalar QED	σ_{TT}	τ_{TT}	τ^{a}_{TT}	σ_{TL}	σ_{LT}	τ_{TL}	τ^{a}_{TL}	σ_{LL}

Table 5.3: Table from Ref. [5]: List of individual contributions to each of the eight helicity amplitudes. A cross indicates the absence of a contribution in the given channel. The relevant cross sections for each channel are given in Appendix 5.A.

in the even case, and

$$\frac{4\nu^3}{\pi}\int_{\nu_0}^{\infty} d\nu' \, \frac{\sqrt{X'}\sigma_0(\nu')}{\nu'^2(\nu'^2-\nu^2-i\epsilon)} = 16\pi^2\alpha^2 \, \frac{\nu^3 X_P}{\nu_P^2(\nu_P^2-\nu^2)} \left[F_{\mathcal{P}\gamma^*\gamma^*}(Q_1^2,Q_2^2)\right]^2 , \tag{5.14}$$

in the odd case, where $X_P \equiv \nu_P^2 - Q_1^2 Q_2^2$.

5.3.1 Parametrization of the form factors

In this Subsection, we briefly review the available information on the transition form factors of the exchanged mesons in the hadronic model, and present the parametrization we use in fitting the lattice HLbL amplitudes. While detailed information is available in the case of the pion from lattice QCD, no experimental data is presently available at doubly virtual kinematics in any channel. In these cases, a monopole or dipole ansatz, in which the Q_1^2 and Q_2^2 dependence factorizes, is made to describe the photon-virtuality dependence, even though such an ansatz might not have the asymptotic behavior predicted by the operator-product expansion. Our motivation is that this type of parametrization is used in model calculations of a_μ^{HLbL}. Also, given our goal of performing fits to the HLbL amplitudes computed on the lattice, the number of free parameters characterizing the transition form factors should be commensurate with the precision of the lattice data.

Pseudoscalar mesons

For pseudoscalar mesons, experimental data are available when at least one photon is on-shell, and in this case a good parametrization of the data is obtained using a monopole form factor [200–203]. However, as shown in Ref. [189], a monopole form factor failed to reproduce the lattice data in the doubly-virtual case, in contrast to the LMD+V model. Furthermore, the LMD+V model is compatible with the Brodsky-Lepage behavior [204–206] in the singly-virtual case and with the operator-product expansion (OPE) prediction [207, 208] in the $Q_1^2 = Q_2^2$ doubly-virtual case. We therefore use this model for the pion transition form factor, of which the parameters were determined in Ref. [189] for each ensemble listed in Table 5.1.

Scalar mesons

Scalar mesons can be produced by two transverse (T) or two longitudinal (L) photons. Correspondingly, the amplitude is parametrized by two form factors, $F^T_{S\gamma^*\gamma^*}$ and $F^L_{S\gamma^*\gamma^*}$. Only the first one has been measured experimentally: this was done for the $f_0(980)$ meson in the

region $Q^2 < 30\,GeV^2$ by the Belle Collaboration [209], and the results are compatible with a monopole form factor with a monopole mass $M_S = 0.800(50)$ GeV. Therefore, we assume the form

$$\frac{F^T_{\mathcal{S}\gamma^*\gamma^*}(Q_1^2, Q_2^2)}{F^T_{\mathcal{S}\gamma^*\gamma^*}(0,0)} = \frac{1}{(1+Q_1^2/M_S^2)(1+Q_2^2/M_S^2)}\,. \tag{5.15}$$

For simplicity, we also assume that the transverse and longitudinal form factors are equal (the longitudinal one is only relevant for the amplitudes M^a_{TL}, M^τ_{TL} and M_{LL}),

$$F^L_{\mathcal{S}\gamma^*\gamma^*}(Q_1^2, Q_2^2) = -F^T_{\mathcal{S}\gamma^*\gamma^*}(Q_1^2, Q_2^2)\,. \tag{5.16}$$

The normalization is obtained from the experimentally measured two-photon decay width $\Gamma_{\gamma\gamma}$ given by (see Table 5.2)

$$\Gamma_{\gamma\gamma} = \frac{\pi\alpha^2}{4} m_S \left[F^T_{\mathcal{S}\gamma^*\gamma^*}(0,0)\right]^2\,, \tag{5.17}$$

while the monopole mass M_S will be treated as a free parameter.

Axial mesons

For axial mesons, we have two form factors, $F^{(0)}_{\mathcal{A}\gamma^*\gamma^*}$ and $F^{(1)}_{\mathcal{A}\gamma^*\gamma^*}$, corresponding to the two helicity states of the meson. We use the same parametrization as in Ref. [76], inspired by quark models,

$$F^{(0)}_{\mathcal{A}\gamma^*\gamma^*}(Q_1^2, Q_2^2) = m_A^2 A(Q_1^2, Q_2^2)\,, \tag{5.18a}$$

$$F^{(1)}_{\mathcal{A}\gamma^*\gamma^*}(Q_1^2, Q_2^2) = -\frac{\nu}{X}\left(\nu + Q_2^2\right) m_A^2 A(Q_1^2, Q_2^2)\,, \tag{5.18b}$$

$$F^{(1)}_{\mathcal{A}\gamma^*\gamma^*}(Q_2^2, Q_1^2) = -\frac{\nu}{X}\left(\nu + Q_1^2\right) m_A^2 A(Q_1^2, Q_2^2)\,, \tag{5.18c}$$

in which $2\nu = m_A^2 + Q_1^2 + Q_2^2$ with m_A the meson mass,

$$\frac{A(Q_1^2, 0)}{A(0,0)} = \frac{1}{(1+Q_1^2/M_A^2)^2}\,, \tag{5.19}$$

and assuming factorization such that $A(Q_1^2, Q_2^2) = A(Q_1^2, 0)A(0, Q_2^2)/A(0,0) = A(Q_2^2, Q_1^2)$. In particular, the form factor $F^{(1)}_{\mathcal{A}\gamma^*\gamma^*}$ is not symmetric in the photon virtualities Q_1^2, Q_2^2. These form factors have been measured by the L3 Collaboration for one real and one virtual photon in the region $Q^2 < 5$ GeV^2 [210, 211] for the isoscalar resonance. Using the previous parametrization, the authors obtain the dipole mass $M_A = 1040(78)$ MeV for the $f_1(1285)$ meson. We obtain the normalization of the form factors from the values given in [77] for the effective two-photon width, defined as

$$\tilde{\Gamma}_{\gamma\gamma} \equiv \lim_{Q_1^2\to 0} \frac{m_A^2}{Q_1^2}\frac{1}{2}\Gamma(\mathcal{A}\to\gamma_L^*\gamma_T) = \frac{\pi\alpha^2}{4}\frac{m_A}{3}\left[F^{(1)}_{\mathcal{A}\gamma^*\gamma^*}(0,0)\right]^2\,, \tag{5.20}$$

and we will consider M_A as a free parameter in our fits.

Tensor mesons

We now turn our attention to the tensor mesons. The singly-virtual form factors of the isoscalar resonance f_2 for helicities $\Lambda = 2, 1, (0, T)$ have also been measured experimentally in the region $Q^2 < 30$ GeV^2 by the Belle Collaboration [209], where the data are compatible

	$\Lambda = 2$	$\Lambda = (0,T)$	$\Lambda = 1$	$\Lambda = (0,L)$
$F^{(\Lambda)}_{\mathcal{T}\gamma^*\gamma^*}(0,0)$	0.500 ± 0.034	0.095 ± 0.011	0.24 ± 0.05	-0.90 ± 0.30

Table 5.4: Table from Ref. [5]: Tensor form factor normalizations for the isoscalar meson $f_2(1270)$. For helicities $\Lambda = 2$ and $\Lambda = (0,T)$ the normalization is obtained using Eq. (5.22) and the measured two-photon decay width. For helicities $\Lambda = 1$ and $\Lambda = (0,L)$ the results are extracted from Ref. [77].

with a dipole form factor [77]. Therefore, we use the following parametrization for all helicities $\Lambda = (0,T), (0,L), 1, 2$,

$$\frac{F^{(\Lambda)}_{\mathcal{T}\gamma^*\gamma^*}(Q_1^2, Q_2^2)}{F^{(\Lambda)}_{\mathcal{T}\gamma^*\gamma^*}(0,0)} = \frac{1}{(1 + Q_1^2/M^2_{T,(\Lambda)})^2 (1 + Q_2^2/M^2_{T,(\Lambda)})^2}\,, \tag{5.21}$$

where we allow for a different dipole mass for each helicity. The normalization of the transverse form factors is computed from the experimentally measured two-photons widths [80], $\Gamma_{\gamma\gamma} = \Gamma^{(0)}_{\gamma\gamma} + \Gamma^{(2)}_{\gamma\gamma}$, assuming that the ratio of helicity 2 to helicity 0 decays is $r = 91.3$ % (see Ref. [212]):

$$\begin{aligned}
\Gamma^{(0)}_{\gamma\gamma} &= \pi\alpha^2\, m_T\, \frac{2}{15}\, \left[F^{(0,T)}_{\mathcal{T}\gamma^*\gamma^*}(0,0)\right]^2\,, \\
\Gamma^{(2)}_{\gamma\gamma} &= \frac{\pi\alpha^2}{4}\, m_T\, \frac{1}{5}\, \left[F^{(2)}_{\mathcal{T}\gamma^*\gamma^*}(0,0)\right]^2\,.
\end{aligned} \tag{5.22}$$

In Ref. [77], the authors obtain the normalization of the two other form factors by saturating two different sum rules involving one real and one virtual photon; their results are summarized in Table 5.4.

Finally, based on large-N arguments reviewed in the full text of Ref. [5], we assume the following relationship between the two-photon decay widths of the isoscalar and isovector mesons,

$$\Gamma_{\gamma\gamma}(f_X) = \frac{25}{9}\, \Gamma_{\gamma\gamma}(a_X)\,. \tag{5.23}$$

In particular, we observe that this approximation works well for the tensor meson, where the two-photon decay widths have been measured both for the isovector and isoscalar mesons (see Table 5.2).

5.4 Fitting the $\gamma^*\gamma^* \to$ hadrons model to the lattice HLbL amplitudes

We fit simultaneously the eight forward light-by-light amplitudes using the phenomenological model described in Sec. 5.3. We have checked that we can reproduce the results given in Refs. [76, 77] in the limit where only one photon is virtual to the quoted accuracy [2] (Tables I and II of [76] and Table III and IV of [77]). Moreover, fits have been checked using two different routines: the Minuit package from CERN [213] and the GSL library [214].

[2] In the second paper, the authors worked in the narrow width approximation.

	M_S	M_A	$M_T^{(2)}$	$M_T^{(0,T)}$	$M_T^{(1)}$	$M_T^{(0,L)}$	χ^2/d.o.f.
E5	1.38(11)	1.26(10)	1.93(3)	2.24(5)	2.36(4)	0.60(10)	4.22
F6	1.12(14)	1.44(5)	1.66(9)	2.17(5)	1.85(14)	0.89(28)	1.15
F7	1.04(18)	1.29(8)	1.61(12)	2.08(7)	2.03(7)	0.57(16)	1.19
G8	1.07(10)	1.36(5)	1.37(24)	2.03(6)	1.63(13)	0.73(14)	1.13
N6	0.86(37)	1.59(3)	1.72(17)	2.19(4)	1.72(18)	0.51(8)	1.35

Table 5.5: Table from Ref. [5]: Results of the simultaneous fit to the eight subtracted amplitudes $\overline{\mathcal{M}}_{TT}$, $\overline{\mathcal{M}}^{\tau}_{TT}$, $\overline{\mathcal{M}}^{a}_{TT}$, $\overline{\mathcal{M}}_{TL}$, $\overline{\mathcal{M}}_{LT}$, $\overline{\mathcal{M}}^{a}_{TL}$, $\overline{\mathcal{M}}^{\tau}_{TL}$ and $\overline{\mathcal{M}}_{LL}$ for the five lattice ensembles. The six mass parameters are given in units of GeV.

5.4.1 Fit of the eight helicity amplitudes

It appears that the five subtracted amplitudes $\overline{\mathcal{M}}_{TT}$, $\overline{\mathcal{M}}^{\tau}_{TT}$, $\overline{\mathcal{M}}^{a}_{TT}$, $\overline{\mathcal{M}}_{TL}$ and $\overline{\mathcal{M}}_{LT}$ are statistically more precise than the three other amplitudes $\overline{\mathcal{M}}^{\tau}_{TL}$, $\overline{\mathcal{M}}^{a}_{TL}$ and $\overline{\mathcal{M}}_{LL}$. Moreover, these last three amplitudes also depend on the longitudinal scalar form factor and on the tensor form factor with helicity $\Lambda = (0, L)$ which are unknown from experiment and for which we use values from phenomenology (see Table 5.4). As shown in the last row of Table 5.6, the contribution from scalar QED is always small and therefore we do not try to fit the associated monopole mass which is explicitly set to the rho mass computed on the lattice. We therefore have six fit parameters, which correspond to the monopole and dipole masses of the scalar (M_S), axial (M_A) and tensor ($M_T^{(2)}, M_T^{(0,T)}, M_T^{(1)}, M_T^{(0,L)}$) mesons. The results are given in Table 5.5, and the corresponding plots for the ensemble F6 are shown in Figs. (5.1 and 5.2. The quoted error on the fit parameters is only statistical and estimated using the jackknife method. The quoted χ^2 correspond to uncorrelated fits. The χ^2 per degree of freedom are slightly above unity, with the exception of the value for ensemble E5. Here we attribute its large value to the fact that the statistical errors are smallest on E5 and that finite-volume effects could be significant for this ensemble. Given that lattice artifacts and finite-size effects are not taken into account by the χ^2, we consider the obtained description of the data on the other ensembles to be satisfactory.

In Table 5.6, we show the relative contribution of each channel to the different amplitudes at $Q_1^2 = 0.352$ GeV^2, $\nu = 0.467$ GeV^2 and for two values of Q_2^2. The amplitudes $\overline{\mathcal{M}}^{a}_{TT}$, $\overline{\mathcal{M}}^{\tau}_{TT}$, $\overline{\mathcal{M}}^{\tau}_{TL}$ and $\overline{\mathcal{M}}^{a}_{TL}$ involve interference cross sections and are not sign-definite: we observe large cancellations between the different contributions. The latter help to stabilize the fit due to the enhanced sensitivity to the relative size of these contributions. In particular, fitting only the amplitudes $\overline{\mathcal{M}}_{TT}$, $\overline{\mathcal{M}}_{TL}$ and $\overline{\mathcal{M}}_{LT}$ leads to unstable fits. Figures 5.5 and 5.6, in addition to displaying the ν-dependence of the amplitudes for two sets of values of (Q_1^2, Q_2^2), show the contributions of the individual mesons. The pseudoscalar and tensor mesons give the dominant contribution to the amplitudes $\overline{\mathcal{M}}_{TT}$, $\overline{\mathcal{M}}^{\tau}_{TT}$ and $\overline{\mathcal{M}}^{a}_{TT}$, which involve two transverse photons. As stated above, the scalar QED contribution is always small, except for $\overline{\mathcal{M}}_{LL}$. The axial form factor is mainly constrained from $\overline{\mathcal{M}}_{TL}$, $\overline{\mathcal{M}}_{LT}$ where the axial and tensor mesons make the dominant contribution; this is clearly visible from Figs. 5.5 and 5.6. It also contributes significantly to the amplitudes $\overline{\mathcal{M}}^{a}_{TL}$ and $\overline{\mathcal{M}}^{\tau}_{TL}$, which involve one transverse and one longitudinal photon. On the other hand, the axial meson does not contribute significantly to the amplitudes $\overline{\mathcal{M}}_{TT}$, $\overline{\mathcal{M}}^{\tau}_{TT}$ and $\overline{\mathcal{M}}^{a}_{TT}$ involving two transverse photons, especially at low virtualities. This suppression is expected since axial mesons have vanishing contribution when at least one photon is real according to the Landau-Yang theorem [215, 216]. Finally, the tensor meson contributes significantly to all amplitudes.

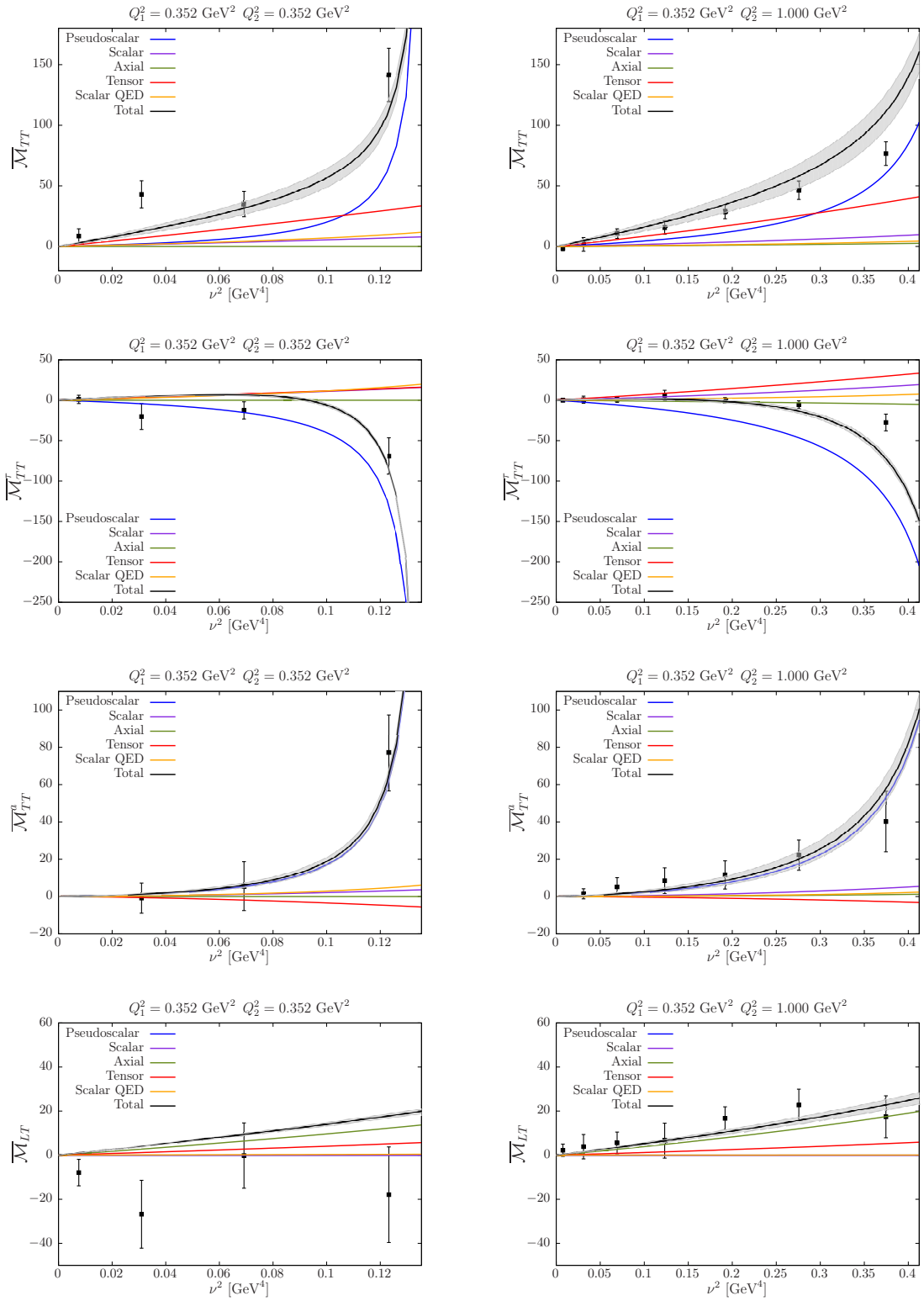

Figure 5.5: Figure from Ref. [5]: The dependence of the amplitudes $\overline{\mathcal{M}}_{TT}$, $\overline{\mathcal{M}}^{\tau}_{TT}$, $\overline{\mathcal{M}}^{a}_{TT}$ and $\overline{\mathcal{M}}_{LT}$ ($\times 10^6$) on ν for two different values of Q_2^2, the virtuality $Q_1^2 = 0.352\text{GeV}^2$ being fixed. The results correspond to the lattice ensemble G8. Note that at fixed photon virtualities, the form factors are completely determined. The black line corresponds to the total contribution and each colored line represents a single-meson contribution.

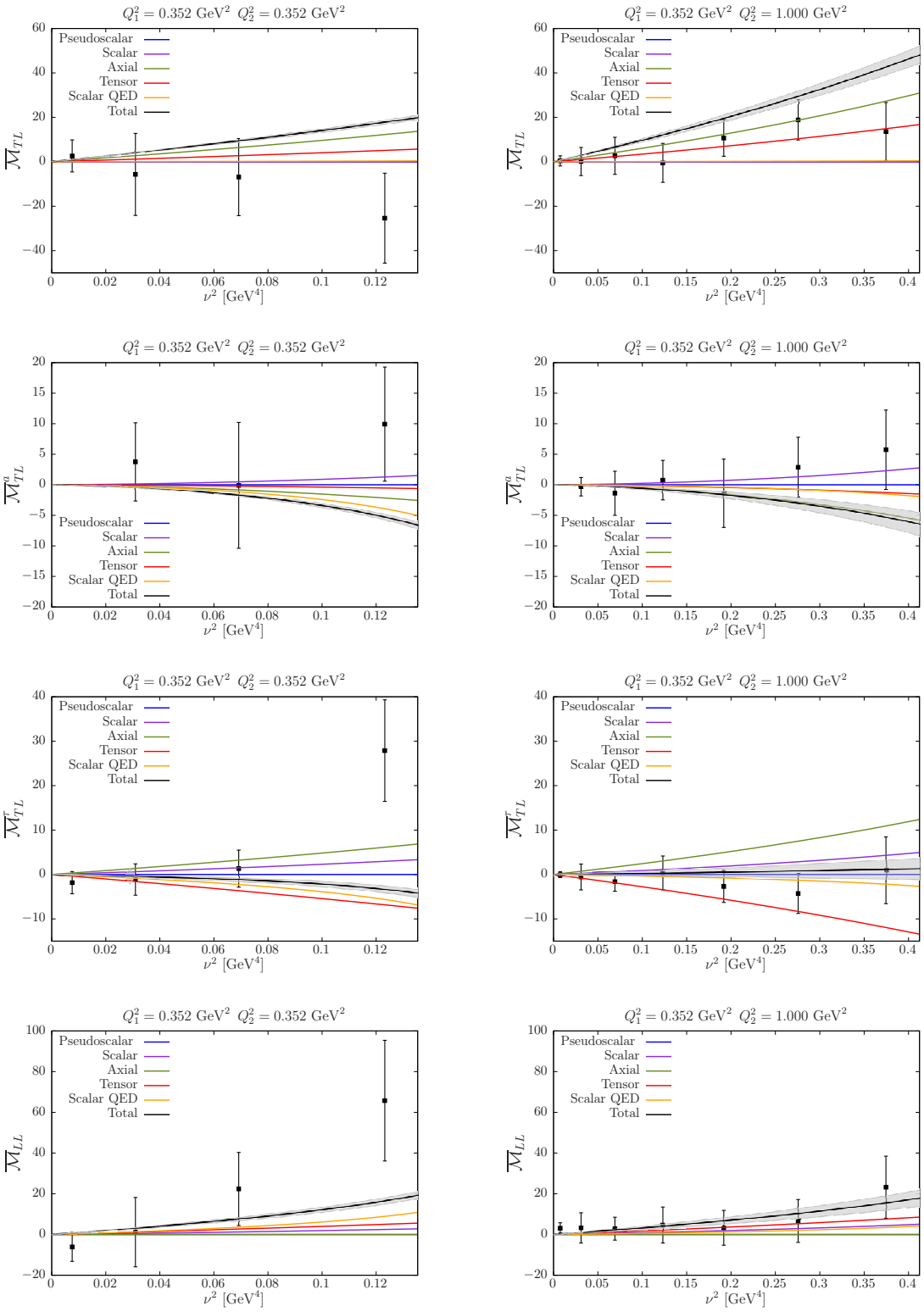

Figure 5.6: Figure from Ref. [5]: The dependence of the amplitudes $\overline{\mathcal{M}}_{TL}$, $\overline{\mathcal{M}}^a_{TL}$, $\overline{\mathcal{M}}^\tau_{TL}$, $\overline{\mathcal{M}}_{LL}$ ($\times 10^6$) on ν for two different values of Q_2^2, the virtuality $Q_1^2 = 0.352\text{GeV}^2$ being fixed. The results correspond to the lattice ensemble G8. Note that at fixed photon virtualities, the form factors are completely determined. The black line corresponds to the total contribution and each colored line represents a single-meson contribution.

	Q_2^2 [GeV^2]	$\overline{\mathcal{M}_{TT}}$	$\overline{\mathcal{M}_{TT}^\tau}$	$\overline{\mathcal{M}_{TT}^a}$	$\overline{\mathcal{M}_{TL}}$	$\overline{\mathcal{M}_{LT}}$	$\overline{\mathcal{M}_{TL}^a}$	$\overline{\mathcal{M}_{TL}^\tau}$	$\overline{\mathcal{M}_{LL}}$
0^{-+}	1.0	35	-56	68	$\times$	$\times$	$\times$	$\times$	$\times$
	3.0	30	-38	61	$\times$	$\times$	$\times$	$\times$	$\times$
0^{++}	1.0	7	11	8	$\times$	$\times$	23	14	42
	3.0	5	6	8	$\times$	$\times$	19	9	50
1^{++}	1.0	2	-2	1	43	57	-43	32	$\times$
	3.0	8	-11	11	21	49	-40	23	$\times$
2^{++}	1.0	53	25	-20	56	42	19	-47	25
	3.0	56	44	19	79	51	-38	-67	40
Scalar	1.0	4	5	3	1	< 1	-15	-7	33
QED	3.0	1	1	1	< 1	< 1	-3	-1	10

Table 5.6: Table from Ref. [5]: Relative contributions in % of each particle to the different amplitudes for the ensemble F7 at $Q_1^2 = 0.352$ GeV^2, $\nu = 0.467$ GeV^2 and for two values of Q_2^2. For each Q_2^2 value, the normalization is such that the absolute values of the entries in a given column add up to 100.

5.4.2 Influence of the non-fitted model parameters

In the previous fit, only the monopole and dipole masses entering the form factors were considered as fit parameters. The other parameters ($p = \Gamma, \Gamma_{\gamma\gamma}, \delta m, \dots$) were fixed using phenomenology as described in Sec. 5.3. However, these parameters are sometimes associated with relatively large experimental errors (δp) or modelled (like the global mass shift in the spectrum where we assume $m_X = m_X^{\text{exp}} + \delta m$ with $\delta m = m_\rho^{lat} - m_\rho^{\text{exp}}$). Therefore, we perform exactly the same fit as in the previous Subsection but using $p \pm \delta p$ instead of p (and varying only one parameter at a time). In this way, we can see the influence of these parameters on the monopole and dipole masses obtained in the previous Subsection. The results are summarized in Table 5.7 for the ensemble F6. In this table, δm corresponds to the global mass shift applied to the spectrum (see Eq. (5.10)), and is multiplied or divided by a factor of two.

We observe that the experimental error on the total decay widths of the particles have a negligible effect. Increasing the two-photon width (or equivalently, the normalization of the form factor) tends to reduce the associated monopole or dipole mass. Finally, increasing the global mass shift by a factor two leads to a noticeable change in the monopole and dipole masses with little change in the χ^2.

Varying the normalization of the form factor $F^{(0,L)}_{\mathcal{T}\gamma^*\gamma^*}$ leads to negligible changes in all parameters but $M_T^{(0,L)}$; this particular correlation is studied in more detail in the next Subsection.

5.4.3 Bounds for the tensor form factor $F^{(0,L)}_{\mathcal{T}\gamma^*\gamma^*}$

The transition form factor $F^{(0,L)}_{\mathcal{T}\gamma^*\gamma^*}$ of the tensor meson enters only the amplitudes $\mathcal{M}_{TL}^\tau$, $\mathcal{M}_{TL}^a$ and $\mathcal{M}_{LL}$, which are less precisely determined on the lattice. In particular the fit is not able to determine both the dipole mass and the normalization independently, and they are highly correlated. To illustrate this point, we use the previously obtained best fit parameters and compute the χ^2/d.o.f. along a scan in the plane $(M_T^{(0,L)}, F^{(0,L)}_{\mathcal{T}\gamma^*\gamma^*}(0,0))$. The results are shown in Fig. 5.7: for a dipole mass of 1 GeV, a normalization $F^{(0,L)}_{\mathcal{T}\gamma^*\gamma^*}(0,0) \approx -0.4$ is favored but the results show a strong dependence on $M_T^{(0,L)}$.

	M_S	M_A	$M_T^{(2)}$	$M_T^{(0,T)}$	$M_T^{(1)}$	$M_T^{(0,L)}$	χ^2/d.o.f.
Principal	1.12(14)	1.44(5)	1.66(9)	2.17(5)	1.85(14)	0.91(7)	1.15
$\Gamma(a_0)$	×	×	×	×	×	×	1.15
	×	×	×	×	×	×	1.15
$\Gamma_{\gamma\gamma}(a_0)$	−0.09	×	×	×	×	×	1.14
	+0.12	×	×	×	×	×	1.15
$\Gamma(a_1)$	−0.01	+0.03	×	+0.01	×	×	1.14
	−0.01	−0.02	+0.01	×	+0.01	×	1.15
$\tilde{\Gamma}_{\gamma\gamma}(a_1)$	×	−0.10	+0.02	−0.01	+0.02	×	1.17
	+0.03	+0.19	−0.01	+0.02	−0.01	×	1.12
$\Gamma(a_2)$	×	×	×	×	×	×	1.15
	×	×	×	×	×	×	1.15
$F^{(2)}_{\mathcal{T}\gamma^*\gamma^*}$	−0.01	×	−0.06	+0.01	×	×	1.15
	×	×	+0.08	×	+0.01	×	1.14
$F^{(0,T)}_{\mathcal{T}\gamma^*\gamma^*}$	−0.08	×	−0.01	−0.09	−0.01	×	1.13
	+0.08	×	+0.02	+0.11	+0.02	×	1.17
$F^{(1)}_{\mathcal{T}\gamma^*\gamma^*}$	×	×	×	×	−0.14	×	1.14
	−0.01	×	×	×	+0.21	×	1.15
$\delta m^{\times 2}_{\times 0.5}$	+0.20	+0.13	+0.11	+0.13	+0.14	+0.10	1.17
	−0.10	−0.06	−0.05	−0.08	−0.06	−0.05	1.15

Table 5.7: Table from Ref. [5]: Fit variations for F6. The first row corresponds to the results obtained in the previous Subsection. Then, each row corresponds to a new fit using $p \pm \delta p$ and varying only one parameter at a time: the quoted number is the shift observed for the monopole/dipole mass, in units of GeV. A cross indicates that the parameter remains unchanged to all indicated digits of the central values in the first row. For instance, using $\Gamma_{\gamma\gamma}(a_0) + \delta\Gamma_{\gamma\gamma}(a_0)$ instead of $\Gamma_{\gamma\gamma}(a_0)$, the scalar monopole mass is shifted by −0.09 GeV, the other monopole/dipole masses being unaffected. In the last row, the mass shift δm applied to the spectrum (see Eq. (5.10)) is varied by a factor of two.

5.5 Conclusions

With the hadronic light-by-light contribution to the muon anomalous magnetic moment a_μ^{HLbL} in mind, we have studied the eight forward light-by-light amplitudes for spacelike photons in $N_f = 2$ lattice QCD. Via dispersive sum rules, we have tested whether the type of hadronic models used to estimate a_μ^{HLbL} provides a good description of lattice results. All in all, we found that by fitting the virtuality dependence of six meson transition form factors, we were able to describe the lattice data within statistical uncertainties. The monopole and dipole masses parametrizing the transition form factors compare reasonably well in magnitude with phenomenological determinations for the $I = 0$ isospin partner, with the notable exception of the dipole masses of the tensor meson for helicities $\Lambda = 1$ and $\Lambda = (0, T)$, where we find that the form factors fall off far more slowly. The simultaneous fit to all eight amplitudes allowed us to test the individual relevance of the various resonance contributions, given that they appear with different weights and signs in different amplitudes. Thus our study provides evidence, by a completely independent method, that the resonance-exchange model widely used in calculating a_μ^{HLbL} is not missing a large contribution.

We regard the present calculation as exploratory, and leave a more quantitative comparison

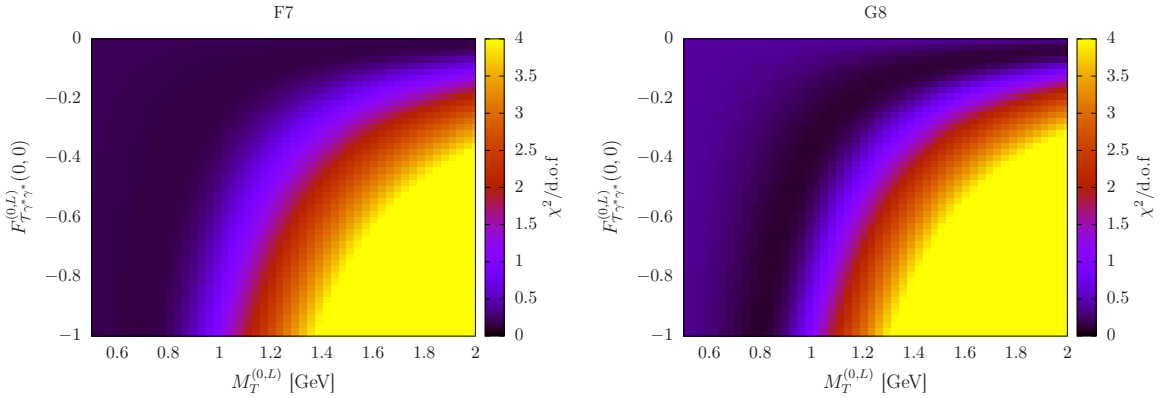

Figure 5.7: Figure from Ref. [5]: Value of χ^2/d.o.f. for different dipole masses and form factor normalizations (tensor form factor, helicity $\Lambda = (0, L)$). Left: ensemble F7, right: ensemble G8.

of monopole and dipole masses, including an estimate of systematic errors, for the future. Indeed we were only able to perform stable fits by making model assumptions, for instance about the masses of the lightest resonances in the scalar, axial-vector and tensor sectors in $N_f = 2$ QCD at non-physical quark masses. In addition to neglecting the three classes of diagrams containing at least one isolated vector current insertion in a quark loop, we had to assume various relations between the two-photon decay widths of isospin-partner resonances that are justified only for a large number of colors N. Also, the employed parametrization of the axial-vector resonance form factors is a further vulnerable assumption.

Appendices

5.A Cross sections $\gamma^*\gamma^* \to X$

This Appendix is from Ref. [5], which in turn is based on the Appendix of Ref. [76]. We collect the relevant formulae needed to evaluate the sum rules in the general case with two virtual photons.

The metric tensor of the subspace orthogonal to q_1 and q_2 is given by

$$R^{\mu\nu}(q_1, q_2) = -g^{\mu\nu} + \frac{1}{X}\left\{(q_1 \cdot q_2)\,(q_1^\mu\, q_2^\nu + q_2^\mu\, q_1^\nu) - q_1^2\, q_2^\mu\, q_2^\nu - q_2^2\, q_1^\mu\, q_1^\nu\right\}, \tag{5.24}$$

such that $R_{\mu\nu} q_i^\nu = 0$ for $i = 1, 2$. It satisfies $R^{\mu\nu} = R^{\nu\mu}$, $R^\mu{}_\mu = 2$ and $R^\mu{}_\alpha R^{\alpha\nu} = -R^{\mu\nu}$. We use the 'mostly minus' metric convention. The virtual photon flux factor is defined through $X = (q_1 \cdot q_2)^2 - q_1^2 q_2^2 = \nu^2 - Q_1^2 Q_2^2$ with the crossing-symmetric variable ν given by $\nu = q_1 \cdot q_2$

The vectors k_i are defined by

$$k_1 = \sqrt{\frac{-q_1^2}{X}}\left(q_2 - \frac{q_1 \cdot q_2}{q_1^2} q_1\right), \quad k_2 = \sqrt{\frac{-q_2^2}{X}}\left(q_1 - \frac{q_1 \cdot q_2}{q_1^2} q_2\right), \tag{5.25}$$

and satisfy $k_i^2 = 1$, $k_i \cdot q_i = 0$.

Finally, the helicity amplitudes for the $\gamma^*(\lambda_1, q_1)\gamma^*(\lambda_2, q_2) \to X(p_X)$ fusion process are related to the Feynman amplitudes by

$$\mathcal{M}(\lambda_1, \lambda_2) = \mathcal{M}_{\mu\nu}\; \epsilon_1^\mu(\lambda_1)\; \epsilon_2^\nu(\lambda_2)\,. \tag{5.26}$$

5.A.1 Pseudoscalar mesons

The transition $\gamma^*(q_1,\lambda_1)+\gamma^*(q_2,\lambda_2)\to\mathcal{P}$, where $\mathcal{P}$ is a pseudoscalar state, is described by the following amplitude:

$$\mathcal{M}(\lambda_1,\lambda_2) = -i\,e^2\,\varepsilon_{\mu\nu\alpha\beta}\,\varepsilon^\mu(q_1,\lambda_1)\,\varepsilon^\nu(q_2,\lambda_2)\,q_1^\alpha\,q_2^\beta\,F_{\mathcal{P}\gamma^*\gamma^*}(Q_1^2,Q_2^2)\,, \tag{5.27}$$

where $\varepsilon^\mu(q_1,\lambda_1)$ and $\varepsilon^\nu(q_2,\lambda_2)$ are the polarization vectors of the virtual photons with helicities $\lambda_1,\lambda_2=0,\pm1$. The only non-zero helicity amplitudes, which we define in the rest frame of the produced meson, are given by :

$$\mathcal{M}(+1,+1) = -\mathcal{M}(-1,-1) = e^2\,\sqrt{X}\,F_{\mathcal{P}\gamma^*\gamma^*}(Q_1^2,Q_2^2)\,. \tag{5.28}$$

The two-photon decay width is given by

$$\Gamma_{\gamma\gamma} = \frac{\pi\alpha^2}{4}m_P^3\left[F_{\mathcal{P}\gamma^*\gamma^*}(0,0)\right]^2\,, \tag{5.29}$$

and from Eqs. (5.2) and (5.8)

$$\begin{aligned}\sigma_0=\sigma_\perp=2\sigma_{TT}=2\tau_{TT}^a=-\tau_{TT}=16\pi^2\delta(s-m_P^2)\frac{\Gamma_{\gamma\gamma}}{m_P}\frac{2\sqrt{X}}{m_P^2}\left[\frac{F_{\mathcal{P}\gamma^*\gamma^*}(Q_1^2,Q_2^2)}{F_{\mathcal{P}\gamma^*\gamma^*}(0,0)}\right]^2\,,\\ \sigma_{LL}=\sigma_{TL}=\sigma_{LT}=\tau_{TL}=\tau_{TL}^a=0\,.\end{aligned} \tag{5.30}$$

5.A.2 Scalar mesons

The transition $\gamma^*(q_1,\lambda_1)+\gamma^*(q_2,\lambda_2)\to\mathcal{S}$ where $\mathcal{S}$ is a scalar state can be parameterized by one transverse ($F^T_{\mathcal{A}\gamma^*\gamma^*}$) and one longitudinal ($F^L_{\mathcal{A}\gamma^*\gamma^*}$) form factor and is described by the following matrix element

$$\begin{aligned}\mathcal{M}(\lambda_1,\lambda_2) &= e^2\,\varepsilon_\mu(q_1,\lambda_1)\,\varepsilon_\nu(q_2,\lambda_2)\\ &\times \left(\frac{\nu}{m_S}\right)\left\{-R^{\mu\nu}(q_1,q_2)F^T_{\mathcal{S}\gamma^*\gamma^*}(Q_1^2,Q_2^2)+\frac{\nu}{X}\left(q_1^\mu+\frac{Q_1^2}{\nu}q_2^\mu\right)\left(q_2^\nu+\frac{Q_2^2}{\nu}q_1^\nu\right)F^L_{\mathcal{S}\gamma^*\gamma^*}(Q_1^2,Q_2^2)\right\}.\end{aligned}$$

The only non-zero helicity amplitudes are given by

$$\begin{aligned}\mathcal{M}(+1,+1) &= \mathcal{M}(-1,-1)=e^2\,\frac{\nu}{m_S}\,F^T_{\mathcal{S}\gamma^*\gamma^*}(Q_1^2,Q_2^2)\,,\\ \mathcal{M}(0,0) &= -e^2\,\frac{Q_1Q_2}{m_S}\,F^L_{\mathcal{S}\gamma^*\gamma^*}(Q_1^2,Q_2^2)\,.\end{aligned} \tag{5.31}$$

The two-photon decay width is given by

$$\Gamma_{\gamma\gamma} = \frac{\pi\alpha^2}{4}m_S\left[F^T_{\mathcal{S}\gamma^*\gamma^*}(0,0)\right]^2\,, \tag{5.32}$$

and from Eqs. (5.2) and (5.8)

$$\begin{aligned}\sigma_0=\sigma_\parallel=2\sigma_{TT}=2\tau_{TT}^a=\tau_{TT}=16\pi^2\delta(s-m_S^2)\frac{\Gamma_{\gamma\gamma}}{m_S}\frac{2\nu^2}{m_S^2\sqrt{X}}\left[\frac{F^T_{\mathcal{S}\gamma^*\gamma^*}(Q_1^2,Q_2^2)}{F^T_{\mathcal{S}\gamma^*\gamma^*}(0,0)}\right]^2\,,\\ \sigma_{LL}=16\pi^2\delta(s-m_S^2)\frac{\Gamma_{\gamma\gamma}}{m_S}\frac{2Q_1^2Q_2^2}{m_S^2\sqrt{X}}\left[\frac{F^L_{\mathcal{S}\gamma^*\gamma^*}(Q_1^2,Q_2^2)}{F^T_{\mathcal{S}\gamma^*\gamma^*}(0,0)}\right]^2\,,\\ \tau_{TL}=\tau_{TL}^a=-16\pi^2\delta(s-m_S^2)\frac{\Gamma_{\gamma\gamma}}{m_S}\frac{Q_1Q_2}{m_S}\frac{\nu}{m_S\sqrt{X}}\frac{F^T_{\mathcal{S}\gamma^*\gamma^*}(Q_1^2,Q_2^2)F^L_{\mathcal{S}\gamma^*\gamma^*}(Q_1^2,Q_2^2)}{\left[F^T_{\mathcal{S}\gamma^*\gamma^*}(0,0)\right]^2}\,.\end{aligned} \tag{5.33}$$

5.A.3 Axial mesons

The transition $\gamma^*(q_1,\lambda_1) + \gamma^*(q_2,\lambda_2) \to \mathcal{A}(p_A,\Lambda)$, where $\mathcal{A}$ is an axial-vector state, can be parameterized by two form factors $F^{(0)}_{\mathcal{A}\gamma^*\gamma^*}$ and $F^{(1)}_{\mathcal{A}\gamma^*\gamma^*}$, where the superscript indicates the helicity state (Λ) of the axial-vector meson

$$\begin{aligned}
\mathcal{M}(\lambda_1,\lambda_2;\Lambda) &= e^2\,\varepsilon_\mu(q_1,\lambda_1)\,\varepsilon_\nu(q_2,\lambda_2)\,\varepsilon^{\alpha *}(p_f,\Lambda) \\
&\times\; i\,\varepsilon_{\rho\sigma\tau\alpha}\left\{R^{\mu\rho}(q_1,q_2)R^{\nu\sigma}(q_1,q_2)\,(q_1-q_2)^\tau\,\frac{\nu}{m_A^2}\,F^{(0)}_{\mathcal{A}\gamma^*\gamma^*}(Q_1^2,Q_2^2)\right. \\
&\quad + R^{\nu\rho}(q_1,q_2)\left(q_1^\mu + \frac{Q_1^2}{\nu}q_2^\mu\right) q_1^\sigma\, q_2^\tau\,\frac{1}{m_A^2}\,F^{(1)}_{\mathcal{A}\gamma^*\gamma^*}(Q_1^2,Q_2^2) \\
&\quad \left. + R^{\mu\rho}(q_1,q_2)\left(q_2^\nu + \frac{Q_2^2}{\nu}q_1^\nu\right) q_2^\sigma\, q_1^\tau\,\frac{1}{m_A^2}\,F^{(1)}_{\mathcal{A}\gamma^*\gamma^*}(Q_2^2,Q_1^2)\right\}. \qquad (5.34)
\end{aligned}$$

The only non-zero helicity amplitudes are given by

$$\begin{aligned}
\mathcal{M}(+1,+1;\Lambda=0) = -\mathcal{M}(-1,-1;\Lambda=0) &= e^2\,(Q_1^2-Q_2^2)\,\frac{\nu}{m_A^3}\,F^{(0)}_{\mathcal{A}\gamma^*\gamma^*}(Q_1^2,Q_2^2)\,, \\
\mathcal{M}(0,+1;\Lambda=-1) &= -\,e^2\,Q_1\left(\frac{X}{\nu m_A^2}\right)F^{(1)}_{\mathcal{A}\gamma^*\gamma^*}(Q_1^2,Q_2^2)\,, \\
\mathcal{M}(-1,0;\Lambda=-1) &= -\,e^2\,Q_2\left(\frac{X}{\nu m_A^2}\right)F^{(1)}_{\mathcal{A}\gamma^*\gamma^*}(Q_2^2,Q_1^2)\,. \qquad (5.35)
\end{aligned}$$

In this case, the equivalent two-photon width is defined by

$$\tilde{\Gamma}_{\gamma\gamma} \equiv \lim_{Q_1^2\to 0}\frac{m_A^2}{Q_1^2}\frac{1}{2}\Gamma(\mathcal{A}\to\gamma_L^*\gamma_T) = \frac{\pi\alpha^2}{4}\frac{m_A}{3}\left[F^{(1)}_{\mathcal{A}\gamma^*\gamma^*}(0,0)\right]^2, \qquad (5.36)$$

and from Eqs. (5.2) and (5.8)

$$\begin{aligned}
\sigma_0 = \sigma_\perp = 2\sigma_{TT} = 2\tau^a_{TT} = -\tau_{TT} &= 16\pi^2\delta(s-m_A^2)\frac{3\tilde{\Gamma}_{\gamma\gamma}}{m_A}\frac{(Q_1^2-Q_2^2)^2}{m_A^4}\frac{2\nu^2}{m_A^2\sqrt{X}}\left[\frac{F^{(0)}_{\mathcal{A}\gamma^*\gamma^*}(Q_1^2,Q_2^2)}{F^{(1)}_{\mathcal{A}\gamma^*\gamma^*}(0,0)}\right]^2, \\
\sigma_{LT} &= 16\pi^2\delta(s-m_A^2)\frac{3\tilde{\Gamma}_{\gamma\gamma}}{m_A}\frac{2X\sqrt{X}}{\nu^2 m_A^2}\frac{Q_1^2}{m_A^2}\left[\frac{F^{(1)}_{\mathcal{A}\gamma^*\gamma^*}(Q_1^2,Q_2^2)}{F^{(1)}_{\mathcal{A}\gamma^*\gamma^*}(0,0)}\right]^2, \\
\sigma_{TL} &= 16\pi^2\delta(s-m_A^2)\frac{3\tilde{\Gamma}_{\gamma\gamma}}{m_A}\frac{2X\sqrt{X}}{\nu^2 m_A^2}\frac{Q_2^2}{m_A^2}\left[\frac{F^{(1)}_{\mathcal{A}\gamma^*\gamma^*}(Q_2^2,Q_1^2)}{F^{(1)}_{\mathcal{A}\gamma^*\gamma^*}(0,0)}\right]^2, \\
\tau_{TL} = -\tau^a_{TL} &= 16\pi^2\delta(s-m_A^2)\frac{3\tilde{\Gamma}_{\gamma\gamma}}{m_A}\frac{Q_1Q_2}{m_A^2}\frac{X\sqrt{X}}{\nu^2 m_A^2}\left[\frac{F^{(1)}_{\mathcal{A}\gamma^*\gamma^*}(Q_1^2,Q_2^2)}{F^{(1)}_{\mathcal{A}\gamma^*\gamma^*}(0,0)}\frac{F^{(1)}_{\mathcal{A}\gamma^*\gamma^*}(Q_2^2,Q_1^2)}{F^{(1)}_{\mathcal{A}\gamma^*\gamma^*}(0,0)}\right], \\
\sigma_{LL} &= 0\,. \qquad (5.37)
\end{aligned}$$

5.A.4 Tensor mesons

The transition $\gamma^*(q_1,\lambda_1)+\gamma^*(q_2,\lambda_2)\to\mathcal{T}(\Lambda)$ where $\mathcal{T}$ is a tensor state with helicity $\Lambda=\pm2,\pm1,0$ can be parameterized by four form factors $T^{(\Lambda)}$,

$$\begin{aligned}
\mathcal{M}(\lambda_1,\lambda_2;\Lambda) &= e^2\,\varepsilon_\mu(q_1,\lambda_1)\,\varepsilon_\nu(q_2,\lambda_2)\,\varepsilon^*_{\alpha\beta}(p_f,\Lambda)\\
&\times \left\{\left[R^{\mu\alpha}(q_1,q_2)R^{\nu\beta}(q_1,q_2)+\frac{s}{8X}\,R^{\mu\nu}(q_1,q_2)(q_1-q_2)^\alpha\,(q_1-q_2)^\beta\right]\,\frac{\nu}{m_T}\,F^{(2)}_{\mathcal{T}\gamma^*\gamma^*}(Q_1^2,Q_2^2)\right.\\
&\quad + R^{\nu\alpha}(q_1,q_2)(q_1-q_2)^\beta\left(q_1^\mu+\frac{Q_1^2}{\nu}q_2^\mu\right)\,\frac{1}{m_T}\,F^{(1)}_{\mathcal{T}\gamma^*\gamma^*}(Q_1^2,Q_2^2)\\
&\quad + R^{\mu\alpha}(q_1,q_2)(q_2-q_1)^\beta\left(q_2^\nu+\frac{Q_2^2}{\nu}q_1^\nu\right)\,\frac{1}{m_T}\,F^{(1)}_{\mathcal{T}\gamma^*\gamma^*}(Q_2^2,Q_1^2)\\
&\quad + R^{\mu\nu}(q_1,q_2)(q_1-q_2)^\alpha\,(q_1-q_2)^\beta\,\frac{1}{m_T}\,F^{(0,T)}_{\mathcal{T}\gamma^*\gamma^*}(Q_1^2,Q_2^2)\\
&\quad \left.+\left(q_1^\mu+\frac{Q_1^2}{\nu}q_2^\mu\right)\left(q_2^\nu+\frac{Q_2^2}{\nu}q_1^\nu\right)(q_1-q_2)^\alpha(q_1-q_2)^\beta\,\frac{1}{m_T^3}\,F^{(0,L)}_{\mathcal{T}\gamma^*\gamma^*}(Q_1^2,Q_2^2)\right\}, \qquad (5.38)
\end{aligned}$$

where $\varepsilon_{\alpha\beta}(p_f,\Lambda)$ is the polarization tensor for the tensor meson with four-momentum p_f and helicity Λ. The different non-vanishing helicity amplitudes are

$$\begin{aligned}
\mathcal{M}(+1,-1;\Lambda=+2)=\mathcal{M}(-1,+1;\Lambda=-2) &= e^2\,\frac{\nu}{m_T}\,F^{(2)}_{\mathcal{T}\gamma^*\gamma^*}(Q_1^2,Q_2^2)\,,\\
\mathcal{M}(0,+1;\Lambda=-1) &= -e^2\,Q_1\,\frac{1}{\sqrt{2}}\left(\frac{2X}{\nu m_T^2}\right)\,F^{(1)}_{\mathcal{T}\gamma^*\gamma^*}(Q_1^2,Q_2^2)\,,\\
\mathcal{M}(-1,0;\Lambda=-1) &= -e^2\,Q_2\,\frac{1}{\sqrt{2}}\left(\frac{2X}{\nu m_T^2}\right)\,F^{(1)}_{\mathcal{T}\gamma^*\gamma^*}(Q_2^2,Q_1^2)\,,\\
\mathcal{M}(+1,+1;\Lambda=0)=\mathcal{M}(-1,-1;\Lambda=0) &= -e^2\,\sqrt{\frac{2}{3}}\left(\frac{4X}{m_T^3}\right)\,F^{(0,T)}_{\mathcal{T}\gamma^*\gamma^*}(Q_1^2,Q_2^2)\,,\\
\mathcal{M}(0,0;\Lambda=0) &= -e^2\,Q_1Q_2\,\sqrt{\frac{2}{3}}\left(\frac{4X^2}{\nu^2 m_T^5}\right)\,F^{(0,L)}_{\mathcal{T}\gamma^*\gamma^*}(Q_1^2,Q_2^2)\,. \qquad (5.39)
\end{aligned}$$

The two-photon decay widths for helicities $\Lambda=0,2$ are respectively given by

$$\begin{aligned}
\Gamma^{(0)}_{\gamma\gamma} &= \pi\alpha^2\,m_T\,\frac{2}{15}\,\left[F^{(0,T)}_{\mathcal{T}\gamma^*\gamma^*}(0,0)\right]^2\,,\\
\Gamma^{(2)}_{\gamma\gamma} &= \frac{\pi\alpha^2}{4}\,m_T\,\frac{1}{5}\,\left[F^{(2)}_{\mathcal{T}\gamma^*\gamma^*}(0,0)\right]^2\,. \qquad (5.40)
\end{aligned}$$

and from Eqs. (5.2) and (5.8)

$$\sigma_0 = 16\pi^2\delta(s-m_T^2)\frac{5\tilde{\Gamma}^{(0)}_{\gamma\gamma}}{m_T}\frac{8X\sqrt{X}}{m_T^6}\left[\frac{F^{(0,T)}_{\mathcal{T}\gamma^*\gamma^*}(Q_1^2,Q_2^2)}{F^{(0,T)}_{\mathcal{T}\gamma^*\gamma^*}(0,0)}\right]^2,$$

$$\sigma_2 = 16\pi^2\delta(s-m_T^2)\frac{5\tilde{\Gamma}^{(2)}_{\gamma\gamma}}{m_T}\frac{2\nu^2}{m_T^2\sqrt{X}}\left[\frac{F^{(2)}_{\mathcal{T}\gamma^*\gamma^*}(Q_1^2,Q_2^2)}{F^{(2)}_{\mathcal{T}\gamma^*\gamma^*}(0,0)}\right]^2,$$

$$\sigma_\parallel = \sigma_0 + \frac{\sigma_2}{2},$$

$$\sigma_\perp = \frac{\sigma_2}{2},$$

$$\sigma_{LT} = 16\pi^3\delta(s-m_T^2)\alpha^2\frac{Q_1^2}{m_T^2}\frac{X\sqrt{X}}{\nu^2 m_T^2}\left[F^{(1)}_{\mathcal{T}\gamma^*\gamma^*}(Q_1^2,Q_2^2)\right]^2,$$

$$\sigma_{TL} = 16\pi^3\delta(s-m_T^2)\alpha^2\frac{Q_2^2}{m_T^2}\frac{X\sqrt{X}}{\nu^2 m_T^2}\left[F^{(1)}_{\mathcal{T}\gamma^*\gamma^*}(Q_2^2,Q_1^2)\right]^2,$$

$$\tau_{TL} = 16\pi^3\delta(s-m_T^2)\alpha^2\frac{X\sqrt{X}}{\nu^2 m_T^2}\frac{Q_1Q_2}{m_T^2}\left[\frac{2}{3}\frac{4X}{m_T^4}F^{(0,T)}_{\mathcal{T}\gamma^*\gamma^*}(Q_1^2,Q_2^2)F^{(0,L)}_{\mathcal{T}\gamma^*\gamma^*}(Q_1^2,Q_2^2)\right.$$
$$\left.-\frac{1}{2}F^{(1)}_{\mathcal{T}\gamma^*\gamma^*}(Q_1^2,Q_2^2)F^{(1)}_{\mathcal{T}\gamma^*\gamma^*}(Q_2^2,Q_1^2)\right],$$

$$\tau^a_{TL} = 16\pi^3\delta(s-m_T^2)\alpha^2\frac{X\sqrt{X}}{\nu^2 m_T^2}\frac{Q_1Q_2}{m_T^2}\left[\frac{2}{3}\frac{4X}{m_T^4}F^{(0,T)}_{\mathcal{T}\gamma^*\gamma^*}(Q_1^2,Q_2^2)F^{(0,L)}_{\mathcal{T}\gamma^*\gamma^*}(Q_1^2,Q_2^2)\right.$$
$$\left.+\frac{1}{2}F^{(1)}_{\mathcal{T}\gamma^*\gamma^*}(Q_1^2,Q_2^2)F^{(1)}_{\mathcal{T}\gamma^*\gamma^*}(Q_2^2,Q_1^2)\right],$$

$$\sigma_{LL} = 16\pi^3\delta(s-m_T^2)\alpha^2\frac{Q_1^2Q_2^2}{m_T^4}\frac{16}{3}\frac{X^3\sqrt{X}}{\nu^4 m_T^6}\left[F^{(0,L)}_{\mathcal{T}\gamma^*\gamma^*}(Q_2^2,Q_1^2)\right]^2.$$

Chapter 6

Summary and conclusions

The results described in this thesis can be summarized, in the order of presentation, as follows.

■ **Evaluation of the forward CS off protons.**

We evaluated the forward Compton scattering off the proton, based on Kramers-Kronig kind of relations which express the Compton amplitudes in terms of integrals of total photoabsorption cross sections. This allowed us to obtain the following:

- Updated evaluation of the **proton polarizabilities sum rules**.

  Most notably, for the sum of proton electric and magnetic dipole polarizabilities governed by the Baldin sum rule, we obtain the following updated average (between our two fits):

$$\alpha^p_{E_1} + \beta^p_{M_1} = 14.0(2) \times 10^{-4} \text{ fm}^3.$$

  An analogous sum rule involving the quadrupole polarizabilities of the proton is evaluated too, as well as the GDH and the FSP sum rules. For the GDH integral, we obtain 204.5(21.4) μb, in agreement with the sum rule prediction 204.784481(4) μb. For the FSPs, we obtain $\gamma_0 = -92.9(10.5) \times 10^{-6}$ fm^4 and $\bar{\gamma_0} = 48.4(8.2) \times 10^{-6}$ fm^6, improving on the accuracy of previous evaluations.

- First-time evaluation of both f **and** g **forward CS amplitudes**.

  Both the spin-averaged (f) and the spin-dependent (g) forward amplitudes of proton Compton scattering are evaluated in a broad energy range. The results are in agreement with previous evaluations, χPT predictions, and the only currently available experimental data point for the f amplitude at 2.2 GeV.

- First-time evaluation of the **forward CS observables**.

  The two amplitudes contain all the information about the forward CS process and we hence have reconstructed the two observables: the CS differential cross section at zero scattering angle and the Σ_{2z} asymmetry. These two are again in remarkable agreement with the χPT low-energy prediction. Being inaccessible in a direct CS experiment, the forward observables, obtained in the model-independent way, can serve as an important additional constraint when fitting the angle-dependent data.

■ **Direct access to the forward CS via di-lepton photoproduction.**

We showed how to experimentally measure the near-forward CS amplitude by exploiting the di-lepton photoproduction process with the arising interference between the competing TCS and Bethe-Heitler (BH) processes at the appropriate kinematics with both the four-momentum transfer $-t$ and the lepton pair mass M_{ll} sufficiently low. The interference term is accessed through the forward-backward asymmetry (A_{FB}) — the asymmetry of the outgoing leptons interchanged in the di-lepton photoproduction process.

- Evaluation of the **TCS − BH interference**.

We explicitly presented the evaluation of the tree-level BH – TCS interference term for the case of the spin-averaged amplitude, with the assumption of the vanishingly small $-t$ and M_{ll}.

- Estimates of $\boldsymbol{A_{FB}}$ **for** $\boldsymbol{\gamma p \to e^+e^-p}$ **at JLab and EIC**.

  We presented estimates of the A_{FB} for the di-lepton photoproduction on the proton at the appropriate kinematics at JLab and EIC and showed that with a reasonable precision it would be possible, in particular, to distinguish between different state-of-the-art fits to the total photoabsorption cross section off the proton, while the latter are connected to the forward CS amplitude through the dispersion relations. We argued that the sufficiently high energy measurement of the asymmetry could provide a clue on the correct model for the high-energy asymptotic behaviour and the rate of the Froissart bound saturation.

■ **Estimates of the quarkonium – proton forward scattering amplitudes.**

Similarly, we conducted a study of the forward J/ψ-p and Υ-p scattering amplitudes by relating these processes to the photoproduction of the corresponding quarkonia off the proton via VMD assumption.

- Extraction of the $\boldsymbol{J/\psi}$ **binding energy in nuclear matter**.

  We provided an updated analysis of the forward J/ψ-p scattering amplitude, relating its imaginary part to $\gamma p \to J/\psi p$ and $\gamma p \to c\bar{c}X$ cross section data, and calculating its real part through a once-subtracted dispersion relation. From a global fit to both differential and total cross section data, we extracted a value for the spin-averaged J/ψ-p s-wave scattering length $a_{\psi p} = 0.046(5)$ fm, which can be translated into a J/ψ binding energy in nuclear matter

$$B_\psi = 2.7(3) \text{ MeV}.$$

- Estimates of $\boldsymbol{A_{FB}}$ **for** $\boldsymbol{\gamma p \to J/\psi p \to e^+e^-p}$ **at JLab**.

  We estimated the forward-backward asymmetry to the $\gamma p \to e^-e^+p$ process around the J/ψ resonance. We showed that to good approximation this asymmetry depends linearly on $a_{\psi p}$, and can reach values around -25% for forthcoming J/ψ threshold production experiments at JLab. Its measurement can thus provide a very sensitive observable for a refined extraction of $a_{\psi p}$.

- Predictions for the $\boldsymbol{\Upsilon}$ **binding energy extraction sensitivity at an EIC**.

  Using a similar technique of fitting the corresponding photoproduction data, we performed a feasibility study for Υ photoproduction experiments at an EIC and discussed the sensitivity and precision that can be reached in the extraction of the Υ-p scattering length. For our most reasonable scenario we estimated the scattering length to take a value of $a_{\Upsilon p} = 0.066(3)$ fm, corresponding to the binding energy in nuclear matter $B_\Upsilon = 3.23(16)$ MeV, with the uncertainties based on the higher energy beam setting data generated for the EIC.

■ **Model fit to the lattice QCD calculation of the forward HLbL.**

We compared the dispersive model prediction of the eight forward HLbL amplitudes to the first-principles lattice QCD computation. By performing a complex fit with free parameters of the model to the lattice data, we provided an additional approach to constrain the phenomenological estimates of a_μ^{HLbL}, as well as to test the validity of lattice QCD computations in view of resolving the ongoing a_μ discrepancy between theory and experiment, while awaiting for the upcoming improved precision results from Fermilab and J-PARC.

As an overall conclusion, one may say that the presented data-driven approach of predicting or constraining the related quantities based on the very basic properties of QFT (or, more specifically, the S-matrix) up to date, while sometimes overlooked, remains a very powerful and promising tool in the area of hadron physics, where the direct calculations are mostly notoriously impracticable. In many cases it appears to be possible to find the required solid ground for phenomenological model calculations, as we have shown in particular cases of our study of the TCS as involved in the di-lepton photoproduction, the quarkonium – proton scattering and the HLbL processes.

That said, in the context of an outlook for our research, we may mention several natural topics of interest, for which the results of this thesis may serve as a basis. One of the straightforward and major additions to our study of the CS is its extension to the scattering off the neutron. A suitable experimental substitute for the neutron in this case could be the polarized ^{3}He target [26, 217]. The helicity-dependent total inclusive ^{3}He cross section was measured with circularly polarized photons in the energy range $200 < \nu < 500$ MeV at MAMI [218]. The study of the threshold quarkonium photoproduction could be additionally extended in multiple ways. One notable attempt for the ϕ meson case was already initiated, but was right-away limited by the current noisy cross section database, and a full absence of the data for the open strange production $\gamma p \to s\bar{s}X$ cross section. In addition, an analysis for the forward-backward asymmetry measurement of the di-lepton photoproduction for the Υ case could be performed for the existing and upcoming experiments. For the obtained asymmetry estimates it may be important to consider the higher-order corrections to the Bethe-Heitler amplitude, as for now we have only accounted for the tree-level contribution. The leading-order corrections were recently calculated in Ref. [219] and could be readily employed for our cases.

Bibliography

[1] J. Green, O. Gryniuk, G. von Hippel, H. B. Meyer, and V. Pascalutsa, "Lattice QCD calculation of hadronic light-by-light scattering", Phys. Rev. Lett. **115**, 222003 (2015), arXiv:1507.01577 [hep-lat].

[2] O. Gryniuk, F. Hagelstein, and V. Pascalutsa, "Evaluation of the forward Compton scattering off protons: Spin-independent amplitude", Phys. Rev. D **92**, 074031 (2015), arXiv:1508.07952 [nucl-th].

[3] O. Gryniuk, F. Hagelstein, and V. Pascalutsa, "Evaluation of the forward Compton scattering off protons: II. Spin-dependent amplitude and observables", Phys. Rev. D **94**, 034043 (2016), arXiv:1604.00789 [nucl-th].

[4] O. Gryniuk and M. Vanderhaeghen, "Accessing the real part of the forward J/ψ-p scattering amplitude from J/ψ photoproduction on protons around threshold", Phys. Rev. D **94**, 074001 (2016), arXiv:1608.08205 [hep-ph].

[5] A. Gérardin, J. Green, O. Gryniuk, G. von Hippel, H. B. Meyer, V. Pascalutsa, and H. Wittig, "Hadronic light-by-light scattering amplitudes from lattice QCD versus dispersive sum rules", Phys. Rev. D **98**, 074501 (2018), arXiv:1712.00421 [hep-lat].

[6] O. Gryniuk, S. Joosten, Z.-E. Meziani, and M. Vanderhaeghen, "Υ photo-production on the proton at the Electron-Ion Collider", (2020), arXiv:2005.09293 [hep-ph].

[7] J. Green, N. Asmussen, O. Gryniuk, G. von Hippel, H. B. Meyer, A. Nyffeler, and V. Pascalutsa, "Direct calculation of hadronic light-by-light scattering", PoS **LATTICE2015**, 109 (2016), arXiv:1510.08384 [hep-lat].

[8] A. Gérardin, J. Green, O. Gryniuk, G. von Hippel, H. B. Meyer, V. Pascalutsa, and H. Wittig, "Light-by-light forward scattering amplitudes in Lattice QCD", EPJ Web Conf. **175**, edited by M. Della Morte, P. Fritzsch, E. Gámiz Sánchez, and C. Pena Ruano, 06030 (2018), arXiv:1710.09359 [hep-lat].

[9] I. Anikin et al., "Nucleon and nuclear structure through dilepton production", Acta Phys. Polon. B **49**, 741–784 (2018), arXiv:1712.04198 [nucl-ex].

[10] N. Asmussen, A. Gérardin, J. Green, O. Gryniuk, G. von Hippel, H. B. Meyer, A. Nyffeler, V. Pascalutsa, and H. Wittig, "Hadronic light-by-light scattering contribution to the muon g – 2 on the lattice", EPJ Web Conf. **179**, edited by G. D'Ambrosio, M. Iacovacci, M. Passera, G. Venanzoni, and S. Mastroianni, 01017 (2018), arXiv:1801.04238 [hep-lat].

[11] J. Buchwald, *The rise of the wave theory of light: optical theory and experiment in the early nineteenth century* (University of Chicago Press, Chicago, 1989).

[12] R. G. Newton, "Optical theorem and beyond", American Journal of Physics **44**, 639–642 (1976).

[13] E. Sellmeier, Ann. Phys. (Leipzig) **143**, 272 (1871).

[14] H. J. Strutt, "Xv. on the light from the sky, its polarization and colour", The London, Edinburgh, and Dublin Philosophical Magazine and Journal of Science **41**, 107–120 (1871).

[15] M. Mie, Ann. Phys. (Leipzig) **25**, 377 (1908).

[16] R. de L. Kronig, "On the theory of dispersion of x-rays", J. Opt. Soc. Am. **12**, 547–557 (1926).

[17] H. A. Kramers, "La diffusion de la lumière par les atomes", Atti Cong. Intern. Fisici **2**, 545–557 (1927).

[18] J. S. Toll, "Causality and the dispersion relation: logical foundations", Phys. Rev. **104**, 1760–1770 (1956).

[19] E. Feenberg, "The scattering of slow electrons by neutral atoms", Phys. Rev. **40**, 40–54 (1932).

[20] J. A. Wheeler, "On the mathematical description of light nuclei by the method of resonating group structure", Phys. Rev. **52**, 1107–1122 (1937).

[21] W. Heisenberg, "Die "beobachtbaren größen" in der theorie der elementarteilchen", Zeitschrift für Physik **120**, 513–538 (1943).

[22] L. Puzikov, R. Ryndin, and I. Smorodinskii, Zh. Eksp. Teor. Fiz. **32**, 592 (1957).

[23] M. Gell-Mann, M. Goldberger, and W. E. Thirring, "Use of causality conditions in quantum theory", Phys. Rev. **95**, 1612–1627 (1954).

[24] M. L. Goldberger, Phys. Rev. **97** (1955).

[25] D. Drechsel, B. Pasquini, and M. Vanderhaeghen, "Dispersion relations in real and virtual Compton scattering", Phys. Rept. **378**, 99–205 (2003), arXiv:hep-ph/0212124.

[26] F. Hagelstein, R. Miskimen, and V. Pascalutsa, "Nucleon Polarizabilities: from Compton Scattering to Hydrogen Atom", Prog. Part. Nucl. Phys. **88**, 29–97 (2016), arXiv:1512.03765 [nucl-th].

[27] B. Pasquini and M. Vanderhaeghen, "Dispersion Theory in Electromagnetic Interactions", Ann. Rev. Nucl. Part. Sci. **68**, 75–103 (2018), arXiv:1805.10482 [hep-ph].

[28] W. Thirring, "Radiative corrections in the non-relativistic limit", The London, Edinburgh, and Dublin Philosophical Magazine and Journal of Science **41**, 1193–1194 (1950).

[29] F. Low, "Scattering of light of very low frequency by systems of spin 1/2", Phys. Rev. **96**, 1428–1432 (1954).

[30] M. Gell-Mann and M. Goldberger, "Scattering of low-energy photons by particles of spin 1/2", Phys. Rev. **96**, 1433–1438 (1954).

[31] D. Almond, "Low-energy theorem for Compton scattering by a spin 1/2 particle, without c, p, and t-invariance", Nucl. Phys. B **11**, 277–285 (1969).

[32] S. Saito, "Low-energy theorem for compton scattering", Phys. Rev. **184**, 1894–1902 (1969).

[33] S. Gerasimov, "A Sum rule for magnetic moments and the damping of the nucleon magnetic moment in nuclei", Sov. J. Nucl. Phys. **2**, 430–433 (1966).

[34] S. Drell and A. C. Hearn, "Exact Sum Rule for Nucleon Magnetic Moments", Phys. Rev. Lett. **16**, 908–911 (1966).

[35] A. M. Baldin, Nucl. Phys. **18**, 310 (1960).

[36] O. Tomalak, "Forward two-photon exchange in elastic lepton–proton scattering and hyperfine-splitting correction", The European Physical Journal C **77** (2017) 10.1140/epjc/s10052-017-5087-z.

[37] H. Bethe and W. Heitler, "On the stopping of fast particles and on the creation of positive electrons", Proc. R. Soc. Lond. A **146**, 83–112 (1934).

[38] V. Pauk and M. Vanderhaeghen, "Lepton Universality Test in the Photoproduction of e^-e^+ Versus $\mu^-\mu^+$ Pairs on a Proton Target", Phys. Rev. Lett. **115**, 221804 (2015).

[39] M. Schumacher, "Polarizability of the nucleon and Compton scattering", Prog. Part. Nucl. Phys. **55**, 567–646 (2005), arXiv:hep-ph/0501167.

[40] B. Pasquini, D. Drechsel, and M. Vanderhaeghen, "Proton spin polarizabilities from polarized Compton scattering", Phys. Rev. C **76**, 015203 (2007), arXiv:0705.0282 [hep-ph].

[41] P. A. Guichon, G. Liu, and A. W. Thomas, "Virtual Compton scattering and generalized polarizabilities of the proton", Nucl. Phys. A **591**, 606–638 (1995), arXiv:nucl-th/9605031.

[42] P. A. Guichon and M. Vanderhaeghen, "Virtual Compton scattering off the nucleon", Prog. Part. Nucl. Phys. **41**, 125–190 (1998), arXiv:hep-ph/9806305.

[43] B. Pasquini, D. Drechsel, M. Gorchtein, A. Metz, and M. Vanderhaeghen, "Dispersion relation formalism for virtual Compton scattering and the generalized polarizabilities of the nucleon", Phys. Rev. C **62**, 052201 (2000), arXiv:hep-ph/0007144.

[44] B. Pasquini, M. Gorchtein, D. Drechsel, A. Metz, and M. Vanderhaeghen, "Dispersion relation formalism for virtual Compton scattering off the proton", Eur. Phys. J. A **11**, 185–208 (2001), arXiv:hep-ph/0102335.

[45] D. Kharzeev, "Quarkonium interactions in QCD", Proc. Int. Sch. Phys. Fermi **130**, edited by A. Di Giacomo and D. Diakonov, 105–131 (1996), arXiv:nucl-th/9601029.

[46] M. Voloshin, "Charmonium", Prog. Part. Nucl. Phys. **61**, 455–511 (2008), arXiv:0711.4556 [hep-ph].

[47] A. Hosaka, T. Hyodo, K. Sudoh, Y. Yamaguchi, and S. Yasui, "Heavy Hadrons in Nuclear Matter", Prog. Part. Nucl. Phys. **96**, 88–153 (2017), arXiv:1606.08685 [hep-ph].

[48] S. J. Brodsky, I. Schmidt, and G. de Teramond, "NUCLEAR BOUND QUARKONIUM", Phys. Rev. Lett. **64**, 1011 (1990).

[49] D. Wasson, "Comment on 'Nuclear bound quarkonium.'", Phys. Rev. Lett. **67**, 2237 (1991).

[50] M. E. Luke, A. V. Manohar, and M. J. Savage, "A QCD Calculation of the interaction of quarkonium with nuclei", Phys. Lett. B **288**, 355–359 (1992), arXiv:hep-ph/9204219.

[51] M. E. Peskin, "Short Distance Analysis for Heavy Quark Systems. 1. Diagrammatics", Nucl. Phys. B **156**, 365–390 (1979).

[52] G. Bhanot and M. E. Peskin, "Short Distance Analysis for Heavy Quark Systems. 2. Applications", Nucl. Phys. B **156**, 391–416 (1979).

[53] S. J. Brodsky and G. A. Miller, "Is J/ψ - nucleon scattering dominated by the gluonic van der Waals interaction?", Phys. Lett. B **412**, 125–130 (1997), arXiv:hep-ph/9707382.

[54] S. H. Lee and C. Ko, "Charmonium in nuclear matter", edited by M. Buballa, W. Norenberg, B. Schaefer, and J. Wambach, 257–264 (2000), arXiv:nucl-th/0208003.

[55] K. Tsushima, D. Lu, G. Krein, and A. Thomas, "J/Ψ-nuclear bound states", Phys. Rev. C **83**, 065208 (2011), arXiv:1103.5516 [nucl-th].

[56] A. Yokota, E. Hiyama, and M. Oka, "Possible existence of charmonium–nucleus bound states", PTEP **2013**, 113D01 (2013), arXiv:1308.6102 [nucl-th].

[57] S. Beane, E. Chang, S. Cohen, W. Detmold, H. .-.-W. Lin, K. Orginos, A. Parreño, and M. Savage, "Quarkonium-Nucleus Bound States from Lattice QCD", Phys. Rev. D **91**, 114503 (2015), arXiv:1410.7069 [hep-lat].

[58] G. Krein, "Charmed hypernuclei and nuclear-bound charmonia", AIP Conf. Proc. **2130**, edited by L. Tang and R. Schumacher, 020022 (2019).

[59] T. Sugiura, Y. Ikeda, and N. Ishii, "Charmonium-nucleon interactions from $2+1$ flavor lattice QCD", PoS **LATTICE2018**, 093 (2019), arXiv:1905.02336 [nucl-th].

[60] J. Sakurai, "Theory of strong interactions", Annals of Physics **11**, 1–48 (1960).

[61] W. Heisenberg and H. Euler, "Consequences of Dirac's theory of positrons", Z. Phys. **98**, 714–732 (1936), arXiv:physics/0605038.

[62] R. Karplus and M. Neuman, "The scattering of light by light", Phys. Rev. **83**, 776–784 (1951).

[63] M. Aaboud et al., "Evidence for light-by-light scattering in heavy-ion collisions with the ATLAS detector at the LHC", Nature Phys. **13**, 852–858 (2017), arXiv:1702.01625 [hep-ex].

[64] A. Keshavarzi, D. Nomura, and T. Teubner, "Muon $g-2$ and $\alpha(M_Z^2)$: A new data-based analysis", Phys. Rev. D **97**, 114025 (2018).

[65] G. Bennett et al., "Final Report of the Muon E821 Anomalous Magnetic Moment Measurement at BNL", Phys. Rev. D **73**, 072003 (2006), arXiv:hep-ex/0602035.

[66] J. Grange et al., "Muon (g-2) Technical Design Report", (2015), arXiv:1501.06858 [physics.ins-det].

[67] T. Blum, A. Denig, I. Logashenko, E. de Rafael, B. Roberts, T. Teubner, and G. Venanzoni, "The Muon (g-2) Theory Value: Present and Future", (2013), arXiv:1311.2198 [hep-ph].

[68] M. Otani, "Design of the J-PARC MUSE H-line for the Muon g-2/EDM Experiment at J-PARC (E34)", JPS Conf. Proc. **8**, 025010 (2015).

[69] G. Venanzoni, "The New Muon g$-$2 experiment at Fermilab", Nucl. Part. Phys. Proc. **273-275**, edited by M. Aguilar-Benítez, J. Fuster, S. Martí-García, and A. Santamaría, 584–588 (2016), arXiv:1411.2555 [physics.ins-det].

[70] G. Colangelo, M. Hoferichter, M. Procura, and P. Stoffer, "Dispersive approach to hadronic light-by-light scattering", JHEP **09**, 091 (2014), arXiv:1402.7081 [hep-ph].

[71] G. Colangelo, M. Hoferichter, B. Kubis, M. Procura, and P. Stoffer, "Towards a data-driven analysis of hadronic light-by-light scattering", Phys. Lett. B **738**, 6–12 (2014), arXiv:1408.2517 [hep-ph].

[72] G. Colangelo, M. Hoferichter, M. Procura, and P. Stoffer, "Dispersion relation for hadronic light-by-light scattering: theoretical foundations", JHEP **09**, 074 (2015), arXiv:1506.01386 [hep-ph].

[73] V. Pauk and M. Vanderhaeghen, "Anomalous magnetic moment of the muon in a dispersive approach", Phys. Rev. D **90**, 113012 (2014), arXiv:1409.0819 [hep-ph].

[74] F. Hagelstein and V. Pascalutsa, "Dissecting the Hadronic Contributions to $(g-2)_\mu$ by Schwinger's Sum Rule", Phys. Rev. Lett. **120**, 072002 (2018), arXiv:1710.04571 [hep-ph].

[75] V. Pascalutsa and M. Vanderhaeghen, "Sum rules for light-by-light scattering", Phys. Rev. Lett. **105**, 201603 (2010), arXiv:1008.1088 [hep-ph].

[76] V. Pascalutsa, V. Pauk, and M. Vanderhaeghen, "Light-by-light scattering sum rules constraining meson transition form factors", Phys. Rev. D **85**, 116001 (2012), arXiv:1204.0740 [hep-ph].

[77] I. Danilkin and M. Vanderhaeghen, "Light-by-light scattering sum rules in light of new data", Phys. Rev. D **95**, 014019 (2017), arXiv:1611.04646 [hep-ph].

[78] L.-Y. Dai and M. Pennington, "Pascalutsa-Vanderhaeghen light-by-light sum rule from photon-photon collisions", Phys. Rev. D **95**, 056007 (2017), arXiv:1701.04460 [hep-ph].

[79] P. J. Mohr, B. N. Taylor, and D. B. Newell, *The 2014 CODATA Recommended Values of the Fundamental Physical Constants*, (Web Version 7.0) http://physics.nist.gov/constants.

[80] K. Olive et al., "Review of Particle Physics", Chin. Phys. C **38**, 090001 (2014).

[81] M. Tanabashi et al., "Review of Particle Physics", Phys. Rev. D **98**, 030001 (2018).

[82] M. Damashek and F. J. Gilman, "Forward Compton Scattering", Phys. Rev. D **1**, 1319–1332 (1970).

[83] T. Armstrong et al., "Total hadronic cross-section of gamma rays in hydrogen in the energy range 0.265-GeV to 4.215-GeV", Phys. Rev. D **5**, 1640–1652 (1972).

[84] U. Schroder, "Calculation of the Electric Polarizabilities of Proton and Neutron", Nucl. Phys. B **166**, 103–112 (1980).

[85] D. Babusci, G. Giordano, and G. Matone, "A New evaluation of the Baldin sum rule", Phys. Rev. C **57**, 291–294 (1998), arXiv:nucl-th/9710017.

[86] V. de Leon et al., "Low-energy Compton scattering and the polarizabilities of the proton", Eur. Phys. J. A **10**, 207–215 (2001).

[87] H. Alvensleben et al., "Experimental verification of the Kramers-Kronig relation at high energy", Phys. Rev. Lett. **30**, 328–332 (1973).

[88] J. Ahrens et al., "Helicity dependence of gamma p –¿ N pi below 450-MeV and contribution to the Gerasimov-Drell-Hearn sum rule", Phys. Rev. Lett. **84**, 5950–5954 (2000).

[89] J. Ahrens et al., "First measurement of the Gerasimov-Drell-Hearn integral for Hydrogen from 200 to 800 MeV", Phys. Rev. Lett. **87**, 022003 (2001), arXiv:hep-ex/0105089.

[90] H. Dutz et al., "First measurement of the Gerasimov-Drell-Hearn sum rule for H-1 from 0.7-GeV to 1.8-GeV at ELSA", Phys. Rev. Lett. **91**, 192001 (2003).

[91] H. Dutz et al., "Experimental Check of the Gerasimov-Drell-Hearn Sum Rule for H-1", Phys. Rev. Lett. **93**, 032003 (2004).

[92] B. Pasquini, P. Pedroni, and D. Drechsel, "Higher order forward spin polarizability", Phys. Lett. B **687**, 160–166 (2010), arXiv:1001.4230 [hep-ph].

[93] V. Lensky and V. Pascalutsa, "Manifestly-covariant chiral PT calculation of nucleon Compton scattering", Pisma Zh. Eksp. Teor. Fiz. **89**, 127–132 (2009), arXiv:0803.4115 [nucl-th].

[94] V. Lensky and V. Pascalutsa, "Predictive powers of chiral perturbation theory in Compton scattering off protons", Eur. Phys. J. C **65**, 195–209 (2010), arXiv:0907.0451 [hep-ph].

[95] V. Lensky, J. McGovern, and V. Pascalutsa, "Predictions of covariant chiral perturbation theory for nucleon polarisabilities and polarised Compton scattering", Eur. Phys. J. C **75**, 604 (2015), arXiv:1510.02794 [hep-ph].

[96] H. Griesshammer, J. McGovern, D. Phillips, and G. Feldman, "Using effective field theory to analyse low-energy Compton scattering data from protons and light nuclei", Prog. Part. Nucl. Phys. **67**, 841–897 (2012), arXiv:1203.6834 [nucl-th].

[97] J. McGovern, D. Phillips, and H. Griesshammer, "Compton scattering from the proton in an effective field theory with explicit Delta degrees of freedom", Eur. Phys. J. A **49**, 12 (2013), arXiv:1210.4104 [nucl-th].

[98] V. Lensky, J. A. McGovern, D. R. Phillips, and V. Pascalutsa, "What different variants of chiral EFT predict for the proton Compton differential cross section - and why", Phys. Rev. C **86**, 048201 (2012), arXiv:1208.4559 [nucl-th].

[99] D. Babusci, G. Giordano, A. L'vov, G. Matone, and A. Nathan, "Low-energy Compton scattering of polarized photons on polarized nucleons", Phys. Rev. C **58**, 1013–1041 (1998), arXiv:hep-ph/9803347.

[100] K. Levenberg, "A Method for the Solution of Certain Non-Linear Problems in Least Squares", Q. Appl. Math. **2**, 164–168 (1944).

[101] D. W. Marquardt, "An algorithm for least-squares estimation of nonlinear parameters", J. Soc. Ind. Appl. Math. **11(2)**, 431–441 (1963).

[102] D. Drechsel, S. Kamalov, and L. Tiator, "Unitary Isobar Model - MAID2007", Eur. Phys. J. A **34**, 69–97 (2007), arXiv:0710.0306 [nucl-th].

[103] R. L. Workman, M. W. Paris, W. J. Briscoe, and I. I. Strakovsky, "Unified Chew-Mandelstam SAID analysis of pion photoproduction data", Phys. Rev. C **86**, 015202 (2012), arXiv:1202.0845 [hep-ph].

[104] M. MacCormick et al., "Total photoabsorption cross-sections for H-1, H-2 and He-3 from 200-MeV to 800-MeV", Phys. Rev. C **53**, 41–49 (1996).

[105] O. Bartalini et al., "Measurement of the total photoabsorption cross section on a proton in the energy range 600-MeV - 1500-MeV at the GRAAL", Phys. Atom. Nucl. **71**, 75–82 (2008).

[106] D. O. Caldwell et al., "Measurements of the Photon Total Cross-Section on Protons from 18-GeV to 185-GeV", Phys. Rev. Lett. **40**, 1222 (1978).

[107] S. Aid et al., "Measurement of the total photon-proton cross-section and its decomposition at 200-GeV center-of-mass energy", Z. Phys. C **69**, 27–38 (1995), arXiv:hep-ex/9509001.

[108] S. Chekanov et al., "Measurement of the photon proton total cross-section at a center-of-mass energy of 209-GeV at HERA", Nucl. Phys. B **627**, 3–28 (2002), arXiv:hep-ex/0202034.

[109] R. Barnett et al., "Review of particle physics. Particle Data Group", Phys. Rev. D **54**, 1–720 (1996).

[110] K. Helbing, "The Gerasimov-Drell-Hearn Sum Rule", Prog. Part. Nucl. Phys. **57**, 405–469 (2006), arXiv:nucl-ex/0603021.

[111] B. R. Holstein, D. Drechsel, B. Pasquini, and M. Vanderhaeghen, "Higher order polarizabilities of the proton", Phys. Rev. C **61**, 034316 (2000), arXiv:hep-ph/9910427.

[112] N. Bianchi and E. Thomas, "Parameterization of [sigma(1/2) - sigma(3/2)] for Q**2 ¿= 0 and nonresonance contribution to the GDH sum rule", Phys. Lett. B **450**, 439–447 (1999), arXiv:hep-ph/9902266.

[113] See Supplemented Material for the numerical values of the resulting forward amplitudes and observables of proton CS: http://journals.aps.org/prd/abstract/10.1103/PhysRevD.94.034043#supplemental.

[114] N. Krupina, V. Lensky, and V. Pascalutsa, "Partial-wave analysis of proton compton scattering data below the pion-production threshold", Physics Letters B **782**, 34–41 (2018).

[115] L. G. Parratt, "Probability and Experimental Errors in Science", (1961).

[116] R. Tarrach, "Invariant Amplitudes for Virtual Compton Scattering Off Polarized Nucleons Free from Kinematical Singularities, Zeros and Constraints", Nuovo Cim. A **28**, 409 (1975).

[117] B. R. Holstein, V. Pascalutsa, and M. Vanderhaeghen, "Sum rules for magnetic moments and polarizabilities in QED and chiral effective-field theory", Phys. Rev. D **72**, 094014 (2005), arXiv:hep-ph/0507016.

[118] W.-Y. Tsai, L. Deraad, and K. Milton, "Compton scattering. ii. differential cross-sections and left-right asymmetry", Phys. Rev. D **6**, [Erratum: Phys.Rev.D 11, 703–703 (1975)], 1428–1438 (1972).

[119] K. Milton, W.-Y. Tsai, and L. Deraad, "Compton scattering. i. spectral forms for the invariant amplitudes to order e-to-the-4", Phys. Rev. D **6**, 1411–1427 (1972).

[120] M. M. Block, "Hadronic forward scattering: Predictions for the Large Hadron Collider and cosmic rays", Phys. Rept. **436**, 71–215 (2006), arXiv:hep-ph/0606215.

[121] G. Pancheri and Y. Srivastava, "Introduction to the physics of the total cross-section at LHC: A Review of Data and Models", Eur. Phys. J. C **77**, 150 (2017), arXiv:1610.10038 [hep-ph].

[122] A. Donnachie and P. Landshoff, "Does the hard pomeron obey Regge factorization?", Phys. Lett. B **595**, 393–399 (2004), arXiv:hep-ph/0402081.

[123] R. Godbole, A. Grau, G. Pancheri, and Y. Srivastava, "Total photoproduction cross-section at very high energy", Eur. Phys. J. C **63**, 69–85 (2009), arXiv:0812.1065 [hep-ph].

[124] M. Froissart, "Asymptotic behavior and subtractions in the Mandelstam representation", Phys. Rev. **123**, 1053–1057 (1961).

[125] M. Block and F. Halzen, "Evidence for the saturation of the Froissart bound", Phys. Rev. D **70**, 091901 (2004), arXiv:hep-ph/0405174.

[126] G. Antchev et al., "First determination of the ρ parameter at $\sqrt{s} = 13$ TeV: probing the existence of a colourless C-odd three-gluon compound state", Eur. Phys. J. C **79**, 785 (2019), arXiv:1812.04732 [hep-ex].

[127] G. Pancheri, S. Pacetti, and Y. Srivastava, "Analysis and Implications of precision near-forward TOTEM data", Phys. Rev. D **99**, 034014 (2019), arXiv:1811.00499 [hep-ph].

[128] F. Cornet, C. A. Garcia Canal, A. Grau, G. Pancheri, and S. Sciutto, "Photoproduction total cross section and shower development", Phys. Rev. D **92**, 114011 (2015), arXiv:1510.07279 [hep-ph].

[129] A. Accardi et al., "Electron Ion Collider: The Next QCD Frontier: Understanding the glue that binds us all", Eur. Phys. J. A **52**, edited by A. Deshpande, Z. Meziani, and J. Qiu, 268 (2016), arXiv:1212.1701 [nucl-ex].

[130] J. Bernauer et al., "High-precision determination of the electric and magnetic form factors of the proton", Phys. Rev. Lett. **105**, 242001 (2010), arXiv:1007.5076 [nucl-ex].

[131] J. Bernauer et al., "Electric and magnetic form factors of the proton", Phys. Rev. C **90**, 015206 (2014), arXiv:1307.6227 [nucl-ex].

[132] E. R. Berger, M. Diehl, and B. Pire, "Time - like Compton scattering: Exclusive photoproduction of lepton pairs", Eur. Phys. J. C **23**, 675–689 (2002), arXiv:hep-ph/0110062.

[133] S. L. Olsen, T. Skwarnicki, and D. Zieminska, "Nonstandard heavy mesons and baryons: Experimental evidence", Rev. Mod. Phys. **90**, 015003 (2018), arXiv:1708.04012 [hep-ph].

[134] S. Dubynskiy and M. Voloshin, "Hadro-Charmonium", Phys. Lett. B **666**, 344–346 (2008), arXiv:0803.2224 [hep-ph].

[135] R. Aaij et al., "Observation of $J/\psi p$ Resonances Consistent with Pentaquark States in $\Lambda_b^0 \to J/\psi K^- p$ Decays", Phys. Rev. Lett. **115**, 072001 (2015), arXiv:1507.03414 [hep-ex].

[136] R. Aaij et al., "Observation of a narrow pentaquark state, $P_c(4312)^+$, and of two-peak structure of the $P_c(4450)^+$", Phys. Rev. Lett. **122**, 222001 (2019), arXiv:1904.03947 [hep-ex].

[137] L. Roca, J. Nieves, and E. Oset, "LHCb pentaquark as a $\bar{D}^*\Sigma_c - \bar{D}^*\Sigma_c^*$ molecular state", Phys. Rev. D **92**, 094003 (2015), arXiv:1507.04249 [hep-ph].

[138] M. I. Eides, V. Y. Petrov, and M. V. Polyakov, "Narrow Nucleon-$\psi(2S)$ Bound State and LHCb Pentaquarks", Phys. Rev. D **93**, 054039 (2016), arXiv:1512.00426 [hep-ph].

[139] M. I. Eides, V. Y. Petrov, and M. V. Polyakov, "New LHCb pentaquarks as hadrocharmonium states", (2019), arXiv:1904.11616 [hep-ph].

[140] A. Hayashigaki, "J/ψ nucleon scattering length and in-medium mass shift of J/ψ in QCD sum rule analysis", Prog. Theor. Phys. **101**, 923–935 (1999), arXiv:nucl-th/9811092.

[141] O. Lakhina and E. S. Swanson, "Hybrid meson potentials and the gluonic van der Waals force", Phys. Lett. B **582**, 172–178 (2004), arXiv:hep-ph/0304273.

[142] A. Kaidalov and P. Volkovitsky, "Heavy quarkonia interactions with nucleons and nuclei", Phys. Rev. Lett. **69**, 3155–3156 (1992).

[143] A. Sibirtsev and M. Voloshin, "The Interaction of slow J/ψ and ψ' with nucleons", Phys. Rev. D **71**, 076005 (2005), arXiv:hep-ph/0502068.

[144] K. Yokokawa, S. Sasaki, T. Hatsuda, and A. Hayashigaki, "First lattice study of low-energy charmonium-hadron interaction", Phys. Rev. D **74**, 034504 (2006), arXiv:hep-lat/0605009.

[145] T. Kawanai and S. Sasaki, "Charmonium-nucleon potential from lattice QCD", Phys. Rev. D **82**, 091501 (2010), arXiv:1009.3332 [hep-lat].

[146] D. Kharzeev and H. Satz, "Quarkonium interactions in hadronic matter", Phys. Lett. B **334**, 155–162 (1994), arXiv:hep-ph/9405414.

[147] D. Kharzeev, H. Satz, A. Syamtomov, and G. Zinovjev, "J/ψ photoproduction and the gluon structure of the nucleon", Eur. Phys. J. C **9**, 459–462 (1999), arXiv:hep-ph/9901375.

[148] K. Redlich, H. Satz, and G. Zinovjev, "Photoproduction constraints on J/ψ nucleon interactions", Eur. Phys. J. C **17**, 461–465 (2000), arXiv:hep-ph/0003079.

[149] Jefferson Lab Experiment E12-12-006, Co-spokespersons K. Hafidi, Z.-E. Meziani (contact person), X. Qian, N. Sparveris, and Z. Zhao, PAC40, https://www.jlab.org/exp_prog/proposals/12/PR12-12-006.pdf.

[150] Jefferson Lab Experiment E12-12-001, Co-spokespersons M. Guidal, T. Horn, P. Nadel-Turonski (contact person), R. Paremuzyan, and S. Stepanyan, https://misportal.jlab.org/mis/physics/experiments/viewProposal.cfm?paperId=701.

[151] Jefferson Lab Experiment E12-16-007, Co-spokespersons S. Joosten, Z.-E. Meziani (contact person), M. Paolone, C. Chudakov, and M. Jones, PAC44, https://www.jlab.org/exp_prog/proposals/12/PR12-16-007.pdf, https://phys.cst.temple.edu/~meziani/Pc_main-v2.pdf.

[152] A. Ali et al., "First Measurement of Near-Threshold J/ψ Exclusive Photoproduction off the Proton", Phys. Rev. Lett. **123**, 072001 (2019), arXiv:1905.10811 [nucl-ex].

[153] V. D. Barger and R. Phillips, "Properties of psi n Scattering", Phys. Lett. B **58**, 433–436 (1975).

[154] B. Gittelman, K. Hanson, D. Larson, E. Loh, A. Silverman, and G. Theodosiou, "Photoproduction of the psi (3100) Meson at 11-GeV", Phys. Rev. Lett. **35**, 1616 (1975).

[155] U. Camerini, J. Learned, R. Prepost, C. M. Spencer, D. Wiser, W. Ash, R. L. Anderson, D. Ritson, D. Sherden, and C. K. Sinclair, "Photoproduction of the psi Particles", Phys. Rev. Lett. **35**, 483 (1975).

[156] M. E. Binkley et al., "J/ψ Photoproduction from 60 GeV/c to 300 GeV/c", Phys. Rev. Lett. **48**, 73 (1982).

[157] B. H. Denby et al., "Inelastic and Elastic Photoproduction of J/ψ (3097)", Phys. Rev. Lett. **52**, 795–798 (1984).

[158] P. Frabetti et al., "A Measurement of elastic J/ψ photoproduction cross-section at Fermilab E687", Phys. Lett. B **316**, 197–206 (1993).

[159] S. Chekanov et al., "Exclusive photoproduction of J/ψ mesons at HERA", Eur. Phys. J. C **24**, 345–360 (2002), arXiv:hep-ex/0201043.

[160] K. Abe et al., "charm photoproduction at 20 GeV", Phys. Rev. D **30**, 1 (1984).

[161] A. Clark et al., "Cross-Section Measurements for Charm Production by Muons and Photons", Phys. Rev. Lett. **45**, 682–686 (1980).

[162] J. Aubert et al., "Production of charmed particles in 250-GeV μ^+ - iron interactions", Nucl. Phys. B **213**, 31–64 (1983).

[163] M. Adamovich et al., "Cross-sections and Some Features of Charm Photoproduction at γ Energies of 20-GeV to 70-GeV", Phys. Lett. B **187**, 437–441 (1987).

[164] M. Derrick et al., "Study of D*+- (2010) production in e p collisions at HERA", Phys. Lett. B **349**, 225–237 (1995), arXiv:hep-ex/9502002.

[165] J. J. More, B. S. Garbow, and K. E. Hillstrom, "User Guide for Minpack-1", (1980).

[166] J. Aubert et al., "Measurement of J/ψ production in 280-GeV/c μ^+ iron interactions", Phys. Lett. B **89**, 267–270 (1980).

[167] Q. Wang, X.-H. Liu, and Q. Zhao, "Photoproduction of hidden charm pentaquark states $P_c^+(4380)$ and $P_c^+(4450)$", Phys. Rev. D **92**, 034022 (2015), arXiv:1508.00339 [hep-ph].

[168] X.-D. Ji, "A QCD analysis of the mass structure of the nucleon", Phys. Rev. Lett. **74**, 1071–1074 (1995), arXiv:hep-ph/9410274.

[169] W.-J. Deng, H. Liu, L.-C. Gui, and X.-H. Zhong, "Spectrum and electromagnetic transitions of bottomonium", Phys. Rev. D **95**, 074002 (2017), arXiv:1607.04696 [hep-ph].

[170] N. Brambilla, G. Krein, J. Tarrús Castellà, and A. Vairo, "Long-range properties of $1S$ bottomonium states", Phys. Rev. D **93**, 054002 (2016), arXiv:1510.05895 [hep-ph].

[171] C. Adloff et al., "Elastic photoproduction of J/ψ and Upsilon mesons at HERA", Phys. Lett. B **483**, 23–35 (2000), arXiv:hep-ex/0003020.

[172] J. Breitweg et al., "Measurement of elastic Upsilon photoproduction at HERA", Phys. Lett. B **437**, 432–444 (1998), arXiv:hep-ex/9807020.

[173] S. Chekanov et al., "Exclusive photoproduction of upsilon mesons at HERA", Phys. Lett. B **680**, 4–12 (2009), arXiv:0903.4205 [hep-ex].

[174] R. Aaij et al., "Measurement of the exclusive Υ production cross-section in pp collisions at $\sqrt{s} = 7$ TeV and 8 TeV", JHEP **09**, 084 (2015), arXiv:1505.08139 [hep-ex].

[175] A. M. Sirunyan et al., "Measurement of exclusive Υ photoproduction from protons in pPb collisions at $\sqrt{s_{\mathrm{NN}}} = 5.02$ TeV", Eur. Phys. J. C **79**, 277 (2019), arXiv:1809.11080 [hep-ex].

[176] C. Adloff et al., "Measurement of open beauty production at HERA", Phys. Lett. B **467**, [Erratum: Phys.Lett.B 518, 331–332 (2001)], 156–164 (1999), arXiv:hep-ex/9909029.

[177] J. Aubert et al., "Observation of Wrong Sign Trimuon Events in 250-GeV Muon - Nucleon Interactions", Phys. Lett. B **106**, 419–422 (1981).

[178] S. Joosten, Argonne l/A-event Generator (2020), GitLab Repository, https://eicweb.phy.anl.gov/monte_carlo/lager.

[179] E. Martynov, E. Predazzi, and A. Prokudin, "Photoproduction of vector mesons in the soft dipole pomeron model", Phys. Rev. D **67**, 074023 (2003), arXiv:hep-ph/0207272.

[180] R. Fiore, L. Jenkovszky, V. Magas, S. Melis, and A. Prokudin, "Exclusive J/ψ electroproduction in a dual model", Phys. Rev. D **80**, 116001 (2009), arXiv:0911.2094 [hep-ph].

[181] J. Breitweg et al., "Exclusive electroproduction of ρ^0 and J/ψ mesons at HERA", Eur. Phys. J. C **6**, 603–627 (1999), arXiv:hep-ex/9808020.

[182] K. Schilling and G. Wolf, "How to analyze vector meson production in inelastic lepton scattering", Nucl. Phys. B **61**, 381–413 (1973).

[183] T. Blum, S. Chowdhury, M. Hayakawa, and T. Izubuchi, "Hadronic light-by-light scattering contribution to the muon anomalous magnetic moment from lattice QCD", Phys. Rev. Lett. **114**, 012001 (2015), arXiv:1407.2923 [hep-lat].

[184] T. Blum, N. Christ, M. Hayakawa, T. Izubuchi, L. Jin, and C. Lehner, "Lattice Calculation of Hadronic Light-by-Light Contribution to the Muon Anomalous Magnetic Moment", Phys. Rev. D **93**, 014503 (2016), arXiv:1510.07100 [hep-lat].

[185] T. Blum, N. Christ, M. Hayakawa, T. Izubuchi, L. Jin, C. Jung, and C. Lehner, "Connected and Leading Disconnected Hadronic Light-by-Light Contribution to the Muon Anomalous Magnetic Moment with a Physical Pion Mass", Phys. Rev. Lett. **118**, 022005 (2017), arXiv:1610.04603 [hep-lat].

[186] N. Asmussen, J. Green, H. B. Meyer, and A. Nyffeler, "Position-space approach to hadronic light-by-light scattering in the muon $g-2$ on the lattice", PoS **LATTICE2016**, 164 (2016), arXiv:1609.08454 [hep-lat].

[187] N. Asmussen, A. Gérardin, H. B. Meyer, and A. Nyffeler, "Exploratory studies for the position-space approach to hadronic light-by-light scattering in the muon $g-2$", EPJ Web Conf. **175**, edited by M. Della Morte, P. Fritzsch, E. Gámiz Sánchez, and C. Pena Ruano, 06023 (2018), arXiv:1711.02466 [hep-lat].

[188] A. Nyffeler, "Precision of a data-driven estimate of hadronic light-by-light scattering in the muon $g-2$: Pseudoscalar-pole contribution", Phys. Rev. D **94**, 053006 (2016), arXiv:1602.03398 [hep-ph].

[189] A. Gérardin, H. B. Meyer, and A. Nyffeler, "Lattice calculation of the pion transition form factor $\pi^0 \to \gamma^*\gamma^*$", Phys. Rev. D **94**, 074507 (2016), arXiv:1607.08174 [hep-lat].

[190] S. Gerasimov and J. Moulin, "Check of Sum Rules for Photon Interaction Cross-Sections in Quantum Electrodynamics and Mesodynamics", Yad. Fiz. **23**, 142–153 (1976).

[191] V. Budnev, V. Chernyak, and I. Ginzburg, "Kinematics of gamma gamma scattering", Nucl. Phys. B **34**, 470–476 (1971).

[192] V. Budnev, I. Ginzburg, G. Meledin, and V. Serbo, "The Two photon particle production mechanism. Physical problems. Applications. Equivalent photon approximation", Phys. Rept. **15**, 181–281 (1975).

[193] P. Fritzsch, F. Knechtli, B. Leder, M. Marinkovic, S. Schaefer, R. Sommer, and F. Virotta, "The strange quark mass and Lambda parameter of two flavor QCD", Nucl. Phys. B **865**, 397–429 (2012), arXiv:1205.5380 [hep-lat].

[194] K. G. Wilson, "Confinement of Quarks", edited by J. Taylor, 45–59 (1974).

[195] B. Sheikholeslami and R. Wohlert, "Improved Continuum Limit Lattice Action for QCD with Wilson Fermions", Nucl. Phys. B **259**, 572 (1985).

[196] K. Jansen and R. Sommer, "O(a) improvement of lattice QCD with two flavors of Wilson quarks", Nucl. Phys. B **530**, [Erratum: Nucl.Phys.B 643, 517–518 (2002)], 185–203 (1998), arXiv:hep-lat/9803017.

[197] T. Blum, T. Izubuchi, and E. Shintani, "New class of variance-reduction techniques using lattice symmetries", Phys. Rev. D **88**, 094503 (2013), arXiv:1208.4349 [hep-lat].

[198] L.-Y. Dai and M. R. Pennington, "Comprehensive amplitude analysis of $\gamma\gamma \to \pi^+\pi^-, \pi^0\pi^0$ and $\bar{k}k$ below 1.5 GeV", Phys. Rev. D **90**, 036004 (2014), arXiv:1404.7524 [hep-ph].

[199] I. Larin et al., "A New Measurement of the π^0 Radiative Decay Width", Phys. Rev. Lett. **106**, 162303 (2011), arXiv:1009.1681 [nucl-ex].

[200] H. Behrend et al., "A Measurement of the pi0, eta and eta-prime electromagnetic form-factors", Z. Phys. C **49**, 401–410 (1991).

[201] J. Gronberg et al., "Measurements of the meson - photon transition form-factors of light pseudoscalar mesons at large momentum transfer", Phys. Rev. D **57**, 33–54 (1998), arXiv:hep-ex/9707031.

[202] B. Aubert et al., "Measurement of the gamma gamma* —¿ pi0 transition form factor", Phys. Rev. D **80**, 052002 (2009), arXiv:0905.4778 [hep-ex].

[203] S. Uehara et al., "Measurement of $\gamma\gamma^* \to \pi^0$ transition form factor at Belle", Phys. Rev. D **86**, 092007 (2012), arXiv:1205.3249 [hep-ex].

[204] G. Lepage and S. J. Brodsky, "Exclusive Processes in Quantum Chromodynamics: Evolution Equations for Hadronic Wave Functions and the Form-Factors of Mesons", Phys. Lett. B **87**, 359–365 (1979).

[205] G. Lepage and S. J. Brodsky, "Exclusive Processes in Perturbative Quantum Chromodynamics", Phys. Rev. D **22**, 2157 (1980).

[206] S. J. Brodsky and G. Lepage, "Large Angle Two Photon Exclusive Channels in Quantum Chromodynamics", Phys. Rev. D **24**, 1808 (1981).

[207] V. Nesterenko and A. Radyushkin, "Comparison of the QCD Sum Rule Approach and Perturbative QCD Analysis for $\gamma^*\gamma^* \to \pi^0$ Process", Sov. J. Nucl. Phys. **38**, 284 (1983).

[208] V. Novikov, M. A. Shifman, A. Vainshtein, M. Voloshin, and V. I. Zakharov, "Use and Misuse of QCD Sum Rules, Factorization and Related Topics", Nucl. Phys. B **237**, 525–552 (1984).

[209] M. Masuda et al., "Study of π^0 pair production in single-tag two-photon collisions", Phys. Rev. D **93**, 032003 (2016), arXiv:1508.06757 [hep-ex].

[210] P. Achard et al., "f(1)(1285) formation in two photon collisions at LEP", Phys. Lett. B **526**, 269–277 (2002), arXiv:hep-ex/0110073.

[211] P. Achard et al., "Study of resonance formation in the mass region 1400 to 1500 MeV through the reaction $\gamma\gamma \to K^0_S K^\pm \pi^\mp$", JHEP **03**, 018 (2007).

[212] L.-Y. Dai and M. Pennington, "Two photon couplings of the lightest isoscalars from BELLE data", Phys. Lett. B **736**, 11–15 (2014), arXiv:1403.7514 [hep-ph].

[213] http://lcgapp.cern.ch/project/cls/work-packages/mathlibs/minuit/index.html (2006).

[214] https://www.gnu.org/software/gsl/ (2017).

[215] L. Landau, "On the angular momentum of a system of two photons", Dokl. Akad. Nauk SSSR **60**, 207–209 (1948).

[216] C.-N. Yang, "Selection Rules for the Dematerialization of a Particle Into Two Photons", Phys. Rev. **77**, 242–245 (1950).

[217] J. Krimmer, W. Heil, S. Karpuk, E. W. Otten, and Z. Salhi, "Polarized ^{3}He targets in medium energy physics at MAMI", Journal of Physics: Conference Series **294**, 012015 (2011).

[218] S. Costanza, "Measurement of helicity dependent total inclusive γ–^{3}He cross section and the GDH sum rule on the neutron", Journal of Physics: Conference Series **349**, 012011 (2012).

[219] M. Heller, O. Tomalak, S. Wu, and M. Vanderhaeghen, "Leading order corrections to the Bethe-Heitler process in the $\gamma p \to l^+ l^- p$ reaction", Phys. Rev. D **100**, 076013 (2019).

List of acronyms

CS	Compton Scattering
TCS	Timelike Compton Scattering
fCS	forward Compton Scattering
fTCS	quasi-real-forward Timelike Compton Scattering
HLbL	Hadronic Light-by-Light scattering
CM	(lepton pair) Center-of-Mass frame of reference
DR	Dispersion Relation
OT	Optical Theorem
VMD	Vector Meson Dominance
FSP	Forward Spin Polarizability
χPT	Chiral Perturbation Theory
BχPT	Baryon χPT
HBχPT	Heavy Baryon χPT
NLO	Next-to-Leading Order
QFT	Quantum Field Theory
QED	Quantum ElectroDynamics
QCD	Quantum ChromoDynamics
CERN	European Organization for Nuclear Research
LHC	Large Hadron Collider
CMS	Compact Muon Solenoid
DESY	Deutsches Elektronen-Synchrotron
HERA	Hadron-Electron Ring Accelerator
SAID	Scattering Analysis Interactive Dialin
MAID	Mainz Analysis Interactive Dialin
MAMI	Mainz Microtron
ELSA	Electron Stretcher and Accelerator
BNL	Brookhaven National Laboratory
LEGS	Laser Electron Gamma Source
EIC	Electron-Ion Collider
JLab	Thomas Jefferson National Accelerator Facility
Fermilab	Fermi National Accelerator Laboratory
J-PARC	Japan Proton Accelerator Research Complex
PDG	Particle Data Group
CODATA	Committee on Data for Science and Technology
DL	Donnachie and Landshoff
BlHa	Block and Halzen
BH	Bethe-Heitler
GDH	Gerasimov, Drell and Hearn